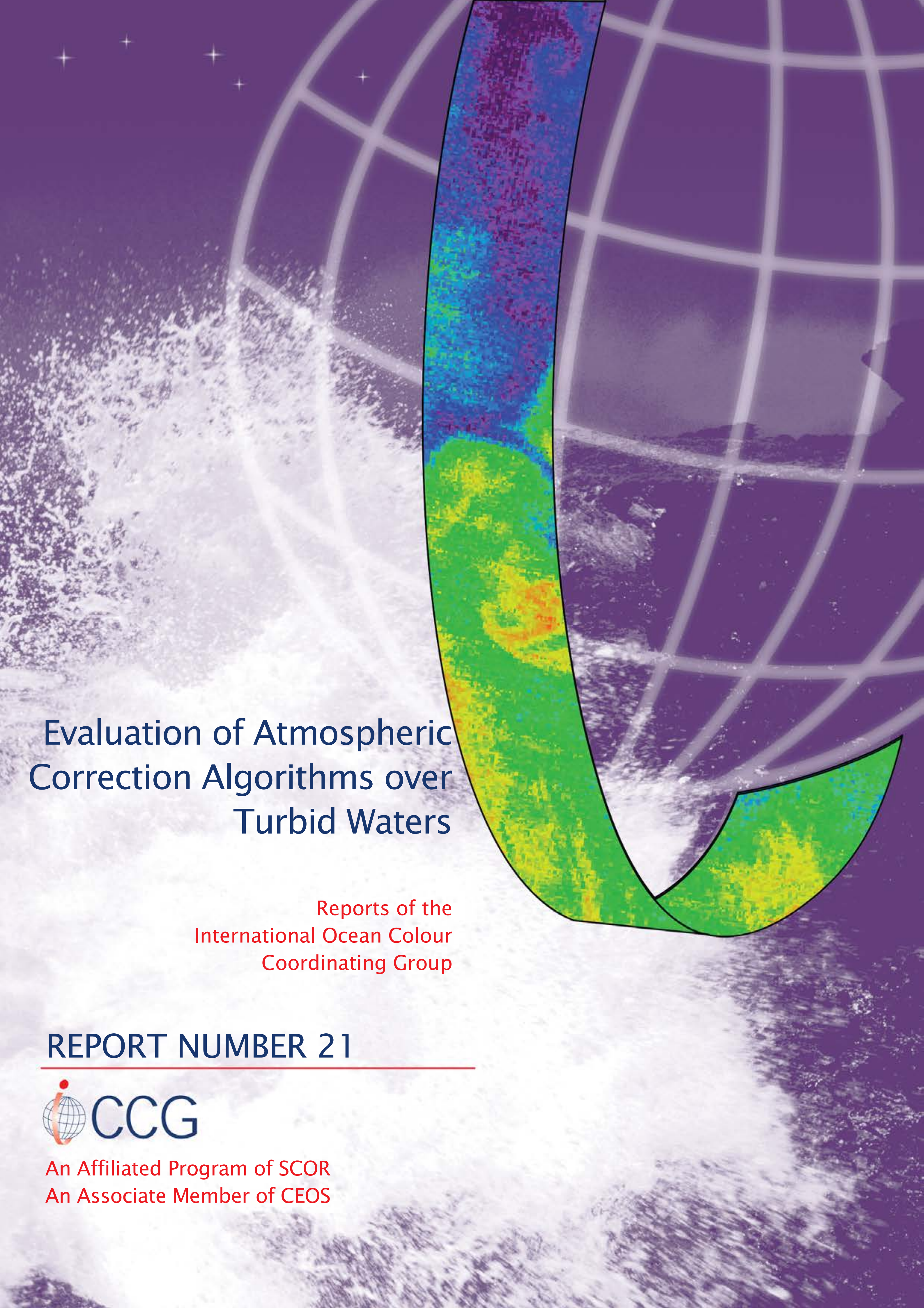

Evaluation of Atmospheric Correction Algorithms over Turbid Waters

Reports of the
International Ocean Colour
Coordinating Group

REPORT NUMBER 21

IOCCG

An Affiliated Program of SCOR
An Associate Member of CEOS

In the IOCCG Report Series:

1. *Minimum Requirements for an Operational Ocean-Colour Sensor for the Open Ocean (1998)*
2. *Status and Plans for Satellite Ocean-Colour Missions: Considerations for Complementary Missions (1999)*
3. *Remote Sensing of Ocean Colour in Coastal, and Other Optically-Complex, Waters (2000)*
4. *Guide to the Creation and Use of Ocean-Colour, Level-3, Binned Data Products (2004)*
5. *Remote Sensing of Inherent Optical Properties: Fundamentals, Tests of Algorithms, and Applications (2006)*
6. *Ocean-Colour Data Merging (2007)*
7. *Why Ocean Colour? The Societal Benefits of Ocean-Colour Technology (2008)*
8. *Remote Sensing in Fisheries and Aquaculture (2009)*
9. *Partition of the Ocean into Ecological Provinces: Role of Ocean-Colour Radiometry (2009)*
10. *Atmospheric Correction for Remotely-Sensed Ocean-Colour Products (2010)*
11. *Bio-Optical Sensors on Argo Floats (2011)*
12. *Ocean-Colour Observations from a Geostationary Orbit (2012)*
13. *Mission Requirements for Future Ocean-Colour Sensors (2012)*
14. *In-flight Calibration of Satellite Ocean-Colour Sensors (2013)*
15. *Phytoplankton Functional Types from Space (2014)*
16. *Ocean Colour Remote Sensing in Polar Seas (2015)*
17. *Earth Observations in Support of Global Water Quality Monitoring (2018)*
18. *Uncertainties in Ocean Colour Remote Sensing (2019)*
19. *Synergy between Ocean Colour and Biogeochemical/Ecosystem Models (2020)*
20. *Observation of Harmful Algal Blooms with Ocean Colour Radiometry (2021)*
21. *Evaluation of Atmospheric Correction Algorithms over Turbid Waters (this volume)*

Reports and Monographs of the International Ocean Colour Coordinating Group

An Affiliated Program of the Scientific Committee on Oceanic Research (SCOR)
An Associated Member of the Committee on Earth Observation Satellites (CEOS)

IOCCG Report Number 21, 2025

Evaluation of Atmospheric Correction Algorithms over Turbid Waters

Edited by:
Cédric Jamet and Sundarabalan V. Balasubramanian

Report of the IOCCG working group on the Intercomparison of Atmospheric Correction Algorithms Over Optically-Complex Waters, chaired by Cédric Jamet, and based on contributions from (in alphabetical order):

Sean Bailey	OB.DAAC/Ocean Biology Processing Group, NASA Goddard Space Flight Center, USA
Sundarabalan V. Balasubramanian	Laboratoire d’Océanologie et de Géosciences, Université du Littoral-Côte d’Opale, France
Xianqiang He	State Key Laboratory of Satellite Ocean Environment Dynamics, Second Institute of Oceanography, Ministry of Natural Resources, China
Cédric Jamet	Laboratoire d’Océanologie et de Géosciences, Université du Littoral-Côte d’Opale, France
Thomas Schroeder	CSIRO, Australia
Palanasimy Shanmugam	Indian Institute of Technology, India
Knut Stamnes	Stevens Institute of Technology, USA
Sindy Sterckx	VITO, Belgium

Series Editor: Raisha Lovindeer

Correct citation for this publication:

IOCCG (2025). Evaluation of Atmospheric Correction Algorithms over Turbid Waters. Jamet, C., Balasubramanian, S. V. (eds.), IOCCG Report Series, No. 21, International Ocean Colour Coordinating Group, Dartmouth, Canada.

The International Ocean Colour Coordinating Group (IOCCG) is an international group of experts promoting the application of remotely-sensed ocean-colour and inland water radiometric data across all aquatic environments, acting as a liaison and communication channel between users, managers and agencies in the ocean colour arena.

This IOCCG working group acknowledges Menghua Wang's input during its initial phase, and Kevin Ruddick for his feedback during the progress of the working group. They also thank François Steinmetz and Chuqun Chen for providing their algorithms, and acknowledge the University of Littoral-Côte d'Opale (ULCO, France) for one-year postdoc funding for Sundarabalan V. Balasubramaniana. The authors thank the PIs, Co-Is, and their staff and funders for establishing and maintaining the eight AERONET-OC stations used in this investigation. Work within the working group was done in the frame of two projects funded by the TOSCA program of CNES. Data were sourced from Australia's Integrated Marine Observing System (IMOS) – IMOS is enabled by the National Collaborative Research Infrastructure Strategy (NCRIS). NCRIS/IMOS and CSIRO are acknowledged for funding the Lucinda Jetty Coastal Observatory. The working group acknowledges the MODIS mission scientists and associated NASA personnel for the production of the Aqua data used in this report.

The IOCCG is sponsored by the Centre National d'Etudes Spatiales (CNES, France), Canadian Space Agency (CSA, Canada), Commonwealth Scientific and Industrial Research Organisation (CSIRO, Australia), Department of Fisheries and Oceans (Bedford Institute of Oceanography, Canada), European Commission/Copernicus Programme, European Organisation for the Exploitation of Meteorological Satellites (EUMETSAT), European Space Agency (ESA), Indian Space Research Organisation (ISRO), Japan Aerospace Exploration Agency (JAXA), Joint Research Centre (JRC, EC), Korea Institute of Ocean Science and Technology (KIOST), National Aeronautics and Space Administration (NASA, USA), National Oceanic and Atmospheric Administration (NOAA, USA), Scientific Committee on Oceanic Research (SCOR), and the State Key Laboratory of Satellite Ocean Environment Dynamics (Second Institute of Oceanography, Ministry of Natural Resources, China)

http://www.ioccg.org

Published by the International Ocean Colour Coordinating Group,
P.O. Box 1006, Dartmouth, Nova Scotia, B2Y 4A2, Canada.

ISSN: 1098-6030
ISBN:

Contents

Executive Summary

Remote sensing of coastal waters is a difficult task. One very important reason to monitor the colour of the ocean in coastal waters is the presence of suspended particulate matter and coloured dissolved organic matter. However, the presence of those optically-complex materials make the processing of ocean colour images challenging. The historic hypothesis on the black pixel, i.e., the ocean being totally absorbent in the near infra-red, is no longer valid. It is, thus, necessary to consider the bright pixel hypothesis in the near infra-red. Numerous methods have been developed over the past two decades that address turbid waters. Round-robin evaluation of all published algorithms is a very hard task and very time-consuming, but is important for the community. In this report, we evaluated ten atmospheric correction algorithms using in-situ measurements and a simulated dataset applied to data from the MODIS-Aqua sensor. We ranked the performances of the atmospheric correction algorithms depending on optical water types from clear to moderately turbid waters. The atmospheric correction algorithms OC-SMART (Ocean Color - Simultaneous Marine and Aerosol Retrieval Tool), NASA's standard atmospheric correction algorithm, and the Near and Shortwave Infrared atmospheric correction algorithm of Wang & Shi (2007, NIRSWIR) appeared to provide the overall best performance when applied to all optical water types over the datasets included in this study. For a specific optical water type, however, the algorithm with the best performance varied. Additional evaluations are required for application to Sentinel-3 OLCI and PACE OCI sensors, including algorithms that utilize specific bands from these sensors, as well as a more diverse array of optical water types, including highly turbid waters.

Chapter 1

Introduction

Sean Bailey, Xianqiang He, Cédric Jamet, Palanasimy Shanmugam, Thomas Schroeder, Knut Stamnes and Sindy Sterckx

This report is the result of an IOCCG Scientific Working Group (WG) on the evaluation of atmospheric correction algorithms over optically-complex waters, which started in 2014. The report aims to be a complementary addition to IOCCG Report 10 (IOCCG 2010), which primarily focuses on open ocean waters and standard atmospheric correction algorithms of NASA/SeaWiFS, ESA/MERIS, JAXA/GLI and NASA/MODIS-Aqua.

Optically-complex waters, especially turbid waters, have been the focus of several research efforts in the past decades. The WG felt it was time, not only to provide a comprehensive evaluation of the most common atmospheric correction schemes used in the ocean colour community, but also to provide guidance to end-users on the use of a specific atmospheric correction algorithm depending on the predominant optical water type (OWT).

The goal of the atmospheric correction process is to obtain accurate ocean colour radiometry (i.e. remote sensing reflectance, R_{rs}) by removing the contribution of the atmosphere from the signal measured by the space-borne sensor. While this process is somewhat simpler in open ocean waters due to the ocean being considered totally absorbing of sunlight in the near-infrared spectral range (NIR), it is more complicated in optically-complex waters, which are often encountered in coastal and inland areas.

Remote sensing of coastal and inland waters is difficult because:

- high concentrations of total suspended particulate matter (SPM) and/or coloured dissolved organic matter (CDOM) can be observed, which complicate the estimation of R_{rs}(NIR) and the correction of the Bidirectional Reflectance Distribution Function (BRDF);
- these areas are highly variable in space and time;
- the surrounding environment can affect the signal measured by the remote sensor (straylight contamination or adjacency effects);
- higher concentrations of non-maritime absorbing aerosols (e.g., dust or smoke) are often not considered by most available atmospheric correction algorithms;
- there may be anthropogenic emissions such as NO_2 absorption in the ultraviolet (UV) and visible (VIS) parts of the spectrum, overlapping with absorption by CDOM.

In this report, the WG focused mainly on turbid waters (non-zero R_{rs}(NIR)) because of the availability of long-term time series of in-situ measurements in coastal areas. Evaluation of atmospheric correction algorithms was done using MODIS-Aqua images, as an example application. MODIS-Aqua was chosen because it was the only remote sensor to have short-wave infra-red (SWIR) bands over a long time-period when the WG began, and MODIS-Aqua provided the longest time series of ocean colour radiometry (20+ years). Since then, Sentinel-3A and -B OLCI, as well as S-NPP, NOAA-20 and NOAA-21 VIIRS, and PACE OCI sensors have been launched. We believe that the results of this evaluation can be applicable to OLCI and VIIRS, because 1) the wavelengths are very similar, and 2) the principles of *most* algorithms are not sensor dependent, with only changes in sensor quality (e.g., Signal-to-Noise Ratio, SNR). Artificial Neural Networks (ANN)-based algorithms, however, do require sensor-specific training data. With a focus on MODIS-Aqua, atmospheric correction algorithms that used the 709 nm band (Moore et al. 1999) or the OLCI 1020 nm band (Gossn et al. 2019) were not included in this report.

The atmospheric correction algorithms chosen to be included in our evaluation are briefly presented in Chapter 2. Datasets used for the evaluation are presented in Chapter 3, with the creation of the synthetic dataset fully described in Chapters 4 and 5, and the definition of the match-up analyses and optical water types provided in Chapter 6. The results based on these datasets, including sensitivity studies, are presented in Chapters 7 and 8, with final algorithm rankings presented in Chapter 9. Chapter 10 discusses the environmental conditions that can further complicate atmospheric correction efforts when observing coastal and inland waters, such as adjacency effects and absorbing aerosols, which have not been considered in the algorithm inter-comparison of this report. Finally, a summary, along with recommendations and future directions are provided in Chapter 11.

Chapter 2

Atmospheric correction over turbid waters

This chapter first presents the basis of atmospheric correction (AC) and then describes the selected algorithms. The selection was based on algorithm availability, the popularity of the algorithms, and the willingness of the developers to share the code of their algorithm or process the data. The WG tried to select commonly used algorithms that are based on different approaches in order to investigate the sensitivity of the outputs to those criteria.

2.1 Principles of atmospheric correction

The purpose of the atmospheric correction process is to remove the contribution of the atmosphere to the signal measured by the remote sensor, leading to the estimation of the water-leaving radiance L_w. In the single-scattering approximation, the signal measured by the remote sensor at the top-of-the atmosphere (TOA) can be decomposed into several terms (Gordon and Wang 1994; Gordon 1997, IOCCG 2010; Mobley et al. 2016; Frouin et al. 2019):

$$L_{TOA} = L_R + L_a + L_{ra} + T \times L_g + t \times L_{wc} + t \times L_w \tag{2.1}$$

with

- L_{TOA}, the radiance measured at the top of the atmosphere
- L_R, the radiance due to scattering by air molecules (Rayleigh scattering) in the absence of aerosols
- L_a, the radiance due to scattering/absorption by aerosols in the absence of air molecules
- L_{ra}, the radiance due to the interaction between aerosols and air molecules (aerosols-Rayleigh scattering)
- L_g, the radiance due to specular reflection of Sunlight by the sea surface (Sun glint)
- L_{wc}, the radiance due to white caps
- L_w, the water-leaving radiance (the final parameter of interest)
- T, the direct transmittance from the surface to the sensor
- t, the diffuse transmittance in the viewing direction

Height, spectral and geometric dependencies were omitted in this notation. Rayleigh scattering, whitecap radiance, and sun glint contributions, as well as gas absorption can be estimated from radiative transfer modelling and ancillary data (Mobley et al. 2016). Thus, the atmospheric correction process aims to estimate the contribution of aerosols using the Rayleigh-corrected radiance:

$$L_{rc} = L_{TOA} - L_R = L_a + L_{ra} + t \times L_w = L_A + t \times L_w \tag{2.2}$$

where L_A is the sum of $L_a + L_{ra}$.

Equation 2.2 can be rewritten using the (dimensionless) reflectance factor $\rho = \frac{\pi L}{(F_0 \times \cos\theta_0)}$, where F_0 is the extraterrestrial solar irradiance and θ_0 is the solar zenith angle, as follows:

$$\rho_{rc} = \rho_{TOA} - \rho_R = \rho_a + \rho_{ra} + t \times \rho_w = \rho_A + t \times \rho_w \tag{2.3}$$

The parameter of interest is, generally, the remote sensing reflectance, $\mathrm{R_{rs}}$. The relationship between ρ_w and $\mathrm{R_{rs}}$ is given by:

$$R_{rs} = \frac{\rho_w}{\pi} \tag{2.4}$$

Over open ocean waters, the water-leaving radiance can generally be considered negligible in the near-infrared (NIR) (black pixel assumption; Gordon and Wang, 1994, Gordon, 1997), so the Rayleigh-corrected measured signal, ρ_{rc}, is only due to aerosols. This assumption no longer holds when intense algal blooms occur, or in the presence of *Sargassum* or sediments at the surface (Siegel et al. 2000; Stumpf et al. 2003; Schamberger et al. 2022). Thus, in turbid waters (the main focus of this report), there is a contribution of the water to the top-of-atmosphere signal in the NIR (IOCCG 2010). To overcome this challenge, many atmospheric correction algorithms have been developed in the past two decades for the major ocean colour remote sensors. These atmospheric correction algorithms can be grouped into the following categories (associated list of references is not exhaustive):

1. Assumptions about the NIR aerosols or water contributions (Hu et al. 2000; Ruddick et al. 2000; Jiang and Wang 2014; Vanhellemont and Ruddick 2021; Wang et al. 2021)
2. Use of shortwave infrared bands (Wang and Shi 2005 2007; Wang 2007; Shi and Wang 2009; Chen et al. 2014; He and Chen 2014; Gossn et al. 2021)
3. Use of blue or ultra-violet (UV) bands (He et al. 2004, 2012, 2013; Oo et al. 2008; Singh et al. 2019; Qiao et al. 2021; Liu et al. 2021; Wang et al. 2021; Bai et al. 2023)
4. Correction or modeling of the non-negligible water signal in the NIR to separate the water and atmospheric signatures and remove the water contribution in the NIR (Moore et al. 1999; Siegel et al. 2000; Stumpf et al. 2003; Lavender et al. 2005; Bailey et al. 2010; Jaelani et al. 2015; Ahn and Park 2020; Xue et al. 2021; Wang et al. 2022)
5. Full spectral coupled ocean/atmosphere inversion based on artificial neural networks (Doerffer and Schiller 2007; Schroeder et al. 2003, 2007, 2022; Fan et al. 2017, 2020, 2021; Ssenyonga et al. 2021; Song et al. 2023; Aryal et al. 2024; Pan and Bélanger 2024)
6. Optimization techniques that model water and atmospheric signals simultaneously (Chomko et al. 2003; Stamnes et al. 2003; Jamet et al. 2004; Brajard et al. 2006, 2012; Kuchinke et al. 2009; Steinmetz et al. 2011; Diouf et al. 2013; Shi et al. 2016; Pan et al. 2017; Ibrahim et al. 2019, 2022; Ssenyonga et al. 2021; Correa et al. 2023).

2.2 Algorithm descriptions

The algorithms used in this evaluation have been chosen based on their availability and use by the ocean colour community. The goal was not to consider all published atmospheric correction algorithms, but to select a subset of algorithms that are based on different assumptions to try to understand how these assumptions impact the accuracy of retrievals.

2.2.1 UV-based AC Algorithm (He et al. 2012)

The principle of the ultraviolet (UV) AC algorithm (UV-AC, He et al. 2012) considers that, in highly turbid waters, the water-leaving radiance at UV wavelengths can be neglected when compared to visible (VIS) or near-infrared (NIR) wavelengths because of strong absorption of UV radiation by detritus and CDOM. In turbid waters, water-leaving radiance increases greatly at longer VIS and NIR wavelengths due to strong particulate scattering, while strong combined absorption by detritus and CDOM cause a rapid decrease of water-leaving radiance in the UV (Bai et al. 2020). In extremely turbid waters, such as coastal and inland waters, water-leaving radiance in the UV is much lower than at NIR, making the UV band better suited for estimating aerosol scattering radiance than an NIR band. For satellite ocean colour sensors with no UV bands, the shortest wavelength (usually at 412 nm) can be used. For example, in SeaWiFS the shortest wavelength at 412 nm was used as the reference to estimate the aerosol scattering radiance. Assuming that the water-leaving reflectance at 412 nm can be neglected in highly turbid waters, the aerosol scattering reflectance at 412 nm can be estimated ($\rho_a(412) = \rho_{rc}(412)$). Based on an extrapolation method, the aerosol scattering reflectance at 865 nm can be estimated as follows:

$$\rho_a(865) = \rho_{rc}(412) \exp\left[c(412 - 865)\right] \tag{2.5}$$

$$c = \frac{\ln\left[\rho_{rc}(765)/\rho_{rc}(865)\right]}{(865 - 765)} \tag{2.6}$$

For application to satellite images from past and current sensors, the UV-AC was applied to the whole target region, which may include clear waters along with turbid waters. To avoid overestimation of aerosol scattering reflectance in clear waters, $\rho_a(865)$ was constrained by $\rho_{rc}(865)$ such that when the estimated $\rho_a(865)$ was larger than the $\rho_{rc}(865)$, it was set as $\rho_{rc}(865)$. Finally, a “white” aerosol scattering reflectance spectrum was assumed for the entire target region, where the aerosol scattering reflectance at all bands was set equal to $\rho_a(865)$.

2.2.2 Gaussian-spectral relationships - SS14 (Singh and Shanmugam 2014)

The AC algorithm of Singh and Shanmugam (2014; SS14) is based on a Gaussian-spectral relationship. To mitigate the correction by the water constituents, a correction factor, κ, is introduced, which is defined in terms of a band ratio to determine the extent of radiance contributed by various optically active water constituents in the NIR bands (Singh and Shanmugam 2014). In the spectral shape parameter (SSP) aerosol correction algorithm (Singh et al. 2019), κ helps in identifying the primary water types by obtaining the spectral slopes from

Rayleigh-corrected reflectance (ρ_{rc}) band ratios. The algorithm calculates the spectral slopes using violet (415 nm), blue (490 nm), green (536 nm), red (667 nm), fluorescence (684 nm), and NIR (747 nm) bands. At the initial stage of the κ estimation, its value is assumed to be unity for all pixels, assuming the reflectance image covers only the clear open oceanic water pixels. The value of κ then gets updated based on the ratios of the Rayleigh-corrected reflectance ρ_{rc} that considers:

1. the ratio of green and blue bands, which are sensitive to suspended sediment such that the value of κ will always be greater than one.
2. the ratio between red and violet, which becomes greater than one for extremely turbid waters.
3. the ratio between the red and fluorescence bands, which is useful for low-moderate productive waters and helps to identify in-water blooms.
4. the ratio between NIR and red bands, which helps to identify pixels dominated by floating algal blooms in highly productive waters.

Once the spectral band ratios are determined for all the pixels, the maximum value is considered the final value of κ and used to correct water contribution in the NIR.

2.2.3 SWIRE AC Algorithm (He and Chen 2014)

In the AC algorithm of He and Chen (2014), a new shortwave infrared extrapolation method (SWIRE) is used to correct the NIR bands. The Rayleigh-corrected reflectances in the SWIR bands (1.24, 1.64, and 2.13 µm) are used to determine an exponential function with respect to wavelength, which is used to correct the NIR bands (748 and 869 nm) for sediment scattering and hence estimate the aerosol scattering reflectances in these bands. The Rayleigh-corrected reflectances can be fitted with an exponential function in the NIR and SWIR bands for open ocean waters, but only in SWIR for turbid waters. The fitted function is called the extrapolated Rayleigh-corrected reflectance and is equal to: $\rho_{ref} = ae^{b\lambda}$, with a and b, the fitting coefficients. Their values are different for each pixel and therefore must be computed for each pixel of a given image. ρ_{ref} is then used to calculate the epsilon parameter ϵ in the NIR bands. The Gordon and Wang, 1994 atmospheric correction approach (GW94) is then applied.

2.2.4 MUMM AC (Ruddick et al. 2000)

The Management Unit of the North Sea Mathematical Models (MUMM; Ruddick et al. 2000), replaces the assumption that the water leaving radiance is zero in the NIR, and instead assumes spatial homogeneity at the 748/869 nm ratio for aerosol and water-leaving reflectances over a sub-scene of interest. The ratio of ρ_A reflectances at 748 and 869 nm (ϵ) is considered a calibration parameter that must be calculated for each sub-scene of interest. In addition, the ratio of ρ_w at 748 and 869 nm, α, is also considered a calibration parameter and is fixed to a value of 1.945 for MODIS-Aqua (Ruddick et al. 2000, 2006). These assumptions are used to extend GW94. Using the definitions of α and ϵ, the equations defining $\rho_A(748)$ and $\rho_A(869)$ become:

$$\rho_A(748) = \epsilon(748, 869) \times [\frac{\alpha\rho_{rc}(869) - \rho_{rc}(748)}{\alpha - \epsilon(748, 869)}] \tag{2.7}$$

$$\rho_A(869) = [\frac{\alpha\rho_{rc}(869) - \rho_{rc}(748)}{\alpha - \epsilon(748, 869)}] \tag{2.8}$$

The atmospheric correction process can be summarized as follows:

1. Use GW94 to produce a scatter plot of Rayleigh-corrected reflectances $\rho_{rc}(765)$ and $\rho_{rc}(865)$ for the region of study. Select the calibration parameter ϵ on the basis of this scatter plot.
2. Redo the atmospheric correction routine with data for Rayleigh-corrected reflectances $\rho_{rc}(748)$ and $\rho_{rc}(869)$ and use Eqns. 2.3 and 2.5 to determine $\rho_A(748)$ and $\rho_A(869)$, while taking account of non-zero water-leaving reflectances.
3. Continue as for the standard GW94.

This algorithm is implemented in SeaDAS, and SeaDAS v7.3 was used to retrieve outputs from this algorithm.

2.2.5 NASA Standard AC Algorithm (Bailey et al. 2010)

The NASA standard AC approach (NASA-AC; Bailey et al. 2010) estimates NIR reflectance through an iterative process based on a reflectance retrieval in red wavelengths (670 nm). The initial condition is based on the black-pixel assumption, from which an estimate of the visible water reflectance is obtained. The backscatter coefficient at 670 nm is estimated by inversion of the reflectance. This inversion assumes that the dominant absorption component is water, although an empirical estimate of the particulate absorption is also employed. A backscatter slope parameter defined by Lee et al. (2010) is derived from the retrieved reflectance spectrum and is used to propagate a backscatter coefficient from the red into the NIR (748 and 869 nm, for MODIS-Aqua). This propagated backscatter coefficient is used in a forward model to retrieve an estimate of water reflectance in the NIR, which is subtracted from the signal prior to the next iteration of the atmospheric correction. The iteration is continued until convergence of the red reflectance or a maximum iteration threshold is reached.

The version used is the one implemented in SeaDAS v7.3 with reprocessing R2018.

2.2.6 NIR-SWIR AC Algorithm (Wang and Shi 2007)

The NIR-SWIR AC algorithm (NIRSWIR; Wang and Shi 2007) combines GW94 for the open ocean waters with an atmospheric correction method using the SWIR bands at 1240 and 2130 nm (Wang and Shi 2005). The switch is based on a turbidity index (Shi and Wang 2007). The principle of NIRSWIR is the same as that for GW94, which considers the ocean to be black in the SWIR bands. This means that the water signal is negligible for those bands, and the top-of-atmosphere signal is only due to the atmospheric contributions. Parameter ϵ is calculated in the SWIR bands (the ratio of $\rho_A(1240)$ over$\rho_A(2130)$) and then used to estimate the aerosol optical properties and models.

The version of the algorithm used in this report is the version implemented in SeaDAS v7.3, with reprocessing R2018. This implementation may differ from the one implemented by NOAA and published by Shi and Wang (2007).

2.2.7 Polymer AC Algorithm (Steinmetz et al. 2011)

The Polymer AC algorithm (Polymer; Steinmetz et al. 2011) is a full-spectrum coupled spectral matching algorithm. It was originally developed for atmospheric correction of MERIS observations, in particular in the presence of sun glint, but has been extended to many other sensors. This algorithm relies firstly on a water reflectance model based on Park and Ruddick (2005) that has only two unknown parameters (chlorophyll concentration, and particulate backscattering) to represent a large variability of oceanic and coastal waters. Secondly, it relies on a model for the atmosphere and surface reflectance, $\rho_{ag}(\lambda)$, represented as a linear combination of three terms: $T_0(\lambda)c_0 + c_1\lambda^{-1} + c_2\rho_{mol}(\lambda)$. This analytical formulation does not rely on aerosol models, and allows accurate fitting of aerosol reflectance as well as other complex atmospheric and surface effects, in particular, residual sun glint. The formulation essentially relies on the general fact that atmospheric effects in $\rho_{ag}(\lambda)$ are spectrally smooth.

An iterative optimization scheme is applied pixel by pixel, using the Nelder-Mead simplex method, to retrieve the water and atmospheric parameters simultaneously. The final values of $\rho_{ag}(\lambda)$ are subtracted from the observation, which preserves fine spectral features from the observation.

Polymer is freely available for non-commercial purposes at `www.hygeos.com/polymer`. Polymer v4.1 was used in the report. Most of the modifications since this version are not applicable to MODIS-Aqua, however the latest version of Polymer may provide slightly different retrievals because of MODIS-Aqua system vicarious calibration and modifications to the spectral response function and Rayleigh correction.

2.2.8 ANN-based FUB AC Algorithm (Schroeder et al. 2007)

One Artificial Neural Network (ANN) algorithm deployed for this working group inter-comparison (hereafter referred to as FUB) was adapted to an approach previously developed by Schroeder (2005) and Schroeder et al. (2007) for MERIS but was based on a different learning algorithm. In contrast to atmospheric correction algorithms based on the black pixel assumption, the ANN method does not attempt to decouple atmospheric and oceanic light fields. Rather, it performs the correction directly on a pixel-by-pixel basis from the full TOA spectrum

A scalar version of the Matrix-Operator-MOdel (MOMO) was used to simulate the light field in a coupled ocean-atmosphere system and build a large database of more than 20 million spectra of R_{rs} at the mean sea level and TOA. A variety of sun and observing angles, as well as different concentrations of oceanic and atmospheric constituents were considered in the simulations and subsequently used to develop the ANN algorithm. The only difference in this study is the adoption of MODIS-Aqua spectral band settings. MODIS band 12 was simulated at 551 nm as the database computations were performed well before the 2009 NASA reprocessing, which redefined 551 nm to be 547 nm.

Inputs to the MOMO radiative transfer code consisted of atmospheric and oceanic inherent optical properties (IOPs) that were derived from Mie computations for the atmosphere, and in-water bio-optical model approximations mainly based on Coastal Surveillance Through Observation of Ocean Color (COASTLOOC) observations (Babin 2000). All simulations were performed for a US standard atmosphere, and eight aerosol assemblages each composed of a maritime and a continental aerosol model in the boundary layer (0–2 km) and troposphere (2–12 km), and a sulfuric acid background aerosol model in the stratosphere (12–50 km). The spectral aerosol extinction coefficients, at relative humidity between 70 and 99%, were provided by variable aerosol optical thickness (AOT) values ranging between 0.03 and 1 at 550 nm. A rough sea surface characterized by wind speeds of 1.5 and 7.2 m s^{-1} and barometric air pressure variations of 980 and 1040 hPa were considered for the atmospheric parameterization.

A total of 100,000 spectra at R_{rs} and TOA reflectances were extracted, of which one input vector consisted of the full TOA spectral reflectance in MODIS ocean colour bands 8-16 ($\lambda = 412.5 - 869.5$ nm), the angular information of the observing geometry transformed into Cartesian coordinates, the cosine of the sun zenith cos and the surface pressure. The associated output vector contained the log-transformed remote sensing reflectance in the MODIS bands 8-15 $(\lambda = 412.5 - 748$ nm).

As there were no direct pathways to obtain the optimum network architecture, a series of 170 different networks were trained by varying the number of hidden layers, the number of neurons on the hidden layers and several noise levels. Training was stopped for each configuration after 1,000 iteration cycles over the full training data set of 100,000 spectra and monitored by the Mean Squared Error (MSE). The best performing network was selected based on the results obtained from a match-up analysis independent of the one provided in this report. Its architecture consisted of 14 input nodes, 80 hidden layer neurons, and 12 neurons for the output layer trained with a random noise level of 0.8% for the TOA reflectance, 0.1% for each the geometry inputs and 2% for the surface pressure.

2.2.9 ANN-based OC-SMART AC Algorithm (Fan et al. 2017, 2021)

The Ocean Color - Simultaneous Marine and Aerosol Retrieval Tool (OC-SMART) is another model based on ANN for retrieval of aerosol optical depth (AOD) and R_{rs} values (Fan et al. 2017, 2021). A radiative transfer model for the coupled atmosphere-water system (AccuRT, Stamnes et al. 2018) was used to simulate the TOA radiances (L_{toa}) and R_{rs} values, simultaneously. This dataset was used to train ANNs to determine AOD and R_{rs} directly from L_{toa}. The simulations included the Ahmad aerosol models (Ahmad et al. 2010), polluted continental aerosol, the polluted maritime aerosol, and the desert aerosol models, from the Optical Properties of Aerosols and Clouds (OPAC) package (Koepke et al. 2015). Three bio-optical models were implemented: a modified Garver-Siegel-Maritorena (GSM) model (Maritorena et al. 2002; Fan et al. 2017), a modified CoastColour Round Robin (CCRR) model (Fan et al. 2016; Ruddick 2010) and the model of Morel et al. (2002). These ANN algorithms are very fast once the neural networks have been properly trained and are therefore suitable for operational use. A significant advantage is that they do not require SWIR bands, which implies significant cost reduction for dedicated OC missions. Such ANN algorithms have been extended for application to extreme atmospheric conditions (i.e. strongly polluted continental aerosols) over turbid coastal water by including appropriate aerosol and ocean bio-optical models to generate the required training datasets.

OC-SMART is freely available at `www.rtatmocn.com/oc-smart/`, and version v1.0 was used.

2.2.10 ANN-based C2RCC AC Algorithm (Doerffer and Schiller 2007)

The Case 2 Regional CoastColour (C2RCC) is the third AC algorithm included in this report based on ANN inversion (Schiller and Doerffer, 1997; Doerffer and Schiller 2007; Doerffer 2015). Similar to FUB and OC-SMART, C2RCC was trained with large datasets of simulated TOA reflectances and water-leaving reflectances. The model of the atmosphere was based on analysis of AERONET data of coastal sites. The water-leaving reflectances were simulated using the Hydrolight software (Mobley, 1989) for a large number of water constituents, including mineral particles and detritus, and various species of phytoplankton, bacteria and protozoa, based on the NASA bio-Optical Marine Algorithm Dataset (NOMAD; Werdell and Bailey 2005) and CoastColour datasets (Ruddick et al. 2010), Five IOPs were considered. The trained ANN performed the inversion of the top of atmosphere to estimate water-leaving reflectances. Similar to FUB and OC-SMART, negative $\mathrm{R_{rs}}$ retrievals were not possible due to logarithmic scaling of the $\mathrm{R_{rs}}$ data during training.

C2RCC code is available at `https://c2rcc.org/neural-nets/`. It was initially developed for MERIS and then for OLCI. A version for MODIS-AQUA exists but has not been fully validated and assessed. The working group decided to include this version in the analysis.

2.3 Important Caveats for Comparison

Algorithms NASA-AC, NIRSWIR, MUMM, UV-AC, SS14, SWIRE and OC-SMART use L_{rc} as inputs while the other algorithms use L_{TOA}. These latter algorithms, thus, do not consider the vicarious calibration of MODIS-Aqua. This difference may introduce a bias in their estimates and favour algorithms using L_{rc}.

While FUB, C2RCC and OC-SMART all belong to the same class of parametric machine learning algorithms, they use slightly different inverse model parametrizations (fixed versus adaptive learning rate, number of iterations, seeds, etc.). They also use different optimization algorithms to minimize the cost function (first-order versus second-order derived methods). More importantly, the simulated datasets used for training these algorithms were different in dimensions of input/output vectors, data scaling and transformation (linear, logarithmic, addition of noise etc.), and radiative transfer codes that had different bio-optical and atmospheric model approximations and assumptions.

Chapter 3

Summary description of datasets

3.1 Satellite dataset

For this algorithm evaluation, all AC algorithms were applied to MODIS-Aqua satellite images. MODIS-Aqua L1B data, reprocessing version 2014.0, were downloaded from NASA's Ocean Biology Processing Group (OBPG, `https://oceancolor.gsfc.nasa.gov`). Although this version was used, it is not expected that new reprocessing would change the conclusion of this report as R2018 and R2020 were concerned only with instrument calibration. Comparisons are available online (https://oceancolor.gsfc.nasa.gov/data/reprocessing/r2022/aqua/). Comparison of R2018 to R2014 showed that the revised absolute instrument calibration contributed to a significant bias shift in all spectral bands, of order 2%-10% on the global deep-water mean. However, as this concerns L1B data, which were the inputs for all algorithms, we do not expect that these reprocessings would change the conclusion of this report.

The L1B data were processed using SeaDAS v7.3.2 software to obtain Rayleigh-corrected reflectance.

3.2 Simulated dataset

An enhanced version of the simulated dataset developed in IOCCG Report 10 (IOCCG 2010) was developed to encompass a wider range of coastal waters.

The AccuRT radiative transfer code was used to generate: TOA radiances; TOA radiances corrected for gas absorptions; TOA radiances corrected for gas absorptions and Rayleigh scattering; aerosol and coupled Rayleigh/aerosol radiances; diffuse transmittance; and remote-sensing reflectance (Jin and Stamnes, 1994; Stamnes et al. 2017, 2018). The AccuRT simulations were checked against Hydrolight simulations and agreed quite well. Extensive comparisons with computations were also performed based on the vector radiative transfer model for the coupled ocean-atmosphere system (PCOART; He et al. 2007, 2010). These efforts are documented in Chapters 4 and 5.

In summary, the aerosol models used were taken from Ahmad et al. (2010). IOPs of the seawater were taken from the CoastColour project (Ruddick et al. 2010). In order to cover a wide range of atmospheric and water conditions, 20,000 cases were generated. For each ocean case, 4 aerosol models were randomly selected among the 80 possible models. Each aerosol model was applied to 5,000 water configurations. For each of the 20,000 cases, the geometry angles were randomly selected in the following ranges, and sun-glint geometry was avoided in the simulations:

- Solar Zenith Angle (SZA; θ_s): 0-70°
- Viewing Zenith Angle (VZA; θ_v): 0-70°
- Relative Azimuth Angle (RAA; $\Delta\phi = \phi_s - \phi_v$): 0-180°.

Simulated datasets were generated for MODIS-Aqua as outlined in Chapter 4. Additional datasets were also generated for SeaWiFS, VIIRS, MERIS and OLCI sensor. All simulated datasets are available in Supplemental Data 1. The datasets contain the following for each sensor:

1. Input parameters for the simulation, in the format: SZA, VZA, RAA, $\tau_a(865)$, angstrom(443/865), f_v, relative humidity (RH), CHL, CDOM, and mineral particles (MIN).
2. TOA radiances for each simulation case. These radiances were simulated with atmospheric gas absorption, Rayleigh scattering, aerosol and ocean IOPs turned on.
3. "Atmospheric-gas-corrected" TOA radiances for each simulation case. The radiances were simulated with atmospheric gas absorption turned off, but Rayleigh scattering, aerosol, and ocean IOPs turned on.
4. "Atmospheric-gas-and-Rayleigh-corrected" TOA radiances using data from the "atmospheric-gas-corrected" TOA radiances with pure Rayleigh scattering radiances subtracted. Pure Rayleigh scattering radiances were simulated with only Rayleigh scattering turned on, and atmospheric gas absorption, aerosol, and ocean IOPs turned off.
5. Remote sensing reflectance $\mathrm{R_{rs}}$ for each simulation case. The remote sensing reflectance was computed as the water leaving radiance divided by the downwelling irradiance just above the surface. The water leaving radiance was simulated as described in Chapter 4.7. The simulation was done with atmospheric gas absorption, Rayleigh scattering, and aerosols turned on in the atmosphere.
6. Reflectance for aerosols (no molecular scattering or absorption, but including molecule/aerosol interactions) at the TOA. These reflectances were computed as $\mathrm{Radiance_{aerosol}(TOA)/E_d(TOA)}$, and correspond to $\rho_a + \rho_{ra}$ as defined by Gordon and Wang (1994). As outlined in Chapter 4, there is a factor of π difference—Gordon and Wang (1994) defines the reflectance as $\rho = \pi L/(\mu_0 F_0)$ (the dimensionless bidirectional radiance reflectance factor), while we use $\rho = L/(\mu_0 F_0)$. $\mathrm{R_{rs}}$ is then calculated as $R_{rs} = \rho_w/\pi$.
7. Two-way diffuse transmittance for aerosols and molecular scattering (no molecular absorption).

3.3 In-situ dataset

In-situ datasets of remote-sensing reflectance and aerosol optical thickness were taken from the AERONET-Ocean Colour (AERONET-OC) network (Zibordi et al. 2009b, 2021). AERONET-OC is the ocean component of the Aerosol Robotic Network (AERONET, Holben et al. 1998) and is a system of autonomous sun photometers deployed around the globe, mainly in the

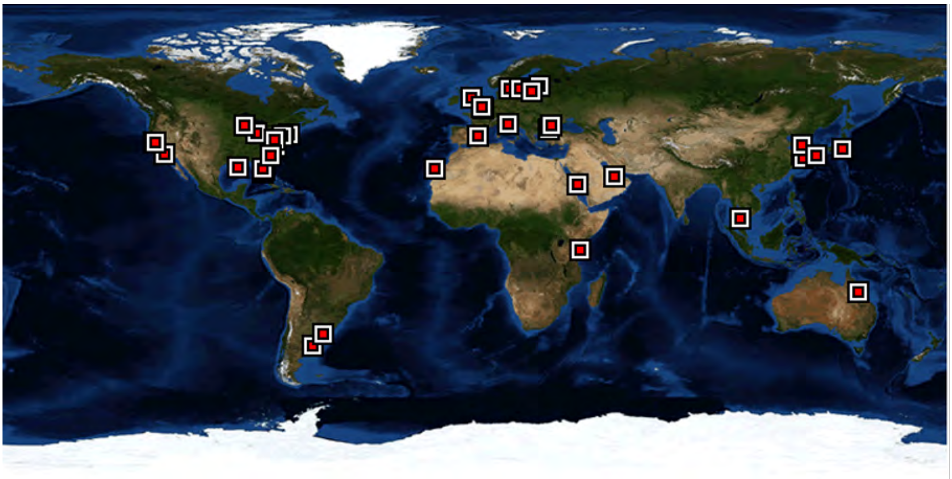

Figure 3.1 Maps of the global AERONET-OC stations. The stations used in this report are mentioned in Table 1. Figure replicated with permission from `https://aeronet.gsfc.nasa.gov`.

Table 3.1 AERONET-OC stations names, locations and number of data (N) used in our analyses

S.No	Station	Year	Lat	Lon	N
1	AAOT	2002-2015	45.31	12.50	1192
2	COVE_SEAPRISM	2006-2015	36.90	-75.71	38
3	Gustav_Dalen_Tower	2005-2015	58.59	17.46	268
4	Helsinki_Lighthouse	2006-2015	59.94	24.92	261
5	MVCO	2004-2015	41.30	-70.55	412
6	GLORIA	2011-2015	44.59	29.35	186
7	LUCINDA	2009-2015	-18.50	146.30	83
8	ZEEBRUGGE-MOW1	2014	51.36	3.12	16

northern hemisphere (Fig. 3.1). The network provides normalized water-leaving radiance (nL_W) and AOT at several wavelengths in the visible spectrum.

Advantages of using AERONET-OC data are that measurements are standardized and use identical systems and protocols, and data are calibrated and processed using a single method and with the same processing codes (Zibordi et al. 2006; 2009; 2021). Measurements are (optimally) taken several times daily, leading to a high number of potential match-ups to satellite data.

Table 3.1 presents the different AERONET-OC stations used for match-up analyses. The number and location of the stations were selected at the start of the working group's analyses, however new stations have since been created in more turbid waters that are not included here. Detailed characteristics of these selected AERONET-OC stations are provided in Feng et al. 2008; Zibordi et al. 2009, 2015, 2021; Mélin 2022; and Van der Zande et al. 2016. Note that many interesting cases with extreme absorption and scattering, or with high phytoplankton blooms were not captured by the AERONET-OC dataset.

Chapter 4

Creating the synthetic dataset

To create the synthetic dataset that mimics the radiative transfer process in the coupled atmosphere-water system, we adopted IOPs of the atmosphere and water that are based on empirical data. The purpose was not to create the most realistic top-of-the-atmosphere (TOA) radiances, but to simply create a dataset that was consistent with current knowledge of IOPs. This was to ensure that when these IOPs were used as input to a radiative transfer model (RTM) for the coupled system, plausible radiances would be produced for testing the AC algorithms. Like in the natural environment, the radiances were dependent on the IOPs of both the atmosphere and the underlying water column, as well as the reflection/transmission occurring at the air-water interface (in both directions).

4.1 Radiometric definitions

The total TOA radiance is usually written as in Eqn. 4.1 in units of W m^{-2} nm^{-1} sr^{-1}, or, if ignoring the part of the surface-reflected background sky radiance at the sea surface (L_{sky}) that reaches the TOA (L_{sky}^{TOA}), as in Eqn. 4.2.

$$L_t = L_R + [L_a + L_{aR}] + L_g^{TOA} + L_{sky}^{TOA} + L_{wc}^{TOA} + L_w^{TOA} \tag{4.1}$$

$$L_t = L_R + [L_a + L_{aR}] + TL_g + L_{sky}^{TOA} + tL_{wc} + tL_w \tag{4.2}$$

where L_t is the TOA total upward radiance; L_R is the TOA radiance due to molecular (Rayleigh) scattering only; L_a is the TOA radiance due to scattering/absorption by aerosols only; L_{aR} is the TOA radiance due to aerosol-molecule multiple scattering; L_g^{TOA} is the the part of the direct Sun glint radiance (L_g) that reaches the TOA; L_{wc}^{TOA} is the the part of the whitecap radiance L_{wc} that reaches the TOA; L_w^{TOA} is the the part of the water-leaving radiance (L_w) that reaches the TOA; and T is the direct transmittance between the sea surface and the TOA along the viewing direction.

We may refer to the total TOA radiance in terms of reflectance ($\rho \equiv \pi L/E_d$) as the unitless bidirectional reflectance factor (BRF) to distinguish it from the bidirectional reflection distribution function (BRDF) which has units sr^{-1}. The downward TOA irradiance, E_d, $= \mu_0 F_0$ where $\mu_0 = \cos\theta_0$, and F_0 is the TOA solar irradiance. Note that while the BRDF is an inherent optical property, the BRF is not. $\rho \equiv \pi L/E_d$ is unitless since π has units of sr and E_d has units of W m^{-2} nm^{-1}.

$$\rho_t = \rho_R + [\rho_a + \rho_{aR}] + T\rho_g + t\rho_{wc} + t\rho_w \tag{4.3}$$

where total TOA reflectance factor, $\rho_t = \pi L_t/E_d$; TOA reflectance factor due to molecular (Rayleigh) scattering only, $\rho_R = \pi L_R/E_d$; TOA reflectance factor due to aerosols only, $\rho_a = \pi L_a/E_d$; TOA reflectance factor due to molecule/aerosol multiple scattering only, $\rho_{aR} = \pi L_{aR}/E_d$; TOA reflectance factor due to aerosols + molecule/aerosol interactions, $\rho_{atm} = \pi[L_a + L_{aR}]/E_d = \rho_a + \rho_{aR}$; part of the glint reflectance factor $\pi L_g/E_d$ that reaches the TOA, $T\rho_g = T(\pi L_g/E_d)$; part of the whitecap reflectance, $\rho_{wc} = \pi L_{wc}/E_d$ that reaches the TOA, $t\rho_{wc} = t(\pi L_{wc}/E_d)$; part of the water-leaving reflectance factor, $\rho_w = (\pi L_w/E_d(\tau_a^+))$ reaching TOA, $t\rho_w = t(\pi L_w/E_d)$ with t being the the diffuse transmittance in the viewing direction.

4.2 Aerosol model and atmospheric profile

If we know the size distribution and the refractive index of the aerosol particles, we may use available aerosol models to generate aerosol IOPs: absorption and scattering coefficients and the scattering phase function. For atmospheric correction of ocean colour imagery, Gordon and co-workers (Gordon and Wang, 1994; Gordon 1997) selected 16 candidate aerosol models consisting of several types of particles, each having its own characteristic chemical composition, size distribution, and hygroscopicity. We used the aerosol models described by Ahmad et al. (2010), which are currently employed in SeaDAS. Based on AERONET data (Holben et al. 1998, 2001), Ahmad et al. (2010) adopted a bimodal log-normal volume size distribution as in Eqn. 4.4

$$v(r) = \frac{dV(r)}{dr} = \frac{1}{r}\frac{dV(\ln r)}{d\ln r} = \sum_{i=1}^{2} \frac{V_i}{\sqrt{2\pi}\sigma_i}\frac{1}{r}\exp\left[-\left(\frac{\ln r - \ln r_{vi}}{\sqrt{2}\sigma_i}\right)^2\right] \tag{4.4}$$

where the subscript i represents the mode, V_i the total volume of particles with mode i, r_{vi} the mode radius, also called the volume geometric mean radius, and σ_i the geometric standard deviation. Integration over all sizes for both modes, yields:

$$\int_0^\infty v(r)dr = V_1 + V_2 = V_f + V_c = V \tag{4.5}$$

where the subscript f stands for *fine* mode and the subscript c for *coarse* mode.

A change in the relative humidity (RH) will affect the size of the particle as well as the refractive index. The magnitude of the particle growth and the change of refractive index with increasing RH depends on the size of the dry aerosol, and on aerosol type (Hänel 1976; Shettle and Fenn 1979; Yan et al. 2002). To use Eqn. 4.4 for the bimodal log-normal volume size distribution, one must specify the fine mode volume fraction $f_v = V_f/V$, the volume mode radii r_{vf} and r_{vc}, the corresponding standard deviations σ_f and σ_c, and the refractive index of the particles relative to air (which may be assumed to be the same for both modes). We used the Ahmad et al. (2010) aerosol models implemented in SeaDAS with:

- 10 different aerosol fine mode volume fractions:
  $f_v = 0, 0.01, 0.02, 0.05, 0.10, 0.20, 0.30, 0.50, 0.80, 0.95$
- 8 different relative humidities (in percent):
  RH = 30, 50, 70, 75, 80, 85, 90, 95

yielding a total of 80 discrete aerosol models to represent aerosols over the ocean including coastal areas. Additional models may be added to represent aerosol conditions not included in the SeaDAS dataset.

Finally, we assumed a flat atmosphere-water interface and used the U.S. standard atmospheric profile with surface pressure of 1013 mbar, and an ozone column of 348 Dobson units in the simulations to compute Rayleigh scattering coefficients and absorption coefficients by all relevant gases.

4.3 Ocean bio-optical model and synthetic IOP dataset

The CoastColour Round Robin bio-optical model (CCRR; version 1.2, `https://coastcolour.org/round_robin.html` accessed 5 October 2010) was used. It can be applied to both Case 1 and Case 2 waters, and has a choice of three water parameters: chlorophyll-a concentration (CHL; mg m^{-3}), mineral particle mass concentration (MIN; g m^{-3}), and CDOM absorption coefficient at 443 nm (m^{-1}). The CCRR bio-optical model is fully described in Chapter 4.5.

The CCRR simulation dataset was used. This was similar to the synthetic dataset from IOCCG Report # 5 (IOCCG 2006). The simulation dataset has 5,000 combinations of the three water parameters (CHL, MIN, and CDOM) paired with 5,000 simulated remote sensing reflectances ($R_{rs}(\lambda_i)$) generated by the Hydrolight v5.0 radiative transfer model (Mobley 1994; Mobely et al. 1993). The 5,000 combinations of the ocean parameters are sampled so that the covariation between each pair of parameters matched that obtained from field measurements in coastal waters around Europe (Babin et al. 2003a).

Fig. 4.1 shows the covariation (panels a, b, and c) and the distribution (panel d) of the three input parameters. Note that the IOPs needed as input to the RTM are parametrized in terms of CHL, MIN, and CDOM (as explained in Chapter 4.5) in this synthetic dataset.

Fig. 4.2 shows a comparison between $R_{rs}(\lambda_i)$ values generated with the Hydrolight RTM (Mobley 1994) and with the AccuRT RTM (Stamnes et al. 2018), using the three water parameters (CHL, MIN, CDOM) in the CCRR simulation dataset (see Fig. 4.1) to generate water IOPs (see Chapter 4.5). Details about the computational procedure are provided in Chapter 4.6.

As shown in Fig. 4.2, the correlation between the two sets of $R_{rs}(\lambda_i)$ values has an R^2 of no less than 0.999 for all wavelengths. This good match means that for the same input IOPs the AccuRT RTM produces output very close to that of the Hydrolight RTM. We considered the CCRR synthetic IOP dataset, generated by varying the three water parameters (CHL, MIN, CDOM), to be very suitable for testing the atmospheric correction algorithms.

4.4 Procedure

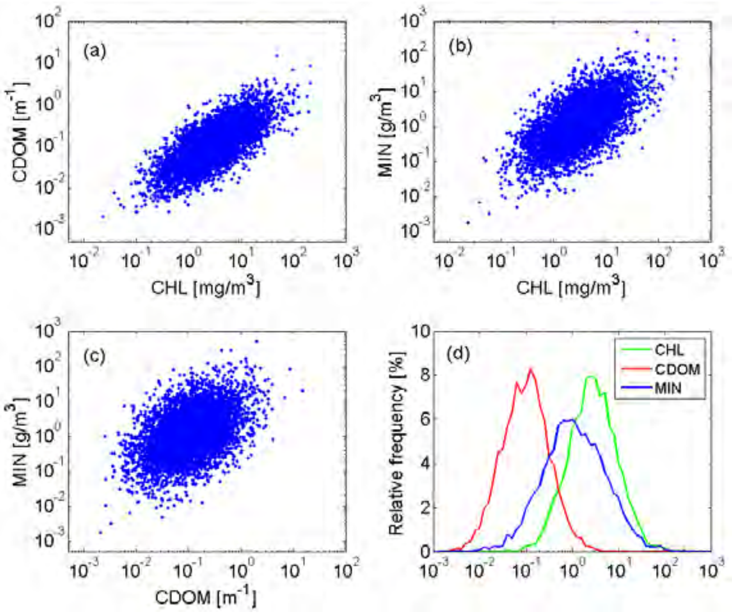

Figure 4.1 Covariation and distribution of CHL, MIN and CDOM in the CCRR synthetic dataset. Panels (a), (b) and (c) show the covariation between CHL and CDOM, between CHL and MIN, and between CDOM and MIN, respectively. Panel (d) shows the distribution of CHL (green), MIN (blue) and CDOM (red), the units of CHL, MIN and CDOM are given on the vertical axis in the first 3 panels.

4.4.1 Simulation dataset

In order to cover a wide range of atmospheric and water conditions, we generated 20,000 cases. As mentioned, for each ocean case, 4 aerosol models were randomly selected among the 80 possible models (4 aerosol configurations × 5,000 water configurations). For each of these 20,000 cases, the geometry angles were randomly selected in the following ranges

- SZA (θ_0): 0–70°
- VZA (θ_v): 0–70°
- RAA ($\Delta\phi = \phi_0 - \phi_v$): 0-180°.

The Sun-sensor geometry is illustrated in Fig. 4.3. The channels of existing and planned next generation sensors, including UV and SWIR bands, were included in the simulation datasets as summarized in Chapter 4.4.6. Algorithm developers may select channels appropriate for a particular sensor. Alternatively, by making a different channel selection, the *optimum* sensor could be determined.

4.4.2 Test dataset

A dataset for testing purposes included geometry angles and simulated TOA radiances for particular sensors for the 20,000 cases described above. Algorithm developers can use this dataset to retrieve aerosol parameters and $R_{rs}(\lambda_i)$ values on a case-by-case basis.

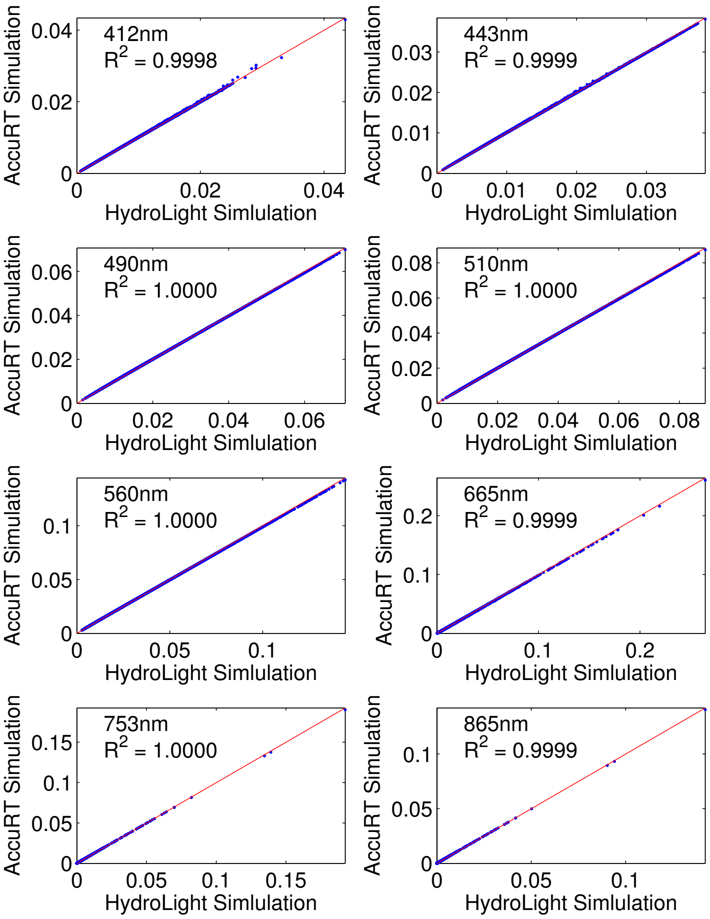

Figure 4.2 Comparison between R_{rs} values for the CCRR simulation dataset generated with Hydrolight and with AccuRT at 8 wavelengths: 412, 443, 490, 510, 560, 665, 753, and 865 nm.

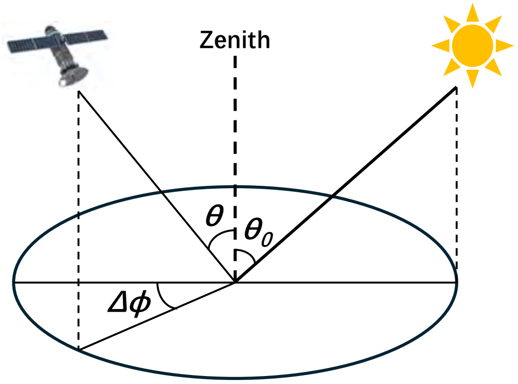

Figure 4.3 Sun-sensor geometry. Note that $\Delta\phi = 0$ corresponds to specular reflection.

4.4.3 Validation dataset

A dataset used exclusively for validation purposes contained the *answer key*, that is, the aerosol and water IOPs (scattering and absorption coefficients and the scattering phase function) for all 20,000 cases in the test dataset. This validation dataset can include, on a case-by-case basis, the input aerosol parameters (τ_{865} and fine mode bimodal fraction f_v), the water parameters (CHL, MIN, and CDOM), and corresponding $R_{rs}(\lambda_i)$ values, which are then compared with retrieval results (τ_{865}, f_v or Ångström coefficient, and $R_{rs}(\lambda_i)$ values).

4.4.4 Algorithm Evaluation & Assessment

A statistical validation was conducted, to provide a comprehensive way to assess the performance of each algorithm. The following major points were considered:

- Assessment of *atmosphere correction* performance: examination of the retrieved aerosol optical depth (AOD) and fine mode aerosol fraction f_v (or Ångström coefficient), and analysis of how the performance depends on aerosol loading, humidity, and water type (turbidity).
- The influence of water type: an assessment of how the accuracy of the retrieved $R_{rs}(\lambda_i)$ values depend on water type (see Fig. 4.1).
- The influence of geometry: assess how the retrieval error depends on geometry.
- Sensor channel selection: since different sensors have different channels, it may be possible to use the validation results to determine the best choice of channels for ocean colour retrieval. This can attempt to address the question of which combination of channels provided the best atmospheric correction, and hence the most reliable remote sensing reflectances.

4.4.5 Sunglint treatment validation

In the synthetic dataset described above, sun-glint geometry angles were avoided. It is possible to add a sun-glint dataset that can be used to test how the various atmospheric correction algorithms participating in this study deal with the sun-glint correction problem. To include this, algorithm providers can be given wind speed and direction along with the simulated satellite radiances in the glint area, which can be used to conduct sunglint correction.

4.4.6 Data files and format

Synthetic datasets were generated for 6 sensors: MODIS, MERIS, SeaWiFS, VIIRS, OLCI, and Copernicus Sentinel-3 Sea and Land Surface Temperature Radiometer (SLSTR). However, only MODIS was considered in this study. The centre wavelengths for each sensor are given in Table 4.1.

Seven files were generated for each sensor, named as follows, and as described in Chapter 3.2 and the accompanying README in Supplemental Data 1.

1. ”*sensor*_InputParameter.txt”,
2. ”*sensor*_RadianceTOA.txt”,

Table 4.1 Sensors and wavelengths for simulated data in the synthetic dataset.

Sensor	Wavelengths [nm]
MODIS	412 443 469 488 531 547 555 645 667 678 748 859 869 1240 1640 2130
MERIS	412 443 490 510 560 620 665 681 709 754 761 779 865 885 900
SeaWiFS	412 443 490 510 555 670 765 865
VIIRS	412 443 486 551 671 745 862 1238 1610 2257
OCLI	400 412 443 490 510 560 620 665 674 681 709 754 761 764 768 779 865 885 900 940 1020
SLSTR	555 659 865 1375 1610 2250

3. ”*sensor*_RadianceTOA_gas_corrected.txt”,
4. ”*sensor*_RadianceTOA_gas_rayleigh_corrected.txt”
5. ”*sensor*_Rrs.txt”
6. ”*sensor*_aerosolReflectance.txt”
7. ”*sensor*_diffuseTransmittance.txt”

Table 4.2 Solar irradiance (F_0) for MODIS.

λ (nm)	F_0 (W/m^2/nm)	F_0 (mW/cm^2/μm)	λ [(nm)	F_0 [(W/m^2/nm)	F_0 (mW/cm^2/μm)
412	1.72912	172.912	667	1.52255	152.255
443	1.87622	187.622	678	1.48052	148.052
469	2.05878	205.878	748	1.28065	128.065
488	1.94933	194.933	859	0.97174	97.174
531	1.85747	185.747	869	0.95824	95.824
547	1.86539	186.539	1240	0.45467	45.467
555	1.83869	183.869	1640	0.23977	23.977
645	1.57811	157.811	2130	0.09885	9.885

The TOA solar irradiance (normal to the beam) was set to $F_0 = 1.0$ for all the radiance calculations. In order to compare the radiances with satellite measurements, TOA solar irradiance data from the SeaDAS package are provided in Tables 4.2 - 4.5. To obtain the radiances in physical units, a multiplication by the F_0 values was required. These F_0 values are provided in Tables 4.2 - 4.5.

4.5 The CCRR Bio-optical Model

We adopted a bio-optical model used in the CoastColour Round Robin (CCRR) effort (described in Coastcolour-RRP-V1.2).

4.5.1 Pure water IOPs

For pure water we adopted the real part of the refractive index of pure water from Segelstein (1981), and used the absorption coefficient $\alpha_w(\lambda)$ based on data published by Smith and

Table 4.3 Solar irradiance (F_0) for MERIS.

λ (nm)	F_0 (W/m^2/nm)	F_0 (mW/cm^2/μm)	λ [(nm)	F_0 [(W/m^2/nm)	F_0 (mW/cm^2/μm)
412	1.71366	171.366	709	1.40546	140.546
443	1.87751	187.751	754	1.26620	126.620
490	1.92934	192.934	761	1.24979	124.979
510	1.92687	192.687	779	1.17571	117.571
560	1.80049	180.049	865	0.95888	95.888
620	1.64970	164.970	885	0.92975	92.975
665	1.53091	153.091	900	0.89544	89.544
681	1.47022	147.022			

Table 4.4 Solar irradiance (F_0) for SeaWiFS.

λ (nm)	F_0 (W/m^2/nm)	F_0 (mW/cm^2/μm)	λ [(nm)	F_0 [(W/m^2/nm)	F_0 (mW/cm^2/μm)
412	1.72998	172.998	555	1.82997	182.997
443	1.90154	190.154	670	1.51139	151.139
490	1.96438	196.438	765	1.22330	122.330
510	1.88164	188.164	865	0.96264	96.264

Baker (1981), Sogandares and Fry (1997), and Pope and Fry (1997) for wavelengths between 340 and 700 nm, and by Kou et al. (1993) for wavelengths between 720 and 900 nm. Pure water scattering coefficients $\beta_w(\lambda)$ were based on data published by Morel (1974), and the Rayleigh scattering phase function (Eqn. 4.6).

$$p_{Ray}(\cos\Theta) = \frac{3}{3+f}(1 + f\cos^2\Theta) \tag{4.6}$$

with depolarization ratio $\rho = 0.09$, and thus $f = (1-\rho)/(1+\rho) = 0.835$.

4.5.1.1 Scattering phase function for pure water

In AccuRT the expansion of the phase function $p(\cos\Theta)$ in Legendre polynomials is:

$$\chi_\ell = \frac{1}{2}\int_{-1}^{1} d(\cos\Theta)P_\ell(\cos\Theta)p(\cos\Theta) \tag{4.7}$$

where Θ is the scattering angle and $P_\ell(\cos\Theta)$ is the Legendre polynomial. For molecular (Rayleigh) scattering the phase function is given by Eqn. 4.6, and the expansion coefficients (moments) are simply

$$\chi_0 = 1,\ \ \chi_1 = 0,\ \ \chi_2 = \frac{2f}{5(3+f)},\ \ and\ \ \chi_\ell = 0\ \ for\ \ \ell > 2. \tag{4.8}$$

Table 4.5 Solar irradiance (F_0) for VIIRS.

λ (nm)	F_0 (W/m^2/nm)	F_0 (mW/cm^2/μm)	λ [(nm)	F_0 [(W/m^2/nm)	F_0 (mW/cm^2/μm)
412	1.71134	171.134	745	1.27643	127.643
443	1.90214	190.214	862	0.96031	96.031
486	1.98774	198.774	1238	0.45606	45.606
551	1.84122	184.122	1610	0.25084	25.084
671	1.50456	150.456	2257	0.07732	7.732

The parameter f in Eqn.4.8 is given by $f = \frac{1-\rho}{1+\rho}$, where ρ is the depolarization ratio attributed to the anisotropy of the scatterering (molecule). Using $\rho = 0.09$ for water, $f = \frac{1-\rho}{1+\rho} = 0.835$. Hence, for Rayleigh scattering by water molecules the scattering phase function moments become: $\chi_0 = 1, \quad \chi_1 = 0, \quad \chi_2 = 0.0871, \quad$ and $\quad \chi_\ell = 0 \quad$ for $\quad \ell > 2$ (Stamnes et al. 2017).

4.5.2 Water-impurity IOPs

The CCRR bio-optical model consists of the 3 input parameters CHL, MIN, and $\alpha_{CDOM}(443)$, which were allowed to vary. It should be noted that according to this decomposition into three basic components, the mineral particle component can also include non-algae particles, the absorption of which does not covary with that of algae particles.

4.5.2.1 Mineral particles

The absorption coefficient for mineral particles at 443 nm is given by Eqn. 4.9

$$\alpha_{MIN}(443) = 0.031 \times 0.75 \times MIN \tag{4.9}$$

and its spectral variation is described by Eqn. 4.10 (Babin et al. 2003a)[1].

$$\alpha_{MIN}(\lambda) = \alpha_{MIN}(443)[\exp(-0.0123(\lambda - 443))]. \tag{4.10}$$

The scattering coefficient at 555 nm is given by Eqn. 4.11 (Babin et al. 2003b):

$$\beta_{MIN}(555) = 0.51 \times MIN \tag{4.11}$$

and the spectral variation of the attenuation coefficient is as shown in Eqn. 4.12

$$\gamma_{MIN}(\lambda) = \gamma_{MIN}(555) \times (\lambda/\lambda_0)^{-c}; \qquad c = 0.3749, \qquad \lambda_0 = 555\ nm \tag{4.12}$$

where

$$\begin{aligned} \gamma_{MIN}(555) &= \alpha_{MIN}(555) + \beta_{MIN}(555) \\ &= [0.041 \times \exp(-0.0123(555 - 443)) + 0.51] \times MIN = 0.52 \times MIN. \end{aligned}$$

---

[1] Note on units: $\alpha_{MIN}(\lambda)/MIN = 0.041$ has units [m^{2}g^{-1}], so that if MIN has units of [g m^{-3}], then the units of $\alpha_{MIN}(\lambda)$ will be [m^{-1}].

The spectral variation of the scattering coefficient for mineral particles is thus

$$\beta_{MIN}(\lambda) = \gamma_{MIN}(\lambda) - \alpha_{MIN}(\lambda). \tag{4.13}$$

The average Petzold phase function, with a backscattering ratio of 0.026, as tabulated by Mobley (1994), was used to describe the scattering phase function for mineral particles.

4.5.2.2 Algae particles

The absorption coefficient for *pigmented* particles (algae particles or phytoplankton) can be written as in Eqn. 4.14 (Bricaud et al. 1998),

$$\alpha_{pig}(\lambda) = A_\phi(\lambda) \times [CHL]^{E_\phi(\lambda)} \tag{4.14}$$

where the function coefficients $A_\phi(\lambda)$ and $E_\phi(\lambda)$ are given by Bricaud et al. (1998) and CHL is the chlorophyll concentration, which represents the concentration of pigmented particles (algae particles or phytoplankton). The functions $A_\phi(\lambda)$ and $E_\phi(\lambda)$ are displayed in Fig. 4.4. Extrapolation into the UV spectral range was the same as that used in Hydrolight. Extrapolation into the infrared (beyond 700 nm) used a constant value.

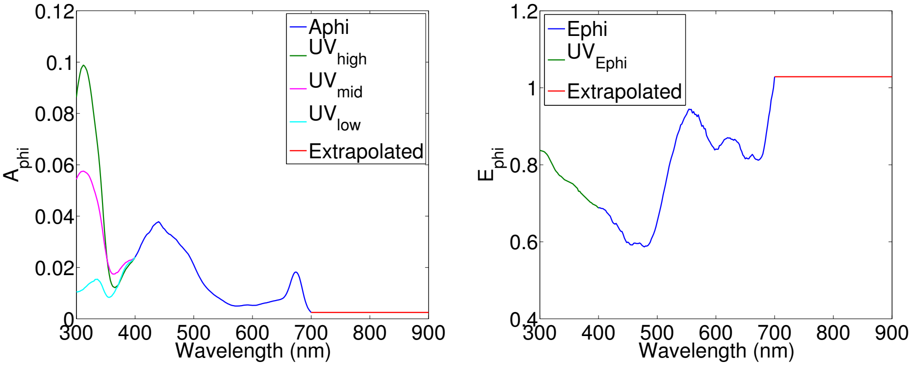

Figure 4.4 Spectral variation of the numerical coefficients $A_\phi(\lambda)$ (left) and $E_\phi(\lambda)$ (right) in Eqn. 4.14. The blue colour indicates original data provided by Bricaud et al. (1998). The red colour indicates extrapolated values.

The attenuation coefficient for pigmented particles at 660 nm is given by Loisel and Morel (1998):

$$\gamma_{pig}(660) = \gamma_0 \times [CHL]^\eta; \qquad \gamma_0 = 0.407; \qquad \eta = 0.795$$

and its spectral variation is as described in Eqn. 4.15 (Morel et al. 2002):

$$\gamma_{pig}(\lambda) = \gamma_{pig}(660) \times (\lambda/660)^\nu \tag{4.15}$$

where

$$\begin{array}{rcll} \nu & = & 0.5 \times [\log_{10} CHL - 0.3] & 0.02 < CHL < 2.0 \\ \nu & = & 0, & CHL > 2.0. \end{array}$$

The spectral variation of the scattering coefficient for pigmented particles follows from the difference between $\gamma_{pig}(\lambda)$ and $\alpha_{pig}(\lambda)$ (Eqn. 4.16).

$$\beta_{pig}(\lambda) = \gamma_{pig}(\lambda) - \alpha_{pig}(\lambda). \tag{4.16}$$

The scattering phase function for pigmented particles is assumed to be described by the Fournier-Forand (FF) phase function (see Chapter 4.5.2.5) with a backscattering ratio equal to 0.006 (Mobley et al. 2002, Morel et al. 2002).

4.5.2.3 Coloured Dissolved Organic Matter (CDOM)

Absorption by CDOM is given by Babin et al. (2003b):

$$\alpha_{CDOM}(\lambda) = \alpha_{CDOM}(443) \times \text{exp}[-0.0176(\lambda - 443)]. \tag{4.17}$$

4.5.2.4 Total Absorption and Scattering Coefficients

Total absorption and scattering coefficients due to water impurities for the CCRR IOP model are given by:

$$\alpha_{tot}(\lambda) = \alpha_{MIN}(\lambda) + \alpha_{pig}(\lambda) + \alpha_{CDOM}(\lambda) \tag{4.18}$$

$$\beta_{tot}(\lambda) \equiv \beta_p(\lambda) = \beta_{MIN}(\lambda) + \beta_{pig}(\lambda). \tag{4.19}$$

4.5.2.5 Scattering phase function for particles

Many measurements have shown that the particle size distribution (PSD) function in oceanic water can be accurately described by an inverse power law (Junge distribution) $F(r) = C_r/r^{\xi}$, where $F(r)$ is the number of particles per unit volume per unit bin width, and r [μm] is the radius of the assumed spherical particle. C_r [cm$^{-3} \cdot \mu$m$^{\xi-1}$] is the Junge coefficient, and ξ is the PSD slope, which typically varies between 3.0 and 5.0 (Diehl and Haardt, 1980; McCave, 1983). By assuming a Junge distribution for the PSD, Fournier and Forand (1994) derived an analytic expression for the scattering phase function of oceanic water (the FF scattering phase function). This FF scattering phase function is described in Eqn. 4.20 (Mobley et al. 2002),

$$\begin{aligned} p_{FF}(\cos\Theta) &= \frac{1}{4\pi(1-\delta)^2\delta^{\nu}}\left\{\nu(1-\delta) - (1-\delta^{\nu}) + \frac{4}{u^2}[\delta(1-\delta^{\nu}) - \nu(1-\delta)]\right\} \\ &+ \frac{1-\delta_{180}^{\nu}}{16\pi(\delta_{180}-1)\delta_{180}^{\nu}}[3\cos^2\Theta - 1] \end{aligned} \tag{4.20}$$

where $\nu = 0.5(3-\xi)$, $u = 2\sin(\Theta/2)$, $\delta \equiv \delta(\Theta) = \frac{u^2}{3(n-1)^2}$, $\delta_{180} = \delta(\Theta = 180°) = \frac{4}{3(n-1)^2}$, Θ is the scattering angle, ξ is the PSD slope, and n is the real part of the refractive index.

Setting $x = \cos\Theta$, and integrating the FF scattering phase function over the backward hemisphere, one obtains the backscattering ratio or backscatter fraction (Mobley et al. 2002)

$$\begin{aligned} b_{FF} &= \frac{1}{2}\int_{\pi/2}^{\pi} p_{FF}(\cos\Theta)\sin\Theta d\Theta = \frac{1}{2}\int_{0}^{1} dx\, p_{FF}(-x) \\ &= 1 - \frac{1-\delta_{90}^{\nu+1} - 0.5(1-\delta_{90}^{\nu})}{(1-\delta_{90})\delta_{90}^{\nu}} \end{aligned} \tag{4.21}$$

where $\delta_{90} = \delta(\Theta = 90°) = \frac{4}{3(n-1)^2}\sin^2(45°) = \frac{2}{3(n-1)^2}$. Eqn. 4.21 can be solved for ν in terms of b_{FF} and δ_{90}, implying that ν and thus ξ can be determined if the real part of the refractive index n and the backscatter fraction b_{FF} are specified. As a consequence, the FF scattering phase function can be evaluated from a measured value of b_{FF} if the real part of the refractive index n is known.

To describe the angular variation of the scattering, we used the FF scattering phase function for phytoplankton and the Rayleigh scattering phase function (Eqn. 4.6) for scattering by pure water. It was shown by Mobley et al. (2002) that with proper choices of n and ξ the FF scattering phase function is an excellent proxy for the well-known Petzold (1972) measurements. In a previous study, Li et al. (2008) used $n = 1.0686$, and $\xi = 3.38$, which corresponded to a backscatter fraction of 0.0056 (see Fig. 2 in Mobley et al. (2002)). As noted by Mobley at al. (2002), this choice of $\{n, \xi\}$ values is consistent with a certain mixture of living microbes and resuspended sediments. In the CCRR bio-optical model adopted here, the Petzold phase function with a backscattering ratio of 0.026 was used to represent mineral (non-algal) particles. These scattering phase functions are shown in Fig. 4.5. The moment-fitting method of Hu et al. (2000) was used to create Legendre expansion coefficients $\chi_{\ell,PET}$

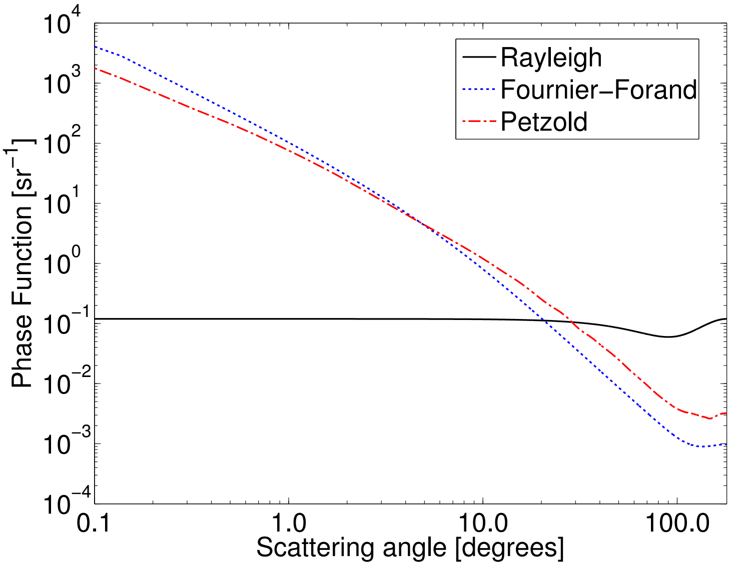

Figure 4.5 Rayleigh, Fournier-Forand and Petzold phase functions used to represent scattering by water molecules, pigmented particles, and non-algal particles, respectively, in AccuRT.

and $\chi_{\ell,FF}$ for the Petzold and FF scattering phase functions. Thus, the total scattering phase function Legendre expansion coefficients were:

$$\chi_\ell = \frac{\beta_{pig}(\lambda)\chi_{\ell,FF} + \beta_{MIN}(\lambda)\chi_{\ell,PET} + \beta_w(\lambda)\chi_{\ell,water}}{\beta_{pig}(\lambda) + \beta_{MIN}(\lambda) + \beta_w(\lambda)} \tag{4.22}$$

where the scattering phase function moments for pure water $\chi_{\ell,water}$ were as described in by Eqn. 4.8.

4.6 BRDF treatment

Suppose a radiometer located just above a water surface measures radiance

$$L_T(\lambda, \tau_a^+, \theta_v, \theta_0, \Delta\phi)$$

when pointed to the surface in direction $(\theta_v, \Delta\phi)$, and radiance

$$L_i(\lambda, \tau_a^+, \theta', \theta_0, \Delta\phi)$$

when pointed to the sky in direction $(\theta', \Delta\phi)$, where θ_0 is the solar zenith angle, and $\Delta\phi = \phi_0 - \phi_v$ is the relative azimuth with respect to the Sun. Here $\tau_a^+ \equiv 0^+$ is the optical depth of the atmosphere just above the water surface, θ_0 is the solar zenith angle, θ_v is the viewing polar angle in air, $\theta' = \sin^{-1}(\sin\theta_v/n_w)$ is the corresponding refracted polar angle (in water), and n_w is the refractive index of water relative to air. Then the water-leaving radiance $L_w(\lambda, \tau_a^+, \theta_v, \theta_0, \Delta\phi)$ (i.e., the radiance emerging from the water just above the surface) is

$$L_w(\lambda, \tau_a^+, \theta_v, \theta_0, \Delta\phi) = L_T(\lambda, \tau_a^+, \theta_v, \theta_0, \Delta\phi) - \rho(\theta_v, \theta_0, \phi, W)L_i(\lambda, \tau_a^+, \theta', \theta_0, \Delta\phi)$$

where $\rho(\theta_v, \theta_0, \Delta\phi, W)$ is the sea surface bidirectional reflectance distribution function (BRDF), and W stands for the wind speed (Zibordi et al. 2009). The normalized water-leaving radiance is defined as in Eqn. 4.23 (dropping the λ-dependence)

$$L_{wN} \equiv \frac{L_w(\tau_a^+, \theta_v, \theta_0, \Delta\phi)\bar{F}_0\varepsilon}{E_d(\tau_a^+)}, \qquad \varepsilon = \bar{d}/d \tag{4.23}$$

where $\bar{F}_0$ = mean extraterrestrial solar irradiance; $\bar{d}$ and d are the mean and actual Earth-Sun distances. Since the downward irradiance just above the water surface is $E_d(\tau_a^+) = t(\mu_0)\mu_0\bar{F}_0\varepsilon$, where $\mu_0 = \cos\theta_0$, $t(\mu_0)$ is the diffuse atmospheric transmittance, Eqn. 4.23 becomes

$$L_{wN} \equiv \frac{L_w(\tau_a^+, \theta_v, \theta_0, \Delta\phi)}{t(\mu_0)\mu_0}. \tag{4.24}$$

4.6.1 The anisotropy correction factor – accurate treatment

The exact normalized water-leaving radiance L_{wN}^{ex} is defined as the radiance that would be measured by a nadir-viewing instrument, if the sun were at zenith in the absence of an atmosphere ($\tau_a = \tau_a^+ = 0$).

Evaluating Eqn. 4.24 for $\theta_0 = \theta_v = 0$ (no $\Delta\phi$ dependence) in the absence of an atmosphere, $\tau_a^+ = 0$ and $t(\mu_0) = 1$, we find the exact normalized water-leaving radiance:

$$L_{wN}^{ex} \equiv L_w(\tau_a^+ = 0, \theta_v = 0, \theta_0 = 0). \tag{4.25}$$

The anisotropy correction factor: $\mathcal{F} \equiv \mathcal{F}(\theta_v, \theta_0, \Delta\phi, IOP^{atm}, W, IOP^{ocn})$

$$\mathcal{F} \equiv \frac{L_w(\tau_a^+, \theta_v, \theta_0, \Delta\phi)/t(\mu_0)\mu_0}{L_w(\tau_a^+ = 0, \theta_v = 0, \theta_0 = 0)} = \frac{L_{wN}}{L_{wN}^{ex}} \tag{4.26}$$

is obtained by dividing L_{wN} by L_{wN}^{ex}, and can be quantified as follows without invoking any unnecessary assumptions:

- compute $L_{wN} = L_{wN}(\theta_v, \theta_0, \Delta\phi, IOP^{atm}, W, IOP^{ocn})$ for the actual environmental conditions using a RT code for the coupled atmosphere-ocean system (such as AccuRT) that considers all radiative transfer processes (in the atmosphere, at the air-water interface, and in the water) influencing the water-leaving radiance;
- compute L_{wN}^{ex} defined by Eqn. 4.25 by ignoring the atmosphere;
- compute the desired anisotropy correction factor as: $\mathcal{F}(\theta_v, \theta_0, \Delta\phi, IOP^{atm}, W, IOP^{ocn}) = L_{wN}/L_{wN}^{ex}$.

4.6.2 The anisotropy correction factor – approximate treatment

For completeness, Eqn. 4.26 can be approximated as described in Eqn. 4.27 (see also equation 13 in Morel et al. 2002)

$$\mathcal{F} \equiv \frac{L_{wN}}{L_{wN}^{ex}} \approx \frac{R(\theta_0, 0^-)}{R_0} \frac{\mathcal{R}(\theta_v)}{\mathcal{R}_0} \frac{Q_0}{Q(\theta_v, \theta_0, \Delta\phi)} = \frac{\mathcal{R}(\theta_v)}{\mathcal{R}_0} \frac{Q_0}{f_0} \frac{Q}{f} \tag{4.27}$$

where

$$Q(\theta_v, \theta_0, \Delta\phi) \equiv Q(\theta', \theta_0, \Delta\phi) \equiv E_u(0^-)/L_u(0^-, \theta', \theta_0, \Delta\phi); \quad Q_0 = Q(\theta_v = 0, \theta_0 = 0)$$

and the irradiance reflectance (denoted f by Morel) is given by

$$f \equiv R(\theta_0, 0^-) = E_u(0^-)/E_d(0^-); \quad f_0 = R_0 = R(\theta_0 = 0, 0^-).$$

Here 0^- refers to *just below* the air-water interface, $E_u(0^-)$ is the upward irradiance, $E_d(0^-)$ is the downward irradiance, and $L_u(0^-)$ the upward radiance. Finally:

$$\mathcal{R}(\theta_v) \equiv \mathcal{R}(\theta', \theta_v) = \frac{(1 - \bar{\rho})[1 - \rho(\theta', \theta_v)]}{[1 - \bar{r}R(\theta_0, 0^-)]n_w^2} \tag{4.28}$$

where $\bar{\rho} = \mathcal{R}(0^+, 0^-)$ is the air-water Fresnel coefficient at the interface for the whole (Sun + sky) downward irradiance, $(1 - \bar{\rho}) = \mathcal{T}(0^+, 0^-)$ is the total (Sun + sky) transmittance through the interface, $\rho(\theta', \theta_v)$ is the internal Fresnel reflectance from the directions (θ', θ_v), and $[1 - \rho(\theta', \theta_v)] = \mathcal{T}(0^-, 0^+; \hat{\Omega}' \to \hat{\Omega})$ is the transmittance from polar angle θ' in water into polar angle θ_v in air. $\bar{r} = \mathcal{R}(0^-, 0^+)$ is the water-air Fresnel reflection for the whole diffuse upward irradiance, $[1 - \bar{r}R(\theta_0, 0^-)]^{-1}$ is due to downward internal reflection at the interface.

Here it should be noted that in Eqn. 4.28:

1. the reflectances $\bar{r}$ and $R(\theta_0, 0^-)$ are apparent optical properties that depend on the illumination conditions, and thus on the atmospheric as well as in-water IOPs and surface state (wind speed);
2. the effect of internal reflections, i.e. the $(1 - \bar{r}R)^{-1}$-term in Eqn. (4.28), appears to be arrived at by assuming that the air-water interface acts as a Lambertian reflector of diffuse light incident on the surface from below;
3. the Lambertian assumption also appears to be invoked when converting the downward irradiance just above the interface into downward irradiance just below the interface according to the relation $E(0^+) = (1 - \bar{\rho})E(0^-)$ in Eqn. 4.28;
4. in general, the reflectance $\bar{\rho}$ is an apparent optical property that depends on illumination conditions as well atmospheric IOPs and surface waves.

It should be emphasized that by using Eqn.4.26 instead of Eqn. 4.27 to compute the anisotropy correction factor the assumptions enumerated above are entirely avoided.

4.7 Computation of water-leaving radiance and diffuse transmittance

The radiance emerging from the sea, that is, the water-leaving radiance, $L_w(\tau_a^+, \mu, \phi)$ was computed using an RTM for the coupled atmosphere-water system as follows, to avoid invoking any of the assumptions discussed above:

$$L_w(\tau_a^+, \theta_v, \Delta\phi) = L_{sea}(\tau = \tau_a^+, \theta_v, \Delta\phi) - L_{black\ sea}(\tau = \tau_a^+, \theta_v, \phi) \tag{4.29}$$

where

$$L_{sea}(\tau = \tau_a^+, \theta_v, \Delta\phi)$$

is computed for a non-black sea, and

$$L_{black\ sea}(\tau = \tau_a^+, \theta_v, \Delta\phi)$$

is computed for a totally absorbing (black) sea.

To quantify the contribution of the radiance emerging from the sea to the TOA radiance $L_{w,TOA}(\tau = 0, \theta_v, \Delta\phi)$, we computed the TOA radiance for a non-black ocean, $L_{sea}(\tau = 0, \theta_v, \phi)$, repeated the computation for a black (totally absorbing) ocean, $L_{black\ sea}(\tau = 0, \theta_v, \phi)$, and then computed the difference:

$$L_{w,TOA}(\tau = 0, \theta_v, \Delta\phi) = L_{sea}(\tau = 0, \theta_v, \Delta\phi) - L_{black\ sea}(\tau = 0, \theta_v, \phi). \tag{4.30}$$

The upward diffuse transmittance was computed as the ratio:

$$t^+(\theta_v) = L_{w,TOA}(\tau = 0, \theta_v)/L_w(\tau_a^+, \theta_v). \tag{4.31}$$

The downward diffuse transmittance was computed as:

$$t^-(\theta_0) = E_d(\tau_a^+)/E_d(\tau = 0) \tag{4.32}$$

where $E_d(\tau_a^+)$ is the downward irradiance at just above the surface and $E_d(\tau = 0)$ is the downward irradiance at TOA.

Finally, the two-way transmittance was computed as:

$$\begin{aligned} t(\theta_v, \theta_0) = t^- \times t^+ &= \frac{E_d(\tau_a^+)}{E_d(\tau = 0)} \times \frac{L_{w,TOA}(\tau = 0, \theta_v)}{L_w(\tau_a^+, \theta_v)} \\ &= \frac{L_{w,TOA}(\tau = 0, \theta_v)/E_d(\tau = 0)}{L_w(\tau_a^+, \theta_v)/E_d(\tau_a^+)}. \end{aligned} \tag{4.33}$$

Chapter 5

Comparisons of Radiative Transfer Models (RTMs)

The purpose of this exercise was to test if two RTMs give the same top-of-the-atmosphere (TOA) radiances and water-leaving radiances for the same input inherent optical properties (IOPs) in the atmosphere and water.

5.1 Radiative Transfer Models

The purpose of radiative transfer models was to simulate TOA radiances, as well as water-leaving radiances, L_w, for the coupled atmosphere-water system pertinent for turbid coastal waters. Models used for this study are briefly reviewed below.

5.1.1 The AccuRT radiative transfer model

An RTM for the coupled atmosphere-water system (Jin and Stamnes 1994; Thomas and Stamnes 1999, Stamnes et al. 2017), can be used to quantify how TOA and L_w radiances depend on atmospheric as well as water IOPs. The atmosphere and ocean were divided into several layers as required to resolve the vertical variation in the IOPs. This RTM for the coupled system, AccuRT, is a well tested, reliable, and robust tool that was well suited for the creation of the proposed synthetic dataset (Cohen et al. 2013, Hamre et al. 2014, Stamnes et al. 2018).

The Phase function moments are as described in Chapter 4.5.1.1. Using $\rho = 0.04$ for air, we get $f = \frac{1-\rho}{1+\rho} = 0.923$, and using $\rho = 0.09$ for water, we get $f = \frac{1-\rho}{1+\rho} = 0.835$. Hence, for Rayleigh scattering the phase function moments become:

- $\chi_0 = 1, \quad \chi_1 = 0, \quad \chi_2 = 0.0941, \quad and \quad \chi_\ell = 0 \quad for \quad \ell > 2$ for air, and
- $\chi_0 = 1, \quad \chi_1 = 0, \quad \chi_2 = 0.0871, \quad and \quad \chi_\ell = 0 \quad for \quad \ell > 2$ for water.

The phase functions adopted for mineral and pigmented particles are as described in Chapter 4.5.2.5.

5.1.2 The PCOART model

He et al. (2007, 2010) have developed a vector RTM for the coupled ocean-atmosphere system (PCOART), using the matrix-operator (or adding-doubling) method. The PCOART RTM includes a rough air-water interface. The atmosphere and ocean are divided into several layers as required to resolve the vertical variation in the IOPs. The PCOART RTM can calculate Stokes vectors and irradiances at any layer boundary. The inputs to PCOART are the optical thickness, the single-scattering albedo, and the scattering phase matrix (or phase function for scalar radiative transfer simulations) of each layer.

5.1.3 R10 simulations (IOCCG 2010)

We used the AccuRT model to simulate some of the results provided in IOCCG Report # 10 (IOCCG 2010), hereafter termed R10 simulations. As for the R10 simulations, 3 layers were used: 2 layers in the atmosphere, and one layer in the ocean. The US standard atmospheric profile was used. The upper layer (2-100 km) had only Rayleigh scattering. Since no gas absorption was included in the R10 simulations, we ignored gas absorption in the results shown here. The lower layer (0-2 km) contained a mixture of molecules and aerosols. As in the R10 simulations, the Shettle/Fenn Maritime aerosol model with 80% humidity was adopted. The water IOPs were generated using the CCRR bio-optical model (see Chapter 4.5), which in addition to pure water includes pigmented particles (CHL), CDOM and non-pigmented particles (MIN). Eight (8) SeaWiFS channels were simulated: 412, 443, 490, 510, 555, 670, 765, and 865 nm. The 3 ocean impurity parameters (CHL, CDOM, and MIN) were adjusted to match the water-leaving radiances provided in R10 (IOCCG 2010).

The following 3 examples are shown in Figs. 5.1 - 5.3: (i) open-ocean water, (ii) CDOM-dominated water, and (iii) sediment-dominated water. In these simulations we used the same atmospheric properties with an aerosol optical depth of $\tau_{865} = 0.1$. The Sun-viewing geometry was chosen to be: a solar zenith angle of $\theta_0 = 45°$, a relative azimuth angle of $\Delta\phi = 90°$, and 5 viewing angles: $\theta = 5°, 25°, 45°, 55°$, and $65°$.

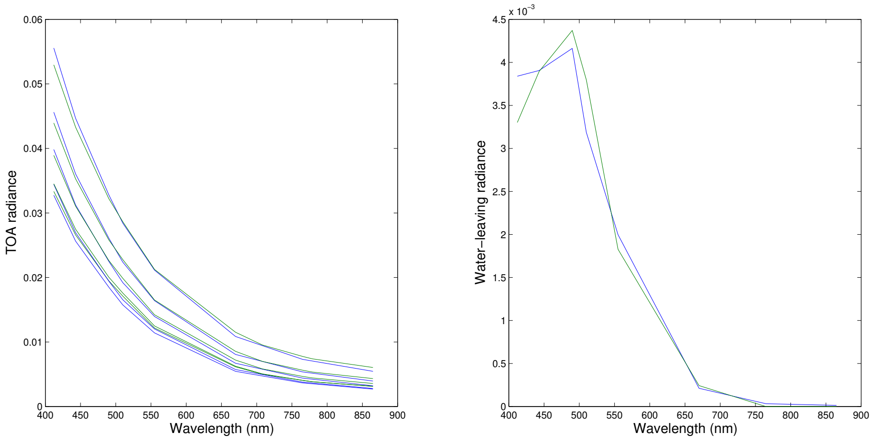

Figure 5.1 Left: TOA radiance. Right: water-leaving radiance. BLUE lines are from AccuRT simulations and GREEN lines are from R10. Case 1 (open ocean) water: CCRR parameters: CHL= 0.3 mg m^{-3}, CDOM = 0.025 m^{-1}, MIN = 0.1 g m^{-3}.

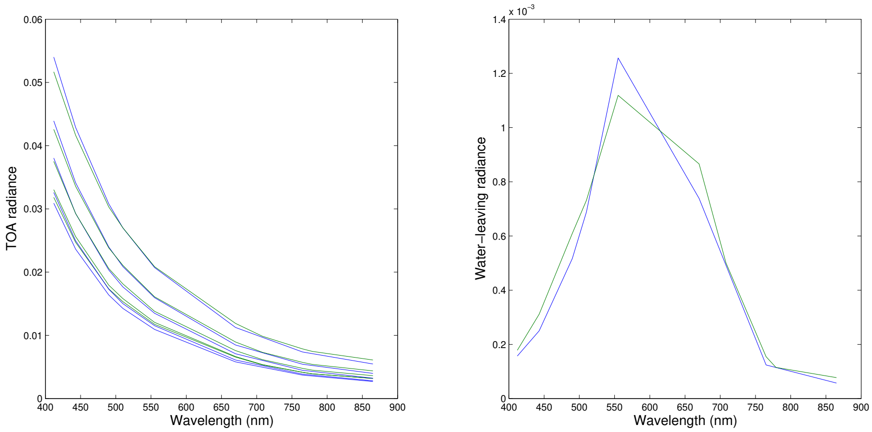

Figure 5.2 Left: TOA radiance. Right: water-leaving radiance. BLUE lines are from AccuRT simulations and GREEN lines are from R10. CDOM dominated water: CCRR parameters: CHL= 0.0 mg m^{-3}, CDOM = 1.8 m^{-1}, MIN = 0.9 g m^{-3}.

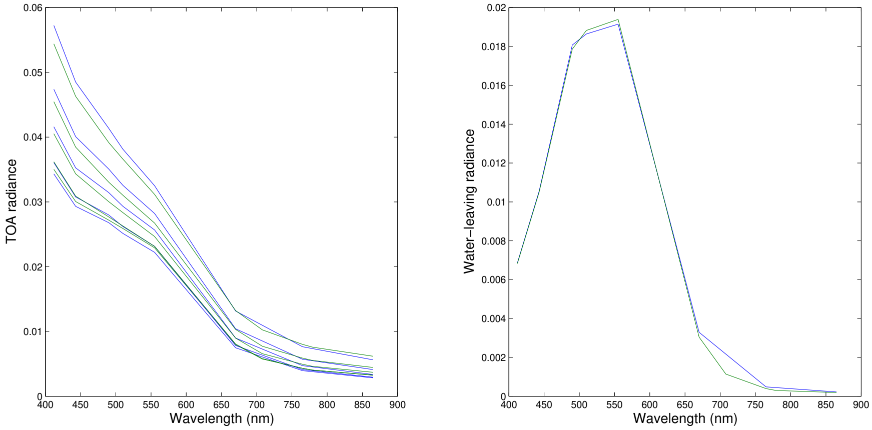

Figure 5.3 Left: TOA radiance. Right: water-leaving radiance. BLUE lines are from AccuRT simulations and GREEN lines are from R10. Sediment dominated water: CHL= 0.0 mg m^{-3}, CDOM = 0.3 m^{-1}, MIN = 3.5 g m^{-3}.

5.2 Test cases

As stated, the purpose of this exercise was to test if the AccuRT and PCOART RTMs gave the same TOA radiances and water-leaving radiances for the same input inherent optical properties in the atmosphere and water. The following test cases were considered, each with increasing complexity:

1. pure Rayleigh scattering atmosphere (no gas absorption) overlying a body of pure water (no impurities) (see Figs. 5.4-5.8).
2. Rayleigh scattering atmosphere (no gas absorption) with an embedded layer of weakly absorbing aerosol particles overlying a body of pure water (no impurities) (see Figs. 5.9-5.13).
3. Rayleigh scattering atmosphere (no gas absorption) with an embedded layer of weakly absorbing aerosol particles overlying a body of pure water with pigmented particles as the only embedded impurity (see Figs. 5.14-5.18).
4. Rayleigh scattering atmosphere (no gas absorption) with an embedded layer of weakly absorbing aerosol particles overlying a body of pure water with pigmented particles and mineral particles as the two embedded impurity components (see Figs. 5.19-5.23).
5. Rayleigh scattering atmosphere (no gas absorption) with an embedded layer of weakly absorbing aerosol particles overlying a body of pure water with pigmented particles, mineral particles as well as dissolved matter as the three embedded impurity components (see Figs. 5.24-5.28).

5.2.1 Test case 1

This simple case was for an atmosphere with Rayleigh scattering only (no gas absorption) overlying a flat water body with pure water (no impurities).

5.2.1.1 Wavelengths

8 SeaWiFS channels were used: 412, 443, 490, 510, 555, 670, 765, and 865 nm.

5.2.1.2 Atmosphere parameters

2 layers were used based on the US standard atmosphere:
Layer 1 (2–100 km): Includes only Rayleigh scattering (no gas absorption).
Layer 2 (0–2 km): Includes only Rayleigh scattering (no gas absorption).

5.2.1.3 Ocean parameters

One homogeneous 100 m deep ocean layer was adopted with pure water from the CCRR bio-optical model: CHL = 0 mg m^{-3}, CDOM = 0 m^{-1}, MIN = 0 g m^{-3}.
The bottom albedo was set to 0.0.

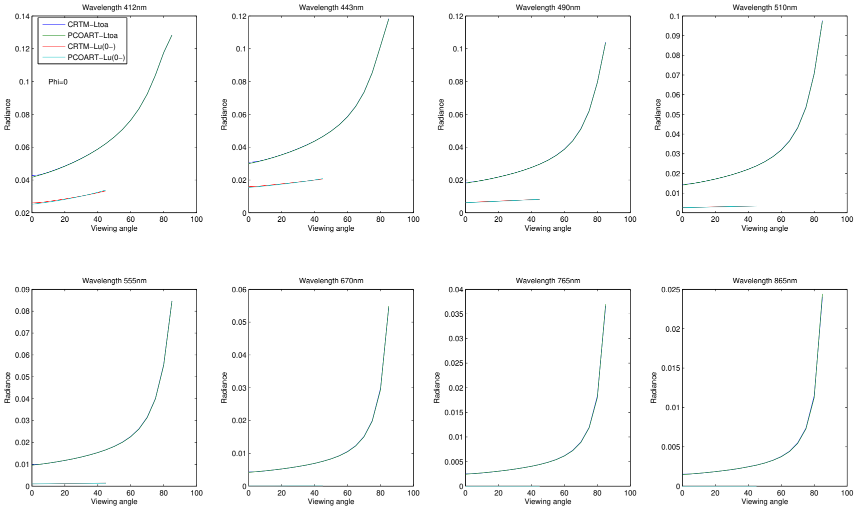

Figure 5.4 Comparison of radiances at TOA (L_{toa}) and just below the air-water interface ($L_u(0^-)$) as a function of polar viewing angle θ for $\Delta\phi = 0°$. Solar zenith angle $\theta_0 = 45°$. The BLUE lines are from AccuRT and the GREEN lines from PCOART simulations. **Test case 1**: Rayleigh atmosphere (no aerosols). Pure water (no impurities).

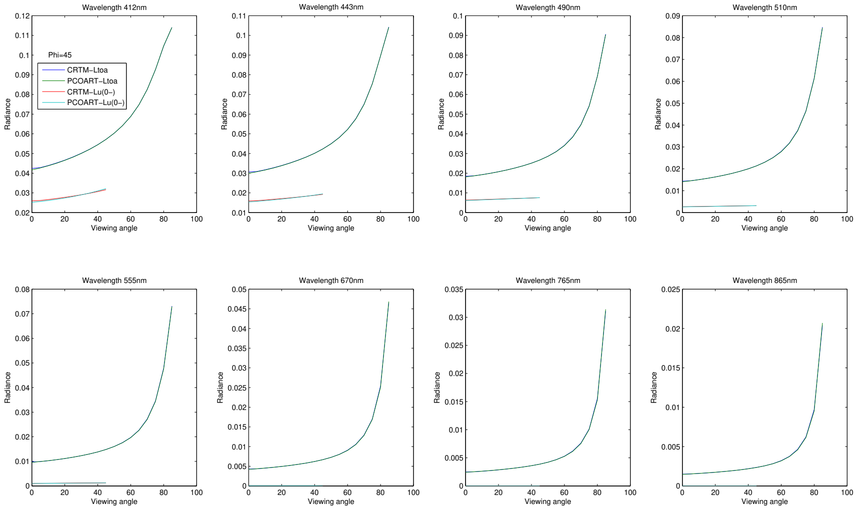

Figure 5.5 Same as Fig. 5.4 except that $\Delta\phi = 45°$.

5.2.1.4 Comparisons

A comparison of results produced by the AccuRT and PCOART models are shown in Figs. 5.4-5.8 for 5 different relative azimuth angles ($\Delta\phi = 0°, 45°, 90°, 135°$, and $180°$). Summary results showed:

1. At TOA the agreement was very good: the curves lie on top of each other.
2. Just below the air-water interface the agreement was also good, but not perfect.

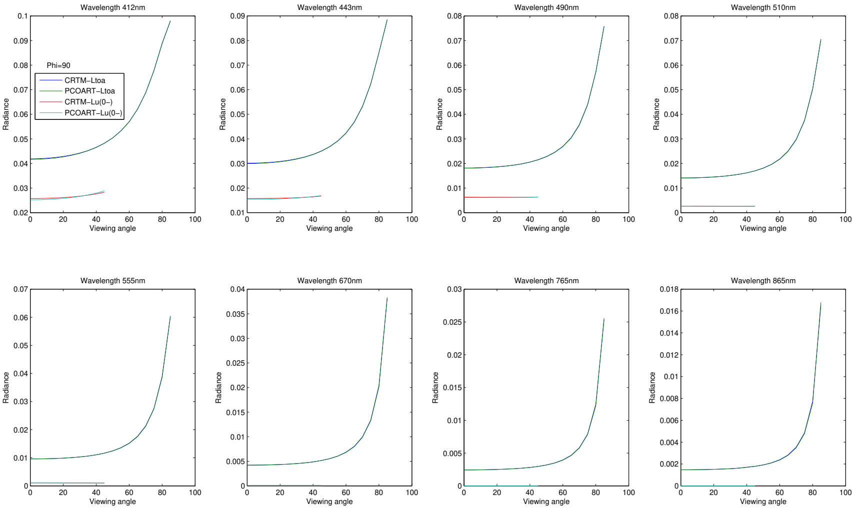

Figure 5.6 Same as Fig. 5.4 except that $\Delta\phi = 90°$.

5.2.2 Test case 2

This simple case was for an atmosphere with molecules (Rayleigh scattering, but no absorption) and aerosols overlying a flat water body with pure water (no impurities).

5.2.2.1 Wavelengths

8 SeaWiFS channels used were: 412, 443, 490, 510, 555, 670, 765, and 865 nm.

5.2.2.2 Atmosphere parameters

2 layers were used based on the US standard atmosphere:
Layer 1 (2–100 km): Includes only Rayleigh scattering (no gas absorption).
Layer 2 (0–2 km): Includes a mixture of molecules and aerosols.
Aerosol model: Shettle & Fenn's Maritime model with RH = 80%. AOD: $\tau_{865} = 0.1$.

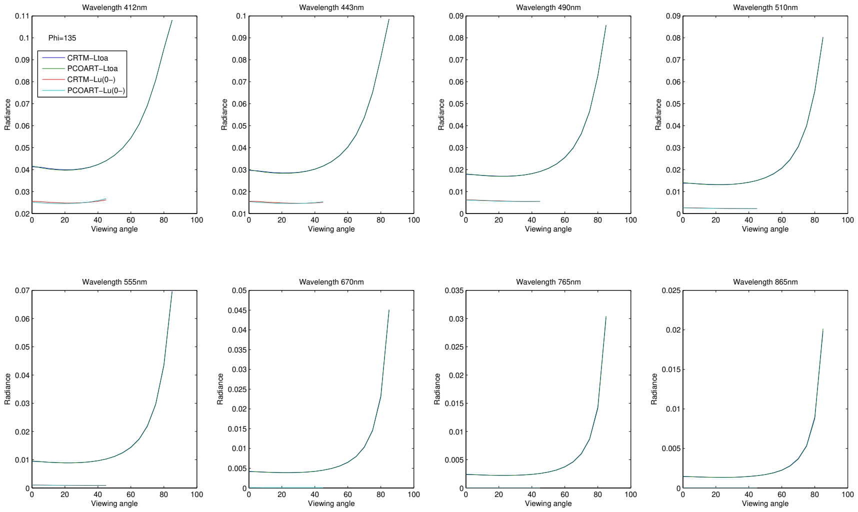

Figure 5.7 Same as Fig. 5.4 except that $\Delta\phi = 135°$.

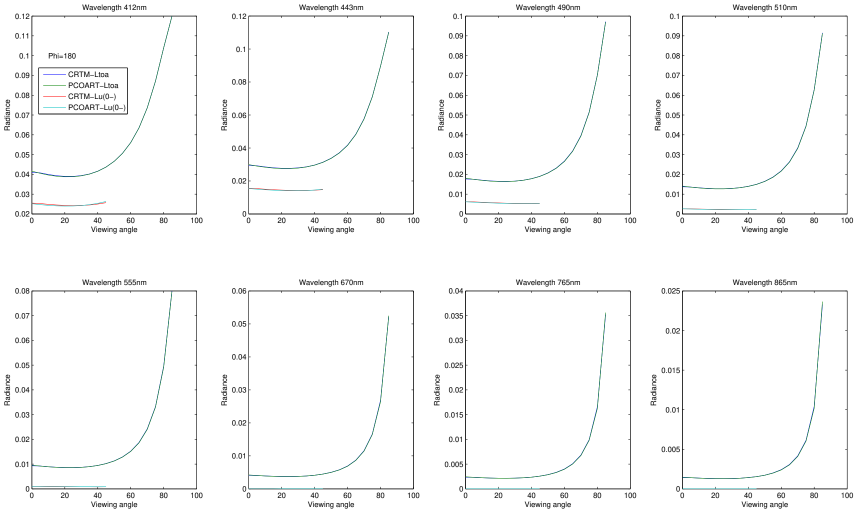

Figure 5.8 Same as Fig. 5.4 except that $\Delta\phi = 180°$.

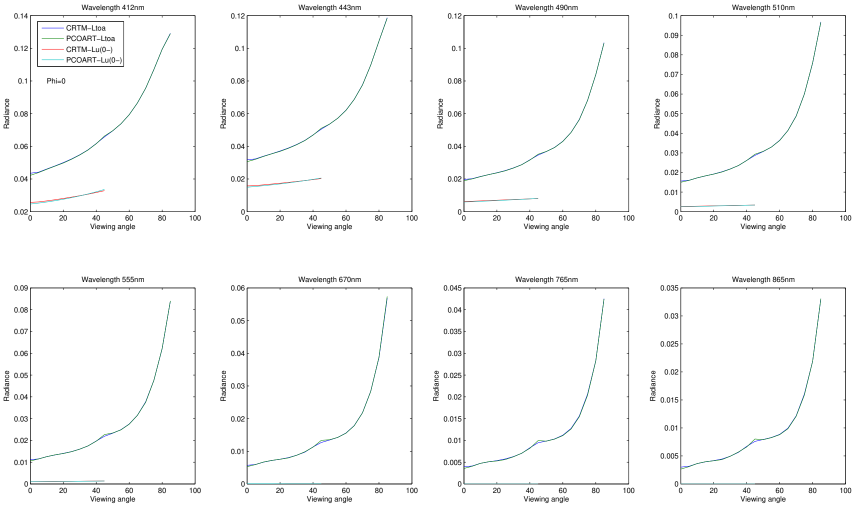

Figure 5.9 Comparison of TOA radiances as a function of polar viewing angle θ for $\Delta\phi = 0°$. Solar zenith angle $\theta_0 = 45°$. The BLUE lines are from AccuRT and the GREEN lines from PCOART simulations. **Test case 2**: Rayleigh atmosphere mixed with aerosols. Pure water (no impurities).

5.2.2.3 Ocean parameters

One homogeneous 100 m deep ocean layer was adopted with pure water from the CCRR bio-optical model: CHL = 0 mg m^{-3}, CDOM = 0 m^{-1}, MIN = 0 g m^{-3}. The bottom albedo was set to 0.0.

5.2.2.4 Comparisons

A comparison of results produced by the AccuRT and PCOART models are shown in Figs. 5.9-5.13 for 5 different relative azimuth angles ($\Delta\phi = 0°, 45°, 90°, 135°$, and $180°$). Summary results showed:

1. Overall, the agreement was very good as can be seen from the plots.
2. The only significant difference, in the specular reflection direction (see Fig. 5.13) was believed to be due to inclusion of the direct beam component in PCOART but not in AccuRT.

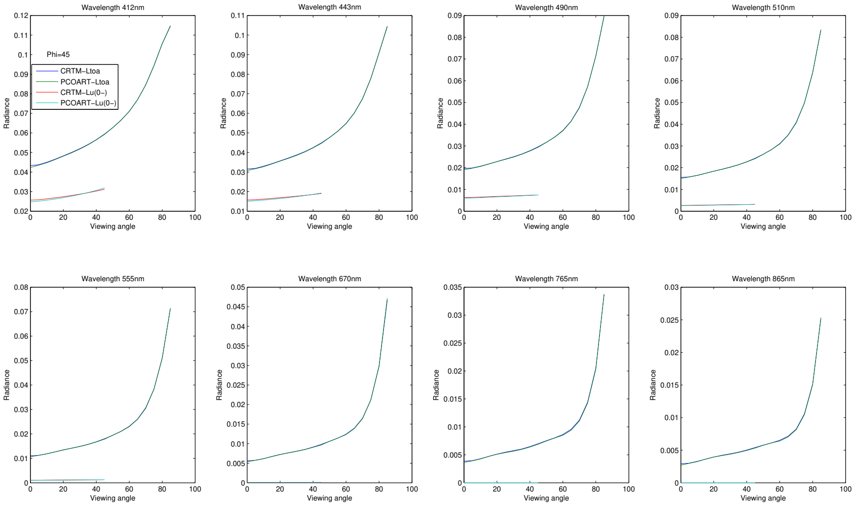

Figure 5.10 Same as Fig. 5.9 except that $\Delta\phi = 45°$.

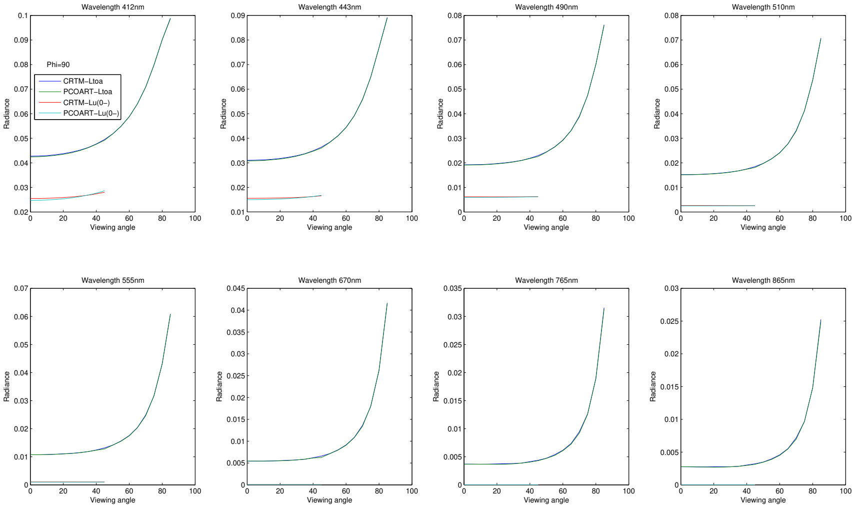

Figure 5.11 Same as Fig. 5.9 except that $\Delta\phi = 90°$.

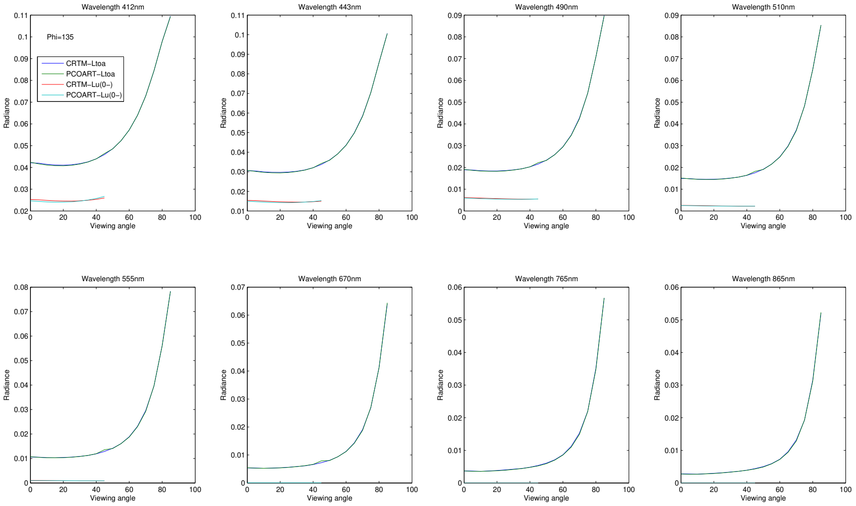

Figure 5.12 Same as Fig. 5.9 except that $\Delta\phi = 135°$.

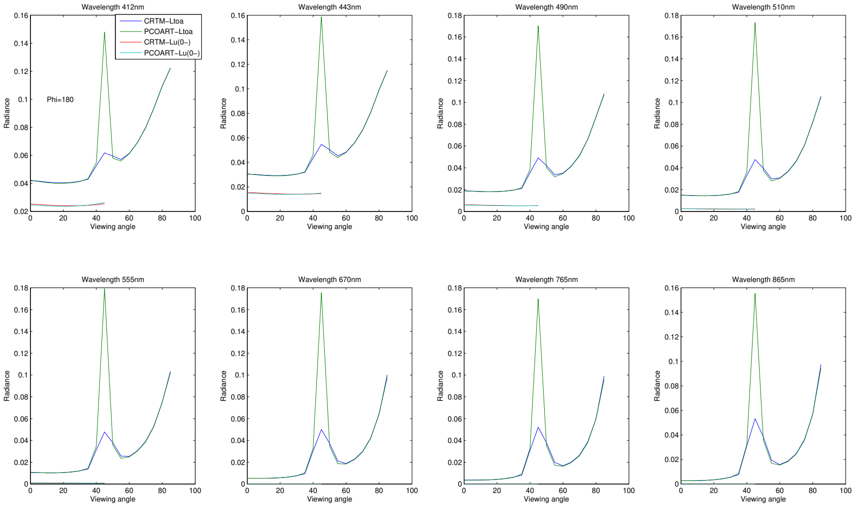

Figure 5.13 Same as Fig. 5.9 except that $\Delta\phi = 180°$.

5.2.3 Test case 3

This case was for an atmosphere (identical to that of test case 2) overlying a flat water body with pure water and pigmented particles (CHL) as the only impurity.

5.2.3.1 Wavelengths

8 SeaWiFS channels used were: 412, 443, 490, 510, 555, 670, 765, and 865 nm.

5.2.3.2 Atmosphere parameters

Same as in test case 2: Two-layer atmosphere with non-absorbing molecules in the upper layer (2–100 km) and a mixture of non-absorbing molecules and weakly absorbing aerosols in the lower layer (0–2 km).

5.2.3.3 Ocean parameters

One homogeneous 100 m deep ocean layer was adopted from the CCRR bio-optical model with pure water and pigmented particles as the only impurity: CHL = 1.0 mg m^{-3}, CDOM = 0 m^{-1}, MIN = 0 g m^{-3}. The bottom albedo was set to 0.0.

5.2.3.4 Phase function

To describe the angular variation of the scattering by pigmented particles, we used the Henyey-Greenstein phase function given by:

$$p(\cos\Theta) = \frac{1 - g^2}{(1 + g^2 - 2g\ \cos\ \Theta)^{3/2}} \tag{5.1}$$

with the asymmetry factor set to $g = 0.95$.

5.2.3.5 Comparison

A comparison of results produced by the AccuRT and PCOART models are shown in Figs. 5.14-5.18 for 5 different relative azimuth angles ($\Delta\phi = 0°, 45°, 90°, 135°$, and $180°$). Summary results showed:

1. Overall, the agreement was very good except for some discrepancies when the viewing angle was equal to the angle of incidence.
2. As in the previous case, in the direction of specular reflection (see Fig. 5.18) there was a significant difference believed to be due to inclusion of the direct beam component in PCOART but not in AccuRT.

5.2.4 Test case 4

This case was for an atmosphere (identical to test case 2) overlying a flat water body with pure water and embedded pigmented particles and mineral particles as the two impurity components.

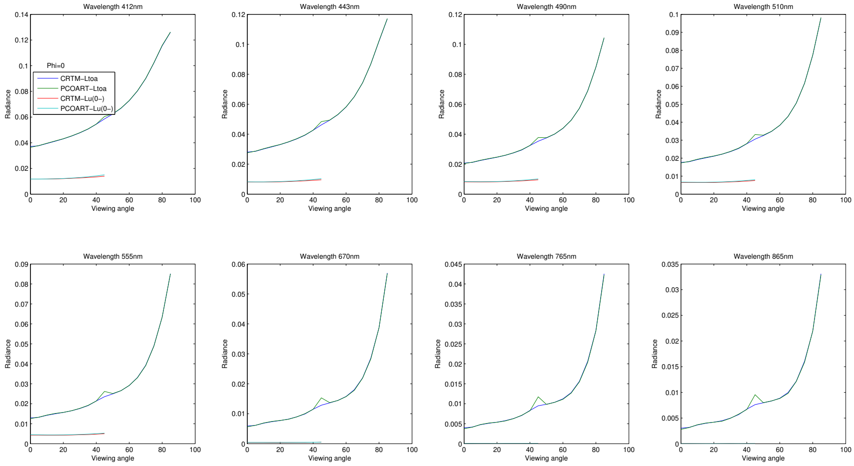

Figure 5.14 Comparison of TOA radiances as a function of polar viewing angle θ for $\Delta\phi = 0°$. Solar zenith angle $\theta_0 = 45°$. The BLUE lines are from AccuRT and the GREEN lines from PCOART simulations. **Test case 3**: Rayleigh atmosphere mixed with aerosols. Pure water plus pigmented particles.

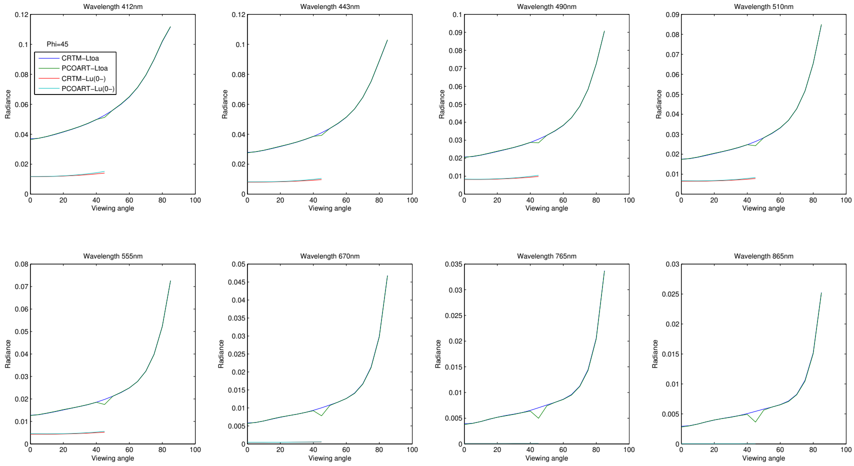

Figure 5.15 Same as Fig. 5.14 except that $\Delta\phi = 45°$.

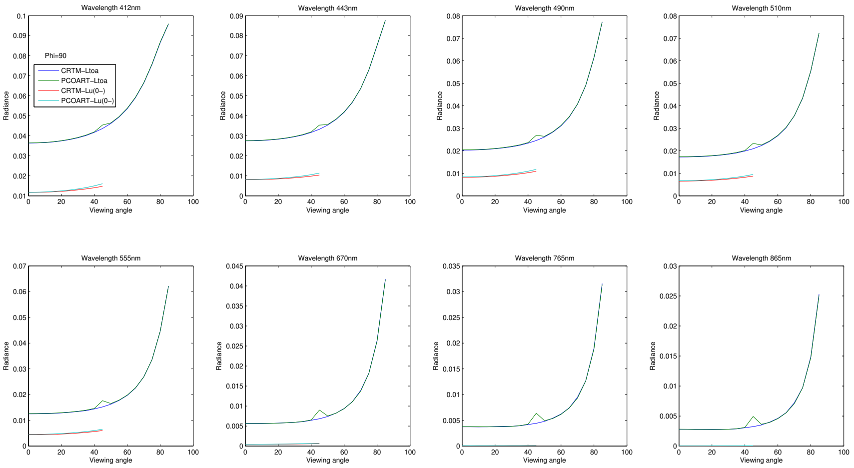

Figure 5.16 Same as Fig. 5.14 except that $\Delta\phi = 90°$.

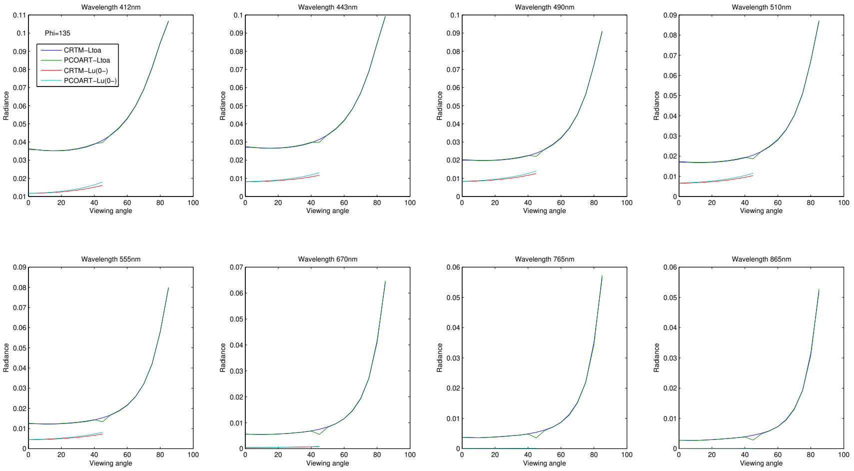

Figure 5.17 Same as Fig. 5.14 except that $\Delta\phi = 135°$.

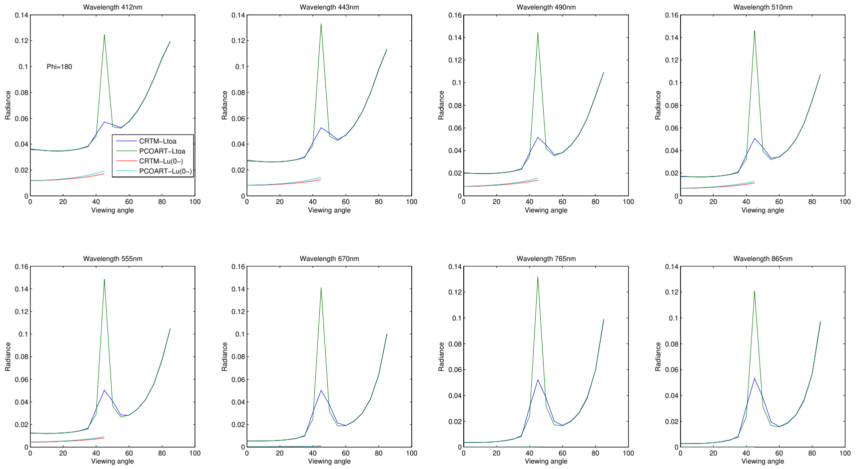

Figure 5.18 Same as Fig. 5.14 except that $\Delta\phi = 180°$.

5.2.4.1 Wavelengths

8 SeaWiFS channels used were: 412, 443, 490, 510, 555, 670, 765, and 865 nm.

5.2.4.2 Atmosphere parameters

Same as in test case 2: two-layer atmosphere with non-absorbing molecules in the upper layer (2–100 km) and a mixture of non-absorbing molecules and weakly absorbing aerosols in the lower layer (0–2 km).

5.2.4.3 Ocean parameters

One homogeneous 100 m deep ocean layer was adopted from the CCRR bio-optical model with pure water and embedded impurities CHL = 1.0 mg m^{-3}, CDOM = 0.0 m^{-1}, MIN = 1.0 g m^{-3}. The bottom albedo was set to 0.0.

5.2.4.4 Comparison

A comparison of results produced by the AccuRT and PCOART models are shown in Figs. 5.19-5.23 for 5 different relative azimuth angles ($\Delta\phi = 0°, 45°, 90°, 135°$, and $180°$). Summary results showed:

1. Overall, the agreement was very good except for some discrepancies when the viewing angle was close to the angle of incidence.
2. The upward radiances just beneath the water surface were close, except for at large viewing angles.

3. As in the previous cases, in the direction of specular reflection (see Fig. 5.23) there was a significant difference believed to be due to the inclusion of the direct beam component in PCOART but not in AccuRT.

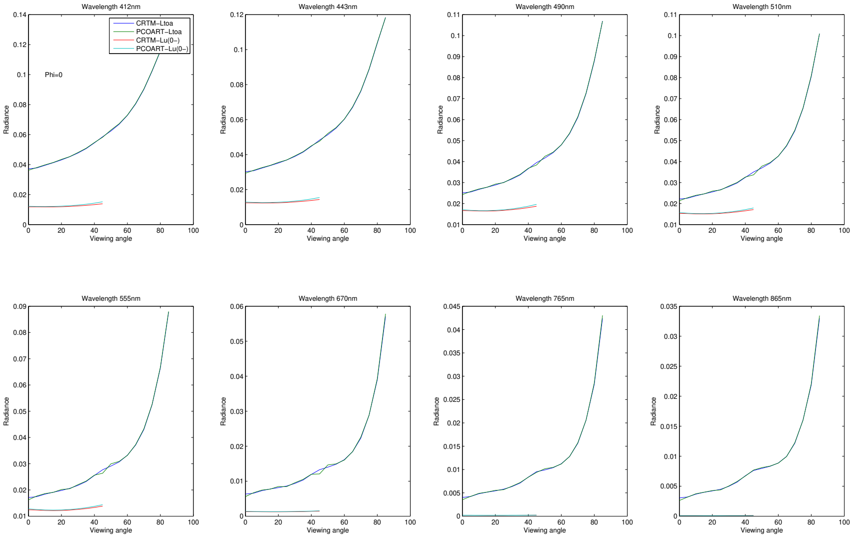

Figure 5.19 Comparison of TOA radiances as a function of polar viewing angle θ for $\Delta\phi = 0°$. Solar zenith angle $\theta_0 = 45°$. The BLUE lines are from AccuRT and the GREEN lines from PCOART simulations. Test case 4: Rayleigh atmosphere mixed with aerosols. Pure water mixed with pigmented particles and mineral particles (no CDOM absorption).

5.2.5 Test case 5

This case was for an atmosphere (identical to test case 2) overlying a flat water body with pure water and embedded pigmented particles, mineral particles as well as coloured dissolved organic matter (CDOM).

5.2.5.1 Wavelengths

8 SeaWiFS channels used were: 412, 443, 490, 510, 555, 670, 765, and 865 nm.

5.2.5.2 Atmosphere parameters

Same as in test case 2: two-layer atmosphere with non-absorbing molecules in the upper layer (2–100 km) and a mixture of non-absorbing molecules and weakly absorbing aerosols in the lower layer (0–2 km).

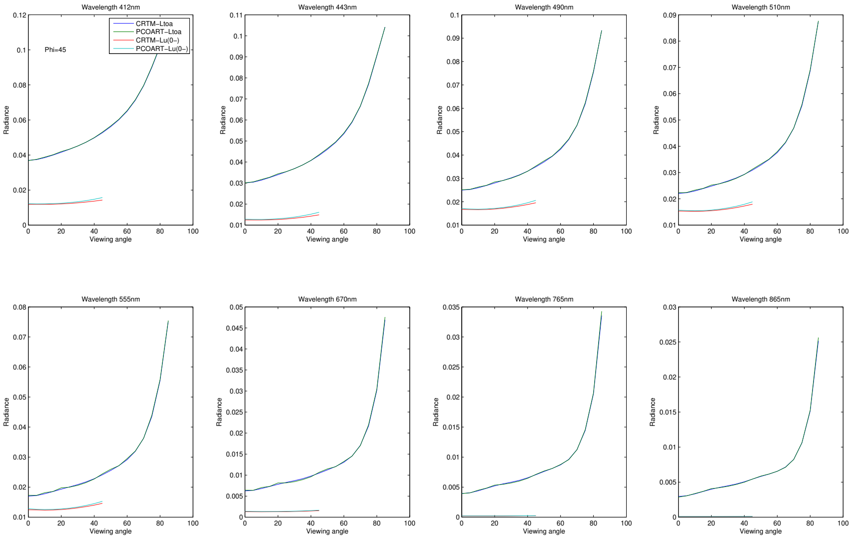

Figure 5.20 Same as Fig. 5.19 except that $\Delta\phi = 45°$.

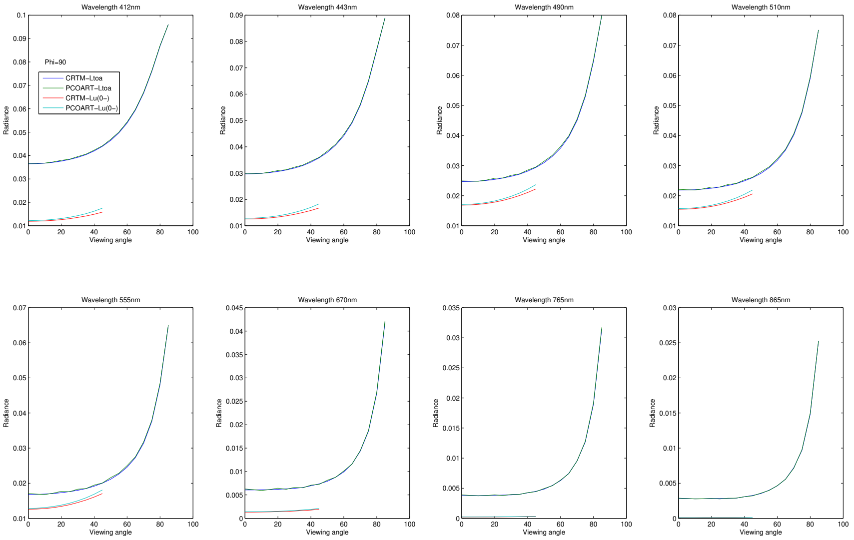

Figure 5.21 Same as Fig. 5.19 except that $\Delta\phi = 90°$.

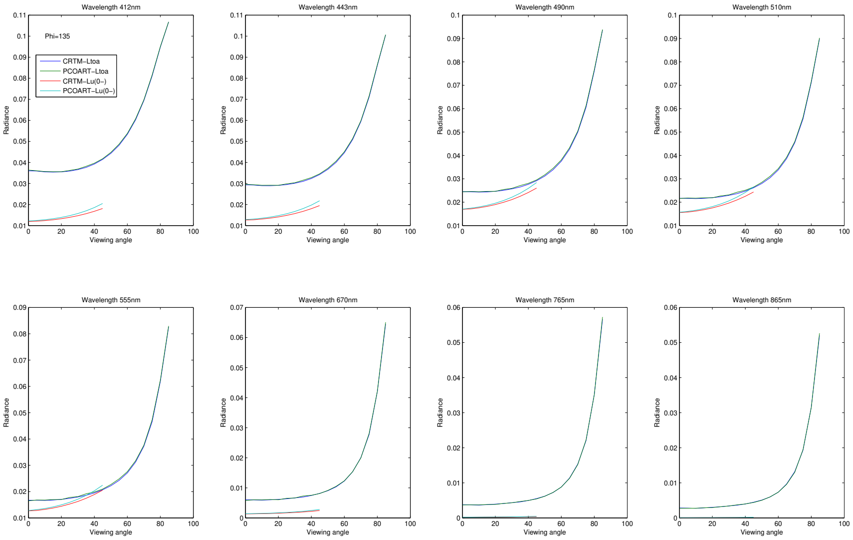

Figure 5.22 Same as Fig. 5.19 except that $\Delta\phi = 135°$.

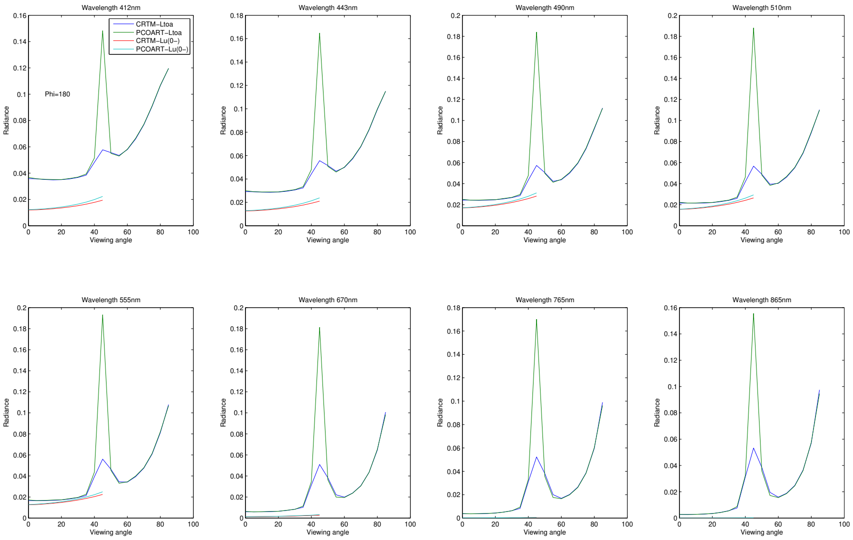

Figure 5.23 Same as Fig. 5.19 except that $\Delta\phi = 180°$.

5.2.5.3 Ocean parameters

One homogeneous 100 m deep ocean layer was adopted from the CCRR bio-optical model with pure water, CHL = 1.0 mg m^{-3}, CDOM = 1.0 m^{-1}, MIN = 1.0 g m^{-3}.
The bottom albedo was set to 0.0, and the spectral variation of the CDOM absorption coefficient was given by:

$$a_{\mathrm{C}DOM}(\lambda) = \mathrm{C}DOM \times \exp(-0.0176(\lambda - 443)). \tag{5.2}$$

5.2.5.4 Comparison

A comparison of results produced by the AccuRT and PCOART models are shown in Figs. 5.24-5.28 for 5 different relative azimuth angles ($\Delta\phi = 0°, 45°, 90°, 135°$, and $180°$). Summary results showed:

1. Overall, the agreement was very good except for some small discrepancies for viewing angles close to the angle of incidence.
2. The upward radiances just beneath the water surface were close. After adding CDOM, the absorption was large in the visible bands. The largest upward radiance just beneath the water surface was at 555 nm.
3. As in the previous cases, in the direction of specular reflection (see Fig. 5.28) there was a significant difference, believed to be due to inclusion of the direct beam component in PCOART but not in AccuRT.

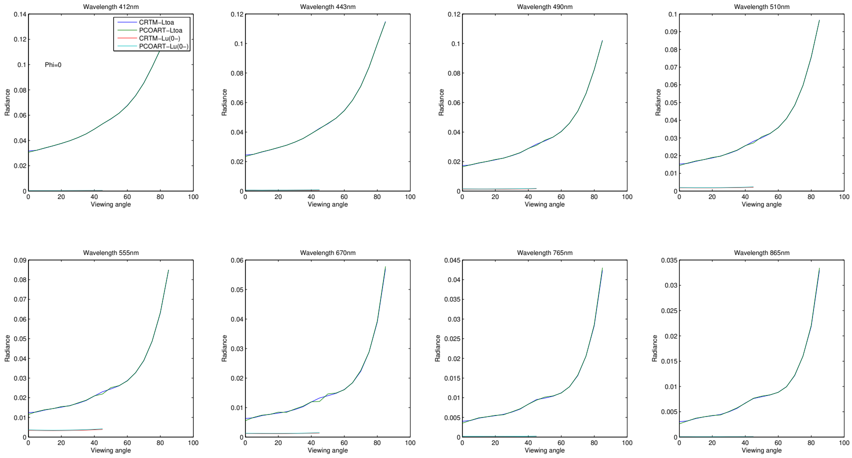

Figure 5.24 Comparison of TOA radiances as a function of polar viewing angle θ for $\Delta\phi = 0°$. Solar zenith angle $\theta_0 = 45°$. The BLUE lines are from AccuRT and the GREEN lines from PCOART simulations. **Test case 5**: Rayleigh atmosphere mixed with aerosols. Pure water mixed with pigmented particles, mineral particles, and coloured dissolved organic matter.

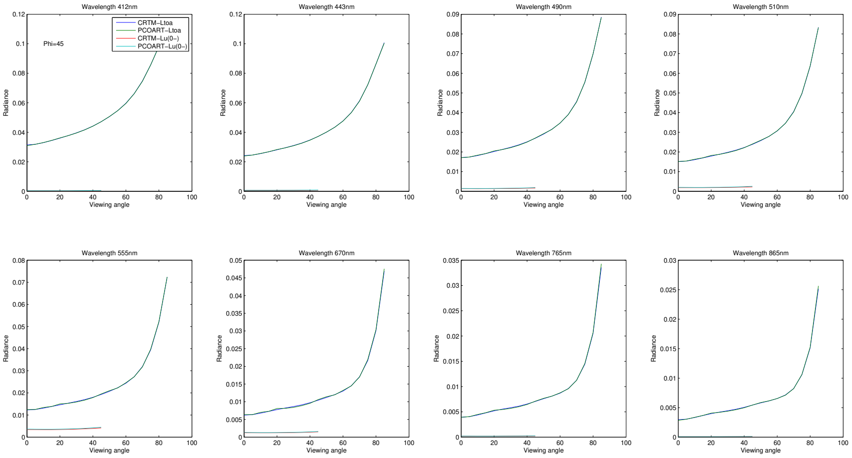

Figure 5.25 Same as Fig. 5.24 except that $\Delta\phi = 45°$.

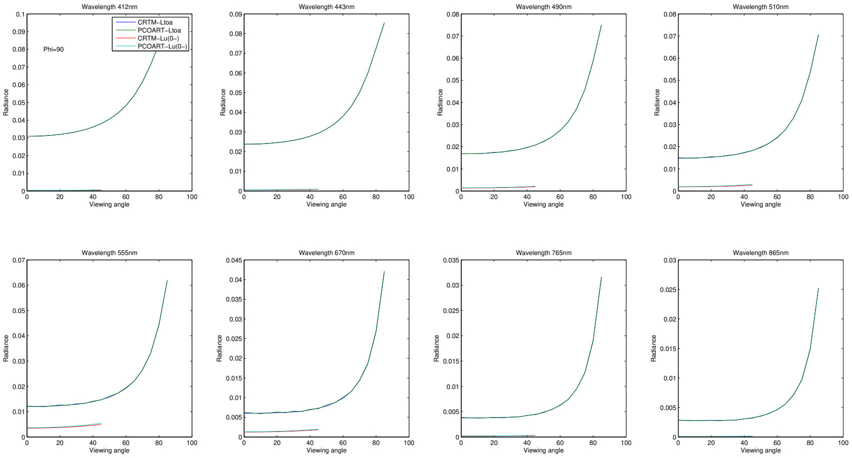

Figure 5.26 Same as Fig. 5.24 except that $\Delta\phi = 90°$.

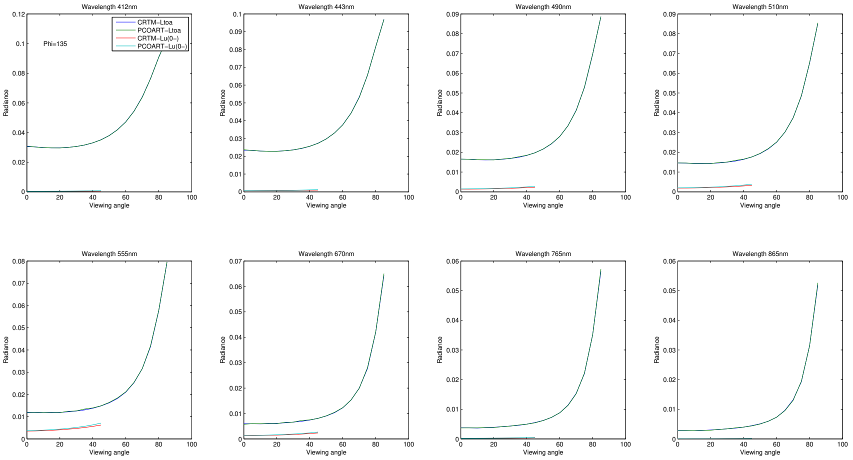

Figure 5.27 Same as Fig. 5.24 except that $\Delta\phi = 135°$.

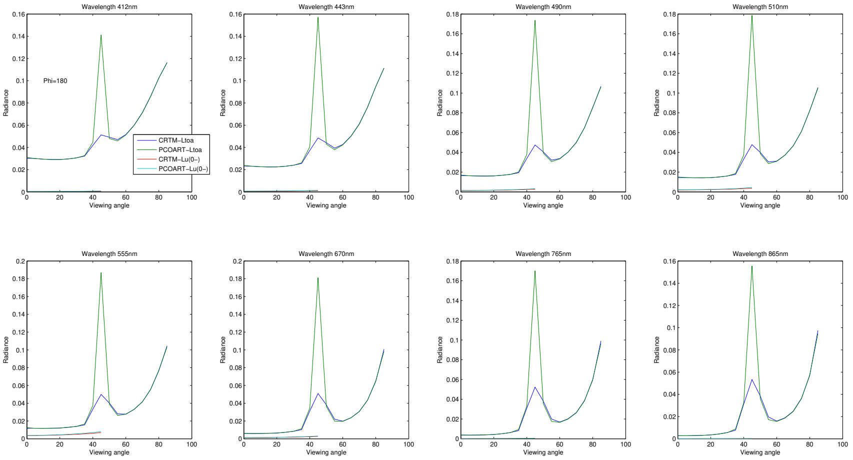

Figure 5.28 Same as Fig. 5.24 except that $\Delta\phi = 180°$.

Chapter 6

Match-up analyses

6.1 Extraction of match-up data

Validation of the selected AC algorithms was done via classic match-up analyses as described in Bailey and Werdell (2006). SeaDAS L2 flags and flags provided by FUB were considered for the match-ups exercise. The following conditions and steps were used to determine match-up data:

1. A 1-hour interval between the satellite overpass and the AERONET-OC measurement
2. Extraction over a 3-by-3-pixel box centreed over the AERONET-OC station
3. Validity of 6 out of 9 pixels over the 3-by-3-pixel box
4. A coefficient of variability, CV, calculated by using the standard deviation divided by the mean values over the 3-by-3-pixel box for $\mathrm{R_{rs}}(547)$
5. A valid match-up if $\mathrm{CV(R_{rs}(547))} < 0.2$
6. Mean values calculated over the valid pixels
7. AERONET-OC data filtered to only include turbid waters as defined by Robinson et al. (2003), using an $\mathrm{R_{rs}}(667) > 0.0012\ \mathrm{sr^{-1}}$

Considering these 7 conditions and steps, only 889 match-ups remained out of a total of 2456 possible match-ups. Concha et al. (2021) studied the impact of the steps taken during selection of match-up data, and concluded that the choice of validation protocol impacted the statistics, making them difficult to compare with other studies that use different validation protocols. By considering only the match-up data common across all AC algorithms, a resulting sub-set of 83 match-ups remained.

6.2 Statistical parameters on individual $R_{rs}(\lambda)$

To quantitatively evaluate the performance of each selected AC algorithm, the following statistical parameters were calculated:

1. Relative difference (RD) as mean absolute difference: $\frac{1}{N}\sum(100\times\frac{|R_{rs}^{sat}-R_{rs}^{obs}|}{R_{rs}^{obs}})$
2. Root-mean-square difference (RMSD): $\sqrt{(\frac{\sum(R_{rs}^{sat}-R_{rs}^{obs})^2}{N})}$
3. Slope and intercept of the regression line
4. Bias: $\frac{1}{N}\sum(100\times\frac{R_{rs}^{sat}-R_{rs}^{obs}}{R_{rs}^{obs}})$
5. Determination coefficient: R^2
6. Overall difference (Pahlevan et al. 2021): with $\beta = 100\times\sin(z)(10^{|Z|}-1)$ with $Z =$

Median$(log_{10}(\frac{R_{rs}^{sat}}{R_{rs}^{obs}}))$

7. Relative bias in log (Pahlevan et al. 2021): with $\alpha = 100\times(10^{Y} - 1)$ with $Y =$ Median$(|log_{10}(\frac{R_{rs}^{sat}}{R_{rs}^{obs}})|)$

6.3 Statistical evaluation of the retrieved spectra

In addition to the classic statistical parameters listed in the previous section, investigations were also performed on the shape of the retrieved spectra as follows:

- Quality Assurance Score (QAS; Wei et al. 2016): this parameter provided quantification of the full R_{rs} spectrum quality of retrievals with regards to reference spectra. The values of QAS varied between 0 and 1, with 1 indicating that the retrieved spectra matched the reference spectra.
- χ^2: this parameter provided information about the full spectrum relative differences, with desirable values closer to 0.
- The Spectral Angle Mapper (SAM; Kruse et al. 1993; Keshava 2004): this parameter indicated the mean of the full spectrum difference between the retrieved R_{rs} and *in-situ* R_{rs} spectra, with desired values closer to 0°.

This list is not exhaustive, as other parameters may be used to provide information about the spectral shape of the R_{rs} retrievals. For example, Dierssen et al. (2022) developed the Quality Water Index Polynomial (QWIP) score to provide levels of uncertainty about retrieved spectra.

The following wavelengths were considered in our analyses: 412, 443, 488, 531, 547, and 667 nm.

6.4 Ranking of the algorithms using a score scheme

A scoring scheme developed by Müller et al. (2015) was used to classify and compare the algorithms using a relative score (S). The scheme is based on: the slope and intercept of the linear regression line; bias; root-mean-squared difference (RMSD); relative difference (RD); R^2; and the number of valid match-up data points (N). The highest possible score results from the number of statistical parameters multiplied by the number of wavelengths. In our case, this resulted in a maximal value of 42 (7 parameters by 6 wavelengths).

The total score, S_{total}, was calculated using the sum of scores for each statistical parameter (Eqn. 6.1):

$$S_{total} = \sum_{i=1}^{6}(S_{slope}(\lambda_i) + S_{intercept}(\lambda_i) + S_{RMSD}(\lambda_i) + S_{RD}(\lambda_i) + S_{bias}(\lambda_i) + S_{R^2}(\lambda_i) + S_N(\lambda_i)) \quad (6.1)$$

where each score (S_X) is a normalized value between 0 and 1 for each statistical parameter, X. 0 is given to the lowest value and 1 to the highest value. As the highest value for a given statistical parameter was not always the most desirable score (e.g. relative difference is best at

0 and not 1), a normalization was adopted for each score. The normalization was calculated using Eqn. 6.2 for $S_{intercept}$ and S_{bias}; Eqn. 6.3 for S_{RD} and S_{RMSD}; Eqn. 6.4 for S_N; Eqn. 6.5 for S_{R^2}; and Eqn. 6.6 for S_{slope}.

$$S_X(\lambda_i) = \frac{|X(\lambda_i)| - max(|X(\lambda_i)|)}{min(|X(\lambda_i)|) - max(|X(\lambda_i)|)} \tag{6.2}$$

where X represents the intercept or bias.

$$S_X(\lambda_i) = \frac{X(\lambda_i) - max(X(\lambda_i))}{min(X(\lambda_i)) - max(X(\lambda_i)|)} \tag{6.3}$$

where X represents RD or RMSD.

$$S_N(\lambda_i) = \frac{N(\lambda_i)}{max(N(\lambda_i))} \tag{6.4}$$

$$S_{R^2}(\lambda_i) = \frac{R^2(\lambda_i) - min(R^2(\lambda_i))}{max(R^2(\lambda_i)) - min(R^2(\lambda_i))} \tag{6.5}$$

$$S_{slope}(\lambda_i) = \frac{|1 - slope(\lambda_i)| - max(|1 - slope(\lambda_i)|)}{min(1 - |slope(\lambda_i)|) - max(1 - |slope(\lambda_i)|)} \tag{6.6}$$

6.5 Optical water types

Optical water types (OWT) classify water masses depending on their optical properties (shape of R_{rs} and range of IOPs). Several algorithms exist to classify water types (Moore et al. 2009; Vantrepotte and al. 2012; Hieronymi et al. 2023) and there is now an IOCCG working group on the classification of optical water types in aquatic radiometry. For this report, a self-organizing map (SOM, Kohonen 2013) was used to initially cluster the AERONET-OC and simulated datasets in an SOM topology map. Each sample was assigned to a node (cluster centre), which represents one of the possible classes. For the input layer, normalized remote sensing reflectances (R_{rs_n}) at 412, 443, 488, 531, 547 and 667 nm were used. The normalization was done following Eqn 6.7

$$R_{rs_n}(\lambda) = \frac{2}{3}\frac{R_{rs}(\lambda) * \overline{R_{rs}}(\lambda)}{\sigma(R_{rs}(\lambda))} \tag{6.7}$$

where R_{rs_n} is the normalized R_{rs} spectrum, and $\overline{R_{rs}}$ and $\sigma(R_{rs})$ are the mean and standard deviation of the R_{rs} spectra for the whole training dataset, respectively.

The classification of an OWT was based on the simulated dataset. The other initial parameters for the SOM were 100 training steps to cover the input space, an initial neighbourhood size of 3, a hexagonal pattern for the topology function, and a layer-based distance function between the layer's neurons given their position.

A 3-by-3 architecture was initially selected for the SOM, but this was deemed insufficient to cluster the different shapes of the R_{rs} spectra. The N-by-N architecture was increased one by

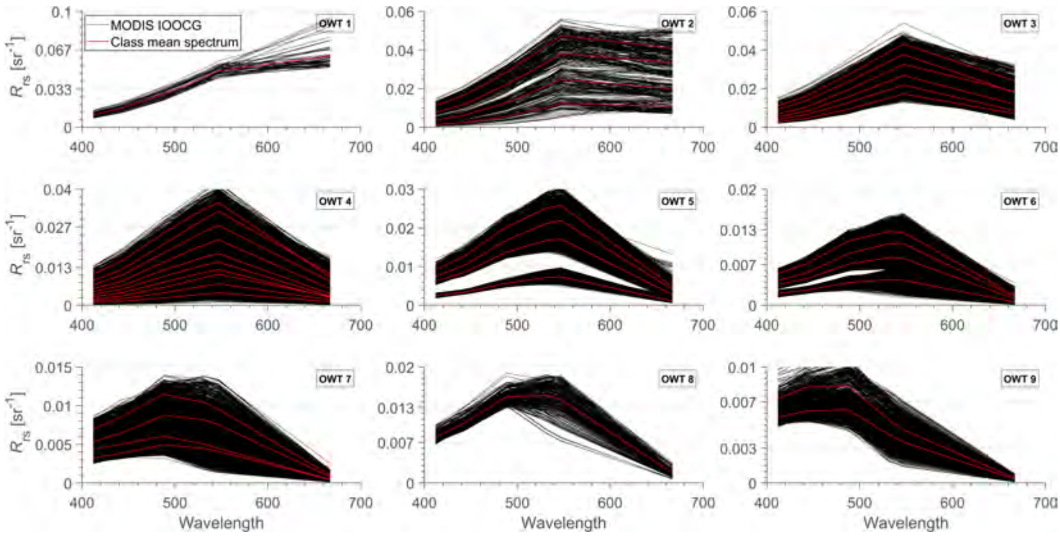

Figure 6.1 R_{rs} spectra (black) and reference spectra (red) for each of nine optical water types (OWT1 - OWT9) based on the simulated dataset.

one, until a 6-by-6 architecture was deemed sufficient. For each of the 6-by-6 nodes, the mean R_{rs} spectrum was calculated. This spectrum was used as a reference to regroup the classes based on the spectral shape. For each sample and each mean spectrum (36 in all), the Euclidean distance was calculated, and the minimum distance was used to select the corresponding class for each sample.

Re-grouping of the classes was done using a Hierarchical Ascending Classification (Niang et al. 2006; El Hourany et al. 2019a, b) and the 36 mean spectra were assigned to 9 classes based on the shape of each mean spectrum (Fig. 6.1). At this step, an emphasis was placed on the contribution of each IOP to the R_{rs} spectrum (Fig. 6.2 and Fig. 6.3). Classes 1 and 2 corresponded to highly turbid waters, with a clear plateau between 547 and 667 nm due to high backscattering in the red, especially for class 1. For classes 3 and 4, R_{rs} had a more triangular shape, with a maximum at 547 nm and lower R_{rs} in the blue than in the red, an indication of waters with mixed composition. There was a gradual increase in the impact of pure water absorption and scattering properties on the R_{rs} spectrum for classes 5 to 9, switching the peak from green towards blue, and with an increase in the magnitude of R_{rs} at blue wavelengths.

This classification was applied to the match-up dataset. The reference spectra and the AERONET-OC spectra for each OWT is shown for the individual match-up dataset in Fig. 6.4, and for the common match-up dataset in Fig. 6.5. For both datasets, there are no AERONET-OC spectra attached to the most turbid waters (OWT1 and OWT2). For the common AERONET-OC dataset (Fig. 6.5), there were no spectra attached to the most oligotrophic waters (OWT9). Considering only turbid waters (Robinson et al. 2003), the number of spectra per OWT for each dataset is provided in Table 6.1.

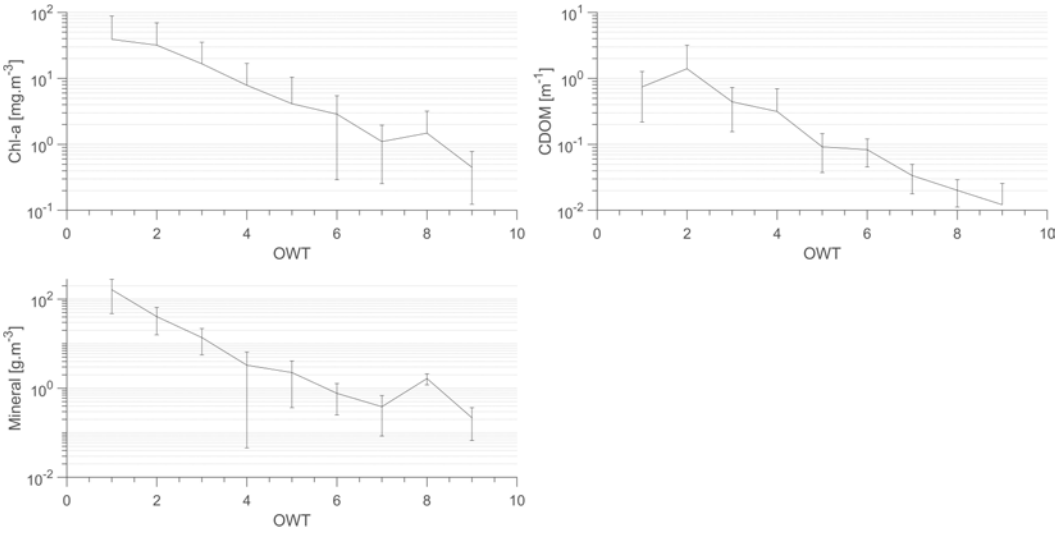

Figure 6.2 Values of chlorophyll-a (mg m^{-3}), CDOM (m^{-1}) and mineral concentrations (g m^{-3}) for each optical water type.

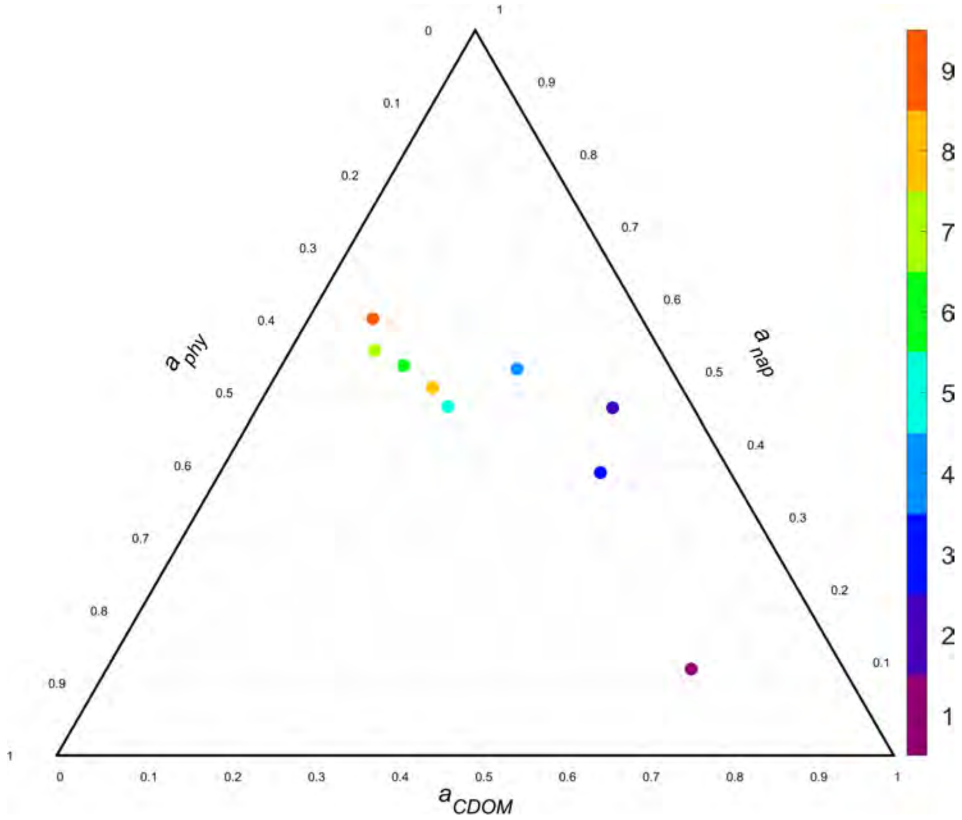

Figure 6.3 Triangle diagram showing the distribution of the nine optical water classes depending of the values of $a_{CDOM}(443)$, $a_{phy}(443)$ and $a_{nap}(443)$.

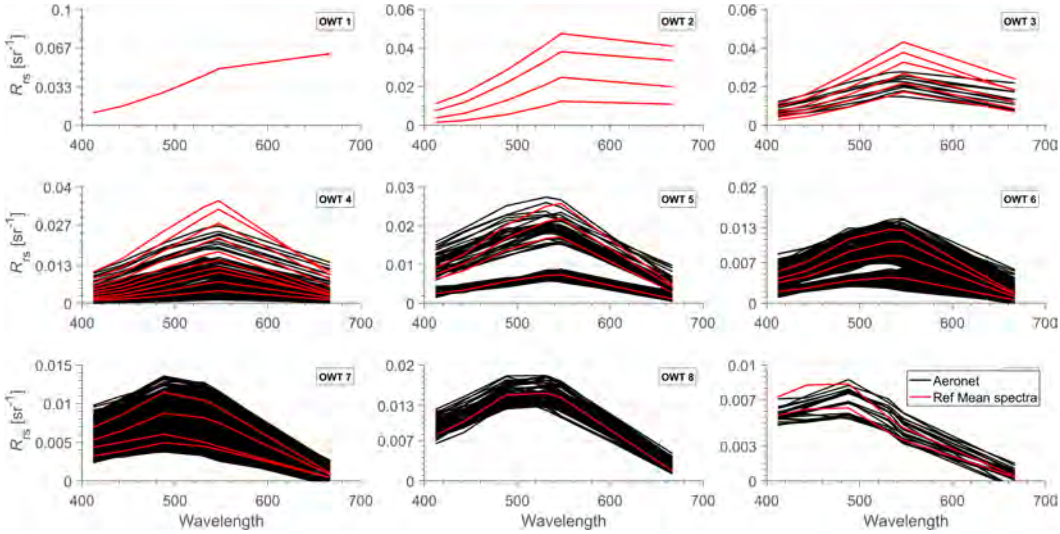

Figure 6.4 Spectra (black) and reference spectra (red) for each optical water type based on the AERONET-OC total dataset. The OWTs are the same as in Fig. 6.3: OWT1 to OWT9 reading from left to right, from upper-left to lower-right.

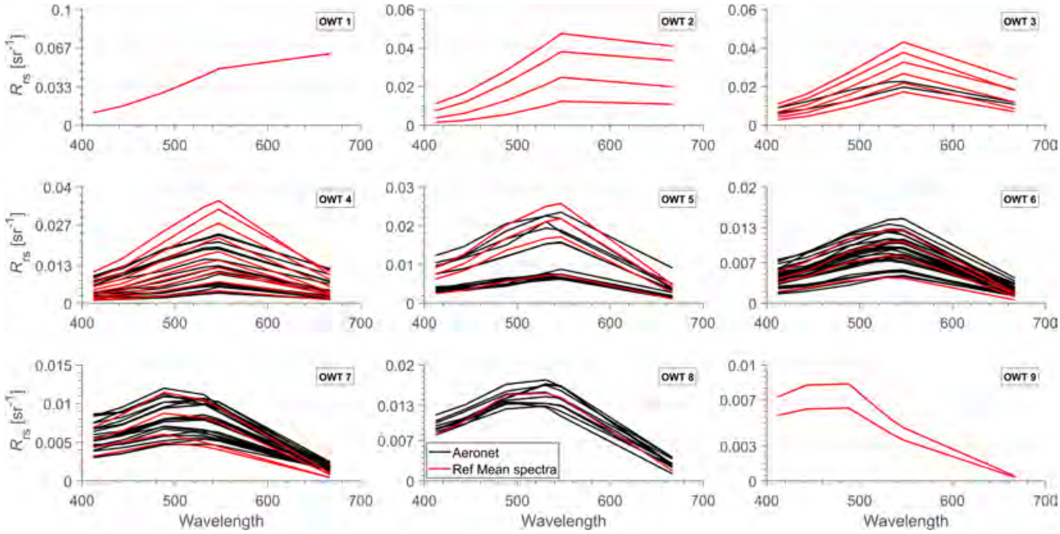

Figure 6.5 Spectra (black) and reference spectra (red) for each optical water type based on the AERONET-OC common dataset. The OWTs are the same as in Fig. 6.3: OWT1 to OWT9 reading from left to right, from upper-left to lower-right.

Table 6.1 Number of spectra per optical water types over the AERONET-OC match-ups and simulated datasets

DATASET	OWT1	OWT2	OWT3	OWT4	OWT5	OWT6	OWT7	OWT8	OWT9
Individual match-up	0	0	10	174	165	302	177	66	2
Common match-up	0	0	2	16	14	24	19	8	0
Simulated	53	369	1656	6399	1898	1577	113	236	0

Chapter 7

Results based on the in-situ dataset

In this section, the evaluation results for the in-situ dataset are presented for both the global match-up dataset and for the match-ups that are common across all algorithms (the common match-up dataset). The first dataset provides information about global statistics and is more specifically focused on the number of match-ups. The second dataset allows for the direct comparison of the statistics of the retrievals from the ten AC algorithms.

7.1 Individual spectra match-up analyses

The results for all individual match-ups obtained by each AC algorithm are presented in this section. Fig. 7.1 shows scatterplots of the satellite-retrieved $\mathrm{R_{rs}}$ vs the AERONET-OC *in-situ* values for all ten AC algorithms. Table 7.1 provides the statistical results. The number of match-ups, N (Table 7.1), varied from 242 for SWIRE to 896 for SS14. Negative $\mathrm{R_{rs}}$ ($\mathrm{N}_{R_{rs}}$<0) was also retrieved in the blue or red bands, as was the case for NASA-AC (6 at 412 nm), NIRSWIR (3 at 412 nm), MUMM (19 at 412 nm and 5 at 443 nm) and Polymer (1 each at 488, 531 and 547 nm). Other AC algorithms did not provide any negative results. These two parameters are of high importance for global and regional time series, as we expect to use AC algorithms that provide the highest number of match-ups without any negative values.

Fig. 7.1 shows that high scattering was observed at 412 and 443 nm for all AC models, while scattering around the 1:1 line decreased at 488, 531 and 547 nm. This is a common behaviour of AC algorithms (Goyens et al. 2013; Melin 2022). At 412 and 443 nm, some algorithms provided high values of $\mathrm{R_{rs}}$ for low AERONET-OC $\mathrm{R_{rs}}$ (e.g. UV-AC, SS14, SWIRE). Note that UV-AC uses the band at 412 nm as a reference wavelength, to correct for the atmosphere. This explains why $\mathrm{R_{rs}}$ retrievals at this band were not as accurate for this model, compared to 412 nm retrievals from the others AC models.

Relative differences were highest at 412 nm (between 30% for FUB and 95% for SS14) and 443 nm (between 20% for NASA-AC and NIRSWIR and 78% for SWIRE). RD was lowest at 531 and 547 nm (between 12% for NASA-AC and NIRSWIR and 30% for FUB and SWIRE at 531 nm, and between 11% for NASA-AC and 28% for FUB at 547 nm). Low values of the slope of the regression line indicated high scattering, and was observed at 412 and 443 nm (between 0.29 sr^{-1} for SWIRE and 0.86 sr^{-1} for NASA-AC at 412 nm and between 0.61 sr^{-1} for UV and 0.96 sr^{-1} for NASA-AC at 443 nm). The closest values of the slope to 1 were obtained at 531 and 547 nm (between 0.75 sr^{-1} for SS14 and 1.00 sr^{-1} for NASA-AC and NIRSWIR at 531 nm and between 0.78 sr^{-1} for SS14 and 1.02 sr^{-1} for NASA-AC and NIRSWIR at 547 nm). The values

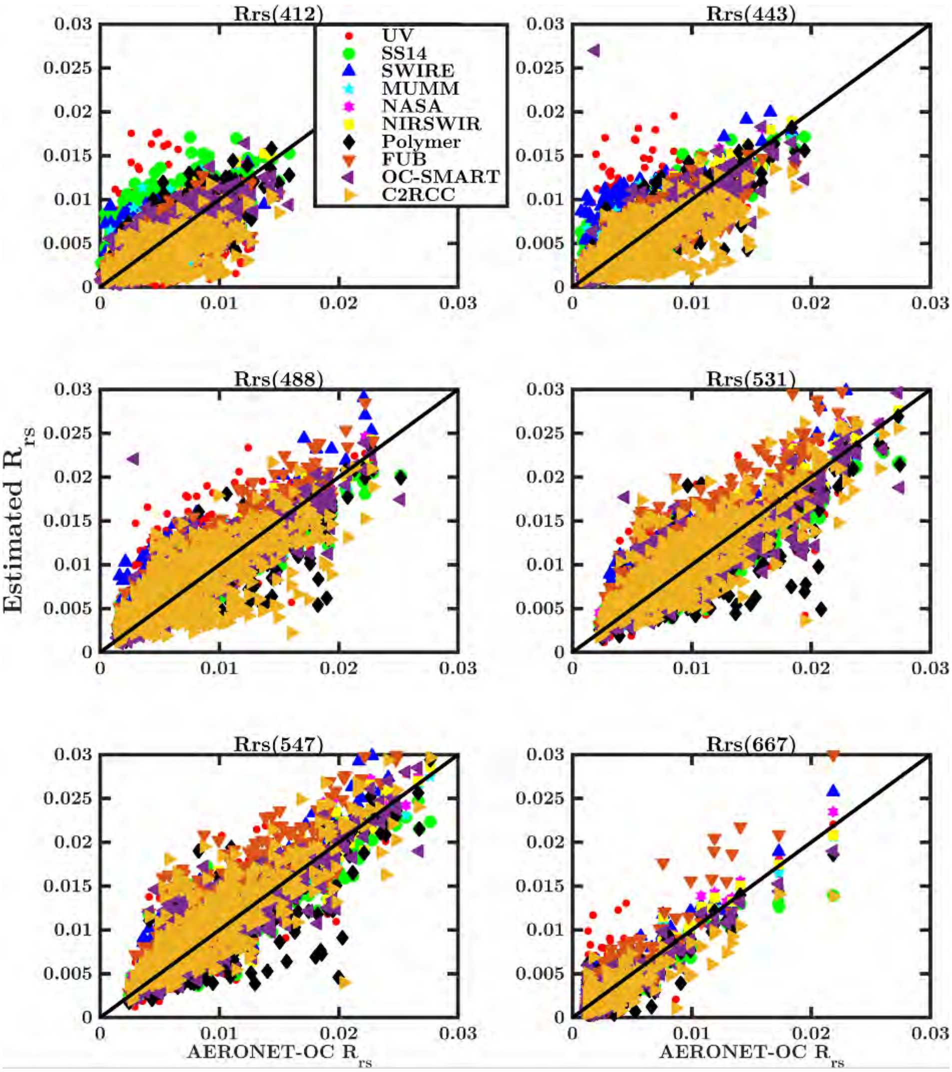

Figure 7.1 Scatterplots of the estimated R_{rs} from all 10 AC algorithms vs in-situ R_{rs} from 412 (top left) to 667 nm (bottom right). The individual scatterplots are provided in Appendix A.

Table 7.1 Statistical results from comparing R_{rs} derived from various atmospheric correction algorithms and AERONET-OC data (*RD* - mean relative difference, *RMSD* – root mean square difference, R^2- regression, β- overall difference, α - relative bias in log, N - number of valid data/model/wavelengths, N<0 - number of negative R_{rs} values).

	RD(%)	**RMSD(sr^{-1})**	**Slope(sr^{-1})**	**Intercept**	**Bias(sr^{-1})**	**R^2**	**β(%)**	**α(%)**	**N**	**N<0**
UV-AC										
$R_{rs}(412)$	67	0.00327	0.35	0.0026	-0.00042	0.11	-40	244	620	0
$R_{rs}(443)$	51	0.00291	0.61	0.0029	0.00069	0.39	22	142	620	0
$R_{rs}(488)$	34	0.00286	0.81	0.0025	0.00103	0.65	15	107	620	0
$R_{rs}(531)$	23	0.00259	0.85	0.0012	-0.00011	0.71	-38	135	620	0
$R_{rs}(547)$	23	0.00359	0.90	0.0009	-0.000005	0.71	-44	137	620	0
$R_{rs}(667)$	53	0.00164	0.92	0.0003	-0.00013	0.59	-69	333	620	0
SS14										
$R_{rs}(412)$	95	0.00323	0.64	0.0394	0.00226	0.40	171	179	896	0
$R_{rs}(443)$	50	0.00227	0.69	0.00298	0.00122	0.65	64	82	896	0
$R_{rs}(488)$	26	0.00185	0.73	0.00250	0.00038	0.82	14	45	896	0
$R_{rs}(531)$	20	0.00190	0.75	0.00248	0.00022	0.82	10	38	896	0
$R_{rs}(547)$	18	0.00182	0.78	0.00222	0.00026	0.82	9	35	896	0
$R_{rs}(667)$	23	0.00081	0.79	0.00037	-0.00014	0.82	-17	57	896	0
SWIRE										
$R_{rs}(412)$	73	0.00273	0.29	0.00375	0.00017	0.13	-13	122	242	0
$R_{rs}(443)$	78	0.00331	0.64	0.00457	0.00239	0.53	106	107	242	0
$R_{rs}(488)$	52	0.00333	0.86	0.00370	0.00253	0.77	76	76	242	0
$R_{rs}(531)$	30	0.00277	0.94	0.00231	0.00178	0.82	41	43	242	0
$R_{rs}(547)$	27	0.00275	1.01	0.00165	0.00175	0.84	36	43	242	0
$R_{rs}(667)$	60	0.00153	1.02	0.00099	0.00106	0.85	111	118	242	0
MUMM										
$R_{rs}(412)$	40	0.00200	0.68	0.000123	-0.000324	0.50	-25	93	412	19
$R_{rs}(443)$	25	0.00158	0.83	0.000902	-0.000117	0.76	-12	50	412	5
$R_{rs}(488)$	16	0.00145	0.91	0.000498	-0.000266	0.89	-15	34	412	0
$R_{rs}(531)$	13	0.00150	0.95	0.000176	-0.000337	0.90	-13	28	412	0
$R_{rs}(547)$	13	0.00144	0.97	-0.000007	-0.000250	0.91	-11	26	412	0
$R_{rs}(667)$	29	0.00082	0.99	-0.000321	-0.000336	0.90	-62	97	412	0
NASA-AC										
$R_{rs}(412)$	33	0.00155	0.86	0.00052	0.00015	0.70	-14	74	510	6
$R_{rs}(443)$	20	0.00121	0.96	0.00028	0.00004	0.87	-0.5	38	510	0
$R_{rs}(488)$	13	0.00121	0.98	0.0000	-0.00011	0.93	-6	25	510	0
$R_{rs}(531)$	12	0.00137	1.00	-0.00025	-0.00019	0.92	-9	24	510	0
$R_{rs}(547)$	11	0.00138	1.02	0.00039	-0.00015	0.92	-8	23	510	0
$R_{rs}(667)$	24	0.00076	1.08	0.00043	-0.00023	0.92	-45	69	510	0

NIRSWIR

R_{rs}(412)	32	0.00159	0.84	0.00072	-0.00005	0.69	-9	68	431	3
R_{rs}(443)	20	0.00130	0.95	0.00047	0.00014	0.86	2	38	431	0
R_{rs}(488)	13	0.00130	0.98	0.00015	-0.00003	0.92	-4	25	431	0
R_{rs}(531)	12	0.00145	1.00	-0.00013	-0.00010	0.91	-7	26	431	0
R_{rs}(547)	12	0.00146	1.02	-0.00028	-0.00005	0.91	-6	23	431	0
R_{rs}(667)	25	0.00081	1.05	-0.00033	-0.00018	0.90	-41	68	431	0

Polymer

R_{rs}(412)	31	0.00146	0.84	0.0012	0.00046	0.74	31	55	892	0
R_{rs}(443)	21	0.00146	0.81	0.0012	0.00012	0.80	12	38	892	0
R_{rs}(488)	17	0.00183	0.79	0.0014	-0.00022	0.81	-2	30	892	1
R_{rs}(531)	16	0.00220	0.78	0.0014	-0.00057	0.76	-12	33	892	1
R_{rs}(547)	16	0.00216	0.82	0.0013	-0.00029	0.75	-6	29	892	1
R_{rs}(667)	28	0.00089	0.85	0.00003	-0.00033	0.80	-47	76	892	0

FUB

R_{rs}(412)	30	0.00152	0.70	0.0013	-0.00014	0.66	-1	70	721	0
R_{rs}(443)	25	0.00162	0.73	0.0013	-0.00023	0.74	-4	62	721	0
R_{rs}(488)	31	0.00244	0.94	0.0019	0.00144	0.81	53	60	721	0
R_{rs}(531)	30	0.00310	1.10	0.0013	0.00220	0.83	62	64	721	0
R_{rs}(547)	28	0.00327	1.16	0.0007	0.00216	0.81	59	61	721	0
R_{rs}(667)	28	0.00119	1.30	-0.00045	0.00029	0.84	11	63	721	0

OC-SMART

R_{rs}(412)	35	0.00209	0.70	0.0011	-0.00026	0.49	-21	76	895	0
R_{rs}(443)	23	0.00165	0.80	0.00087	-0.00027	0.75	-14	49	895	0
R_{rs}(488)	15	0.00162	0.87	0.0075	-0.00028	0.85	-11	28	895	0
R_{rs}(531)	14	0.00179	0.87	0.00068	-0.00055	0.85	-16	27	895	0
R_{rs}(547)	13	0.00171	0.93	0.00044	-0.00022	0.85	-9	24	895	0
R_{rs}(667)	29	0.00082	0.88	-0.00014	-0.000430	0.86	-74	86	895	0

C2RCC

R_{rs}(412)	37	0.00225	0.48	0.0012	-0.00114	0.43	-71	122	786	0
R_{rs}(443)	34	0.00247	0.54	0.0017	-0.00084	0.46	-27	99	786	0
R_{rs}(488)	35	0.00295	0.67	0.0027	0.00024	0.53	23	86	786	0
R_{rs}(531)	25	0.00259	0.84	0.0023	0.00082	0.70	31	56	786	0
R_{rs}(547)	23	0.00253	0.92	0.0018	0.00103	0.74	29	46	786	0
R_{rs}(667)	29	0.00106	0.71	0.0002	-0.00050	0.77	-88	98	786	0

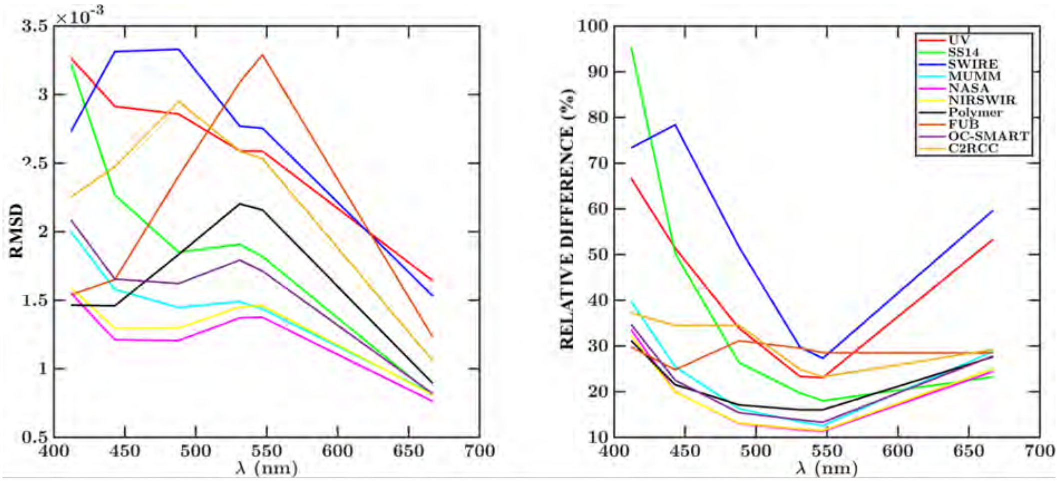

Figure 7.2 Right panel: Variation of the relative difference (RD) as a function of wavelength. Left panel: Variation of the RMSD as a function of wavelength

of the slope were correlated with the R^2 values, with lowest R^2 at 412 (between 0.13 for UV and 0.74 for Polymer) and 443 nm (between 0.39 for UV and 0.87 for NASA-AC) and the highest R^2 at 531 (between 0.70 for C2RCC and 0.92 for NASA-AC) and 547 nm (between 0.71 for UV and 0.92 for NASA-AC). As UV-AC was mainly applicable for highly turbid waters, it is not surprising that its performance was lower for match-ups with the in-situ dataset, which only covers low-to-moderately turbid waters.

Variation of RD and RMSD as a function of wavelength are shown in Fig. 7.2. For RD, a *smiley* shape was observed, as mentioned by Jamet et al. (2011), Goyens et al. (2013) and Melin (2022). This shape is a direct result of overall lower R_{rs} in the blue and NIR and higher R_{rs} in the green for the underlying and predominant OWTs 4-6 (Fig. 6.4). Lower absolute values were usually associated with higher relative differences and vice versa. However, some algorithms were less sensitive to wavelength in term of RMSD (NIRSWIR, NASA-AC and OC-SMART) while others were very sensitive to wavelengths (FUB, Polymer, UV-AC, SWIRE, C2RCC). The shape of the predominant OWTs 4-6 were reproduced by the absolute differences of Polymer and FUB.

A spider plot of all statistical parameters (except the intercept of the regression line) is shown in Fig. 7.3, which provides an overview of the performance of each algorithm. The values of the statistical parameters were normalized so that 1 represented the best value of a given statistical parameter and 0 represented the worst value. Thus, the best overall AC algorithm over our in-situ dataset was the algorithm with the maximum number of 1s. The accuracies of the AC algorithms depended on the wavelength (Fig. 7.3). In the blue bands (412 and 443 nm), NASA-AC, NIRSWIR, and Polymer were the most accurate. At 667 nm, the statistical parameters were not overall consistent and most of the algorithms did not provide accurate retrievals of R_{rs}. At 531 and 547 nm, NASA-AC, NIRSWIR, OC-SMART, and MUMM provided accurate retrievals. Overall, NASA-AC, NIRSWIR and OC-SMART were the most accurate AC algorithms when applied to our *in-situ* dataset covering low-to-moderate turbid waters.

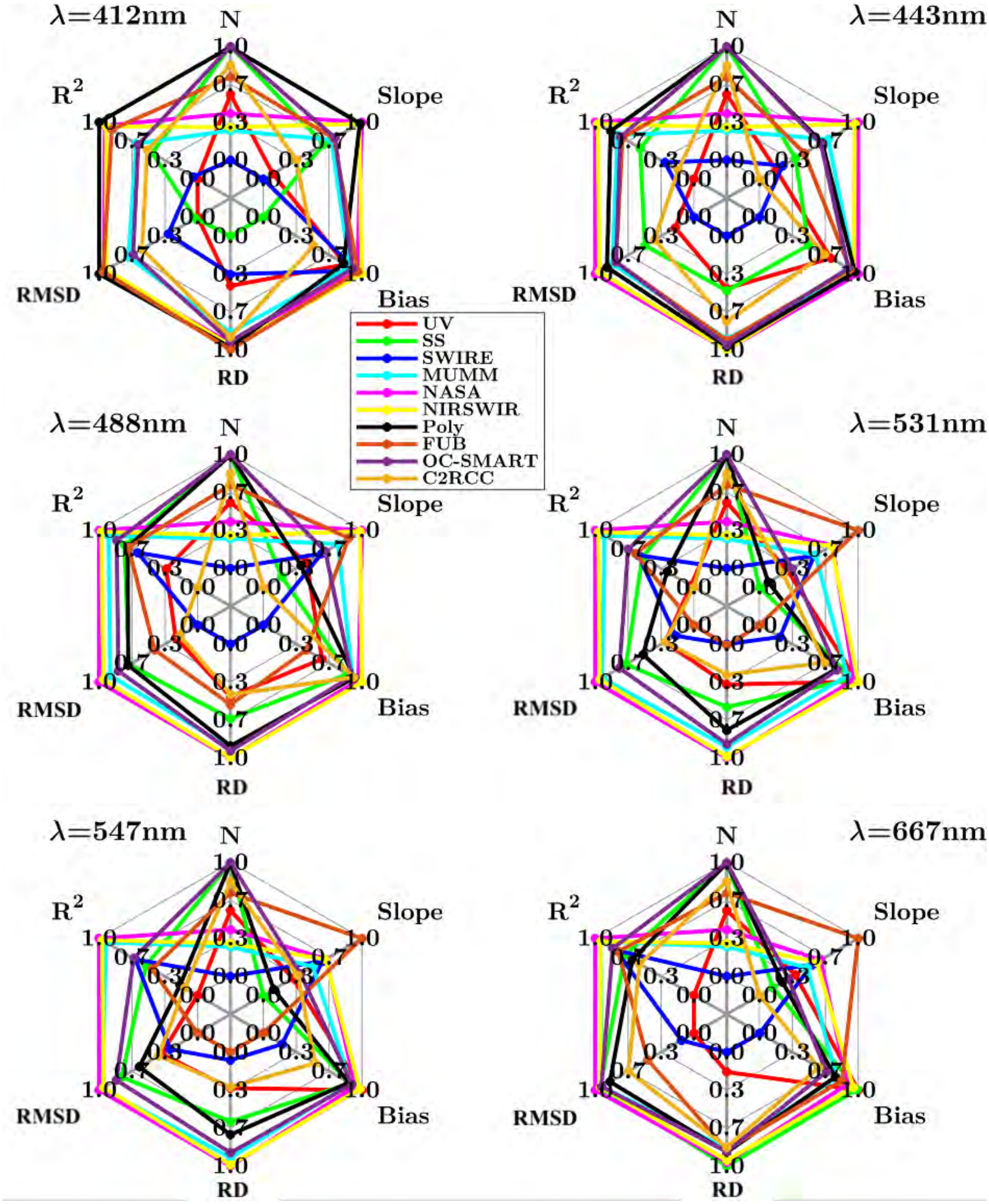

Figure 7.3 Spider-plot of the normalized statistical parameters as a function of wavelength. Colours correspond to AC model colours used in previous figures.

Table 7.2 Values of the statistical parameters calculated over the entire spectra. The bold value highlights the best value for a given statistical parameter.

ALGORITHMS	QAS	χ^2 (%)	SAM (°)	S_{total}
UV-AC	0.78	43.73	9.70	18.24
SS14	0.91	48.14	9.10	27.61
SWIRE	0.82	32.92	8.18	15.91
MUMM	0.95	15.30	5.59	34.59
NASA-AC	0.96	11.01	4.98	**38.15**
NIRSWIR	0.96	10.70	**4.77**	37.55
Polymer	**0.97**	**9.59**	5.08	35.26
FUB	0.93	20.03	6.91	29.31
OC-SMART	0.97	10.66	4.91	36.34
C2RCC	0.94	47.41	9.11	26.45

The results of statistical analysis by spectral shape (QAS, χ^2, SAM) are shown in Table 7.2. The retrieved spectra is compared to the reference spectra through the QAS parameter (Wei et al. 2016). Most of the algorithms retrieved realistic spectra with values of QAS higher than 0.95 for MUMM, NIRSWIR, NASA-AC, Polymer and OC-SMART. Two algorithms showed less realistic spectra with QAS values of 0.78 (UV) and 0.82 (SWIRE). χ^2 and SAM compared the retrieved spectra to in-situ spectra. NIRSWIR, NASA-AC, Polymer, and OC-SMART presented the lowest values (10.70%, 11.01%, 9.59% and 10.66% for χ^2; 4.77°, 4.98°, 5.08° and 4.91° for SAM). Three algorithms (UV, SS13, C2RCC) showed values of χ^2 greater than 40% (43.73%, 48.14% and 47.41%) and values of SAM greater than 9° (9.70°, 9.10° and 9.11°).

Calculation of the overall score (Müller et al. 2015) considered the accuracies per wavelength and the shape of the spectra (Table 7.2). The maximum value of the score was 42. One group of AC algorithms had S_{total} values higher than 35 [NASA-AC (38.15), NIRSWIR (37.55), Polymer (35.26) and OC-SMART (36.34)]. Another group had low values, less than 20 (UV-AC (18.24) and SWIRE (15.91)).

Regarding the statistical parameters for each OWT, only classes 3-9 were included as there were no match-ups for classes 1-2, which corresponded to the most turbid OWTs. S_{total} for the OWTs are provided in Table 7.3. Only four ACs provided retrievals for OWT9: SS14, Polymer, OC-SMART and C2RCC. However, OWT9 represented the least turbid optical waters and only two match-ups concerned this OWT, so the results should be read with caution. Only NIRSWIR had values greater than 30 for all OWTs. Both NASA-AC and OC-SMART had values of S_{total} greater than 30 for OWT 3-7, and values close to 30 (29.87 and 28.49, respectively) for OWT8. SS14 showed similar values of S_{total} for all OWT (around 27), which was not the case for MUMM, Polymer, FUB and C2RCC.

Table 7.3 S_{total} values for all AC as a function of optical water types (OWT). The bold value highlights the best value for a given OWT.

	OWT1	OWT2	OWT3	OWT4	OWT5	OWT6	OWT7	OWT8	OWT9
UV-AC	0	0	21.17	22.87	18.50	20.68	18.84	21.75	0
SS14	0	0	27.30	27.50	28.09	26.50	27.21	28.51	**32.60**
SWIRE	0	0	24.65	10.11	18.34	10.09	10.38	20.80	0
MUMM	0	0	28.76	33.47	34.42	34.83	29.42	24.61	0
NASA-AC	0	0	32.81	**38.86**	**38.45**	**37.79**	**33.46**	29.87	0
NIRSWIR	0	0	33.73	36.88	37.87	36.20	33.35	**30.00**	0
Polymer	0	0	29.62	36.02	25.29	33.98	21.29	25.57	20.39
FUB	0	0	21.46	28.18	25.53	26.85	24.98	21.60	0
OC-SMART	0	0	**34.63**	37.01	31.76	35.94	30.44	28.49	19.24
C2RCC	0	0	29.27	24.16	22.47	26.90	25.13	27.47	31.72

7.2 Common match-up analyses

In the previous section, we examined the performance of the AC algorithms on their overall match-up dataset. Here we directly compare the AC algorithms using only those dates and locations that are common to all algorithms (common match-ups). As SWIRE provided the least number of match-ups (N=242), the common match-up dataset was reduced to N=83 values. Despite the smaller size, this dataset provided a direct comparison of the statistical parameters between the ten AC algorithms.

Scatterplots per wavelength are displayed in Fig. 7.4 for the common match-up dataset (similar to Fig. 7.1). Similar to the overall dataset, there was high scattering in the blue bands (412 and 443 nm) and scattering decreased at 531 and 547 nm. UV-AC, SS14 and SWIRE showed very high values of retrieved R_{rs} compared to *in-situ* data at 412 and 443 nm. All algorithms appeared to provide similar R_{rs} from 488 to 667 nm, except for FUB and C2RCC which provided high values for *in-situ* $R_{rs}>0.2$ sr^{-1} for a few points at 531, 547 and 667 nm.

All statistical parameters per wavelength are provided in Table 7.4 (similar to Table 7.1). For the common match-up dataset, no algorithm provided negative values of R_{rs}. All statistical values were better, indicating that all algorithms provided more accurate retrievals of R_{rs} on the common match-up dataset. Five AC algorithms (NASA-AC, NIRSWIR, MUMM, Polymer, OC-SMART) provided accurate retrievals at 488, 531 and 547 nm (Table 7.4 and Fig. 7.4), with RD lower than 15% and R^2 higher than 0.86 at those three wavelengths. The other five algorithms (UV-AC, SS14, SWIRE, FUB and C2RCC) provided retrievals with RD higher than 24% for those wavelengths. At 412 nm, low accuracies were obtained for three algorithms (UV-AC, SWIRE and SS14) with RD higher than 40%, leading to low slopes (lower than 0.6) and low R^2 (lower than 0.51). Five algorithms (NASA-AC, NIRSWIR, Polymer, FUB and OC-SMART) provided accurate retrievals in the blue bands with low RD (lower than 23% at 412 nm and lower than 20% at 443 nm). FUB provided accurate retrievals at 412 and 443 nm but less accurate retrievals between 488 and 547 nm. This behavior was in contrast to the other AC algorithms, which tended to have higher differences in the blue bands than in the green and red bands. NASA-AC,

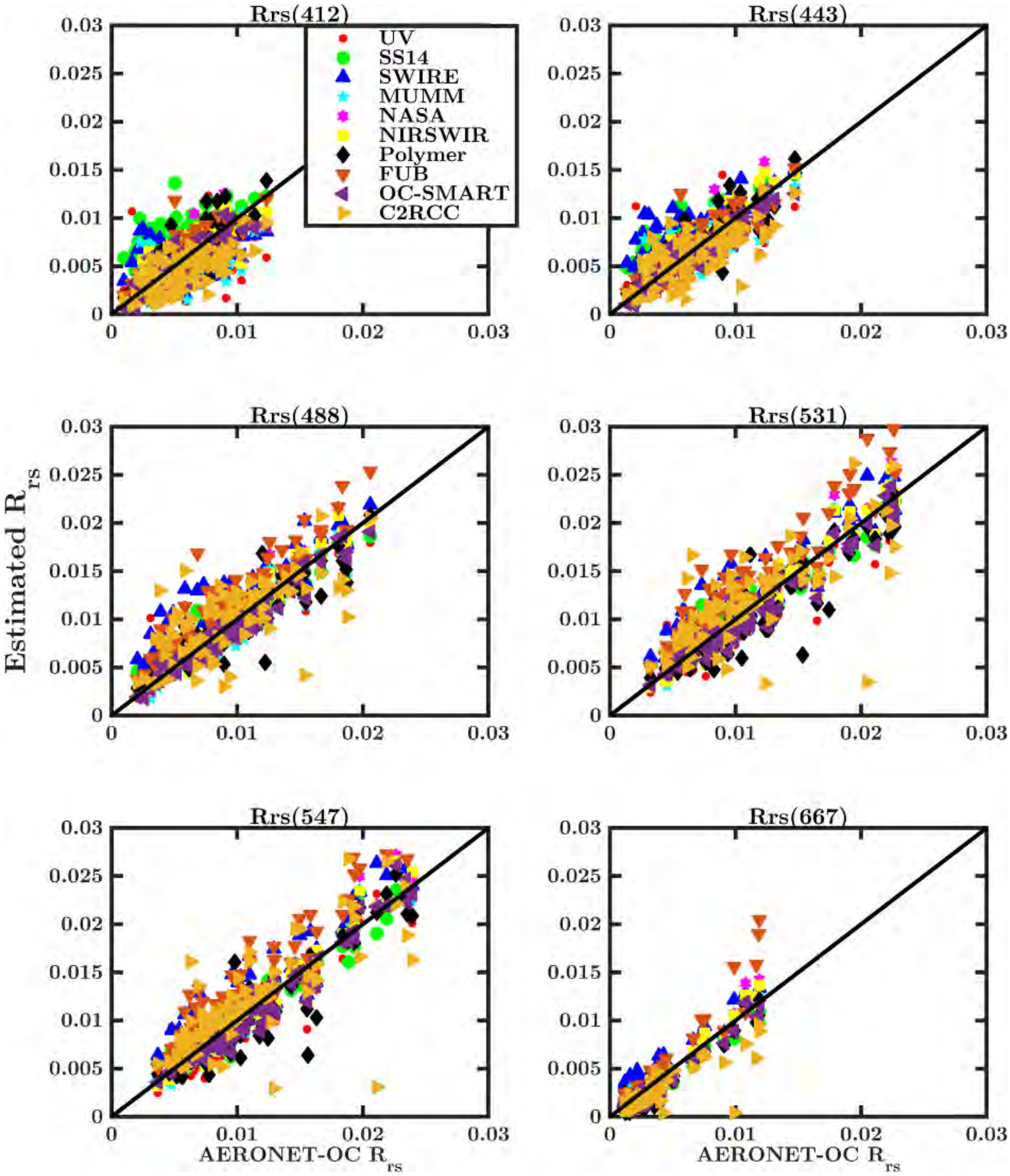

Figure 7.4 Scatterplots of the AC algorithm estimated Rrs vs in-situ Rrs from 412 (top left) to 667 nm (bottom right). Individual scatterplots are provided in Appendix C.

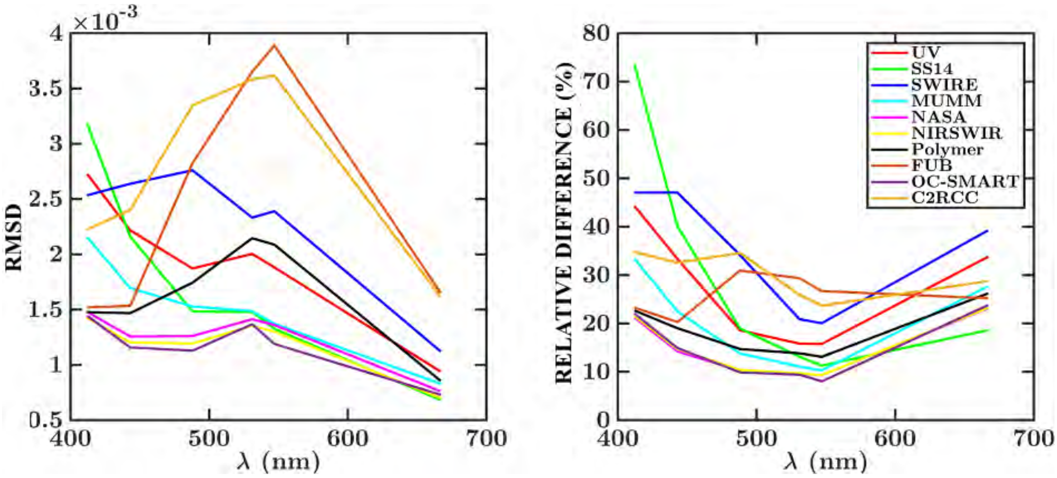

Figure 7.5 (a) Variation of the RD as a function of wavelength, (b) Variation of the RMSD as a function of wavelength.

NIRSWIR and OC-SMART were not very sensitive to wavelength, providing accurate retrievals at all bands with RMSD and RD varying slightly between bands (Fig. 7.5).

Fig. 7.6 presents all statistical parameters as a spider plot (same as Fig. 7.3). For λ=412, 443 and 488 nm, four algorithms (NASA-AC, NIRSWIR, OC-SMART, FUB) showed the best overall performance for the five statistical parameters considered. For λ=667 nm, SWIRE and C2RCC appeared to be the least accurate, while NIRSWIR, NASA-AC, OC-SMART and FUB appeared to be the most accurate (despite their slopes). For λ=531 and 547nm, SWIRE and C2RCC were the least accurate, while MUMM NASA-AC, NIRSWIR, and OC-SMART were the AC algorithms with the best overall statistical parameters.

Table 7.5 provides the statistical parameters on the shape of the retrieved spectra compared to the *in-situ* spectra (same as Table 7.2). For all parameters, the algorithms can be partitioned into three groups depending on values. For S_{total}: 1) $S_{total} \leq 20$ (SWIRE, C2RCC); 2) $20 \leq S_{total} \leq 35$ (UV-AC, SS14, MUMM, FUB, Polymer); and 3) $S_{total} > 37$ (NASA-AC, NIRSWIR and OC-SMART). In terms of shape, the vast majority of the algorithms provided accurate spectra compared to reference spectra with values of QAS >0.90, except for UV-AC (QAS=0.89) and SWIRE (QAS=0.81). Results were similar to the individual match-up dataset for χ^2 and SAM. For χ^2, algorithms clustered as follows: 1) $\chi^2 > 20\%$ (UV-AC, SS14 and C2RCC); 2) $10 \leq \chi^2 \leq 20\%$ (SWIRE, MUMM, Polymer and FUB); and 3) $10\% > \chi^2$ (NASA-AC, NIRSWIR and OC-SMART). For SAM, the algorithms clustered with: 1) SAM>8° (SS14 and C2RCC); 2) 5°≤SAM≤8° (UV-AC, SWIRE, MUMM and FUB); and 3) SAM<5° (NASA-AC, NIRSWIR, Polymer and OC-SMART).

As for the individual match-up dataset, the statistical parameters for each OWT were studied. Only classes 3-8 are included here as SWIRE did not provide any match-ups for OWT9. Values of S_{total} are provided in Table 7.6. The majority of match-ups were available for OWT6-7 (Table 6.1), which were less turbid waters. There were only a few match-ups (2) for OWT3. Results of S_{total} (Table 7.6) were slightly different than for the individual match-up dataset. S_{total} decreased for all AC algorithms for OWT3. This might be explained by the very low number

Table 7.4 Statistical results from comparing R_{rs} derived from various atmospheric correction algorithms and AERONET-OC data for the common match-up dataset (*RD* - mean relative difference, *RMSD* – root mean square difference, R^2- regression, β- overall difference, α - relative bias in log, N - number of valid data/model/wavelengths

	RD(%)	**RMSD (sr^{-1})**	**Slope (sr^{-1})**	**Intercept**	**Bias (sr^{-1})**	**β (%)**	**α (%)**	**R^2**	**N**
UV-AC									
$R_{rs}(412)$	44	0.00273	0.25	0.0005	-0.0008	-43	137	0.11	83
$R_{rs}(443)$	33	0.00222	052	0.0018	0.0001	1	57	0.48	83
$R_{rs}(488)$	19	0.00187	0.78	0.0014	0.0002	2	27	0.81	83
$R_{rs}(531)$	16	0.00200	0.89	-0.0003	-0.0009	-28	39	0.87	83
$R_{rs}(547)$	16	0.00188	0.97	-0.0010	-0.0007	-22	34	0.88	83
$R_{rs}(667)$	34	0.00094	0.99	-0.0007	-0.0006	-120	137	0.93	83
SS14									
$R_{rs}(412)$	74	0.00318	0.56	0.00514	0.00264	136	136	0.51	83
$R_{rs}(443)$	40	0.00216	0.71	0.00361	0.00159	45	45	0.78	83
$R_{rs}(488)$	19	0.00148	0.80	0.00238	0.00047	5	24	0.90	83
$R_{rs}(531)$	13	0.00148	0.87	0.00159	0.00003	-2	22	0.91	83
$R_{rs}(547)$	11	0.00132	0.92	0.00089	0.000006	-1	23	0.93	83
$R_{rs}(667)$	19	0.00068	0.91	-0.00005	-0.00032	-31	47	0.95	83
SWIRE									
$R_{rs}(412)$	47	0.00253	0.27	0.00359	-0.000542	-37	112	0.14	83
$R_{rs}(443)$	47	0.00264	0.61	0.00439	0.00171	54	55	0.57	83
$R_{rs}(488)$	34	0.00276	0.82	0.00368	0.00198	47	47	0.80	83
$R_{rs}(531)$	21	0.00233	0.93	0.00202	0.00124	23	32	0.85	83
$R_{rs}(547)$	20	0.00239	1.00	0.00131	0.00136	25	34	0.87	83
$R_{rs}(667)$	39	0.00112	1.05	0.00057	0.00072	65	69	0.91	83
MUMM									
$R_{rs}(412)$	33	0.00215	0.49	0.00233	-0.00056	-18	85	0.36	83
$R_{rs}(443)$	22	0.00169	0.73	0.00170	-0.00018	-8	49	0.70	83
$R_{rs}(488)$	14	0.00153	0.87	0.00086	-0.00034	-9	27	0.88	83
$R_{rs}(531)$	11	0.00149	0.96	-0.00004	-0.00048	-13	23	0.92	83
$R_{rs}(547)$	10	0.00137	1.01	-0.00051	-0.00040	-12	21	0.94	83
$R_{rs}(667)$	28	0.00083	1.04	-0.00052	-0.00040	-44	82	0.93	83
NASA-AC									
$R_{rs}(412)$	22	0.00148	0.78	0.0011	-0.00017	-11	41	0.68	83
$R_{rs}(443)$	14	0.00126	0.94	0.0005	0.00012	-5	26	0.84	83
$R_{rs}(488)$	10	0.00126	1.00	-0.00008	-0.00011	-6	20	0.92	83
$R_{rs}(531)$	10	0.00141	1.05	-0.0008	-0.00030	-11	22	0.93	83
$R_{rs}(547)$	9	0.00136	1.09	-0.0012	-0.00024	-10	19	0.95	83
$R_{rs}(667)$	23	0.00076	1.15	-0.0007	-0.00028	-54	59	0.96	83

NIRSWIR									
R_{rs} (412)	22	0.00143	0.80	0.0010	-0.00011	-1	43	0.69	83
R_{rs}(443)	15	0.00120	0.95	0.0005	0.00016	8	26	0.86	83
R_{rs}(488)	11	0.00120	1.00	-0.0001	-0.00009	-6	22	0.93	83
R_{rs}(531)	10	0.00135	1.05	-0.0008	-0.00029	-11	23	0.94	83
R_{rs}(547)	9	0.00130	1.09	-0.0012	-0.00022	-10	20	0.95	83
R_{rs}(667)	23	0.00070	1.14	-0.0007	-0.00028	-53	57	0.96	83
Polymer									
R_{rs} (412)	23	0.00148	0.84	0.0013	0.00038	21	54	0.70	83
R_{rs}(443)	19	0.00147	0.80	0.0015	0.00010	8	35	0.77	83
R_{rs}(488)	15	0.00174	0.82	0.0014	-0.00033	-7	30	0.84	83
R_{rs}(531)	14	0.00214	0.86	0.0007	-0.00084	-17	32	0.84	83
R_{rs}(547)	13	0.00209	0.93	0.0003	-0.00057	-8	25	0.84	83
R_{rs}(667)	26	0.00085	0.95	-0.0004	-0.00054	-68	77	0.93	83
FUB									
R_{rs} (412)	23	0.00152	0.74	0.00139	-0.00007	-5	50	0.65	83
R_{rs}(443)	20	0.00153	0.79	0.00139	-0.00004	-1	43	0.75	83
R_{rs}(488)	31	0.00282	1.00	0.00217	0.00215	60	60	0.84	83
R_{rs}(531)	29	0.00365	1.17	0.00098	0.00286	74	74	0.88	83
R_{rs}(547)	27	0.00389	1.28	-0.00037	0.00273	63	63	0.87	83
R_{rs}(667)	25	0.00165	1.45	-0.00096	0.00041	1	73	0.91	83
OC-SMART									
R_{rs} (412)	22	0.00144	0.70	0.00120	-0.0005	-21	52	0.71	83
R_{rs}(443)	15	0.00116	0.83	0.00069	-0.0005	-17	33	0.88	83
R_{rs}(488)	10	0.00112	0.91	0.00044	-0.0004	-11	19	0.94	83
R_{rs}(531)	9	0.00137	0.93	0.00008	-0.0007	-14	19	0.94	83
R_{rs}(547)	8	0.00119	1.01	-0.00044	-0.0003	-8	15	0.95	83
R_{rs}(667)	24	0.00073	0.96	-0.00042	-0.0005	-72	72	0.96	83
C2RCC									
R_{rs} (412)	35	0.00222	0.50	0.00017	-0.0011	-87	139	0.43	83
R_{rs}(443)	33	0.00240	0.54	0.00251	-0.0007	-28	88	0.45	83
R_{rs}(488)	35	0.00335	0.59	0.00450	0.0007	22	66	0.45	83
R_{rs}(531)	26	0.00358	0.70	0.00417	0.0009	30	46	0.55	83
R_{rs}(547)	24	0.00362	0.77	0.00346	0.0009	29	49	0.57	83
R_{rs}(667)	29	0.00161	0.62	0.00029	-0.0009	-98	103	0.73	83

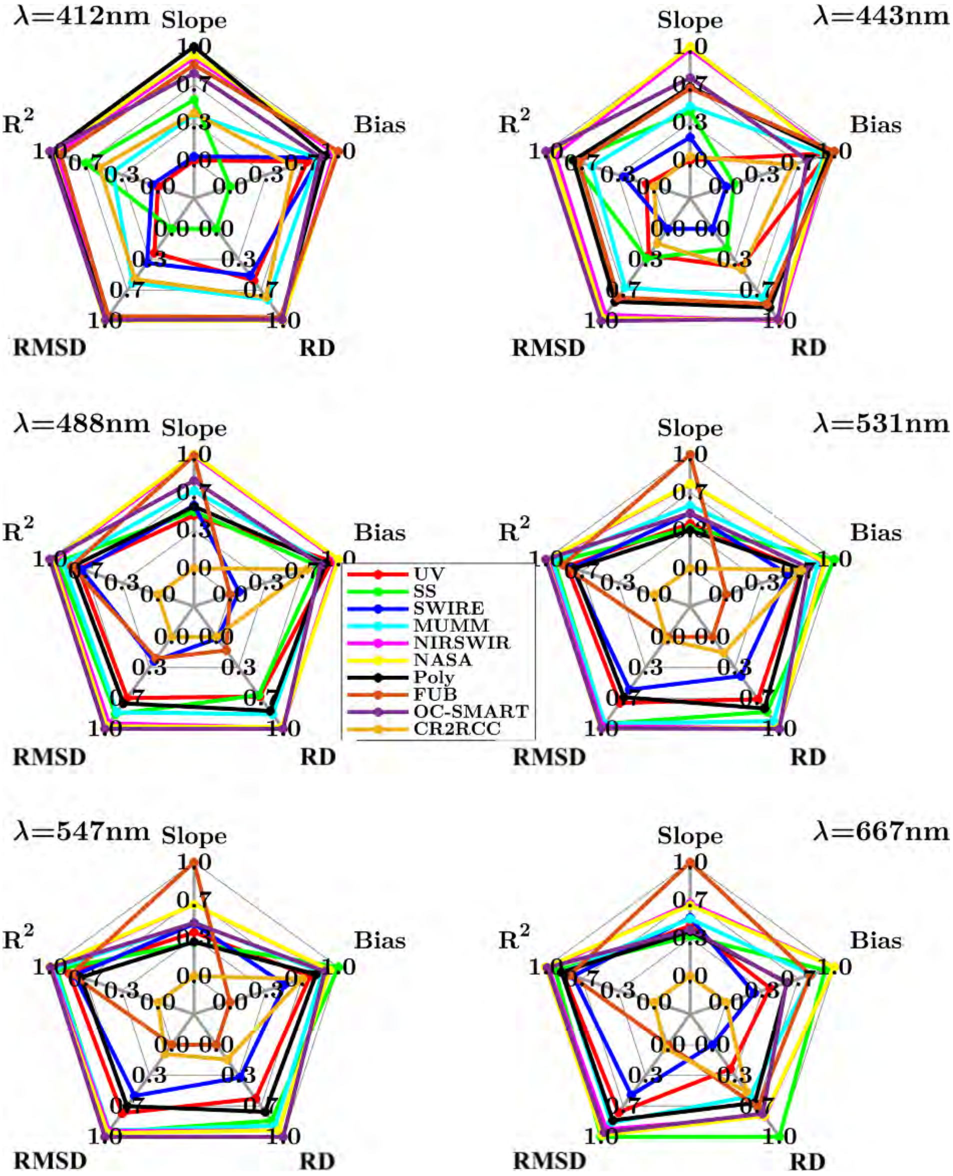

Figure 7.6 Spider-plot of the normalized statistical parameters as a function of wavelength.

Table 7.5 Values of the statistical parameters calculated over the entire spectral range. The bold value highlights the best value for a given statistical parameter.

ALGORITHMS	QAS	χ^2 (%)	SAM (°)	S_{total}
UV-AC	0.89	24.30	7.70	26.83
SS14	0.92	21.94	8.96	29.24
SWIRE	0.81	16.76	7.03	20.95
MUMM	0.96	13.83	5.32	34.28
NASA-AC	0.96	**6.91**	**3.95**	38.76
NIRSWIR	0.96	7.01	3.98	**39.24**
Polymer	**0.97**	11.10	4.97	34.34
FUB	0.95	14.90	6.32	25.06
OC-SMART	0.97	7.56	4.09	38.69
CR2CC	0.95	33.20	8.33	15.58

Table 7.6 S_{total} values for all AC algorithms as a function of OWT. Bold highlights the best value for a given parameter.

	OWT1	OWT2	OWT3	OWT4	OWT5	OWT6	OWT7	OWT8	OWT9
UV-AC	0	0	20.71	31.72	23.68	19.41	22.62	18.65	0
SS14	0	0	16.72	26.75	26.03	25.59	31.17	**37.41**	0
SWIRE	0	0	18.14	21.90	18.05	10.39	25.11	35.39	0
MUMM	0	0	18.39	33.32	33.72	34.69	29.16	22.80	0
NASA-AC	0	0	14.51	39.80	**40.37**	**37.08**	**36.23**	28.21	0
NIRSWIR	0	0	21.69	39.09	39.58	**37.08**	**36.23**	28.21	0
Polymer	0	0	24.21	37.23	24.78	31.07	29.01	12.87	0
FUB	0	0	12.37	26.79	24.80	23.93	24.41	24.05	0
OC-SMART	0	0	**26.02**	**40.56**	35.42	37.17	28.98	26.76	0
C2RCC	0	0	18.37	15.29	17.40	29.88	11.13	20.19	0

of match-ups for this OWT. For OWT4-7, NIRSWIR and NASA-AC showed S_{total} values greater than 36. S_{total} values tended to decrease from OWT4 to OWT8. This can be explained by the fact that all AC algorithms in this study were designed to deal with moderate to very turbid waters, while the turbidity of the OWTs decreased from OWT3 to OWT8.

7.3 Sensitivity studies

The AOT at 869 nm ($\tau(869)$) and turbidity of coastal waters via SPM concentrations were examined for each algorithm. $\tau(869)$ was directly measured by the AERONET-OC stations. SPM was estimated from corresponding *in-situ* R_{rs} using the algorithm of Han et al. (2016). The algorithm uses a switching threshold to better estimate the lower and higher values of SPM at $R_{rs}(667)$, and showed good performance in coastal waters (Subirade et al. 2024).

Ideally, a sensitivity study should be done by fixing all parameters except one. In the case of the AERONET-OC in-situ data, this was difficult to achieve, as information on other covarying constituents such as CDOM and chlorophyll-a (chl-a) were not measured. Therefore, the sensitivity of the relative R_{rs} difference as a function of $\tau(869)$ may include any possible water quality combination (SPM, chl-a, CDOM) and sun/observing geometry for each AOT bin. The same is true for the R_{rs} difference sensitivity as a function of SPM, which may include any possible CDOM, chl-a, $\tau(869)$ and sun/observing geometry combination for each SPM bin. As this sensitivity analysis therefore remains inconclusive, we refer hereafter to the use of SPM- and $\tau(869)$-proxies.

The ratio of R_{rs} commonly used for chl-a concentration: $\frac{R_{rs}(443)}{R_{rs}(547)}$, $\frac{R_{rs}(488)}{R_{rs}(547)}$ and $\frac{R_{rs}(531)}{R_{rs}(547)}$ (O'Reilly et al. 1998, 2019) are also presented.

7.3.1 Individual spectra match-up dataset

7.3.1.1 Sensitivity to $\tau(869)$-proxy

Variation of RD on the retrieval of $R_{rs}(\lambda)$ as a function of $\tau(869)$-proxy for all ten algorithms is shown in Fig. 7.7. Two groups of algorithms emerged: a first group (NASA-AC, NIRSWIR, MUMM, Polymer, OC-SMART, UV-AC) for which RD was *slightly* dependent on the $\tau(869)$-proxy; and a second group (SWIRE, SS14, FUB) for which the accuracy of the retrievals was *highly* dependent on the $\tau(869)$-proxy. This was particularly true for bands between 412 and 488 nm.

7.3.1.2 Sensitivity to SPM-proxy

Variation of RD as a function of SPM that includes the variability of all other parameters is shown in Fig. 7.8. For all algorithms, the shape of RD had a *smiley* form, which meant that they provided better retrievals for a specific range of SPM values. As for the $\tau(869)$-proxy, the same two groups of algorithms emerged based on sensitivities to SPM-proxy values.

7.3.1.3 Estimation of R_{rs} ratios

Fig. 7.9 shows the $R_{rs}(\lambda)$ ratios commonly used in chl-a retrieval algorithms versus the *in-situ* as estimated by the ten AC algorithms. $R_{rs}(\lambda)$ ratios can be of high quality even when individual retrievals of $R_{rs}(\lambda)$ show high differences. Thus, it was necessary to investigate the potential impact of retrieval differences on the estimation of chl-a concentration or SPM. As expected, high scattering around the 1:1 line was observed for $\frac{R_{rs}(443)}{R_{rs}(547)}$, especially for UV-AC, SS14 and SWIRE. This was related to the large differences observed at 443 nm for these algorithms. In contrast, NASA-AC, NIRSWIR and OC-SMART showed less scattering for this ratio. Scattering around the 1:1 line decreased as λ increased. For $\frac{R_{rs}(531)}{R_{rs}(547)}$, most of the AC algorithms provided estimates close to the 1:1 line, except for values higher than 1.3 or less than 0.75. All algorithms tended to overestimate low values of $\frac{R_{rs}(531)}{R_{rs}(547)}$. This was in accordance with the statistical parameters (Table 7.7) which showed a decrease in slopes between $\frac{R_{rs}(488)}{R_{rs}(547)}$ and $\frac{R_{rs}(531)}{R_{rs}(547)}$ for all algorithms.

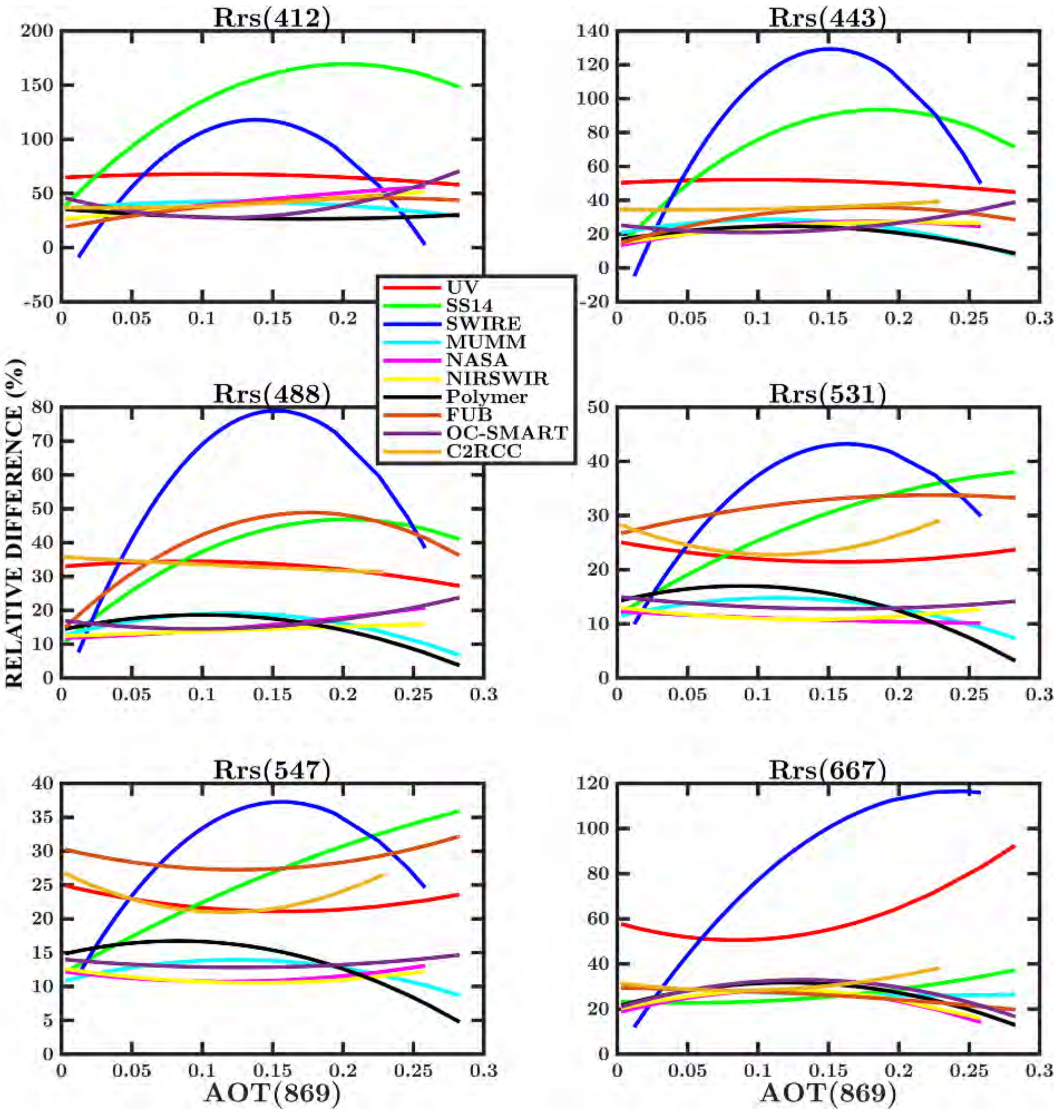

Figure 7.7 Variation of the RD as a function of the aerosol optical thickness $\tau(869)$-proxy for each wavelength.

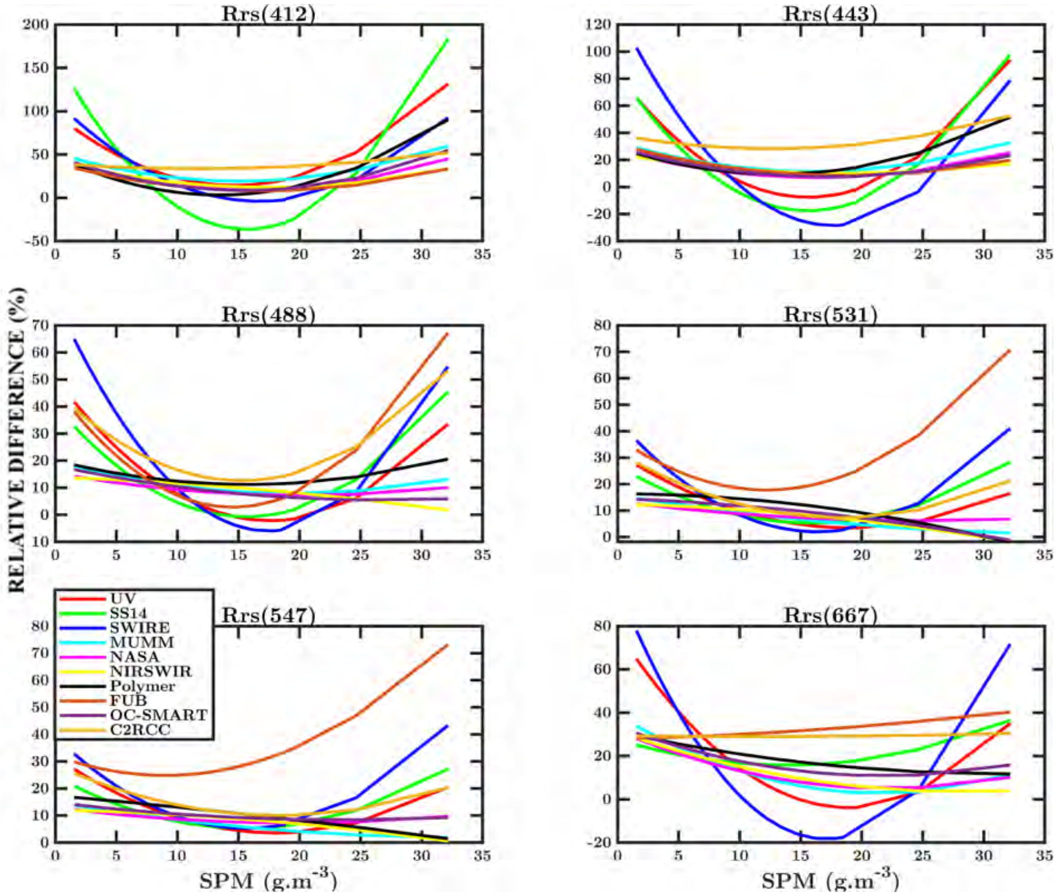

Figure 7.8 Variation of RD as a function of the suspended particulate matter (SPM)-proxy for each wavelength.

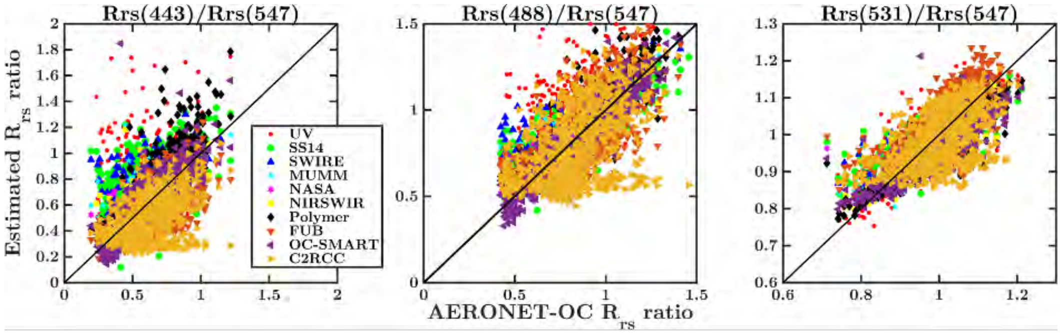

Figure 7.9 Scatterplot of the retrieved versus in-situ ratios of R_{rs} over the individual match-up dataset: left panel: $\frac{R_{rs}(443)}{R_{rs}(547)}$; middle panel: $\frac{R_{rs}(488)}{R_{rs}(547)}$; right panel: $\frac{R_{rs}(531)}{R_{rs}(547)}$. Individual scatterplots for each algorithm are provided in Appendix B.

Table 7.7 Statistical results from R_{rs} ratios derived from AC algorithms and AERONET-OC individual match-up dataset (*RD* - mean relative difference, *RMSD* – root mean square difference, R^2- regression)

	RD(%)	RMSD	Slope	Intercept	Bias	R^2
UV-AC						
$\frac{R_{rs}(443)}{R_{rs}(547)}$	38	0.279	0.54	0.41	0.131	0.14
$\frac{R_{rs}(488)}{R_{rs}(547)}$	24	0.233	0.84	0.29	0.163	0.49
$\frac{R_{rs}(531)}{R_{rs}(547)}$	4	0.051	0.78	0.21	-0.003	0.63
SS14						
$\frac{R_{rs}(443)}{R_{rs}(547)}$	33	0.215	0.61	0.379	0.1408	0.34
$\frac{R_{rs}(488)}{R_{rs}(547)}$	11	0.108	0.66	0.321	0.0352	0.71
$\frac{R_{rs}(531)}{R_{rs}(547)}$	4	0.047	0.55	0.454	0.0026	0.65
SWIRE						
$\frac{R_{rs}(443)}{R_{rs}(547)}$	37	0.234	0.48	0.485	0.157	0.25
$\frac{R_{rs}(488)}{R_{rs}(547)}$	19	0.168	0.66	0.416	0.125	0.66
$\frac{R_{rs}(531)}{R_{rs}(547)}$	3 0.043	0.63	0.380	0.0108	0.72	
MUMM						
$\frac{R_{rs}(443)}{R_{rs}(547)}$	17	0.129	0.73	0.183	0.0159	0.48
$\frac{R_{rs}(488)}{R_{rs}(547)}$	7	0.076	0.83	0.145	0.0023	0.81
$\frac{R_{rs}(531)}{R_{rs}(547)}$	3	0.041	0.65	0.345	-0.0058	0.70
NASA-AC						
$\frac{R_{rs}(443)}{R_{rs}(547)}$	15	0.109	0.79	0.147	0.0225	0.61
$\frac{R_{rs}(488)}{R_{rs}(547)}$	7	0.069	0.86	0.120	0.0063	0.86
$\frac{R_{rs}(531)}{R_{rs}(547)}$	3	0.039	0.71	0.290	-0.0022	0.74

RD and RMSD values decreased from $\frac{R_{rs}(443)}{R_{rs}(547)}$ to $\frac{R_{rs}(531)}{R_{rs}(547)}$. RD varied between 14% (NIR-SWIR and OC-SMART) and 38% (UV-AC) for $\frac{R_{rs}(443)}{R_{rs}(547)}$ and between 3% (NASA-AC, NIRSWIR, MUMM and SWIRE) and 6% (C2RCC) for $\frac{R_{rs}(531)}{R_{rs}(547)}$.

7.3.2 Common spectra match-up dataset

Similar types of sensitivity studies were conducted for the common match-up dataset.

7.3.2.1 Sensitivity to $\tau(869)$-proxy

Variation of RD as a function of $\tau(869)$-proxy values are shown in Fig. 7.10. Values of $\tau(869)$ were limited to 0.15 for the common match-up dataset, compared to up to 0.28 for the individual match-up dataset. The results and trends were similar to those for the individual match-up datasets. Three main groups of algorithms were observed. The first group (UV-AC, SS14, SWIRE) showed high sensitivity to $\tau(869)$-proxy values as RD increased, with higher values of $\tau(869)$-proxy for all wavelengths. The second group (NIRSWIR, NASA-AC, MUMM, Polymer, OC-SMART) showed low sensitivity to $\tau(869)$-proxy values. The third group (FUB)

NIRSWIR					
$\frac{R_{rs}(443)}{R_{rs}(547)}$	14	0.108	0.78	0.161	0.0274	0.60
$\frac{R_{rs}(488)}{R_{rs}(547)}$	6	0.068	0.86	0.127	0.0075	0.85
$\frac{R_{rs}(531)}{R_{rs}(547)}$	3	0.037	0.71	0.287	-0.0031	0.72
Polymer						
$\frac{R_{rs}(443)}{R_{rs}(547)}$	17	0.141	1.10	0.002	0.0637	0.70
$\frac{R_{rs}(488)}{R_{rs}(547)}$	9	0.096	0.96	0.064	0.0271	0.80
$\frac{R_{rs}(531)}{R_{rs}(547)}$	4	0.048	0.75	0.223	-0.0255	0.72
FUB						
$\frac{R_{rs}(443)}{R_{rs}(547)}$	24	0.178	0.73	0.059	-0.108	0.48
$\frac{R_{rs}(488)}{R_{rs}(547)}$	15	0.154	0.78	0.178	-0.0044	0.50
$\frac{R_{rs}(531)}{R_{rs}(547)}$	5	0.062	0.74	0.276	0.0139	0.50
OC-SMART						
$\frac{R_{rs}(443)}{R_{rs}(547)}$	14	0.112	0.91	0.054	-0.0036	0.67
$\frac{R_{rs}(488)}{R_{rs}(547)}$	7	0.077	0.95	0.041	-0.0016	0.85
$\frac{R_{rs}(531)}{R_{rs}(547)}$	4	0.052	0.65	0.323	-0.0315	0.71
C2RCC						
$\frac{R_{rs}(443)}{R_{rs}(547)}$	28	0.222	0.46	0.196	-0.1334	0.22
$\frac{R_{rs}(488)}{R_{rs}(547)}$	20	0.215	0.55	0.334	-0.0440	0.23
$\frac{R_{rs}(531)}{R_{rs}(547)}$	6	0.075	0.48	0.503	-0.0131	0.26

showed a high sensitivity to wavelength at 531 and 547 nm, which corresponded to the bands where this algorithm was less accurate. At other wavelengths, FUB was slightly sensitive to τ(869)-proxy values.

7.3.2.2 Sensitivity to SPM-proxy

Fig. 7.11 shows the variation of RD as a function of SPM-proxy that included all other possible variables. In the common match-up dataset, the values of SPM-proxy were limited to 17 g m^{-3}. As was the case for the individual match-up dataset, two groups of algorithms were observed. The first group (UV-AC, SS14, SWIRE) was very sensitive to SPM-proxy values for all wavelengths, while the second group (NIRSWIR, NASA-AC, MUMM, Polymer, OC-SMART) was only slightly sensitive to SPM-proxy values for all wavelengths (except at 667 nm). Similar to τ(869), FUB was very sensitive to SPM values at 531 and 547 nm with RD varying from 27% to 52% at 531 nm and between 20% and 46% at 547 nm.

7.3.2.3 Estimation of R_{rs} ratios

Scatterplots of the estimated versus *in-situ* R_{rs}ratios of R_{rs} at 443, 488 or 531 to R_{rs}(547) ratios are shown in Fig. 7.12. Similar to the individual match-up dataset, the R_{rs} ratios were better retrieved at $\frac{R_{rs}(531)}{R_{rs}(547)}$ than at $\frac{R_{rs}(443)}{R_{rs}(547)}$. High scattering and over-estimation were observed for $\frac{R_{rs}(443)}{R_{rs}(547)}$, especially for UV-AV, SS14, and SWIRE. FUB and C2RCC appeared to under-estimate

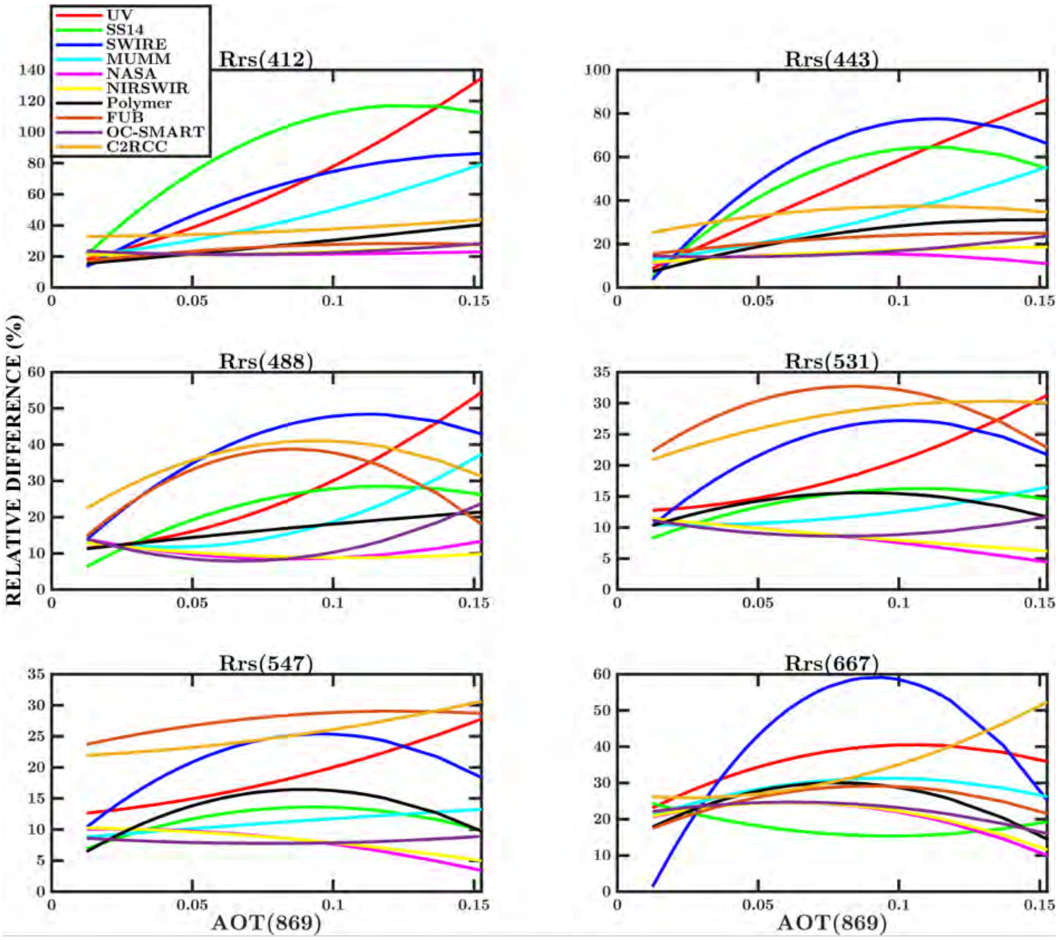

Figure 7.10 Variation of RD as a function of the aerosol optical thickness $\tau(869)$-proxy for each wavelength.

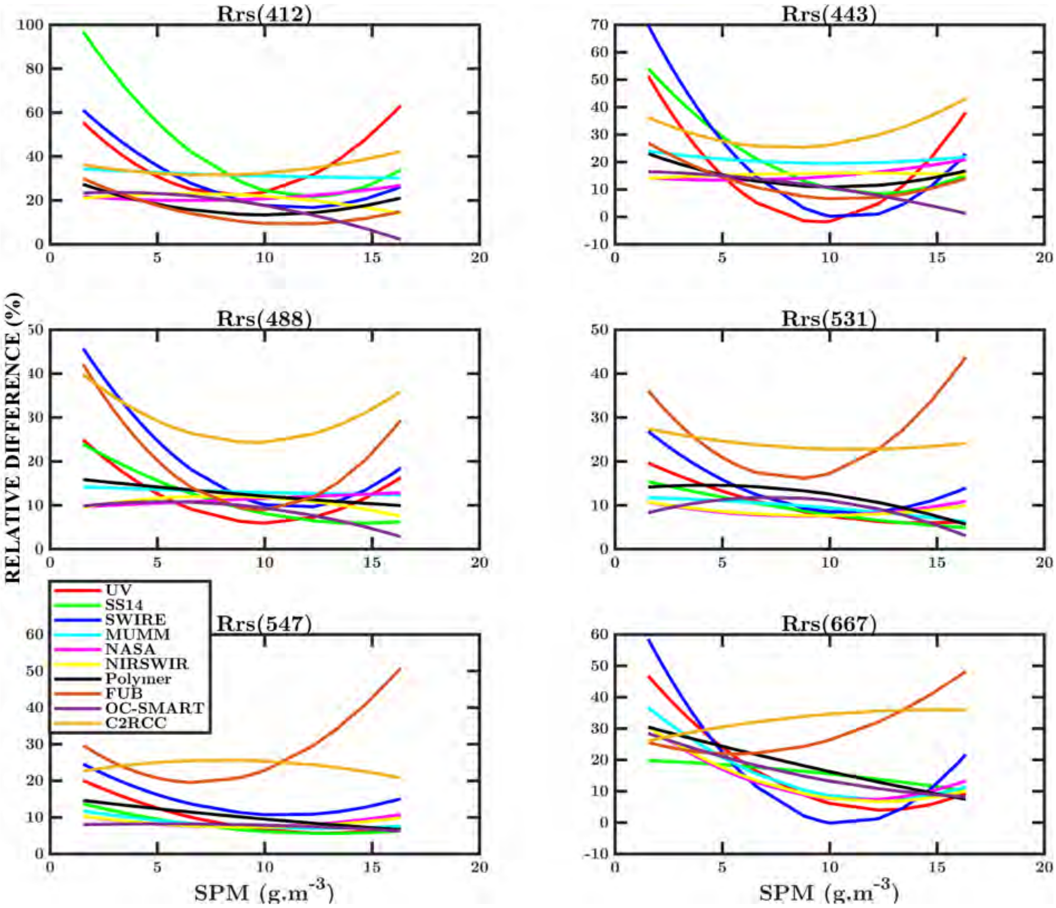

Figure 7.11 Variation of RD as a function of the suspended particulate matter (SPM)-proxy for each wavelength.

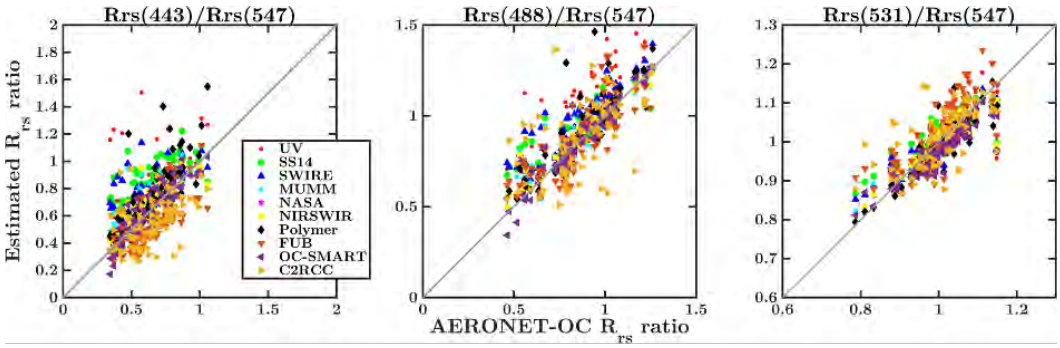

Figure 7.12 Scatterplot of the retrieved vs in-situ ratios of R_{rs} over the common match-up dataset: left panel: $\frac{R_{rs}(443)}{R_{rs}(547)}$; middle panel: $\frac{R_{rs}(448)}{R_{rs}(547)}$; right panel: $\frac{R_{rs}(531)}{R_{rs}(547)}$. The individual scatterplots for each algorithm are provided in Appendix D.

$\frac{R_{rs}(443)}{R_{rs}(547)}$. Most algorithms appeared to over-estimate $\frac{R_{rs}(488)}{R_{rs}(547)}$. This was especially true for UV-AC, SS14, and SWIRE. FUB and C2RCC over-estimated $\frac{R_{rs}(531)}{R_{rs}(547)}$, while all other algorithms provided estimates closer to the 1:1 line. These results can be observed in the statistical parameters in Table 7.8.

7.4 Discussion

7.4.1 Switching between NIR and SWIR bands

NIRSWIR is based on a switching algorithm that uses either the SWIR bands or the NIR bands (same as for NASA-AC) to estimate the aerosol reflectance. To study the advantage of using NIRSWIR compared to NASA-AC (i.e., the advantage of using SWIR bands), we investigated how often NIRSWIR switched to using SWIR bands. On the individual and common match-up datasets, NIRSWIR used SWIR bands 12% of the time (51 out of 426), and 16% of the time (13 out of 83), respectively. This means that the switching procedure was seldom chosen due to the threshold on the turbidity index in NIRSWIR (in agreement with Zhang et al. (2018)). Fig. 7.13 shows scatterplots of R_{rs} estimated by NASA-AC versus by NIRSWIR for the match-ups corresponding to the switch to the SWIR bands. NIRSWIR used SWIR bands for all levels of R_{rs}, however, the number of match-ups was lower (431) than for NASA-AC (510). This is in contract to Zhang et al. (2018), who showed that NIRSWIR could provide more R_{rs} retrievals compared to NASA-AC. This result indicates that the MODIS-Aqua SWIR bands were not optimal for our *in-situ* dataset, which aligns with the fact that the bands were not defined for studying the ocean (Werdell et al. 2010; Wang and Shi 2012; Goyens et al. 2013; Carswell et al. 2017).

Statistical parameters were calculated on the 51 valid match-ups in the individual match-up dataset where the SWIR bands were used instead of the NIR bands (Table 7.9). On our in-situ dataset (i.e. including only low-to-moderate turbid waters) switching to the SWIR bands showed no advantage in RD or RMSD. Along with moderate turbidity, less favorable statistics might also be explained by the low signal-to-noise ratio (SNR) in these bands (Werdell et al.

Table 7.8 Statistical results from R_{rs} ratios derived from AC algorithms and AERONET-OC common match-up dataset (*RD* - mean relative difference, *RMSD* – root mean square difference, R^2- regression)

	RD(%)	RMSD	Slope	Intercept	Bias	R^2
UV-AC						
$\frac{R_{rs}(443)}{R_{rs}(547)}$	30	0.252	0.74	0.296	0.127	0.25
$\frac{R_{rs}(488)}{R_{rs}(547)}$	18	0.189	1.04	0.098	0.136	0.68
$\frac{R_{rs}(531)}{R_{rs}(547)}$	3	0.041	0.95	0.053	-0.001	0.74
SS14						
$\frac{R_{rs}(443)}{R_{rs}(547)}$	34	0.225	0.64	0.410	0.181	0.44
$\frac{R_{rs}(488)}{R_{rs}(547)}$	11	0.107	0.70	0.323	0.064	0.79
$\frac{R_{rs}(531)}{R_{rs}(547)}$	3	0.038	0.64	0.371	0.010	0.76
SWIRE						
$\frac{R_{rs}(443)}{R_{rs}(547)}$	24	0.176	0.60	0.363	0.104	0.38
$\frac{R_{rs}(488)}{R_{rs}(547)}$	14	0.132	0.79	0.282	0.096	0.76
$\frac{R_{rs}(531)}{R_{rs}(547)}$	3	0.035	0.73	0.268	-0.001	0.77
MUMM						
$\frac{R_{rs}(443)}{R_{rs}(547)}$	17	0.124	0.68	0.230	0.027	0.51
$\frac{R_{rs}(488)}{R_{rs}(547)}$	7	0.071	0.84	0.150	0.015	0.86
$\frac{R_{rs}(531)}{R_{rs}(547)}$	2	0.032	0.75	0.247	-0.001	0.81
NASA-AC						
$\frac{R_{rs}(443)}{R_{rs}(547)}$	12	0.093	0.76	0.194	0.0391	0.74
$\frac{R_{rs}(488)}{R_{rs}(547)}$	5	0.056	0.97	0.129	0.021	0.92
$\frac{R_{rs}(531)}{R_{rs}(547)}$	2	0.030	0.77	0.221	-0.0009	0.83

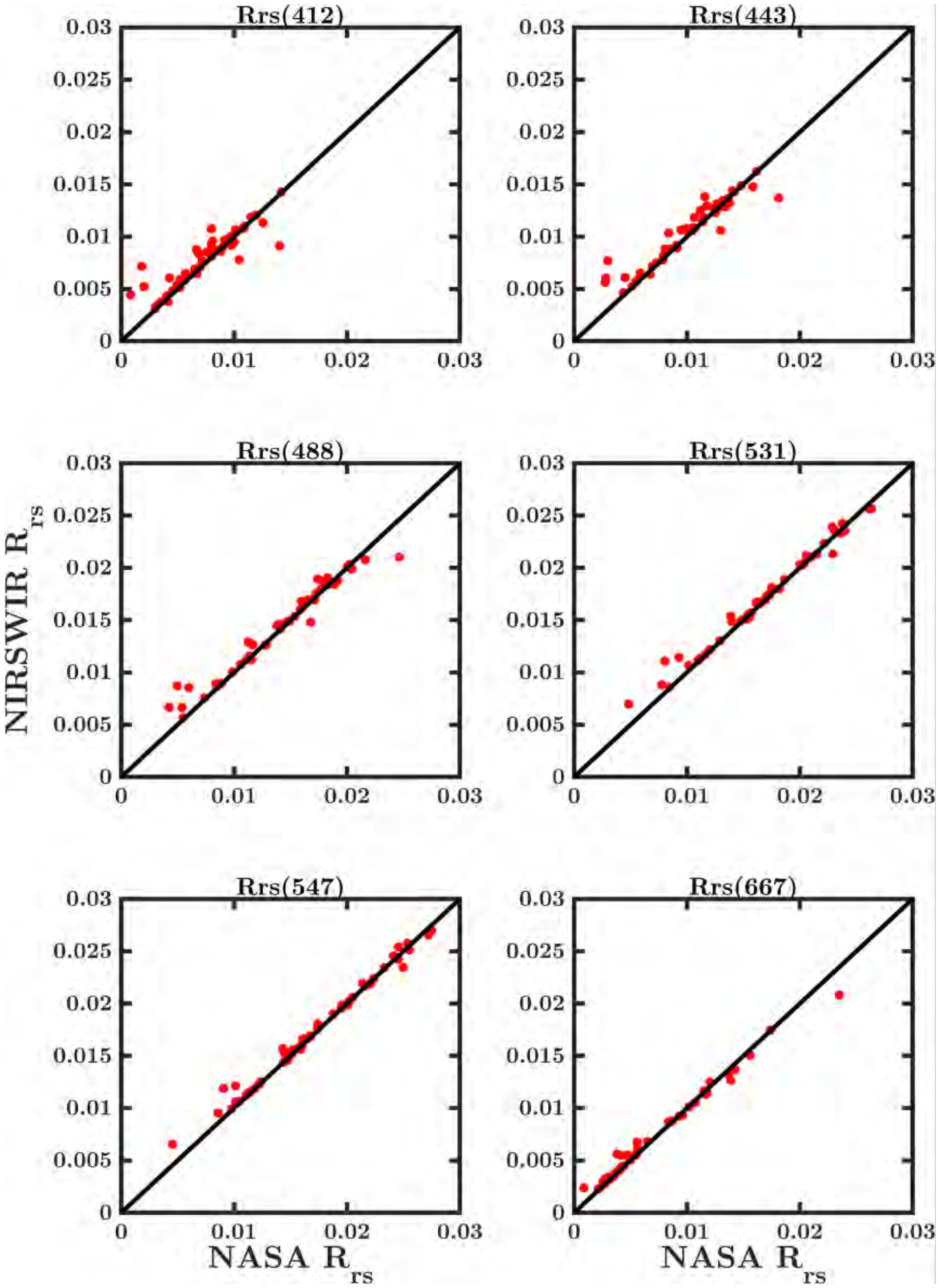

Figure 7.13 Scatterplot of NASA-AC-estimated R_{rs} versus NIRSWIR-estimated R_{rs} from the individual match-up dataset for 412 (top left) to 667 nm (bottom right) for the 51 match-ups for which NIRSWIR used SWIR bands.

NIRSWIR

$\frac{R_{rs}(443)}{R_{rs}(547)}$	12	0.094	0.74	0.207	0.0391	0.74
$\frac{R_{rs}(488)}{R_{rs}(547)}$	5	0.057	0.87	0.138	0.0192	0.92
$\frac{R_{rs}(531)}{R_{rs}(547)}$	2	0.030	0.77	0.227	-0.0009	0.83

Polymer

$\frac{R_{rs}(443)}{R_{rs}(547)}$	18	0.172	1.13	-0.005	0.083	0.61
$\frac{R_{rs}(488)}{R_{rs}(547)}$	10	0.119	0.99	0.051	0.045	0.73
$\frac{R_{rs}(531)}{R_{rs}(547)}$	3	0.042	0.85	0.137	-0.018	0.75

FUB

$\frac{R_{rs}(443)}{R_{rs}(547)}$	20	0.156	0.85	-0.008	-0.104	0.60
$\frac{R_{rs}(488)}{R_{rs}(547)}$	12	0.129	0.91	0.097	0.020	0.64
$\frac{R_{rs}(531)}{R_{rs}(547)}$	5	0.056	0.90	0.128	0.024	0.62

OC-SMART

$\frac{R_{rs}(443)}{R_{rs}(547)}$	11	0.081	0.99	-0.001	-0.007	0.80
$\frac{R_{rs}(488)}{R_{rs}(547)}$	5	0.054	1.00	-0.0002	0.0008	0.92
$\frac{R_{rs}(531)}{R_{rs}(547)}$	3	0.042	0.73	0.247	-0.0268	0.82

C2RCC

$\frac{R_{rs}(443)}{R_{rs}(547)}$	26	0.195	0.46	0.250	-0.095	0.2
$\frac{R_{rs}(488)}{R_{rs}(547)}$	17	0.193	0.60	0.366	0.016	0.28
$\frac{R_{rs}(531)}{R_{rs}(547)}$	5	0.066	0.55	0.465	0.008	0.33

Table 7.9 Statistics for the 51 match-ups from the individual match-up dataset that used SWIR bands. Bold values highlight the best value for a given parameter.

Wavelengths	**412**	**443**	**488**	**531**	**547**	**667**
Relative difference (%) NASA-AC	**29**	**18**	**12**	**11**	**11**	**19**
Relative difference (%) NIRSWIR	35	23	15	12	12	22
RMSD NASA-AC	**0.0021**	**0.0018**	**0.0018**	0.0020	0.0021	0.0011
RMSD NIRSWIR	0.0022	0.0020	0.0020	0.0020	0.0021	0.0011

2010). Liu et al. (2021) showed that the turbidity index used in the NIRSWIR AC for the switching scheme is not always equal to 1, and varies between 0.7 and 2.2 depending on aerosol concentrations and observing geometries.

When comparing OWTs, NIRSWIR provided less match-ups from the individual match-up dataset than NASA-AC for all OWTs except OWT3 (8 match-ups for both algorithms) and OWT8 (34 for NIRSWIR versus 33 for NASA-AC). The largest difference was observed for OWT4 (114 for NASA-AC versus 86 for NIRSWIR) and OWT6 (177 for NASA-AC versus 151 for NIRSWIR).

7.4.2 Impact of vicarious calibration & choice of in-situ data

NASA-AC and NIRSWIR are vicariously calibrated which is not the case for the other algorithms. This could explain why these algorithms provided the most accurate and stable retrievals. They also use the Ahmad aerosols models, which were derived from AERONET observations.

OC-SMART was based on three different bio-optical models and constructed to provide a seamless transition between clear open ocean water and turbid coastal waters (Fan et al. 2021). It was partly developed on a synthetic dataset generated by using the CoastColour bio-optical model (Ruddick 2010) for coastal waters (among others) and validated using AERONET-OC data, which could explain why OC-SMART was one of the most suitable for the *in-situ* datasets tested here.

SS14 is based on three thresholds calculated using ratios of L_{rc} through a $\aleph$ parameter. SS14 was validated using in-situ measurements along the coasts of India (sediment-laden waters) and in open ocean waters. The $\aleph$ parameter was used to calculate a reference spectrum which was then used to estimate the aerosol reflectance in the visible and NIR. When we examined estimates obtained when $\aleph$ values were classified as in-water algal blooms or floating blooms, the accuracy of the retrievals decreased. This indicates that SS14 considered turbid waters for floating blooms or in-water algal bloom. The definition of $\aleph$ should be revised to better discriminate turbid waters. An updated version of SS14 (UV-NIR) has been published by Singh et al. (2019) for considering extremely turbid waters using the band at 412 nm, and has been applied to HICO images and compared to SS14. The retrievals were compared to AERONET-OC data and the results showed improved estimation of R_{rs} with UV-NIR.

7.4.3 Impact of model construction

UV-AC uses the hypothesis that the ocean is totally absorbing in the UV spectral range due to detritus or CDOM. MODIS-Aqua does not have UV bands so UV-AC used the band at 412 nm as a substitute "UV" band. This helps to explain why retrievals at 412 and 443 nm were not accurate with this algorithm. The ocean color imager on PACE has UV bands, and the UV algorithm may be more suitable for this ocean colour sensor. UV-AC also uses a spectrally flat aerosol reflectance, an assumption that is valid for coastal and maritime aerosol models, typical of coastal regions. He et al. (2012) showed that their algorithm underestimated the water-leaving reflectance for extremely turbid waters. In summary, the assumption of zero water-leaving radiance at UV would tend to overestimate the aerosol scattering reflectance at UV, but on the contrary, the overestimation of the epsilon value would cause the underestimation of the aerosol scattering reflectance at NIR, which was extrapolated from the aerosol scattering reflectance at UV by using the epsilon value. Thus, the two compensating effects could get a reasonable estimation of the aerosol scattering reflectance (please see the details in He et al. 2012). However, our *in-situ* dataset did not represent extremely turbid waters as the maximum estimated *in-situ* SPM values were 32.2 g m^{-3}. One advantage of UV-AC is that it did not provide any negative values of R_{rs}.

SWIRE assumed that the ocean is totally absorbing in the SWIR bands, even for high sediment concentrations, and was based on an extrapolated Rayleigh-corrected reflectance defined as $\varrho_{ef} = \mathrm{ae}^{\mathrm{b}\lambda}$, where a and b are fitting coefficients, the values of which were different for each pixel using the 1.24, 1.64, and 2.13 μm bands. The authors assumed that ϱ_{ef} was the aerosol-related reflectance and therefore could be used to estimate the aerosol parameter ϵ(748,869) and the contribution of aerosols in the visible bands. The lower number of match-ups might be explained by the inadequacy of the extrapolation function, and by the fact that the ocean is not totally absorbing for high concentrations of sediment in the SWIR bands (Knaeps et al. 2012).

MUMM used a constant value for the ratio of the water-leaving reflectances (Ruddick et al. 2006). However, it has been shown that this ratio is no longer constant when turbidity increases (Goyens et al. 2013b, c).

Polymer used a polynomial function for the atmosphere and the model of Park and Ruddick (2005) for the ocean. The atmospheric function is empirical, and is composed of three terms: one for the Rayleigh component; one for the aerosol component; and one for glint. The model of Park and Ruddick was suitable for case 1 and case 2 waters. Polymer tunes five parameters (three for the atmosphere and two for the ocean) with R_{rs} as an indirect product.

The results from the three ANN-based AC algorithms (FUB, OC-SMART, and C2RCC) were somewhat different. Even if the inversion technique was the same, the training datasets and inverse model parameterizations were different, (as explained in Chapter 2) which could explain the differences in accuracies.

7.4.4 Caveats

The AC algorithms may be sensitive to uncertainties in ancillary data (e.g., ozone) and in the correction for whitecaps, and sun glint, as shown by Melin et al. (2022) and Gilerson et al. (2022). We have not considered those uncertainties in our analysis.

Chapter 8

Results based on the simulated dataset

The evaluation results for the simulated dataset are presented in this section for the global match-up dataset. MUMM was excluded from this analysis because of the inherent assumptions of the algorithm—a spatial estimation of the aerosol ratio over a region of 1°-by-1°. C2RCC was also excluded due to its inability to process the format of the simulated dataset.

8.1 Individual match-up dataset studies

Fig. 8.1 shows scatterplots of satellite-retrieved R_{rs} versus the simulated values for the eight AC algorithms analyzed. Table 8.1 provides the statistical results. A total of 12,301 simulated cases were considered turbid waters, using the same threshold as Robinson et al. (2003).

As shown in Table 8.1, the number of match-ups varied highly, from 3,007 for FUB to 12,198 for SS14. The number of retrievals for FUB was low because out-of-scope data were masked and excluded from further processing. FUB ensured that the input and output data were between the minimum and maximum of the ANN training data to avoid extrapolation. In addition to this min/max 'out of range' test, we also excluded simulated data for FUB that were not within the simulated concentration ranges used to train the network (specifically, chl-a=[0.05-50] mg m^{-3}, SPM=[0.05-50] g m^{-3} and CDOM=[0.005-1] m^{-1}).

Negative R_{rs} (Table 8.1) were retrieved for NASA-AC (between 45 (0.6%) at 547 nm and 574 (7.4%) at 412 nm), NIRSWIR (between 73 (0.9%) at 547 nm and 666 (7.8%) at 412 nm), SS14 (between 13 (0.1%) at 488 nm and 90 (0.7%) at 443 nm), SWIRE (between 9 (0.1%) at 667 nm and 4151 (52%) at 412 nm) and UV-AC (between 842 (8%) at 547 nm and 1781 (17%) at 412 nm). Polymer, FUB, and OC-SMART did not yield any negative results. The number of match-ups obtained with NIRSWIR (8,499) was higher than that obtained with NASA-AC (7,720), which showed the contribution of the scheme developed in NIRSWIR for highly turbid waters.

A high degree of scatter (or spread) was observed at all wavelengths (Fig. 8.1). This was especially true at 412 nm for all AC algorithms, except OC-SMART. Scatter tended to decrease as wavelength increased. For example, FUB, OC-SMART and Polymer showed a decrease of scatter around the 1:1 line at 488, 531 and 547 nm. However, a few algorithms still showed high scatter across all bands (e.g. SWIRE, SS14). OC-SMART showed the least scatter across all bands. The reduced scatter for OC-SMART can be explained by the fact that this ANN was partly trained using simulated datasets generated by a forward radiative transfer model for the coupled atmosphere-ocean system (Stamnes et al. 2018) similar to the one used in this study. SWIRE, UV-AC and FUB showed overestimation of R_{rs} at most wavelengths, while SS14

Table 8.1 The statistical results of the remote sensing reflectance, R_{rs} derived from various atmospheric correction algorithms and simulated data R_{rs} (*RD* - mean relative difference, *RMSD* – root mean square difference, R^2- regression, *N*- number of valid data/model/wavelength).

	RD(%)	**RMSD (sr^{-1})**	**Slope (sr^{-1})**	**Intercept**	**Bias (sr^{-1})**	**R^2**	**N**	**N<0**
UV-AC								
$R_{rs}(412)$	93	0.00430	0.48	0.0028	0.0002	0.08	10516	1781
$R_{rs}(443)$	52	0.00371	0.69	0.0026	0.0003	0.34	10516	975
$R_{rs}(488)$	23	0.00322	0.84	0.0026	0.0006	0.73	10516	864
$R_{rs}(531)$	13	0.00277	0.90	0.0022	0.0004	0.89	10516	844
$R_{rs}(547)$	11	0.00262	0.91	0.0020	0.0004	0.92	10516	842
$R_{rs}(667)$	37	0.00194	0.93	0.0006	0.0002	0.93	10516	844
SS14								
$R_{rs}(412)$	53	0.00273	0.43	0.0017	-0.0011	0.24	12198	72
$R_{rs}(443)$	43	0.00388	0.42	0.0012	-0.0029	0.53	12198	90
$R_{rs}(488)$	47	0.00695	0.43	0.0009	-0.0059	0.79	12198	13
$R_{rs}(531)$	45	0.00896	0.48	0.0010	-0.0076	0.84	12198	0
$R_{rs}(547)$	46	0.00981	0.48	0.0009	-0.0083	0.86	12198	0
$R_{rs}(667)$	44	0.00409	0.60	0.0014	-0.0008	0.71	12198	0
SWIRE								
$R_{rs}(412)$	123	0.0582	0.59	0.0041	0.0019	0.0001	8021	4151
$R_{rs}(443)$	79	0.0231	0.75	0.0048	0.0028	0.015	8021	1684
$R_{rs}(488)$	38	0.0092	0.88	0.0047	0.0030	0.28	8021	434
$R_{rs}(531)$	29	0.0081	0.96	0.0046	0.0039	0.58	8021	109
$R_{rs}(547)$	28	0.0081	0.99	0.0044	0.0041	0.65	8021	49
$R_{rs}(667)$	86	0.0061	0.97	0.0026	0.0024	0.66	8021	9
NASA-AC								
$R_{rs}(412)$	30	0.0029	1.08	$-2.62.10^{-5}$	0.00032	0.43	7720	574
$R_{rs}(443)$	18	0.0029	1.08	-0.00011	0.00038	0.59	7720	187
$R_{rs}(488)$	8	0.0028	1.05	-0.00020	0.00038	0.78	7720	55
$R_{rs}(531)$	5	0.0028	1.05	-0.00038	0.00034	0.86	7720	46
$R_{rs}(547)$	4	0.0027	1.05	-0.00044	0.00029	0.89	7720	45
$R_{rs}(667)$	14	0.0028	1.12	$-5.50.10^{-5}$	0.00039	0.67	7720	52

				NIRSWIR				
$R_{rs}(412)$	24	0.0020	0.97	0.0026	0.00012	0.61	8499	666
$R_{rs}(443)$	14	0.0019	0.99	0.0024	0.00018	0.78	8499	340
$R_{rs}(488)$	6.2	0.0018	1.00	0.0020	0.00020	0.92	8499	140
$R_{rs}(531)$	3.7	0.0017	1.01	$9.27.10^{-5}$	0.00018	0.96	8499	78
$R_{rs}(547)$	3.2	0.0017	1.01	$4.56.10^{-5}$	0.00014	0.97	8499	73
$R_{rs}(667)$	9.7	0.0017	0.99	0.0003	0.00022	0.93	8499	159
				Polymer				
$R_{rs}(412)$	80	0.00633	1.37	0.00129	0.00308	0.31	12116	0
$R_{rs}(443)$	38	0.00494	1.19	0.00091	0.00173	0.45	12116	0
$R_{rs}(488)$	16	0.00452	0.96	0.00072	0.00020	0.62	12116	0
$R_{rs}(531)$	11	0.00481	0.95	0.00030	-0.00059	0.74	12116	0
$R_{rs}(547)$	11	0.00497	0.94	$2.61.10^{-5}$	-0.00107	0.77	12116	0
$R_{rs}(667)$	19	0.00363	1.03	-0.00027	-0.00012	0.82	12116	0
				FUB				
$R_{rs}(412)$	36	0.00183	0.93	0.0014	0.00105	0.68	3007	0
$R_{rs}(443)$	24	0.00191	0.92	0.0014	0.00086	0.77	3007	0
$R_{rs}(488)$	26	0.00356	1.07	0.0017	0.00247	0.84	3007	0
$R_{rs}(531)$	30	0.00524	1.15	0.0019	0.00427	0.91	3007	0
$R_{rs}(547)$	25	0.00490	1.13	0.0017	0.00386	0.92	3007	0
$R_{rs}(667)$	38	0.00168	1.01	0.0011	0.00112	0.94	3007	0
				OC-SMART				
$R_{rs}(412)$	3.5	0.0003	0.99	$3.98.10^{-5}$	$4.78.10^{-6}$	0.99	12065	0
$R_{rs}(443)$	3.2	0.0003	1.00	$3.41.10^{-5}$	$4.92.10^{-6}$	0.99	12065	0
$R_{rs}(488)$	2.8	0.0005	1.00	$3.14.10^{-5}$	$5.53.10^{-7}$	0.99	12065	0
$R_{rs}(531)$	2.6	0.0007	1.00	$3.07.10^{-5}$	$-2.49.10^{-6}$	0.99	12065	0
$R_{rs}(547)$	2.7	0.0007	1.00	$2.24.10^{-5}$	$-4.28.10^{-6}$	0.99	12065	0
$R_{rs}(667)$	3.7	0.0006	0.99	$3.94.10^{-5}$	$-8.03.10^{-6}$	0.99	12065	0

showed underestimation for all wavelengths. Polymer tended to overestimate R_{rs} at 412 and 443 and to slightly underestimate R_{rs} at 488, 531 and 547 nm. NASA-AC and NIRSWIR slightly overestimated R_{rs} at 412 and 443 nm, and did not show any bias at the other wavelengths.

Relative difference (Table 8.1; Fig. 8.2) was highest at 412 nm (between 3.5% for OC-SMART and 123% for SWIRE) and 443 nm (between 3.2% for OC-SMART and 79% for SWIRE) and the lowest at 531 and 547 nm (between 2.6% for OC-SMART and 45% for SS14 at 531 nm and between 2.7% for OC-SMART and 46% for SWIRE at 547 nm). The differences in scatter at 412 and 443 nm can be observed with the slope of the regression line values (between 0.43 for SS14 and 0.99 for OC-SMART at 412 nm and between 0.42 for SS14 and 1 for OC-SMART at 443 nm). The closest values of the slope to 1 are obtained at 531 and 547 nm (between 0.48 for SS14 and 1 for OC-SMART at 531 nm and between 0.48 for SS14 and 1 for OC-SMART at 547 nm). Low slope values for SS14 can be explained by the high underestimation of the retrievals obtained with this algorithm. The values of the slope were correlated with the values of the correlation coefficient, R^2. The lowest R^2 were observed at 412 (between 0.0001 for SWIRE and 0.45 for all other algorithms except OC-SMART, FUB and NIRSWIR) and at 443 nm (between 0.015 for SWIRE and 0.7 for all other algorithms except OC-SMART, FUB, and NIRSWIR). The highest values of R^2 were at 531 (between 0.58 for SWIRE and 0.99 for OC-SMART, values being higher than 0.70 for most of the algorithms) and 547 nm (between 0.65 for SWIRE and 0.99 for OC-SMART, values being higher than 0.75 for most of the algorithms; Table 8.1).

Fig. 8.3 shows a spider plot of all statistical parameters, except the intercept of the regression line. Here, the dependence of the accuracies of the AC algorithms on wavelength can be better observed. In the blue bands (412 and 443 nm), OC-SMART, NASA-AC, and NIRSWIR were the most accurate. At 667 nm, most of the algorithms did not provide accurate retrievals of R_{rs} as the statistical parameters were not overall consistent. At 531 and 547 nm, NASA-AC, NIRSWIR, OC-SMART, UV-AC and Polymer provided accurate retrievals. Overall, NASA-AC, NIRSWIR and OC-SMART were the most accurate AC algorithms, and SS14 and SWIRE were the least accurate AC algorithms on our simulated dataset.

Regarding the shape of the retrieval spectra, QAS, χ^2, and SAM were examined and are presented in Table 8.2. The QAS parameter compares the retrieved spectra to reference spectra. The majority of the algorithms retrieved realistic spectra, with values of QAS higher than 0.93 for NIRSWIR, NASA-AC, Polymer, and OC-SMART. Four algorithms showed less realistic spectra, with QAS values lower than 0.90 (0.81 for UV-AC, 0.85 for SWIRE, and 0.87 for SS14 and FUB). χ^2 and SAM compared the retrieved spectra to our simulated spectra. NIRSWIR, NASA-AC, FUB and OC-SMART presented the lowest values for both parameters (χ^2 0.17% - 7.73%; SAM 0.47° - 3.32°). As UV-AC and SWIRE yielded high inaccuracies at 412 and 443 nm, they showed the highest values of χ^2 (150.65% and 130.29%, respectively). SS14 showed the highest value of SAM, at 9.33°.

The overall score, S_{total} with a possible maximum value of 42, considered the accuracies per wavelength and the shape of the spectra (Table 8.2). Algorithms clustered into 3 groups based on S_{total}: $S_{total} > 33$ (NASA-AC at 33.32, NIRSWIR at 37.41, and OC-SMART at 41.93); $S_{total} < 20$ (SWIRE at 11.61m and SS14 at 18.40); $20 < S_{total} < 33$ (FUB at 26.25, UV-AC at 29.05, and Polymer at 30.30).

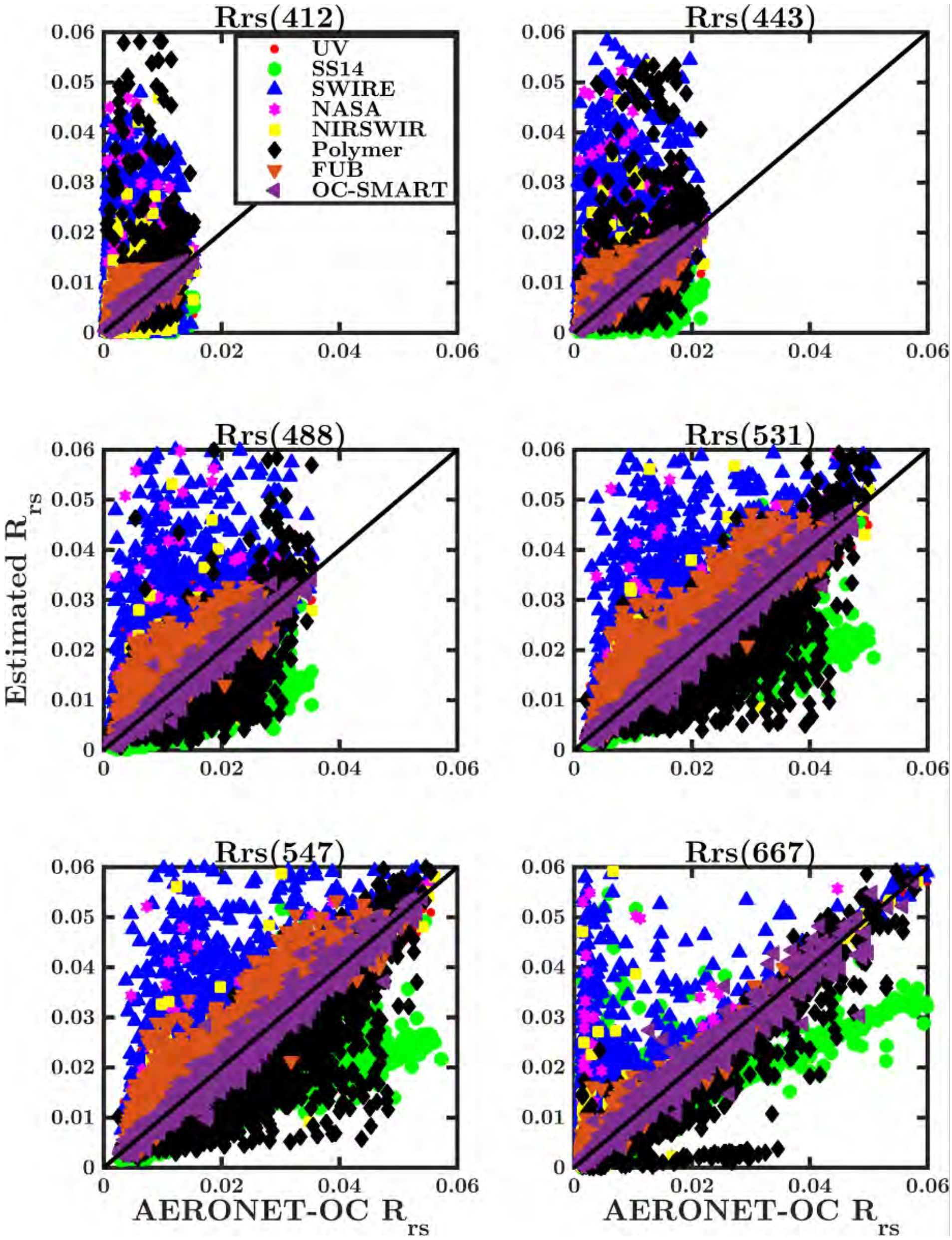

Figure 8.1 Scatterplots of the AC algorithms estimated R_{rs} versus simulated R_{rs} from 412 (top left) to 667 nm (bottom right). The individual scatterplots are provided in Appendix E.

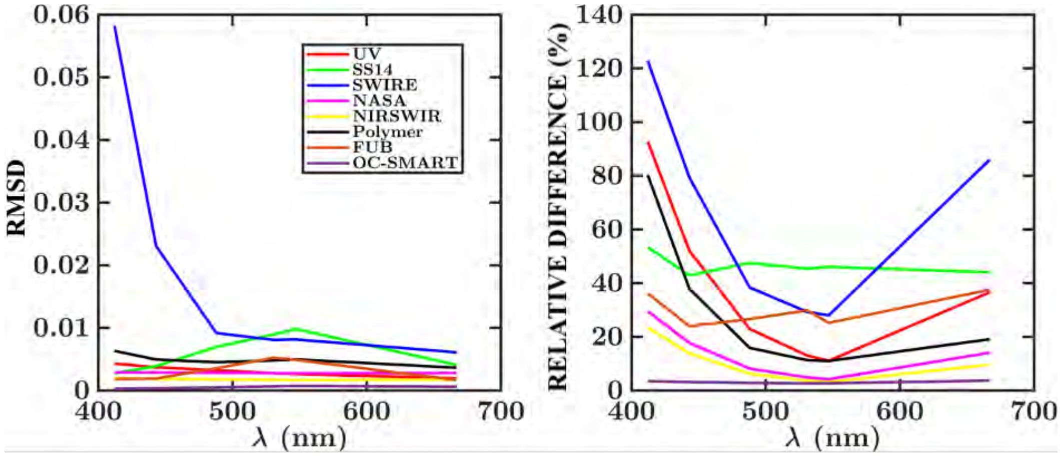

Figure 8.2 (a) Variation of the relative difference as a function of wavelength, (b) Variation of the RMSD as a function of wavelength.

Table 8.2 Statistical parameters calculated over the entire spectra for the simulated dataset. Bold values highlight the best value for a given parameter.

ALGORITHMS	**QAS**	χ^2 **(%)**	**SAM (°)**	S_{total}
UV-AC	0.81	150.65	7.41	29.05
SS14	0.87	27.40	9.33	18.40
SWIRE	0.85	130.29	7.01	11.61
NASA-AC	0.93	7.73	2.26	33.32
NIRSWIR	0.93	5.77	2.03	37.41
Polymer	**0.95**	23.21	7.81	30.30
FUB	0.87	3.88	3.32	26.25
OC-SMART	0.93	**0.17**	**0.47**	**41.93**

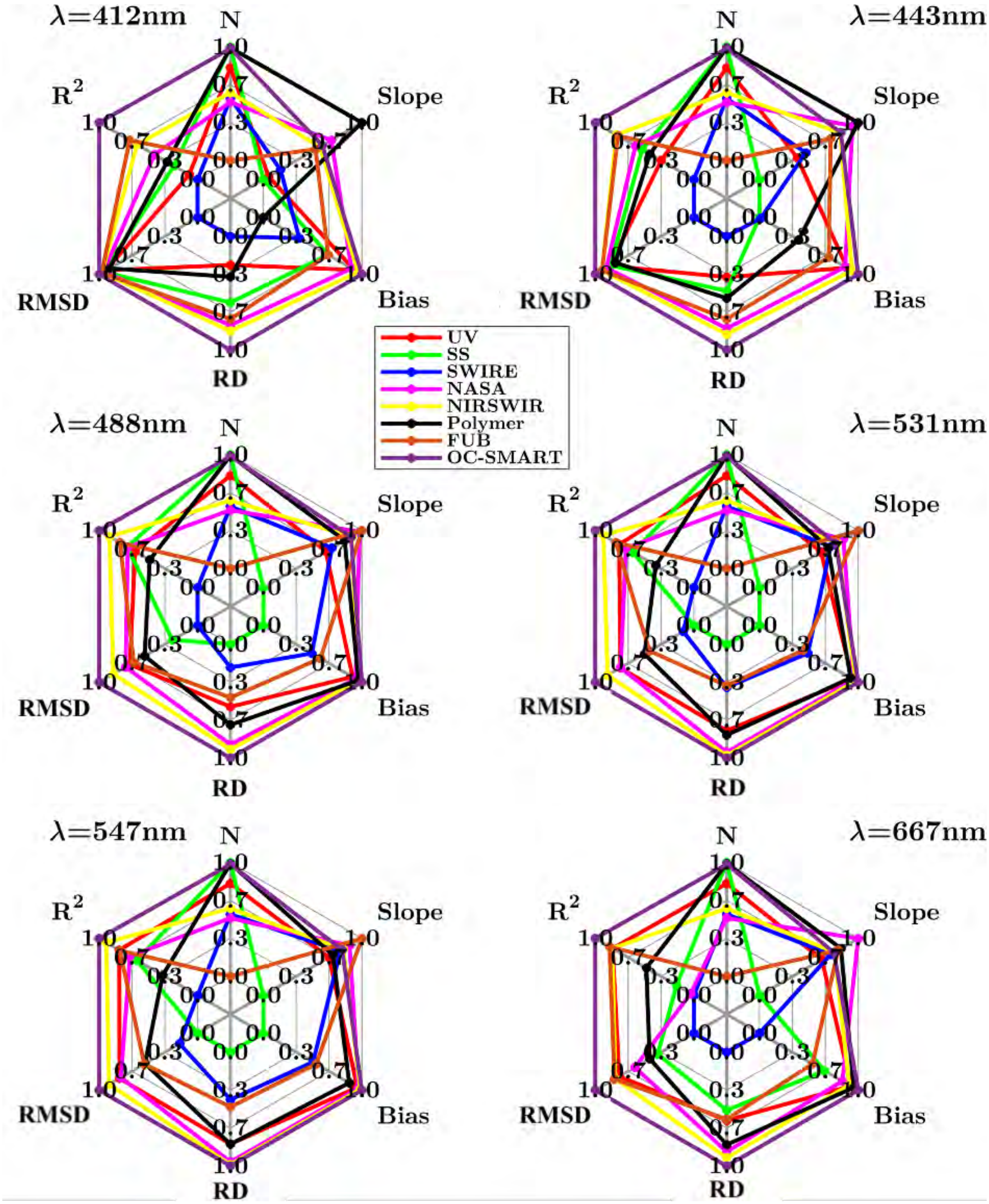

Figure 8.3 Spider-plot of the normalized statistical parameters as a function of wavelength.

Table 8.3 Total scores (S_{total}) for all AC algorithms as a function of OWT.

	OWT1	**OWT2**	**OWT3**	**OWT4**	**OWT5**	**OWT6**	**OWT7**	**OWT8**	**OWT9**
UV-AC	**38.04**	31.97	26.93	25.41	27.30	25.18	32.65	28.97	0
SS14	27.00	17.09	14.24	19.31	17.39	18.72	29.30	15.65	0
SWIRE	31.41	25.66	16.96	9.13	13.44	9.24	5.00	14.83	0
NASA-AC	0	26.50	22.28	33.22	35.91	32.30	38.29	36.38	0
NIRSWIR	36.20	37.42	30.70	37.41	36.39	34.39	38.23	35.87	0
Polymer	7.69	22.14	27.79	31.44	30.38	31.52	33.83	26.71	0
FUB	0	23.84	23.73	25.01	26.18	22.82	27.32	21.49	0
OC-SMART	30.52	**40.00**	**41.88**	**42.00**	**41.97**	**41.98**	**41.50**	**40.84**	0

S_{total} values per OWT are provided in Table 8.3. The simulated dataset was mainly representative of OWT4 and then of OWTs 3, 5 and 6 (Table 6.1). The most oligotrophic waters were not included in the simulated dataset as there were no retrievals for OWT9. OC-SMART showed the highest S_{total} for OWT2 to OWT8. For OWT1, UV-AC had the highest S_{total} (38.04), followed by NIRSWIR (36.20) and SWIRE (31.41). As expected, Polymer had the lowest S_{total} for OWT1 (7.69), as it was not developed for very turbid waters. NASA-AC and FUB did not provide any retrievals for OWT1. NIRSWIR had the highest S_{total} compared to NASA-AC for OWT2 to OWT6, which showed the benefit of the use of the SWIR bands as turbidity increased. NIRSWIR, NASA-AC and Polymer were most relevant for OWTs 4 - 6. UV-AC and FUB showed similar S_{total} for OWTs 3 - 6.

8.2 Sensitivity studies

As mentioned previously, ideally, sensitivity studies should be done by fixing all parameters except one. In these sensitivity studies, the entire simulated dataset was used, without fixing any parameter. As a result, the sensitivities remain inconclusive, and we refer hereafter to proxies.

8.2.1 Sensitivity to τ(869)-proxy

Fig. 8.4 shows the variation of RD on the retrieval of $R_{rs}(\lambda)$ as a function of the τ(869)-proxy for all eight algorithms. For most of the AC algorithms, RD increased as τ(869)-proxy increased. RD was higher at 412 and 667 nm and lower at 531 and 547 nm. For SS14, RD showed a U-shape, with the lowest values for τ(869)-proxy around 0.20-0.25. Two groups of algorithms emerged depending on their RD: NIRSWIR, Polymer, OC-SMART, and SS14 for which RD was slightly dependent on values of τ(869)-proxy; and SWIRE, NASA-AC UV-AC, and FUB, for which the accuracy of the retrievals was highly dependent on the values of τ(869)-proxy.

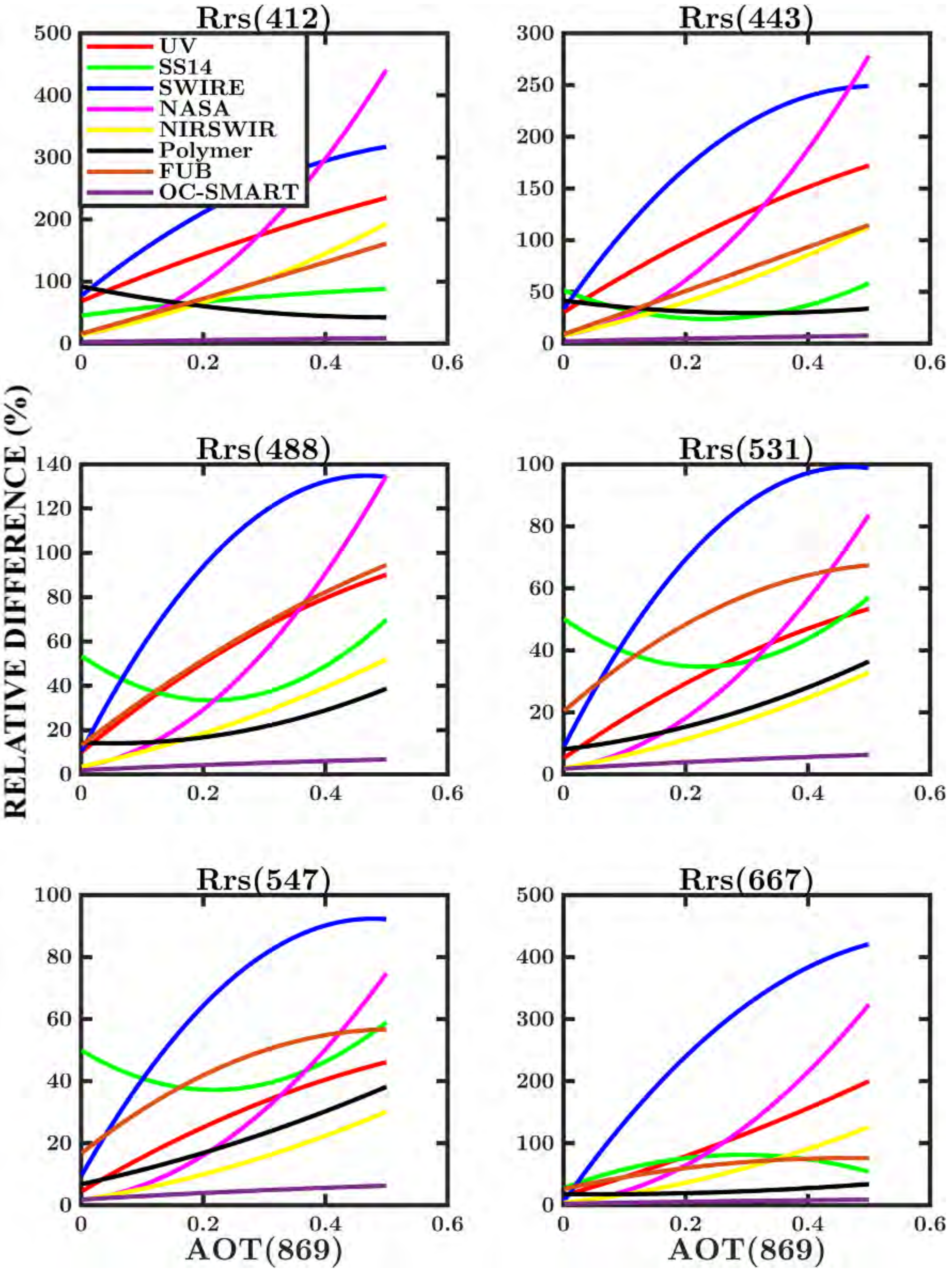

Figure 8.4 Variation of RD as a function of the $\tau(869)$-proxy for each wavelength.

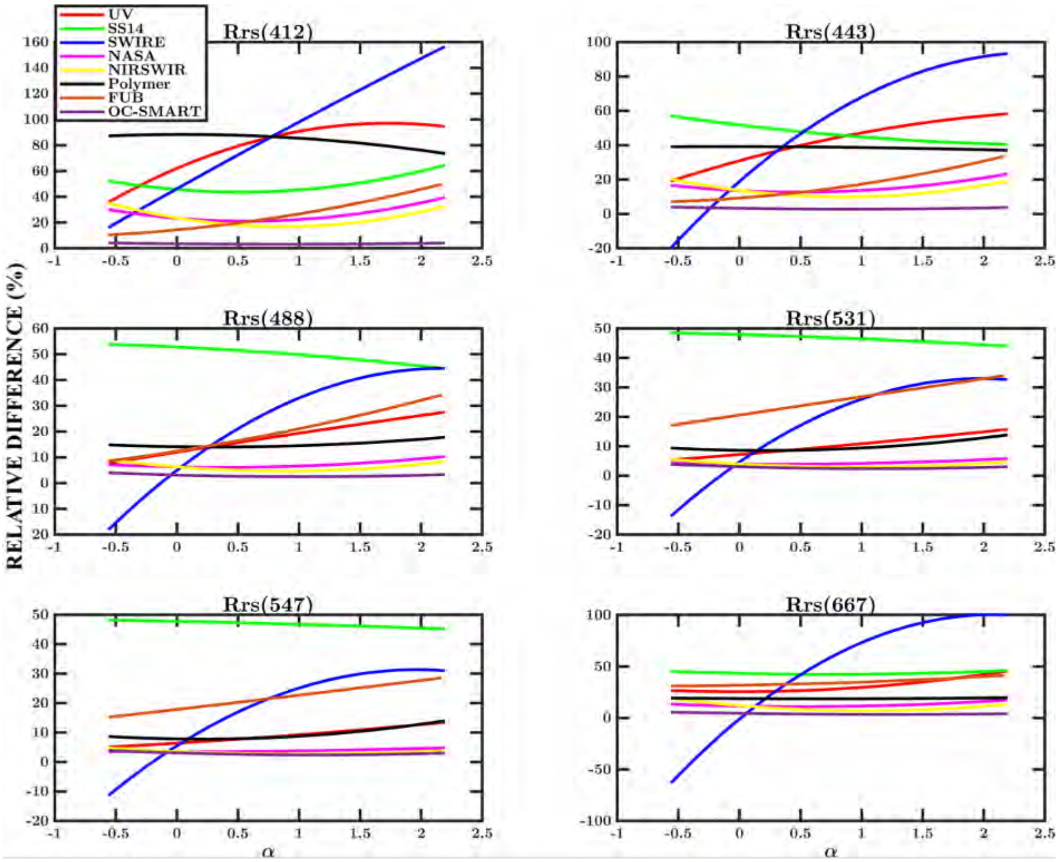

Figure 8.5 Variation of RD as a function of the Ångström coefficient, α(443,869)-proxy, for each wavelength.

8.2.2 Sensitivity to Ångström coefficient α(443,869)-proxy

Fig. 8.5 shows the variation of RD as a function of the Ångström coefficient α(443,869)-proxy for each wavelength. Compared to τ(869)-proxy, RD was slightly dependent on the value of α(443,869)-proxy for all AC algorithms, except for SWIRE, UV-AC and FUB. For SWIRE, RD sharply increased as α(443,869)-proxy increased. For instance, at 412 nm RD increased from 20% (α(443,869)-proxy =-0.5) to 150% (α(443,869)-proxy =2.2). This behavior can be observed at all wavelengths. RD varied slightly with wavelength, with lowest values at 488, 531 and 547 nm.

8.2.3 Sensitivity to SPM-proxy

The variation of RD as a function of SPM-proxy for all algorithms is displayed Fig. 8.6. The values of SPM-proxy varied from 0.09 to 493 g m^{-3}. However, some AC algorithms were unable to retrieve R_{rs} for SPM values greater than 300 g m^{-3}. This was the case for SS14, NASA-AC, NIRSWIR, FUB and OC-SMART. FUB showed the lowest range of values for SPM (up to 42 g m^{-3}) as data were restricted to the upper valid concentration of 50 g m^{-3} for this algorithm.

This ensured that the input and output data were between the minimum and maximum of the ANN training data to avoid extrapolation. In addition to this min/max 'out of range' test, we also excluded simulated data for FUB that were not within the simulated concentration ranges used to train the network (specifically, CHL-a=[0.05-50] mg m^{-3}, SPM=[0.05-50] g m^{-3} and CDOM=[0.005-1] m^{-1}).

All algorithms were slightly sensitive to the variation of SPM-proxy for concentrations up to around 150 g m^{-3}, after which the behaviour of the AC algorithms differed. RD sharply increased for Polymer for all wavelengths. This sharp increase in RD was also observed for NASA-AC, UV-AC and SWIRE. NIRSWIR appeared less sensitive than NASA-AC for high values of SPM-proxy, which was in accordance with the switching procedure's dependence on the turbidity for the use of the SWIR bands.

8.2.4 Sensitivity to CDOM-proxy

Fig. 8.7 shows the variation of RD as a function of CDOM-proxy. As for the SPM-proxy, not all AC algorithms provided retrievals for the entire range of CDOM-proxy values. Such was the case for NASA-AC (max values=4.06 m^{-1}) and FUB (max values=0.99 m^{-1}). Most of the algorithms were not sensitive to the variation of CDOM-proxy for values up to 1 m^{-1}. For values higher than 1 m^{-1}, RD increased for most algorithms. This increase in RD was sharp for UV-AC, SWIRE and Polymer, and less pronounced for SS14, NASA-AC, and NIRSWIR. It is interesting to note that the increased RD was higher for NASA-AC than for NIRSWIR, indicating that for high values of CDOM-proxy, NIRSWIR used the SWIR bands. For OC-SMART, RD did not appear to be sensitive to the values of CDOM-proxy. RD varied differently with CDOM-proxy at 667 nm, with a U-shape and the lowest RD for a given range of CDOM-proxy.

8.2.5 Sensitivity to CHL-proxy

The variation of RD as a function of CHL-proxy for each wavelength is shown in Fig. 8.8. There was a reduced range of CHL-proxy values for each AC algorithm. As for SPM and CDOM, NASA-AC and FUB were not able to estimate R_{rs} for the entire range of CHL-proxy values (NASA-AC range was 0.83 - 214 mg m^{-3}, FUB range was 0.96 - 42 mg m^{-3}). Algorithms were slightly sensitive to CHL-proxy up to 10 mg m^{-3}. For higher CHL-proxy values up to 100 mg m^{-3}, RD increased for most algorithms. Then for lower CHL-proxy values, RD either increased (OC-SMART) or decreased (UV-AC, SS14, SWIRE, NASA-AC, Polymer, FUB). The variation of RD for NIRSWIR was lower than the variation for NASA-AC, but RD was very similar for these algorithms for CHL-proxy up to 2 mg m^{-3}. For higher CHL-proxy values, RD was lower for NIRSWIR than for NASA-AC. OC-SMART, NIRSWIR, NASA-AC and FUB were the least sensitive to CHL-proxy values. At 667 nm, the variation of RD was the inverse of that observed at other wavelengths, with a decrease of RD as CHL-proxy increased up to the highest CHL-proxy values, for which RD increased.

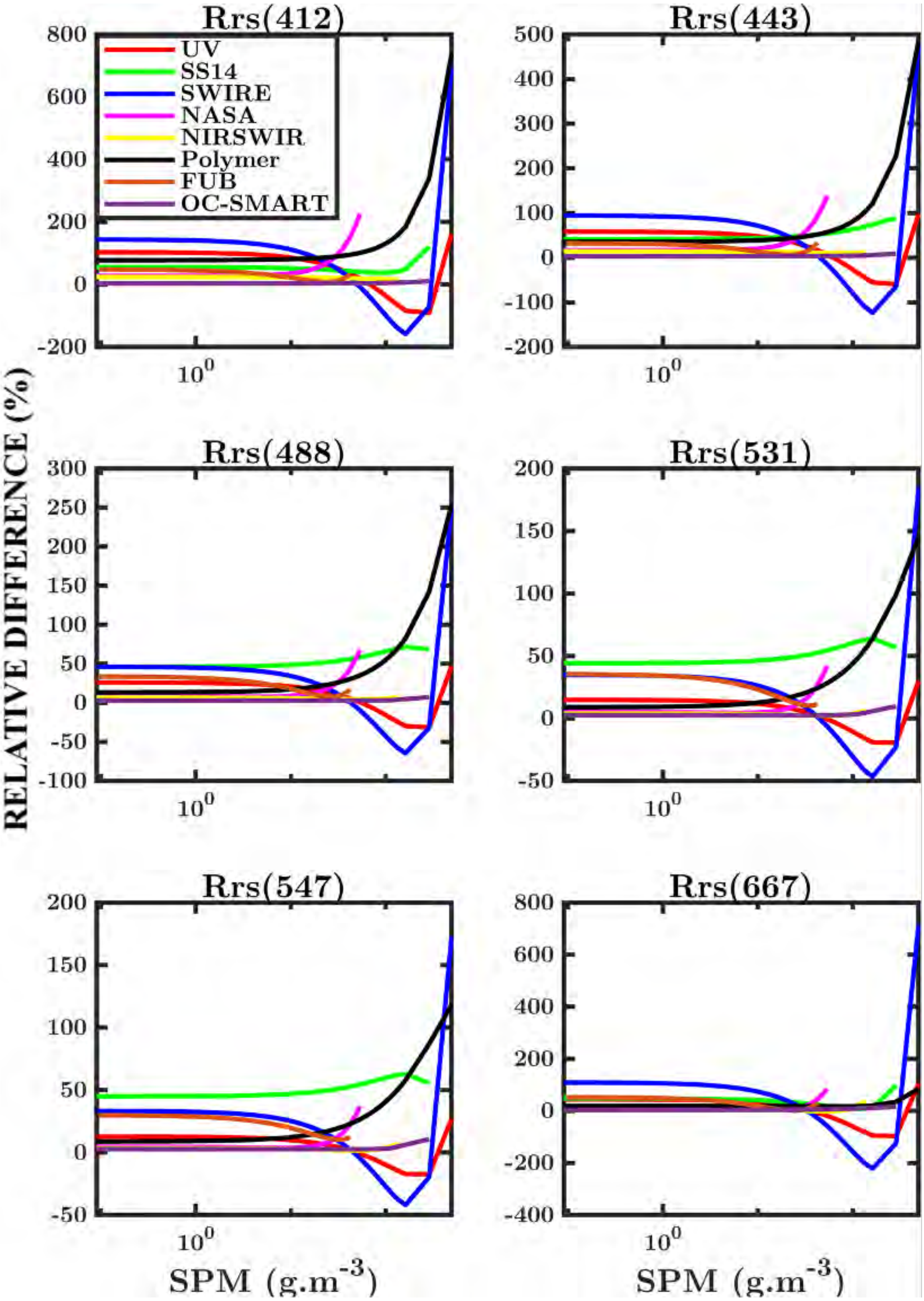

Figure 8.6 Variation of RD as a function of the SPM-proxy for each wavelength.

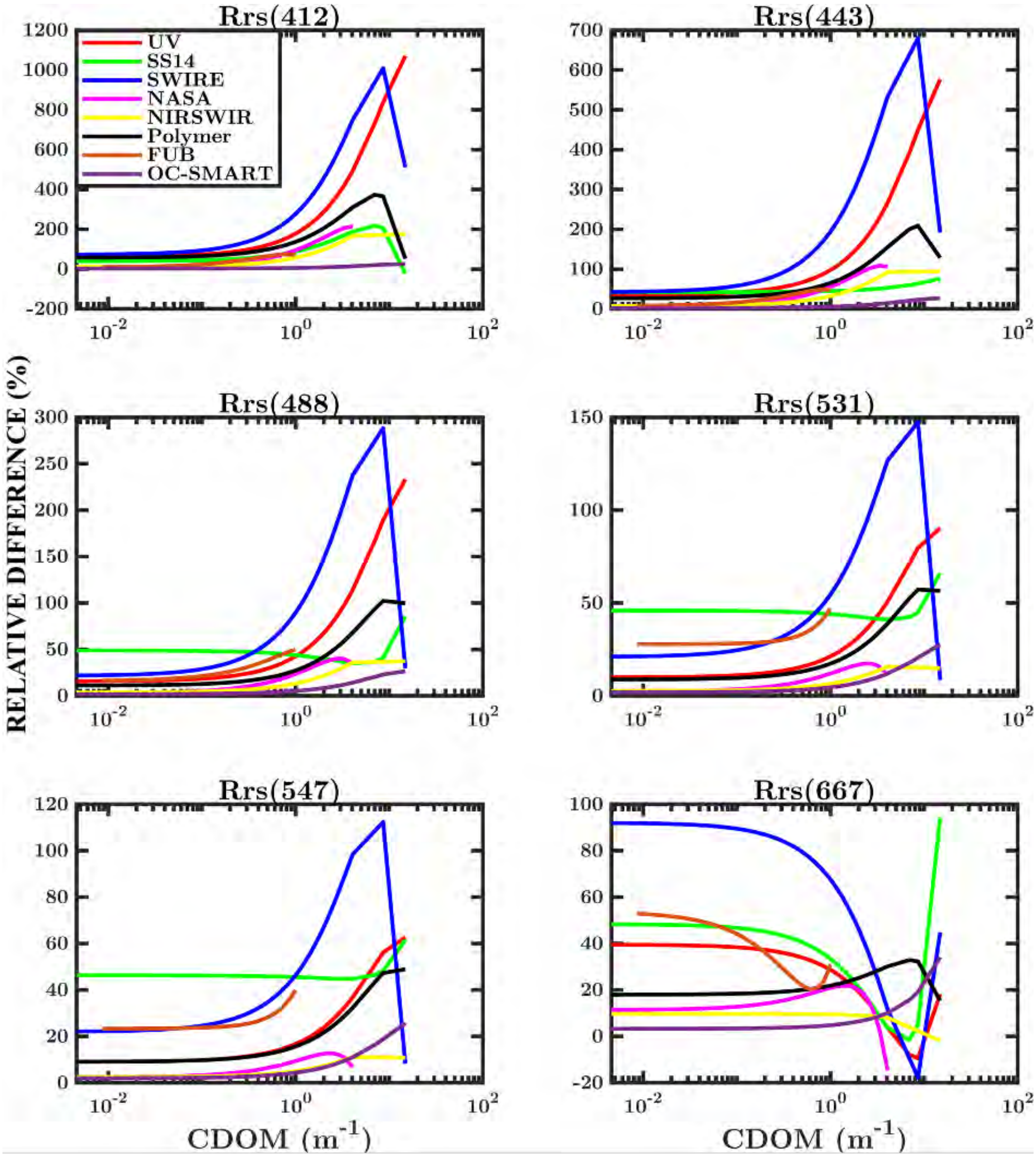

Figure 8.7 Variation of RD as a function of the CDOM-proxy value for each wavelength.

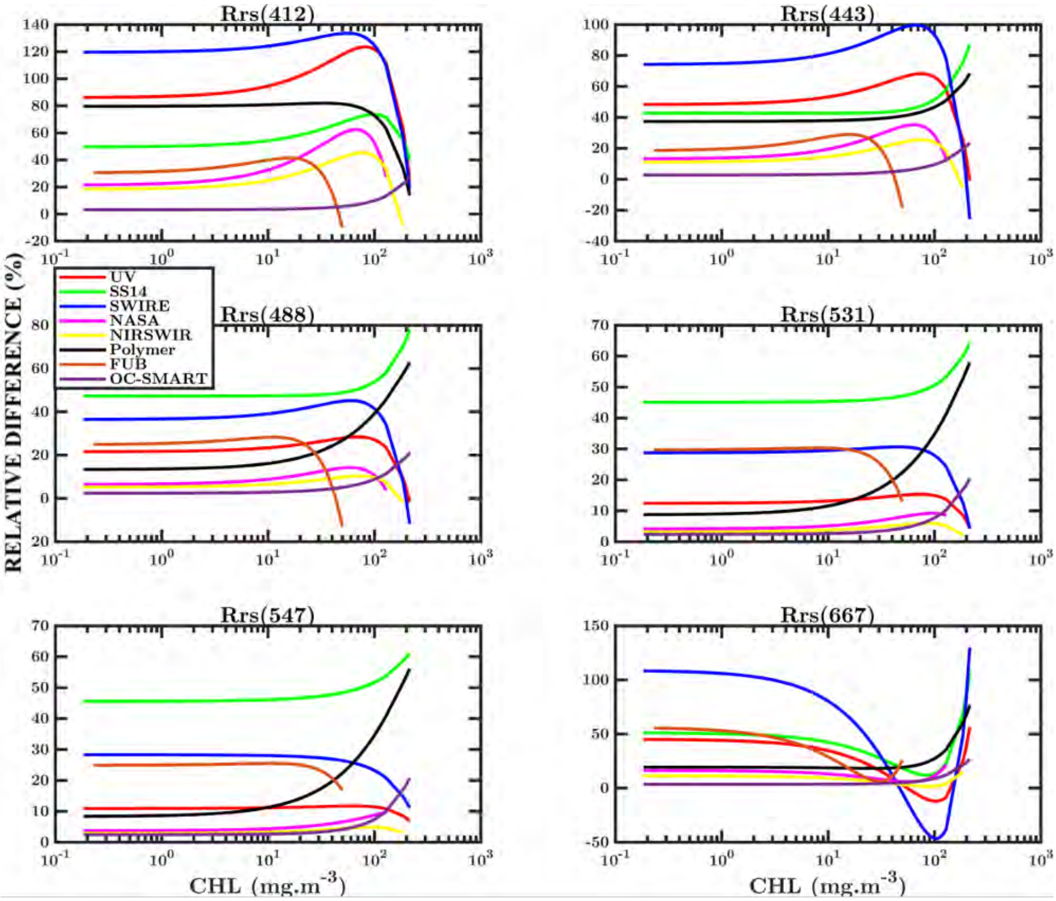

Figure 8.8 Variation of RD as a function of the CHL-proxy value for each wavelength.

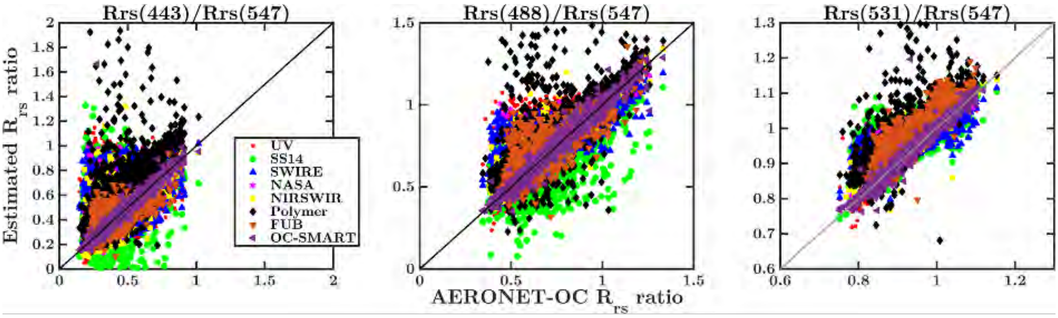

Figure 8.9 Scatterplot of the retrieved versus *in-situ* ratios of R_{rs} over the individual match-up dataset: left panel: $\frac{R_{rs}(443)}{R_{rs}(547)}$; middle panel: $\frac{R_{rs}(488)}{R_{rs}(547)}$; right panel: $\frac{R_{rs}(531)}{R_{rs}(547)}$. Individual scatterplots for each algorithm are provided in Appendix G.

8.2.6 Estimation of R_{rs} ratios

Fig. 8.9 shows the ratios of $R_{rs}(\lambda)$ commonly used in chl-a retrieval algorithms estimated by the eight algorithms versus the simulated ratios. As expected, high scatter around the 1:1 line was observed for $\frac{R_{rs}(443)}{R_{rs}(547)}$ and $\frac{R_{rs}(488)}{R_{rs}(547)}$, especially for UV-AC, SS14, SWIRE and Polymer. This was related to the large RD observed at 443 and 488 for these algorithms. In contrast, NASA-AC, NIRSWIR and OC-SMART showed less scatter for these ratios. OC-SMART showed very good retrievals of all ratios, with almost no scatter around the 1:1 line. Scatter around the 1:1 line decreased as wavelength increased. This was also true for RD and RMSD (Table 8.4), as both parameters decreased from $\frac{R_{rs}(443)}{R_{rs}(547)}$ to $\frac{R_{rs}(531)}{R_{rs}(547)}$. RD varied between 1.7% (OC-SMART) and 42% (Polymer) for $\frac{R_{rs}(443)}{R_{rs}(547)}$ and between 0.3% (OC-SMART) and 4% (FUB) for $\frac{R_{rs}(531)}{R_{rs}(547)}$.

Table 8.4 Statistical results from R_{rs} ratios derived from AC algorithms and the simulated dataset (*RD* - mean relative difference, *RMSD* – root mean square difference, R^2-regression)

	RD(%)	*RMSD*	Slope	Intercept	Bias	R^2
UV-AC						
$\frac{R_{rs}(443)}{R_{rs}(547)}$	35	0.166	0.67	0.14	0.013	0.17
$\frac{R_{rs}(448)}{R_{rs}(547)}$	9.7	0.0.91	0.85	0.12	0.019	0.60
$\frac{R_{rs}(531)}{R_{rs}(547)}$	1.6	0.023	0.90	0.10	0.005	0.81
SS14						
$\frac{R_{rs}(443)}{R_{rs}(547)}$	29	0.147	0.62	0.198	0.0507	0.21
$\frac{R_{rs}(448)}{R_{rs}(547)}$	9.4	0.081	0.71	0.170	-0.0270	0.64
$\frac{R_{rs}(531)}{R_{rs}(547)}$	2	0.030	0.82	0.180	0.0108	0.73
SWIRE						
$\frac{R_{rs}(443)}{R_{rs}(547)}$	33	0.248	0.59	0.200	0.0373	0.07
$\frac{R_{rs}(448)}{R_{rs}(547)}$	9.5	0.095	0.72	0.193	0.0020	0.51
$\frac{R_{rs}(531)}{R_{rs}(547)}$	1.7	0.025	0.79	0.194	0.0012	0.77
NASA-AC						
$\frac{R_{rs}(443)}{R_{rs}(547)}$	11	0.0.68	0.82	0.080	0.0072	0.66
$\frac{R_{rs}(448)}{R_{rs}(547)}$	3.3	0.038	0.91	0.077	0.0079	0.91
$\frac{R_{rs}(531)}{R_{rs}(547)}$	0.65	0.012	0.93	0.069	0.0042	0.96
NIRSWIR						
$\frac{R_{rs}(443)}{R_{rs}(547)}$	10	0.061	0.86	0.061	0.0056	0.72
$\frac{R_{rs}(448)}{R_{rs}(547)}$	3	0.033	0.93	0.055	0.0064	0.93
$\frac{R_{rs}(531)}{R_{rs}(547)}$	5.8	0.010	0.96	0.043	0.0035	0.97
Polymer						
$\frac{R_{rs}(443)}{R_{rs}(547)}$	42	0.297	0.90	0.182	0.145	0.13
$\frac{R_{rs}(448)}{R_{rs}(547)}$	11	0.106	0.88	0.146	0.064	0.64
$\frac{R_{rs}(531)}{R_{rs}(547)}$	3.2	0.048	0.92	0.106	0.029	0.67
FUB						
$\frac{R_{rs}(443)}{R_{rs}(547)}$	14	0.070	0.69	0.095	-0.027	0.62
$\frac{R_{rs}(448)}{R_{rs}(547)}$	8	0.071	0.79	0.143	-0.003	0.66
$\frac{R_{rs}(531)}{R_{rs}(547)}$	4	0.043	1.04	-0.0002	0.0351	0.80
OC-SMART						
$\frac{R_{rs}(443)}{R_{rs}(547)}$	1.7	0.017	1.00	0.0005	0.00065	0.98
$\frac{R_{rs}(448)}{R_{rs}(547)}$	1.1	0.017	1.00	-0.0021	0.00033	0.98
$\frac{R_{rs}(531)}{R_{rs}(547)}$	0.3	0.005	1.00	-0.0027	0.00016	0.99

Chapter 9

Ranking of AC algorithms based on scores

Based on our analyses, we have proposed ranking for MODIS-Aqua AC algorithms, depending on OWTs. Rankings are based on the S_{total} results of analysis with the simulated dataset (Table 8.3) and the match-up analyses (Table 7.6), and are displayed in Tables 9.1 and 9.2, respectively. Combined rankings (Table 9.3) are the sum of S_{total} from both analyses, but excludes MUMM and C2RCC (which were excluded from analyses with the simulated dataset), and also excludes OWTs 1, 2 (no match-ups with in-situ data) and OWT9 (no retrievals in the simulated dataset).

It must be noted that the remarkable performance of OC-SMART on the simulated data is partly due to the fact that its training data included a simulated dataset generated by a bio-optical model that was similar to that used in our analyses, except for the absorption of chlorophyll-a. The full training data of OC-SMART, however, included a much larger set of simulations accounting for other bio-optical models and a significantly wider range of concentrations compared to the simulation dataset used for testing in this study.

Table 9.1 Algorithm ranking based on S_{total} using the simulated dataset (Table 8.3), excluding OWT 9 (no retrievals), MUMM and C2RCC (not included in simulated dataset analysis). No output from NASA-AC and FUB for OWT 1.

Rank	**OWT**								
	1	**2**	**3**	**4**	**5**	**6**	**7**	**8**	**9**
1	UV-AC 38.04	OC-SMART 40.00	OC-SMART 41.88	OC-SMART 42.00	OC-SMART 41.97	OC-SMART 41.97	OC-SMART 41.50	OC-SMART 40.84	n/a
2	NIRSWIR 36.20	NIRSWIR 37.42	NIRSWIR 30.70	NIRSWIR 37.41	NIRSWIR 36.39	NIRSWIR 34.39	NASA-AC 38.29	NASA-AC 36.38	n/a
3	SWIRE 31.41	UV-AC 31.97	Polymer 27.79	NASA-AC 33.22	NASA-AC 35.91	NASA-AC 32.30	NIRSWIR 38.23	NIRSWIR 35.87	n/a
4	OC-SMART 30.52	NASA-AC 26.50	UV-AC 26.93	Polymer 31.44	Polymer 30.38	Polymer 31.52	Polymer 33.83	UV-AC 28.97	n/a
5	SS14 27.00	SWIRE 25.66	FUB 23.73	UV-AC 25.41	UV-AC 27.30	UV-AC 25.18	UV-AC 32.65	Polymer 26.71	n/a
6	Polymer 7.69	FUB 23.84	NASA-AC 22.28	FUB 25.01	FUB 26.18	FUB 22.82	SS14 29.30	FUB 21.49	n/a
7		Polymer 22.14	SWIRE 16.96	SS14 19.31	SS14 17.39	SS14 18.72	FUB 27.32	SS14 15.65	n/a
8		SS14 17.09	SS14 14.24	SWIRE 9.13	SWIRE 13.44	SWIRE 9.24	SWIRE 5.00	SWIRE 14.83	n/a

Table 9.2 Algorithm ranking based on S_{total} from the in-situ AERONET-OC match-up dataset (Table 7.6), excluding OWTs 1 and 2 (no match-ups with in-situ data), and 9 (limited match-ups).

Rank	**OWT**								
	1	**2**	**3**	**4**	**5**	**6**	**7**	**8**	**9**
1	n/a	n/a	OC-SMART 26.02	OC-SMART 40.56	NASA-AC 40.37	OC-SMART 37.17	NASA-AC 36.23	SS14 37.41	n/a
2	n/a	n/a	Polymer 24.21	NASA-AC 39.80	NIRSWIR 39.58	NASA-AC 37.08	NIRSWIR 36.23	SWIRE 35.39	n/a
3	n/a	n/a	NIRSWIR 21.96	NIRSWIR 39.09	OC-SMART 35.42	NIRSWIR 37.08	SS14 31.17	NASA-AC 28.21	n/a
4	n/a	n/a	UV-AC 20.71	Polymer 37.23	MUMM 33.72	MUMM 34.69	MUMM 29.16	NIRSWIR 28.21	n/a
5	n/a	n/a	MUMM 18.39	MUMM 33.32	SS14 26.03	Polymer 31.07	Polymer 29.01	OC-SMART 26.76	n/a
6	n/a	n/a	C2RCC 18.37	UV-AC 31.72	FUB 24.80	C2RCC 29.88	OC-SMART 28.98	FUB 24.05	n/a
7	n/a	n/a	SWIRE 18.14	FUB 26.79	Polymer 24.78	SS14 25.59	SWIRE 25.11	MUMM 22.80	n/a
8	n/a	n/a	SS14 16.72	SS14 26.75	SS14 26.03	FUB 23.93	FUB 24.41	C2RCC 20.19	n/a
9	n/a	n/a	NASA-AC 14.51	SWIRE 21.90	SWIRE 18.05	UV-AC 19.41	UV-AC 22.62	UV-AC 18.65	n/a
10	n/a	n/a	FUB 12.37	C2RCC 15.29	C2RCC 17.40	SWIRE 10.39	C2RCC 11.13	Polymer 12.87	n/a

Table 9.3 Combined algorithm ranking based on the mean S_{total}) excluding MUMM and C2RCC, and OWTs 1, 2 and 9.

Rank	**OWT**								
	1	**2**	**3**	**4**	**5**	**6**	**7**	**8**	**9**
1	n/a	n/a	OC-SMART 54.89	OC-SMART 62.28	OC-SMART 59.68	OC-SMART 60.57	NASA-AC 56.41	OC-SMART 54.22	n/a
2	n/a	n/a	NIRSWIR 41.55	NIRSWIR 56.96	NIRSWIR 56.18	NIRSWIR 52.93	NIRSWIR 56.35	NASA-AC 50.49	n/a
3	n/a	n/a	Polymer 39.90	NASA-AC 53.12	NASA-AC 56.10	NASA-AC 50.84	OC-SMART 55.99	NIRSWIR 49.98	n/a
4	n/a	n/a	UV-AC 37.29	Polymer 50.06	Polymer 42.77	Polymer 47.06	Polymer 48.34	UV-AC 38.30	n/a
5	n/a	n/a	FUB 29.92	UV-AC 41.27	UV-AC 39.14	UV-AC 34.89	SS14 44.89	SS14 34.36	n/a
6	n/a	n/a	NASA-AC 29.54	FUB 38.41	FUB 38.58	FUB 34.79	UV-AC 43.96	SWIRE 32.53	n/a
7	n/a	n/a	SWIRE 26.03	SS14 32.69	SS14 30.14	SS14 31.52	FUB 39.53	FUB 33.52	n/a
8	n/a	n/a	SS14 22.60	SWIRE 20.08	SWIRE 22.47	SWIRE 14.44	SWIRE 17.56	Polymer 33.15	n/a

Chapter 10

Unconsidered corrections and additional complexity

In this section, we briefly describe other issues when observing coastal and inland waters that lead to additional uncertainties in the estimates of R_{rs}. The main issues are the contamination to the TOA reflectance by land (adjacency effect), and the presence of absorbing aerosols, such as smoke and dust. None of the AC algorithms used in this inter-comparison corrected for these issues. Continuous efforts have been made to tackle these issues, and the latest efforts to address these problems have been briefly summarized herein.

10.1 Adjacency effects

Satellite measurements of coastal waters suffer from land adjacency effects. In coastal areas, a fraction of the light reflected by the land reaches the sensor. The adjacency effect occurs when light reflected by nearby land is scattered into the field of view of the sensor. The adjacency effect, thus, modifies the recorded at-sensor radiance of the water pixel. The magnitude of the adjacency effect depends on various factors, such as the aerosol optical properties and vertical distribution/scale height, the contrast between land and water albedo (wavelength dependent), viewing and illumination geometry, and distance to land (Santer and Schmechtig 2000; Bulgarelli and Zibordi 2018a; Bulgarelli et al. 2018).

Adjacency effects can spread beyond the first kilometer offshore, particularly for highly reflecting land (in the NIR) and for highly sensitive sensors. Extensive theoretical simulations of land adjacency effects in typical ocean colour observation conditions (Bulgarelli and Zibordi 2018b; IOCCG 2019) showed that the average adjacency effect in data from MODIS-Aqua, MERIS, and Sentinel-3-OLCI are still detectable (i.e. above the sensor noise level) up to 36 km offshore, except for adjacency effects caused by green vegetation at the red wavelengths.

When neglected, the adjacency effect can introduce significant differences in the retrieved water-leaving signal, leading (in complex ways) to uncertainties in the derived products. The impact of the adjacency effect, however, depends on the characteristics of the AC algorithm. For atmospheric correction schemes that do not derive the atmospheric properties from satellite data and/or from the water pixel, simulations showed that adjacency effect induced artifacts in the water reflectance that were positive for all wavelengths, with biases that monotonically decreased with distance from land (Bulgarelli and Zibordi 2017, 2018a). For atmospheric correction schemes inferring the aerosol properties from NIR data, biases were mainly negative, apart from cloud-induced adjacency effects. Perturbations induced by adjacency effects at NIR and visible wavelengths might compensate each other. Consequently, biases induced by adjacency effects on the water reflectance are not strictly correlated to the intensity of the reflectance of the nearby land. Pan et al. (2022) evaluated ten AC algorithms for Landsat-8 and Sentinel-2 over 300 lakes in Canada, and showed that none of the AC algorithms met the 30% retrieval accuracy target across all bands. To understand the reason, they performed three-dimensional radiative transfer simulations and compared the outputs to satellite observations. Their simulations showed that up to 60% of the TOA reflectance in the NIR bands over the lake was from the adjacent lands covered with green vegetation.

Some studies exclude pixels within a fixed distance from the shoreline. The horizontal range of the adjacency effect is, however, not fixed, and is impacted by various factors, such as the vertical distribution of aerosols in the atmosphere. A conservative threshold might remove water pixels that are not affected by land. Several approaches have been developed to identify and flag pixels influenced by adjacency effects. Sterckx et al. (2011) proposed a method to flag pixels based on the deviations from the NIR similarity spectrum. Jiang et al. (2023) developed new OWTs containing the land-affected signal to flag and mask land-affected observations in inland water scenes. Feng and Hu (2017) explored the elevated radiance in the MODIS SWIR bands at 1240 and 2130 nm to develop a statistical method to quantify land adjacency effects. Burazerovic et al. (2013) proposed spectral unmixing techniques to quantify adjacency effects.

While full 3D Monte-Carlo simulations allow for accurate simulation of adjacency effects, simplified formulations are needed for implementation of an operationally fast correction scheme. Physical correction approaches often involve the use of the atmospheric Point Spread Function (PSF), which allows calculation of contributions from neighboring pixels to the at-sensor radiance from a target pixel. To calculate the atmospheric PSF in a time-efficient manner, these approaches mostly rely on the single scattering approximation (Santer and Schmechting 2000). This primary scattering assumption is used in the sensor-independent adjacency correction algorithm developed by Kiselev et al. (2015). The adjacency correction module is integrated within the Modular Inversion and Processing (MIP) system (Heege et al. 2014). Also, the Improved Contrast between Ocean and Land (ICOL) processor (Santer and Zagolski 2009), developed specifically for MERIS, relies on the primary scattering assumption. RADCOR (Castagna and Vanhellemont 2022) is a new physically based adjacency correction algorithm using Dark Spectrum Fitting (DSF)-integrated adjacency correction algorithm working in the frequency domain. Some approaches incorporate empirical assumptions into the physical methods to determine the adjacency range or background contribution. Sterckx et al. (2015), for instance, proposed the SIMilarity Environment Correction (SIMEC) which estimates the contribution of the background iteratively by checking the correspondence of the retrieved water reflectance with the NIR similarity spectrum defined by Ruddick et al. (2006). Pan and Bélanger (2024) proposed using a machine learning technique to deal with adjacency effects during the atmospheric correction procedure. The latter simultaneously retrieves AOD, sun glint, adjacency effects, R_{rs} and IOPs of seawater, and is based on a genetic optimization scheme. The authors showed improved retrievals of R_{rs} by a factor of almost 2 for all wavelengths, compared to widely used AC schemes (ACOLITE, iCOR+SIMEC) over 100 lakes in Canada.

None of the AC algorithms considered in this report corrected for adjacency effects. We note however, based on extensive testing (Fan et al. 2021), that OC-SMART appeared to be resilient to contamination from sun glint and adjacency effects of land and cloud edges.

10.2 Absorbing aerosols

Most AC algorithms do not consider strongly absorbing aerosols (dust, smoke, etc.). This is especially true for standard AC algorithms from the space agencies and for the algorithms considered in this report. Consideration of strong absorbing aerosols is complicated to handle, and all previously published methods are time-consuming. Absorbing aerosols, especially dust, are not detectable using only NIR bands, because they have a spectral dependency, and have absorbing signatures similar to optically active components of the ocean. Finally, these aerosols absorb in the shorter UV wavelengths, which makes them difficult to detect by the NIR/SWIR algorithms.

Song et al. (2022) calculated the percentage of days dominated by maritime aerosols, dust, smoke, and mixed aerosols, and found that absorbing aerosols occurred frequently over the coasts of the Sahara and Arabian desert, China, south-central Africa, and the Indian Peninsula (Fig. 10.1a and b). The authors also found that the impact of the vertical distribution of absorbing aerosols was up to ±8% for dust and ±10% for smoke based on radiative transfer simulations (Fig. 10.1c). A two-layer atmosphere model may lead to differences of water-leaving radiance up to 30% – 40% in the case of dust in the traditional NASA standard AC algorithm (Song et al. 2022). Based on multiple years of satellite LIDAR (light detection and ranging) observations from CALIPSO (Cloud-Aerosol Lidar and Infrared Pathfinder Satellite Observations), a prediction model of vertical distribution of absorbing aerosol was constructed, which can quantitatively estimate the vertical distribution of absorbing aerosol from meteorological reanalysis products (Song et al. 2020).

Frouin et al. (2019) provided a review of the algorithms dealing with absorbing aerosols, and limitations of the current approaches. AC algorithms incorporating absorbing aerosols have mostly been developed for open ocean waters (Moulin et al. 2001a, 2001b; Chomko and Gordon 1998, 2001; Nobileau and Antoine 2005; Banzon et al. 2009; Mao et al. 2020) and were specifically designed to only detect absorbing aerosols. Few tackle non-zero R_{rs}(NIR) and absorbing aerosols at the same time. Those algorithms are based either on spectral optimization to estimate R_{rs}(Jamet et al. 2004; Brajard et al. 2006, 2012; Kuchinke et al. 2009), spectral relationships of the aerosol reflectance (Al Shehhi et al. 2017), or a modification of a current algorithm such as Polymer (Zhang et al. 2019). Bai et al. (2020, 2023) developed a practical interpolation-based algorithm (UV-SWIR-AC algorithm) to remove absorbing aerosol effects in turbid waters.

Recently, Song et al. (2023) proposed an AC algorithm (OC-XGBRT) to retrieve R_{rs} at short wavelengths of visible light in the presence of absorbing aerosols, that considers the vertical distribution of absorbing aerosol. Based on an extensive simulation dataset, the OC-XGBRT algorithm was established using a machine learning method. The TOA reflectance and R_{rs} were simulated considering multiple types of absorbing aerosols (dust, smoke, and urban aerosols) and their vertical distribution under a comprehensive aquatic environment. Application re-

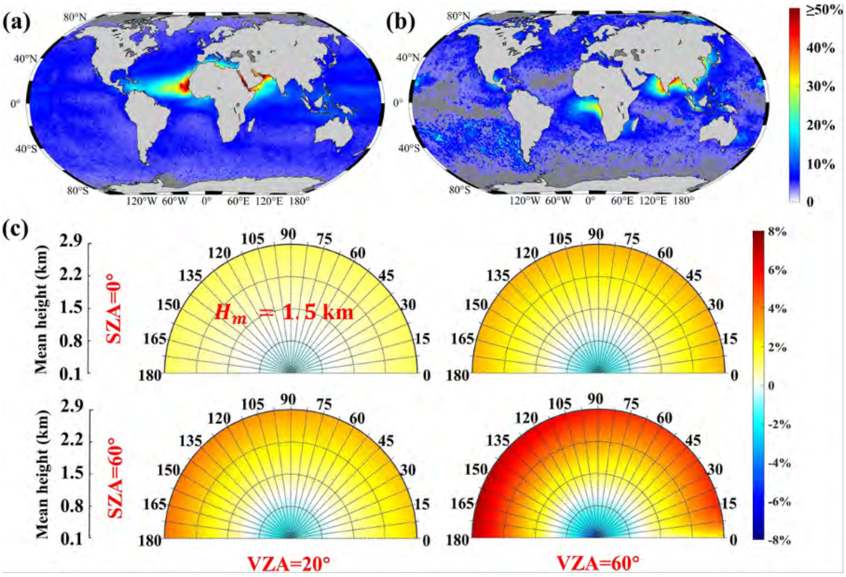

Figure 10.1 (a, b) Spatial distributions of the annual occurrence frequencies of (a) dust and (b) smoke aerosols over the ocean averaged from 2013 to 2020. Dark gray areas indicate no data. (c) Polar diagrams of the relative differences of simulated TOA reflectance (Δ_h) at 412 nm along the mean height (H_m) of dust aerosols (AOD = 0.3) and relative azimuth angle (RAA) with solar zenith angle (SZA) (= 0° and 60°) and viewing zenith angle (VZA) (=20° and 60°) used for the radiative transfer simulations. Note that the radius of the polar diagram represents a change in H_m from 0.1 to 2.9 km in steps of 0.1 km, and the polar angle denotes a change in RAA from 0° to 180° in steps of 5°; RAA = 180° indicates that the sensor and the sun are in the same direction, corresponding to the solar plane. This figure was modified from Song et al. (2022).

sults revealed that the OC-XGBRT algorithm substantially improved the quality of the retrieved R_{rs} at blue light bands compared with the original R_{rs} products in the presence of absorbing aerosols.

Chapter 11

Summary & Conclusions

Atmospheric correction over turbid waters is still a complex task, and numerous AC algorithms have been developed for the past twenty years. For end-users interested in using remote-sensing reflectance data to estimate inherent optical properties of seawater or biogeochemical parameters, it can be difficult to know which AC algorithm to apply. In this IOCCG report, we compared ten AC algorithms for MODIS-Aqua, some of them widely used, that are based on differing assumptions, and applied them to waters covering nine optical water types. We performed a standard match-up analysis using in-situ measurements from the AERONET-OC network to evaluate the accuracy of the different algorithms. As the AERONET-OC stations only represented low to moderate turbid waters, a simulated dataset was also developed for consideration of very turbid waters. We considered only weakly absorbing aerosols, as the aerosol models used in our simulated dataset were the weakly-absorbing aerosol models included in NASA SeaDAS processing.

From our analyses for MODIS-Aqua, we recommend using ANN-based OC-SMART (Fan et al. 2017, 2021), NIRSWIR (Wang and Shi 2007) and NASA-AC (Bailey et al. 2010) for optical water types 3-8 and NIRSWIR for extremely turbid water with OWTs 1 and 2. UV-AC (He et al. 2012) showed best performance for extremely turbid waters classified as OWT1. NIRSWIR showed consistently good performance across all OWTs, however, its performance was highly related to the sensor's signal-to-noise ratio of the SWIR bands, and this was particularly true for low turbidity waters.

Table 11.1 provides a brief overview of some of the advantages and limitations of the AC algorithms studied.

11.1 Applicability to other sensors

This inter-comparison of AC algorithms was applied to MODIS-Aqua, however, most ocean-colour-capable sensors have similar bands, thus, we believe the results of this report could be applicable to other sensors. NASA-AC has been tuned to process all major ocean colour satellite images including OLCI. Algorithms based on the direct inversion of the full TOA spectral signal, such as FUB and CR2CC, are expected to perform differently when applied to other ocean colour missions. OC-SMART has been shown to perform well for eleven different ocean colour sensors (Fan et al. 2021). We expect that accuracy will increase with an increased number of spectral bands, such as for OLCI, and slightly decrease for sensors with fewer bands compared to MODIS-Aqua, such as VIIRS. The overall performance of the ANN-based methods,

Table 11.1 Overview of some advantages and limitations of the AC algorithms reviewed in this report.

Model	**Advantages**	**Limitations**
UV-AC	Applicable to extremely turbid or eutrophic waters	Assumption of negligible water-leaving radiance at UV or short blue bands
	Easy to implement	Assumption of “white’ aerosol reflectance spectrum
	Fast to process the images	
	Applicable to different ocean colour sensors based on the general Rayleigh scattering lookup table	
SS14	Atmospheric correction per optical water types	Applicable only to weakly absorbing aerosols
	Calculation of a single parameter κ	Empirical relationships
	Empirical relationships to correct the aerosol radiance	Extrapolation to estimate the aerosol radiance
	No aerosol models required	Results deteriorated in dense bloom waters
	Easy to implement	
SWIRE	Based on Gordon and Wang (1994)	Applicable only to weakly absorbing aerosols
	Developed for suspended sediments	Extrapolation depends on the dataset used to define the function
	Use of SWIR bands	Need SWIR bands
	Empirical function to extrapolate the Rayleigh-corrected reflectance from SWIR to NIR used as a reference	Developed only for MODIS-Aqua
	Easy to implement	
	Developed specifically for MODIS-Aqua	
MUMM	No aerosol models required	Three steps required
	No bio-optical models required	Need to estimate the epsilon parameter for each pixel of a given image
	Available for SeaWiFS, MODIS-Aqua, MERIS and OLCI	The ocean parameter, α, is not constant when the turbidity is high
	Based on Gordon and Wang (1994) for the first step	Applicable only to weakly absorbing aerosols
	Easy to implement	

NASA-AC	Diverse optical domains	Requires aerosol models
	80 aerosol models	Use of empirical optical models (e.g. spectral backscattering, particulate and dissolved absorption) limits the applicability
	iteration processing	Practical implementation of the iteration scheme can result in conditions of non-convergence
	Based on Gordon and Wang (1994) for the first step	Applicable only to weakly absorbing aerosols
		Requires a first value of the parameters of interest to start the iteration process
NIRSWIR	No bio-optical model required	Requires aerosol models
	Assumption of black pixel	Extrapolation of model aerosol from SWIR to VIS
		Applicable only to weakly absorbing aerosols
		Low SNR for the SWIR bands
Polymer	Spectral matching inversion	Limited to moderate turbid waters due to the bio-optical model
	No aerosol models required	Bio-optical model covering a wide range of optical water types is needed for global applicability
	Spectral approximation of the atmospheric component	The aerosol's diffuse transmittance is fixed to 1.0
	Analytical formulation does not rely on aerosol models	
	Correction of sun glint	
	Applicable to moderately absorbing aerosols	
	Available for MODIS-Aqua, MERIS and OLCI	
C2RCC	Direct inversion	Dependent on the training dataset
	Fast to process the images	
	Available for OLCI, MERIS and MODIS-Aqua, VIIRS, MSI, OLI and SeaWiFS	
	No negative reflectance retrieval due to logarithmic transformation of the training data	

FUB	Direct inversion of full spectral TOA radiance signal	Applicable only to weakly absorbing aerosols
	Fast to process data once the networks are trained	Limited to moderately turbid waters with maximum concentrations of 50 g m^{-3} for SPM and 50 mg m^{-3} for Chl-a with CDOM at 443 nm not exceeding 1 m^{-1}
	Bio-optical model used on forward radiative transfer simulations based on European coastal waters	Dependent on the training dataset
	No negative reflectance retrieval due to logarithmic transformation of the training data	
	Robust to input errors as training included noise	
	Available for MODIS-Aqua, MERIS and OLCI. The MERIS and OLCI plugins for SNAP also provide estimates of Chl-a, SPM and CDOM with per-pixel uncertainties included for OLCI	
OC-SMART	Applicable in open ocean and coastal/inland waters, as well as in extreme conditions such as heavy aerosol loadings, extremely turbid water, etc.	Applicable only to weakly absorbing aerosols
	Applicable to sensors with low signal to noise ratio (SNR)	Based on a scalar RTM (polarization effects not considered)
	Resilient to contamination due to sun glint and adjacency effects of land or cloud edges	Coupled RTM based on a flat air-water interface (surface roughness effects not included) – sky glint and “weak” sun glint included, but not “strong” sun glint
	Only positive R_{rs} value are retrieved	Inelastic scattering processes (Raman, fluorescence scattering) not included in RTM
	Multi-sensor support: SeaWiFS, MODIS/Aqua, SNPP/VIIRS, ISS/HICO, Landsat8/OLI, DSCOVR/EPIC, Sentinel-2/MSI, Sentinel-3/OLCI, COMS/GOCI, GCOM-C/SGLI and FengYun-3D/MERSI2	Dependent on the training dataset

however, will strongly depend on the applicability of the training dataset and the underlying bio-optical model assumptions.

Additional studies support the use of these algorithms for other sensors. Hieronymi et al. (2023) compared five AC algorithms (including Polymer and C2RCC) for OLCI-A and -B on-board Sentinel-3 using mainly the AERONET-OC in-situ dataset. Similar to this work, the authors also provided comparison over different optical water types.

11.2 Limitations of the study

For the convenience of the reader, we summarize here a few of the limitations of the study to keep in mind, previously mentioned within the text:

- The in-situ match-up exercise did not include very turbid waters, as SPM did not exceed 32.2 mg m^{-3}
- Absorbing aerosols and adjacency effects were not considered
- NASA-AC and NIRSWIR were vicariously calibrated, which is not the case for the other AC algorithms discussed
- The design of the sensitivity study remained too complex, as the dependent variables were not fully isolated, resulting in inconclusive interpretation and ambiguous results.
- With a focus on MODIS-Aqua, detailed transfer of AC performance results to other sensors remains problematic and cannot be concluded.
- The BRDF was not considered in the match-up exercise. Pitarch et al. (2025) proposed a new BRDF correction method applicable to a very wide range of optical water types, covering virtually all global waters. Further work in this area will be to apply this correction in order to better assess the uncertainties in R_{rs} retrievals, and examine the impact of not correcting the BRDF.

11.3 Recommendations

Based on the efforts and analysis of the working group, the following perspectives and recommendations are put forward to improve future analyses of atmospheric correction algorithms and their performance:

- There needs to be a continuous effort to collect more in-situ measurements over a wide range of atmospheric and oceanic conditions. The AERONET-OC network is very useful, but diversity of the optical water types should be improved (OWTs 1 - 3). Systematic concomitant measurements of R_{rs}, IOPs and aerosol parameters should be encouraged.
- Future inter-comparison experiments should consider including adjacency effects and absorbing aerosols.
- Future efforts should also include validation of NIR R_{rs} using fiducial references measurements, as many biogeochemical algorithms for coastal waters are based on bands greater than 670 nm.
- With the launch of the PACE mission on 8 February 2024, efforts should be dedicated to

the use of polarization to improve R_{rs} retrievals. Polarization observations can obtain more accurate aerosol scattering/absorption properties which are expected to be greatly helpful for improving AC accuracy, not only in open oceans, but also in turbid waters (Loisel et al. 2008; Frouin et al. 2019; Jamet et al. 2019; He et al. 2024).

- Use of LIDAR techniques could help to quantify highly absorbing aerosols. LIDAR, as an active remote sensing technique, is able to provide profiles of aerosols throughout the atmospheric column, as well as identify aerosol types (Weitkamp 2005; Lolli 2023). The standard AC algorithms do not consider absorbing aerosols, because although it may be possible to discriminate them, it remains difficult to obtain a vertical distribution. It is important to have information about the vertical distribution of the aerosols in order to accurately correct for absorbing aerosol impact. There is currently no space-borne oceanic profiling LIDAR. However, CALIOP (NASA Cloud Aerosol Lidar with Orthogonal Polarization) on-board the CALIPSO mission (2006-2023) was in *the A-Train*, a constellation of satellites (Stephens et al. 2002), and there may be a potential to merge CALIOP and MODIS-Aqua to better estimate $\mathrm{R_{rs}}$ in an atmosphere containing absorbing aerosols. In the near-future, the Italian Space Agency (ASI) and NASA plan to launch a multi-purpose space LIDAR mission dedicated to the observation of the Earth’s atmosphere, surface and oceans. This space-borne LIDAR mission will have ocean capabilities, and will provide the vertical structure of the back-scattering and diffuse attenuation coefficients up to 50 meters depth.
- There should be continuous effort and support from space agencies to compare AC algorithms (including new algorithms) across a wider range of ocean colour sensors, and to establish protocols for sensitivity studies on the atmospheric and bio-optical / biogeochemical parameters.

Appendix A

Individual scatterplots for the individual match-up dataset

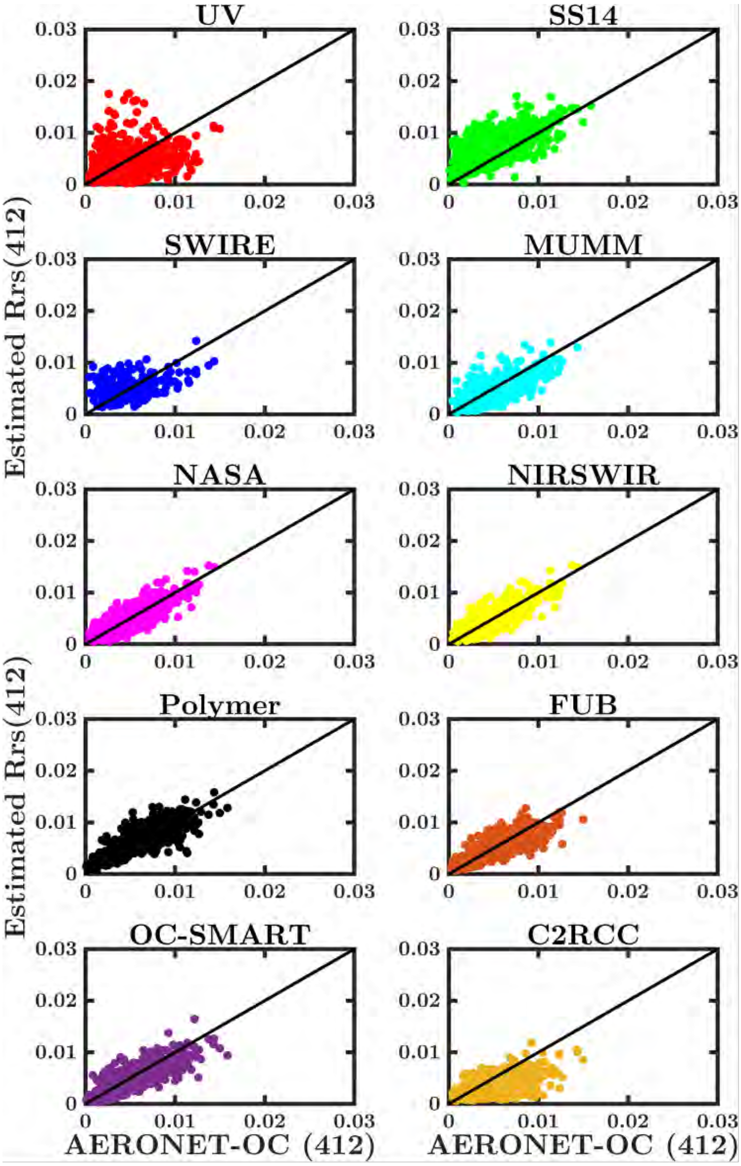

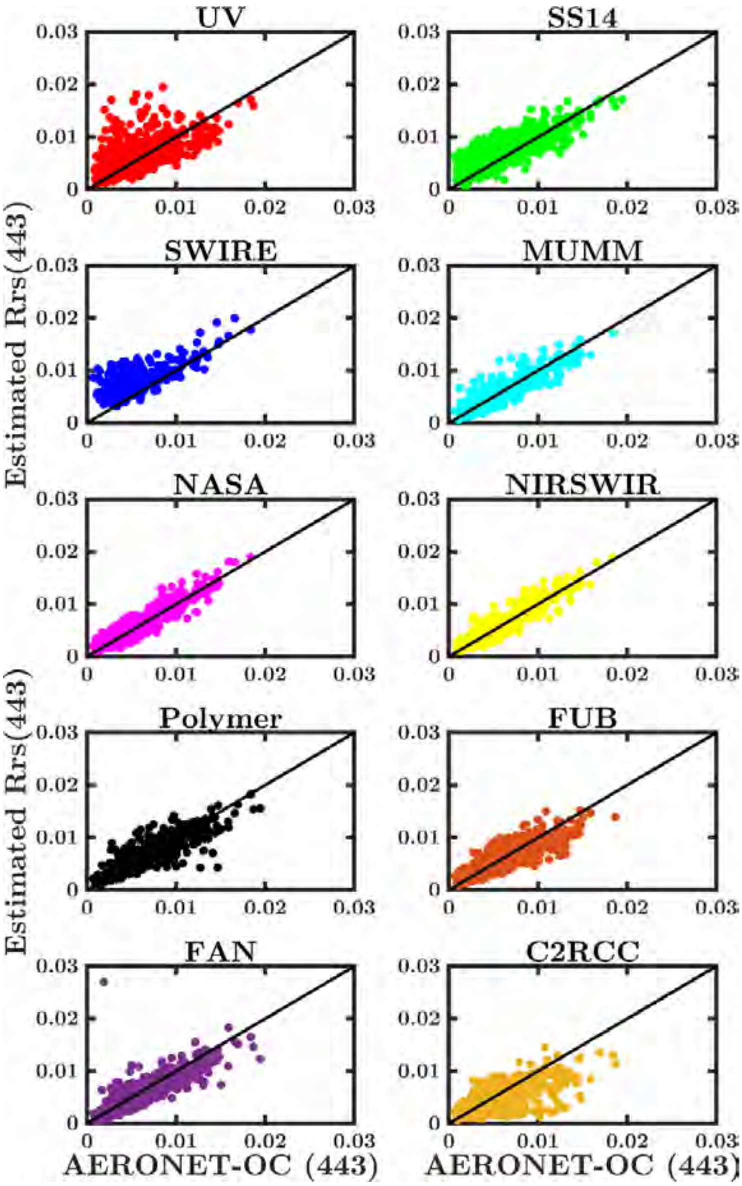
UV
SS14
SWIRE
MUMM
NASA
NIRSWIR
Polymer
FUB
FAN
C2RCC
Estimated Rrs(443)
Estimated Rrs(443)
0
0.01
0.02
0.03
AERONET-OC (443)
AERONET-OC (443)

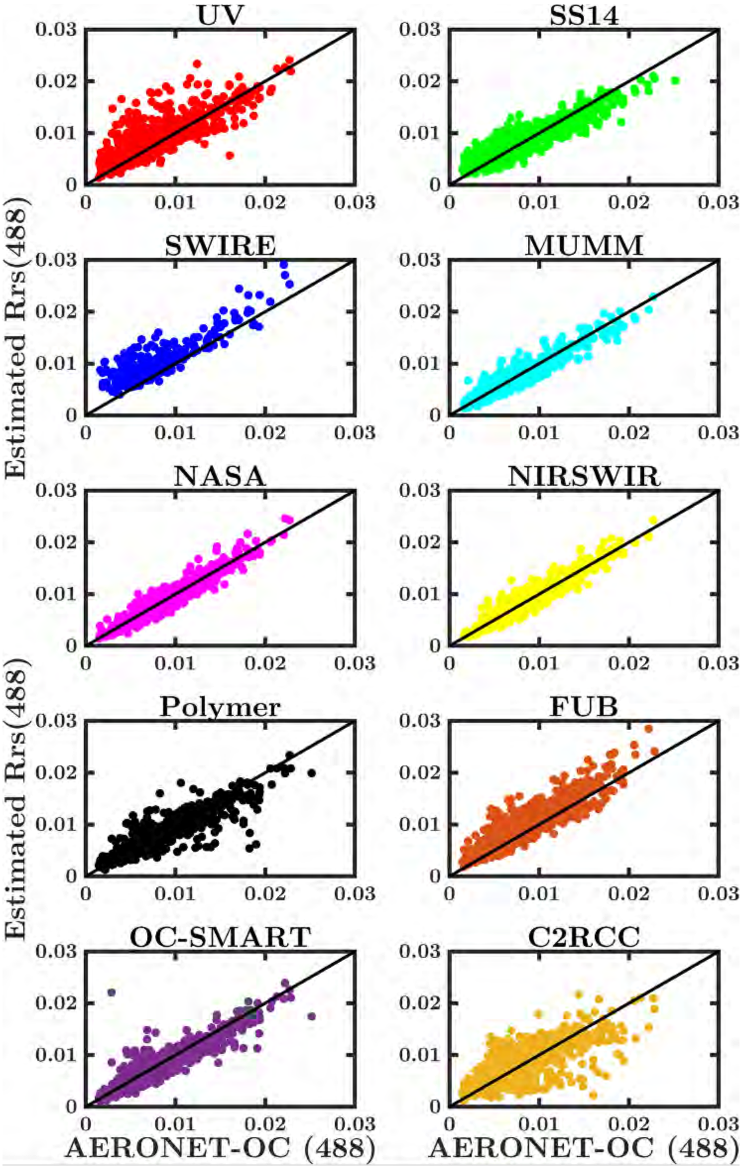
UV
SS14
SWIRE
MUMM
NASA
NIRSWIR
Polymer
FUB
OC-SMART
C2RCC
Estimated Rrs(488)
Estimated Rrs(488)
AERONET-OC (488)
AERONET-OC (488)
0
0.01
0.02
0.03

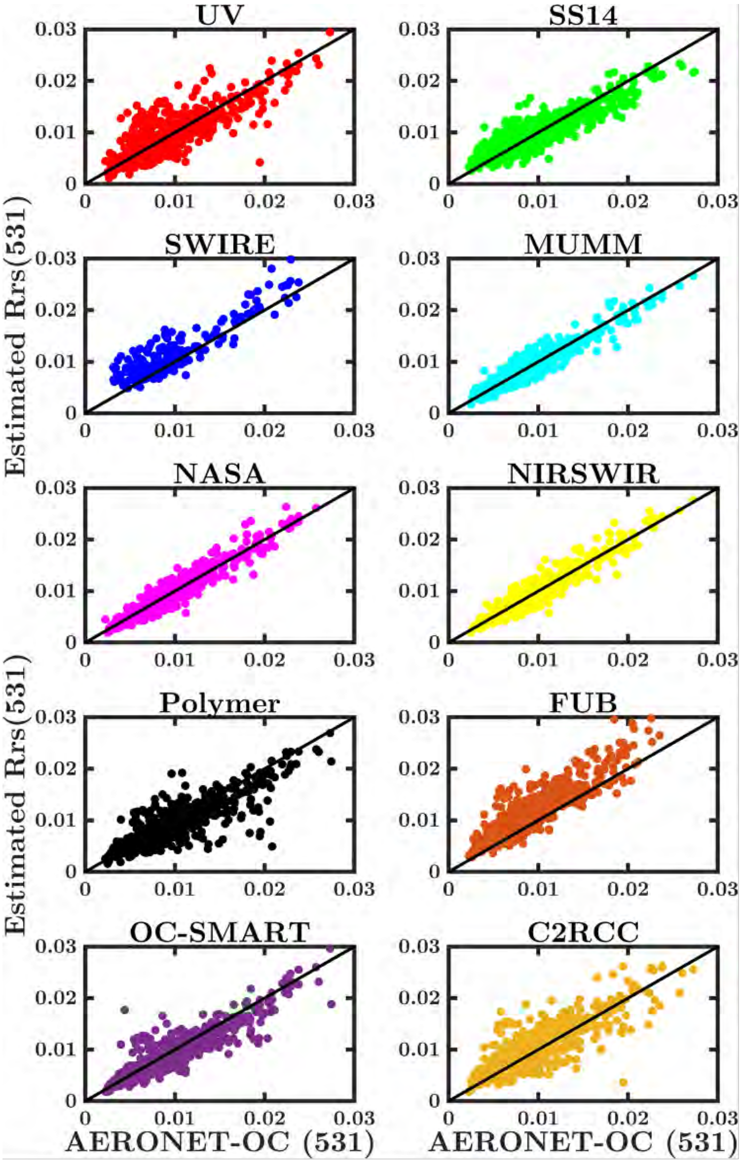
UV
SS14
SWIRE
MUMM
NASA
NIRSWIR
Polymer
FUB
OC-SMART
C2RCC
Estimated Rrs(531)
Estimated Rrs(531)
AERONET-OC (531)
AERONET-OC (531)
0
0.01
0.02
0.03

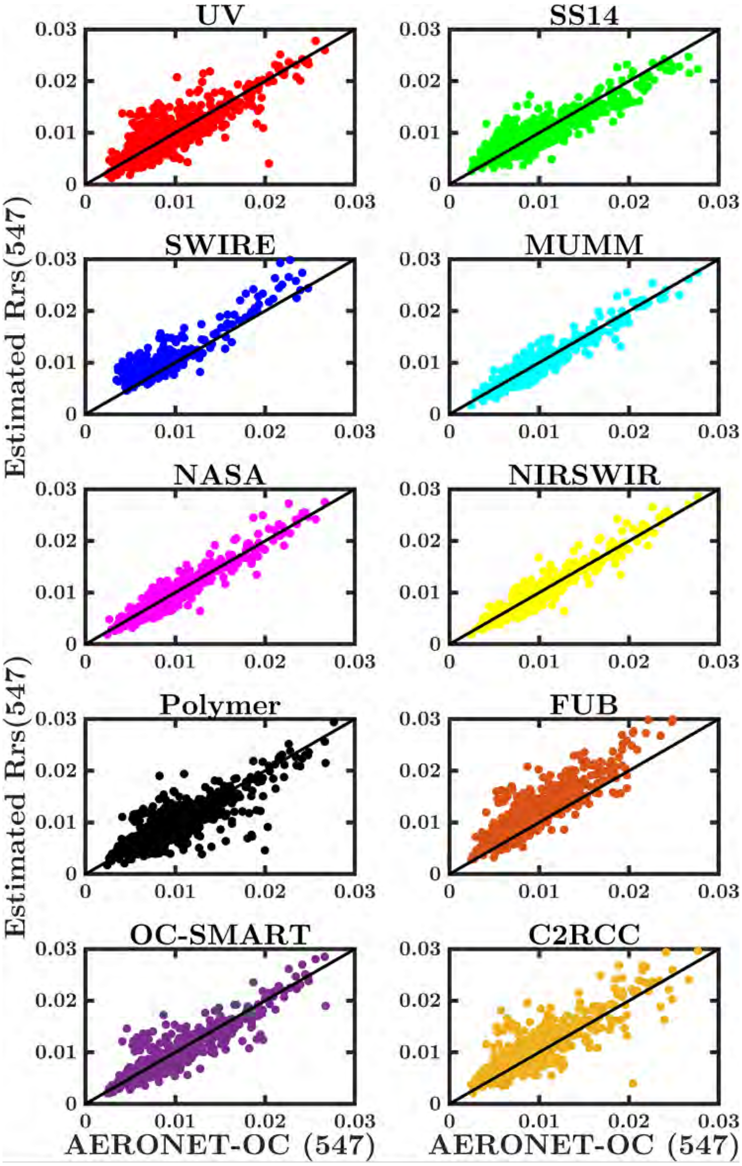
UV
SS14
SWIRE
MUMM
NASA
NIRSWIR
Polymer
FUB
OC-SMART
C2RCC
Estimated Rrs(547)
Estimated Rrs(547)
AERONET-OC (547)
AERONET-OC (547)
0
0.01
0.02
0.03

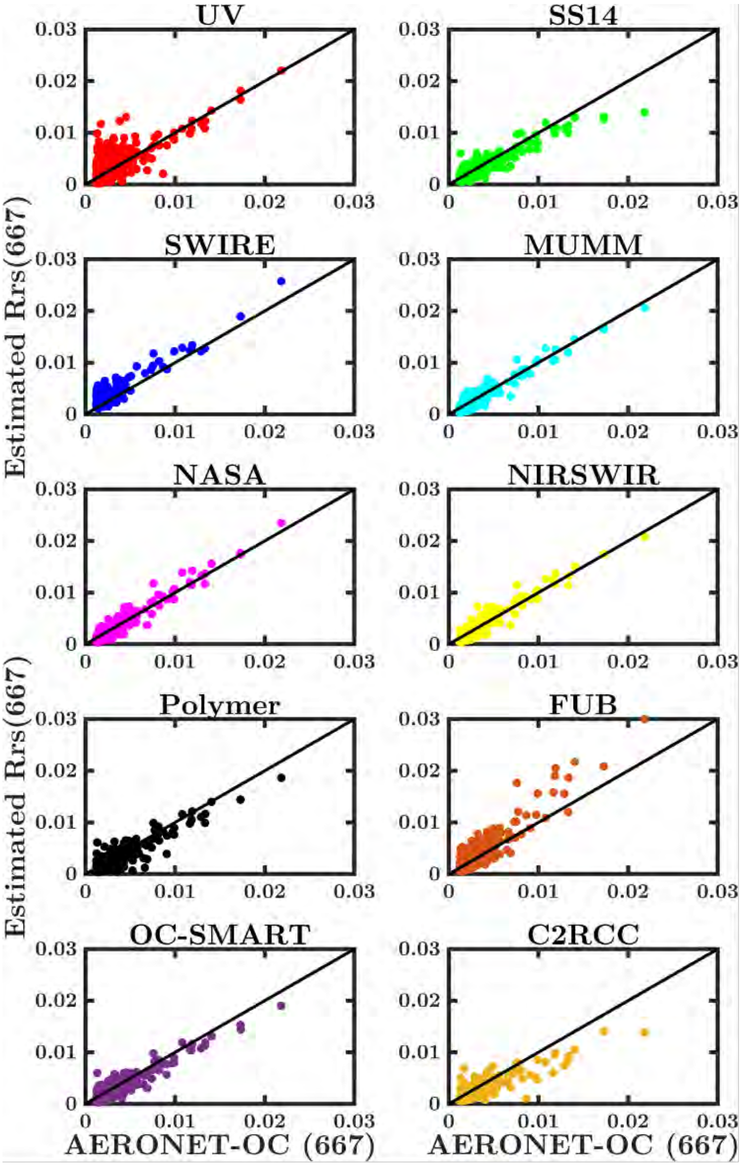
UV
SS14
SWIRE
MUMM
NASA
NIRSWIR
Polymer
FUB
OC-SMART
C2RCC
Estimated Rrs(667)
Estimated Rrs(667)
AERONET-OC (667)
AERONET-OC (667)
0
0.01
0.02
0.03

Appendix B

Scatterplots of $R_{rs}(\lambda)$ ratios for the individual match-up dataset

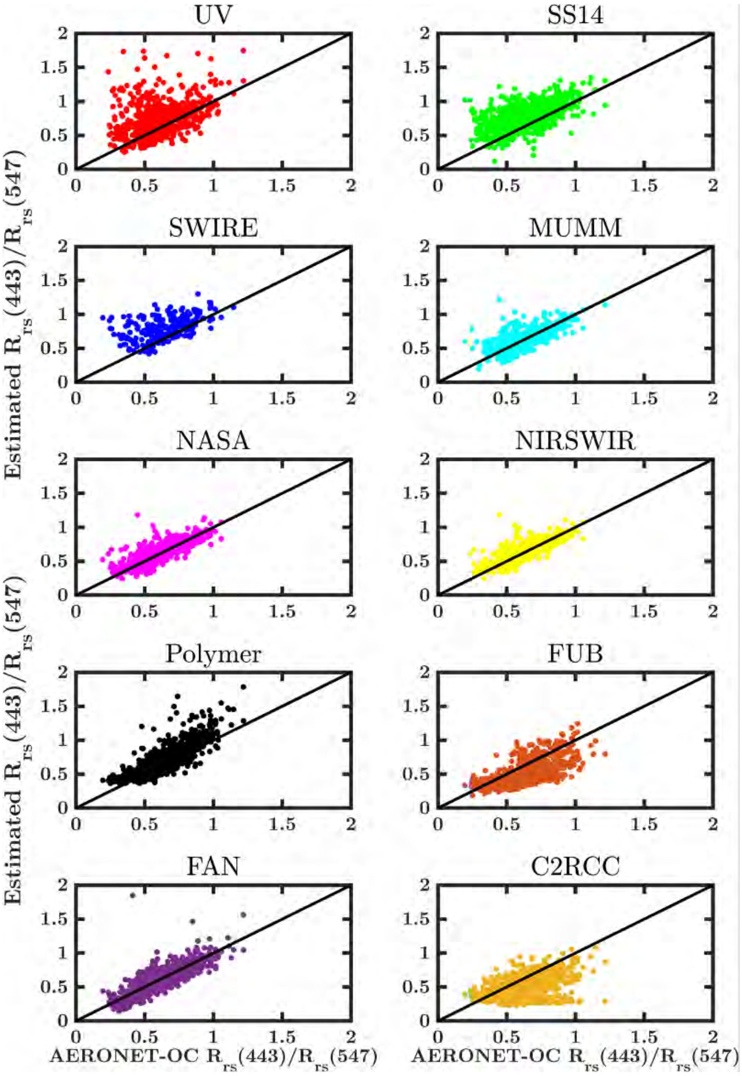

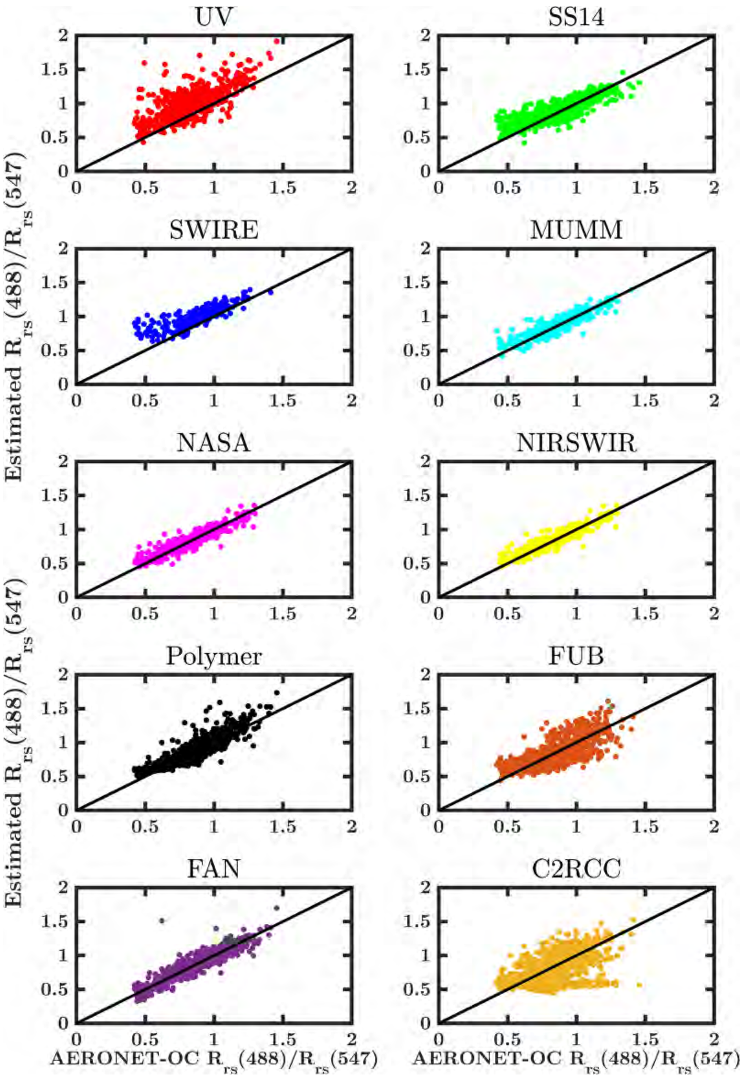
UV
SS14
SWIRE
MUMM
NASA
NIRSWIR
Polymer
FUB
FAN
C2RCC
0
0.5
1
1.5
2
Estimated $R_{rs}(488)/R_{rs}(547)$
AERONET-OC $R_{rs}(488)/R_{rs}(547)$

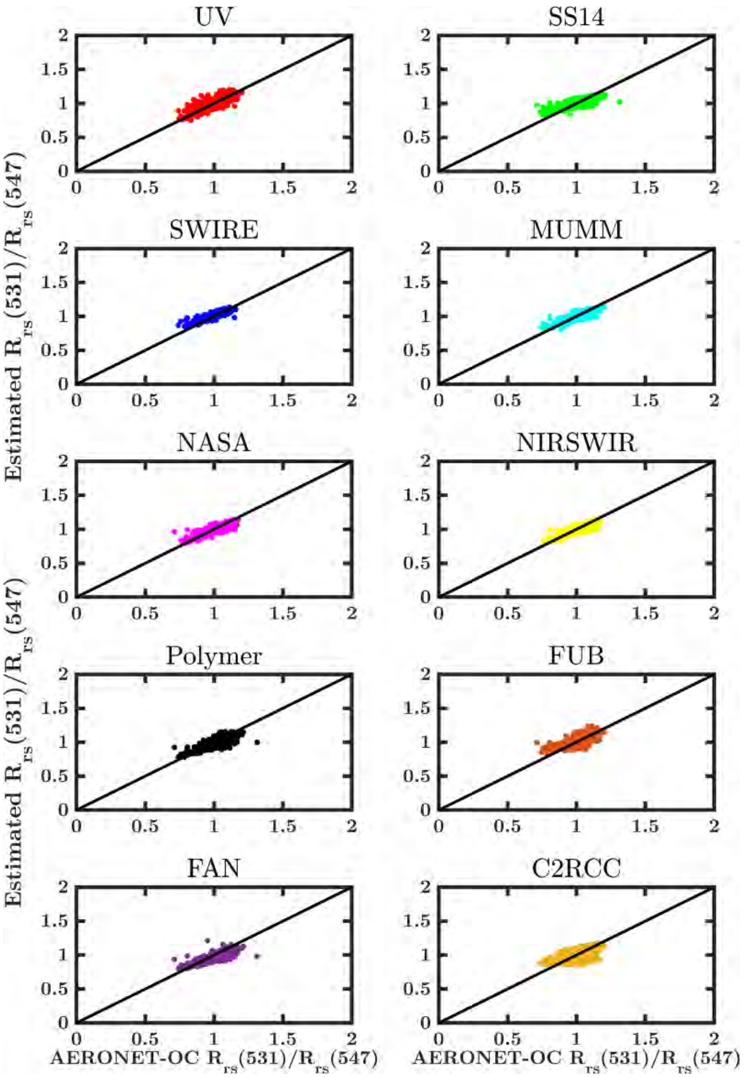
UV
SS14
SWIRE
MUMM
NASA
NIRSWIR
Polymer
FUB
FAN
C2RCC
Estimated R_rs(531)/R_rs(547)
Estimated R_rs(531)/R_rs(547)
AERONET-OC R_rs(531)/R_rs(547)
AERONET-OC R_rs(531)/R_rs(547)
0
0.5
1
1.5
2

Appendix C

Individual scatterplots for the common match-up dataset

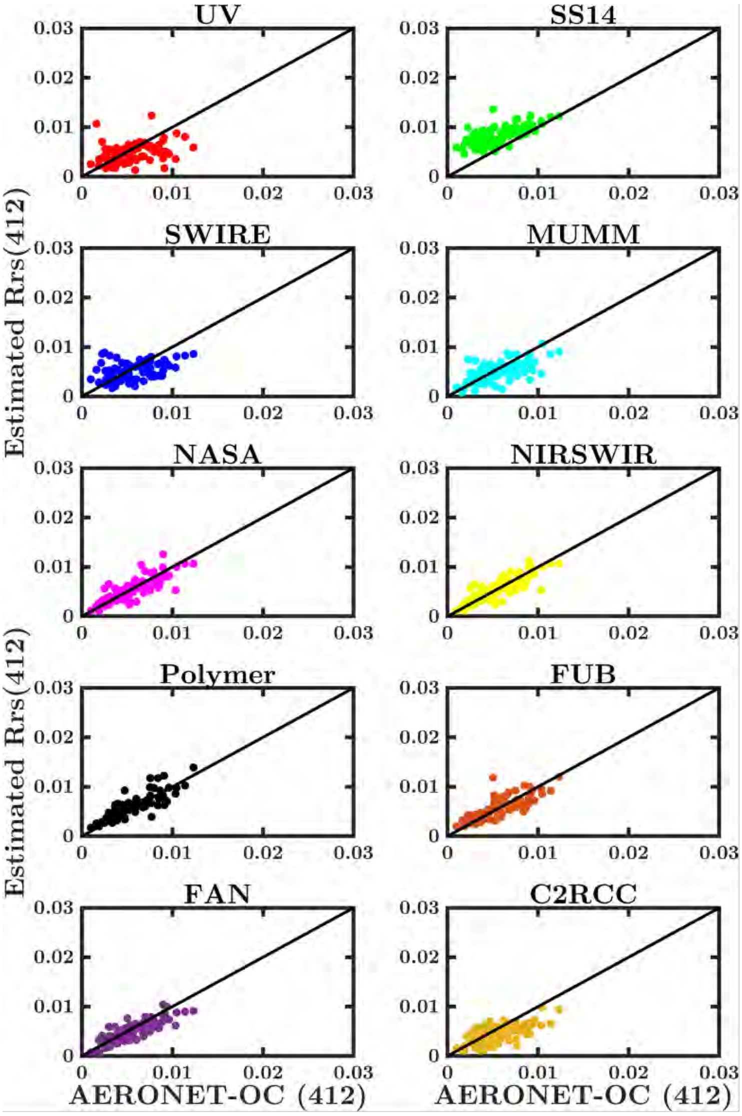

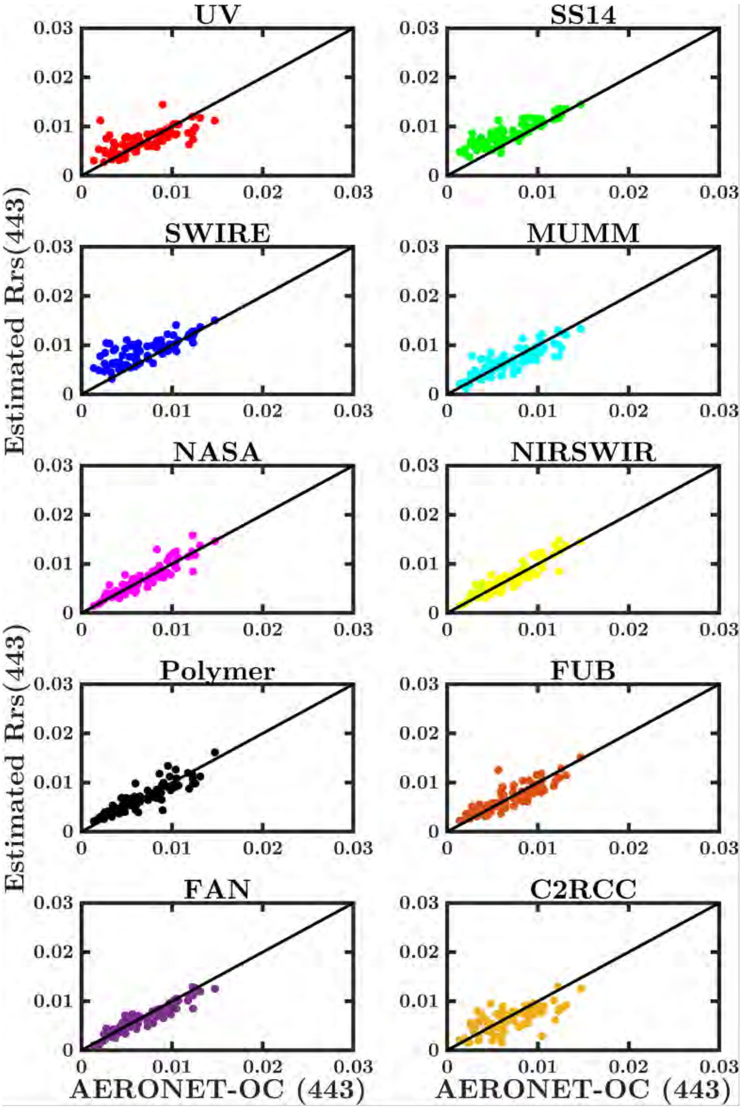
UV
SS14
SWIRE
MUMM
NASA
NIRSWIR
Polymer
FUB
FAN
C2RCC
Estimated Rrs(443)
Estimated Rrs(443)
AERONET-OC (443)
AERONET-OC (443)
0
0.01
0.02
0.03

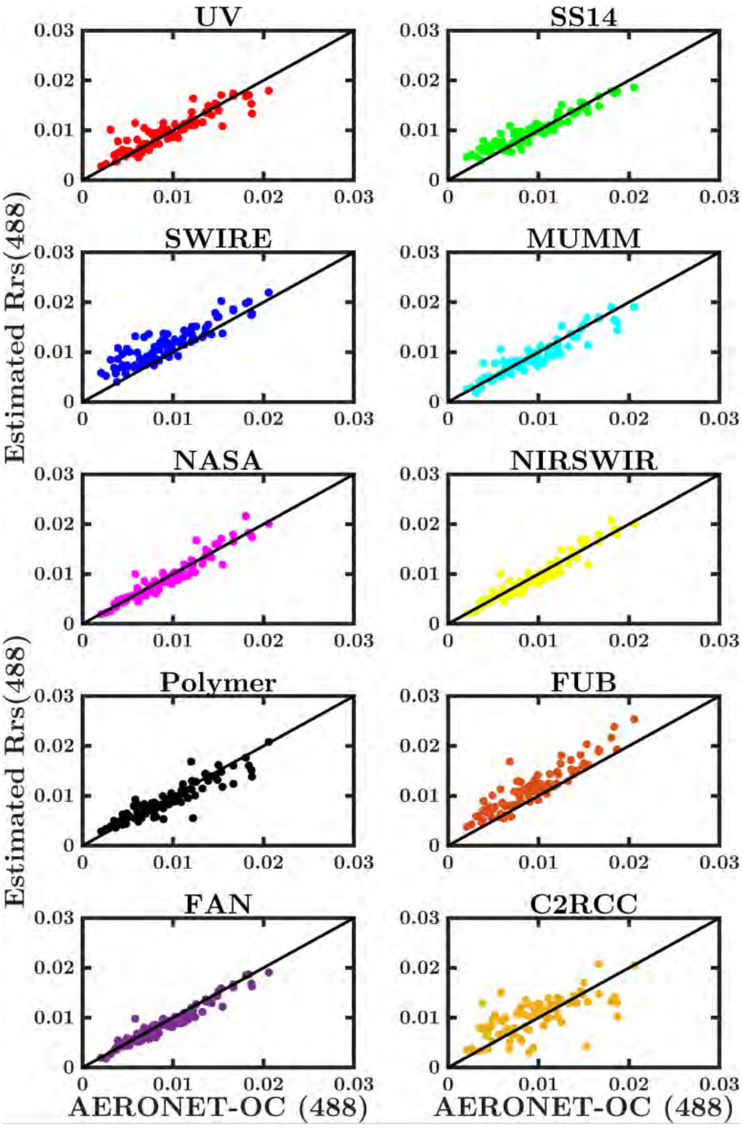
UV
SS14
SWIRE
MUMM
NASA
NIRSWIR
Polymer
FUB
FAN
C2RCC
Estimated Rrs(488)
Estimated Rrs(488)
AERONET-OC (488)
AERONET-OC (488)
0
0.01
0.02
0.03

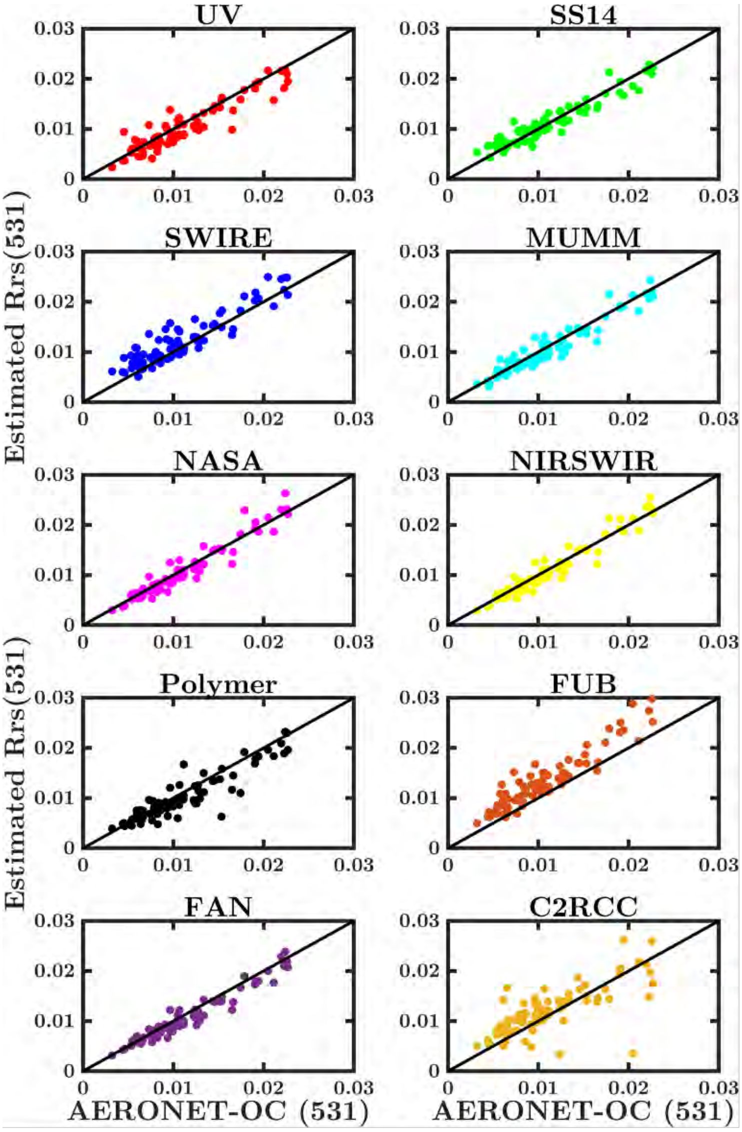
UV
SS14
SWIRE
MUMM
NASA
NIRSWIR
Polymer
FUB
FAN
C2RCC
0.03
0.02
0.01
0
0
0.01
0.02
0.03
Estimated Rrs(531)
Estimated Rrs(531)
AERONET-OC (531)
AERONET-OC (531)

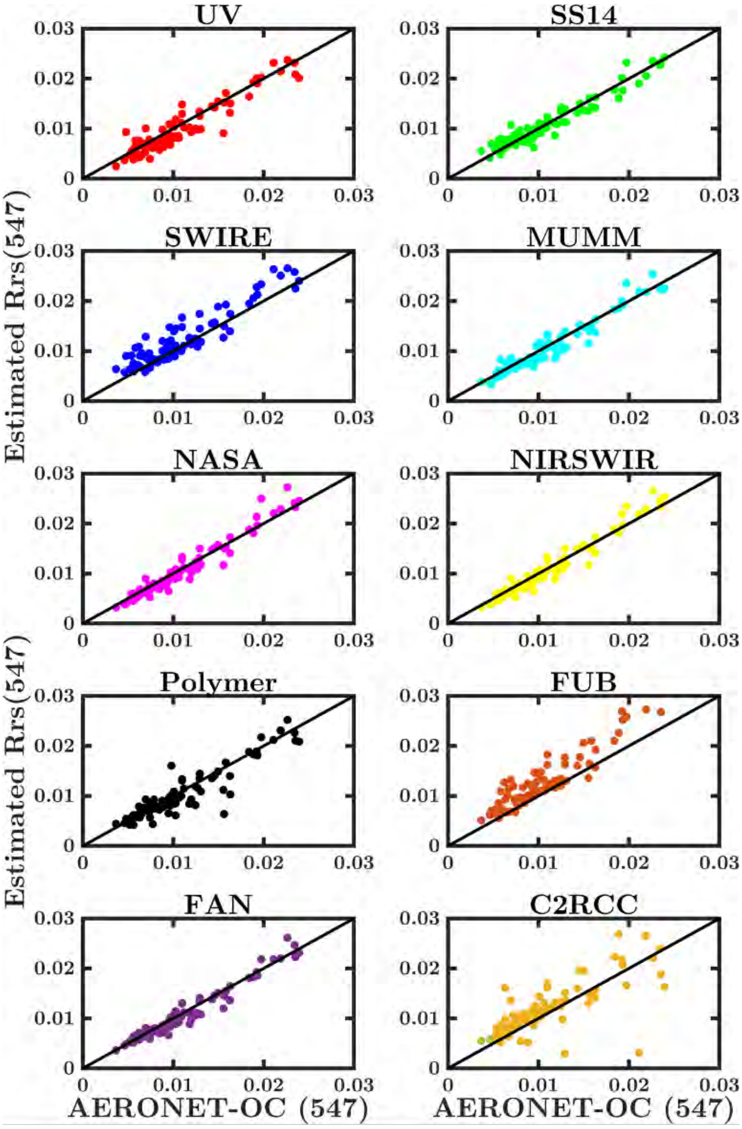
UV
SS14
SWIRE
MUMM
NASA
NIRSWIR
Polymer
FUB
FAN
C2RCC
Estimated Rrs(547)
Estimated Rrs(547)
AERONET-OC (547)
AERONET-OC (547)
0
0.01
0.02
0.03

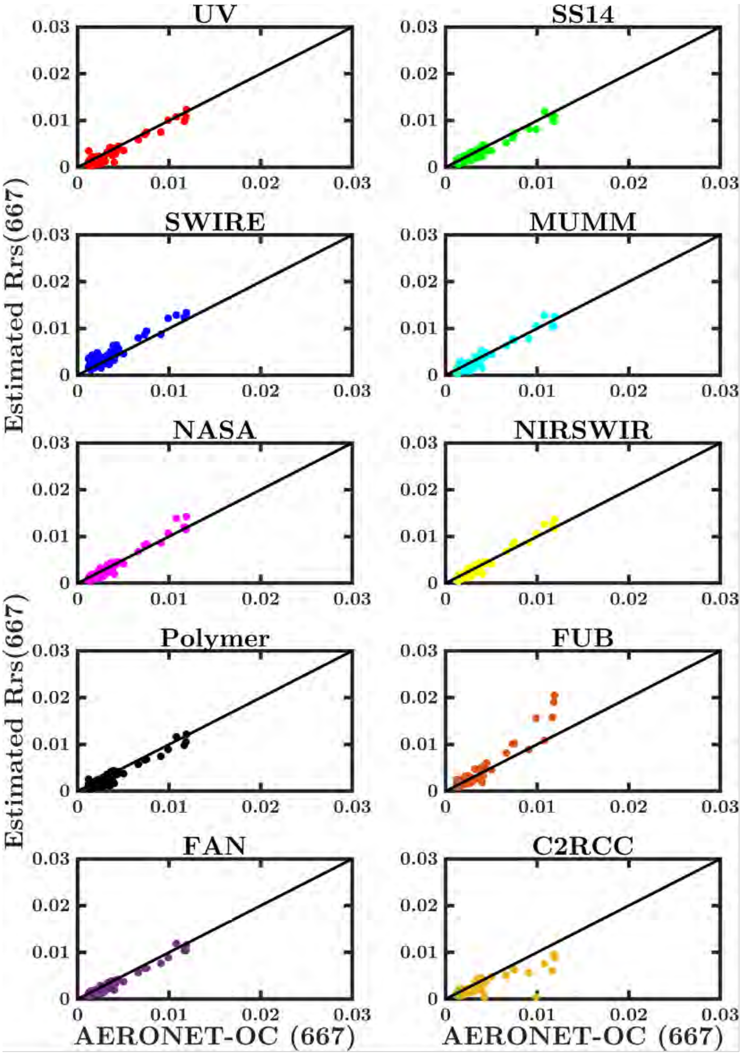
UV
SS14
SWIRE
MUMM
NASA
NIRSWIR
Polymer
FUB
FAN
C2RCC
Estimated Rrs(667)
Estimated Rrs(667)
AERONET-OC (667)
AERONET-OC (667)
0
0.01
0.02
0.03

Appendix D

Scatterplots of $R_{rs}(\lambda)$ ratios for the common match-up dataset

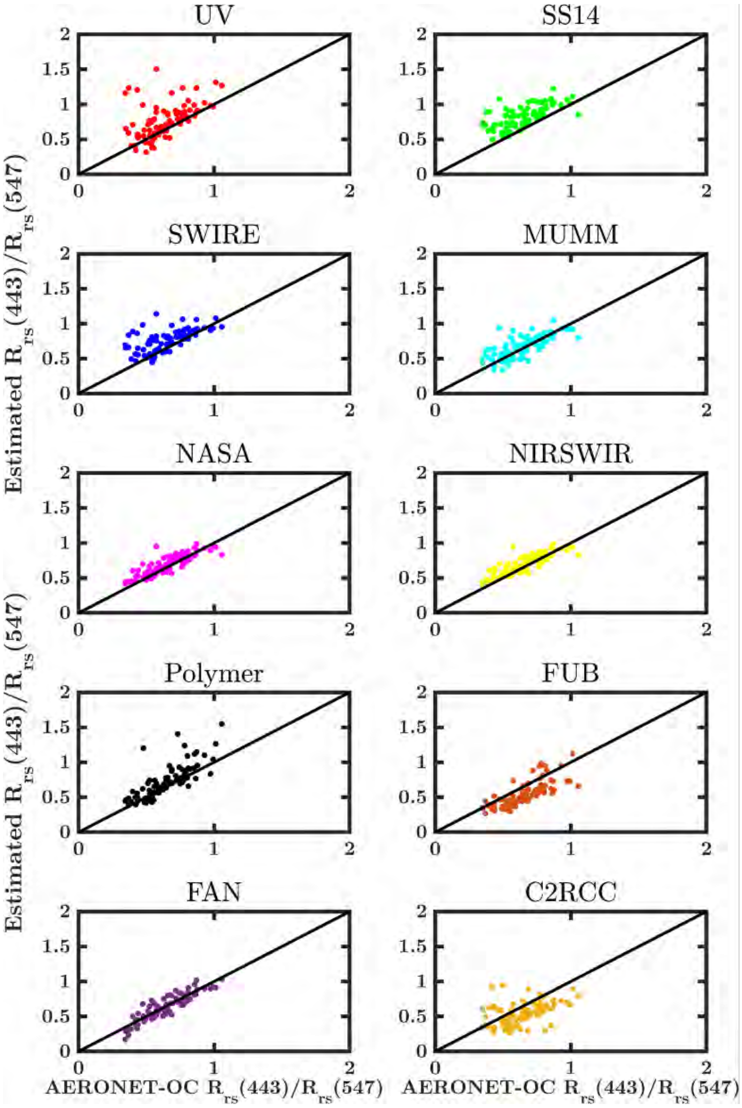

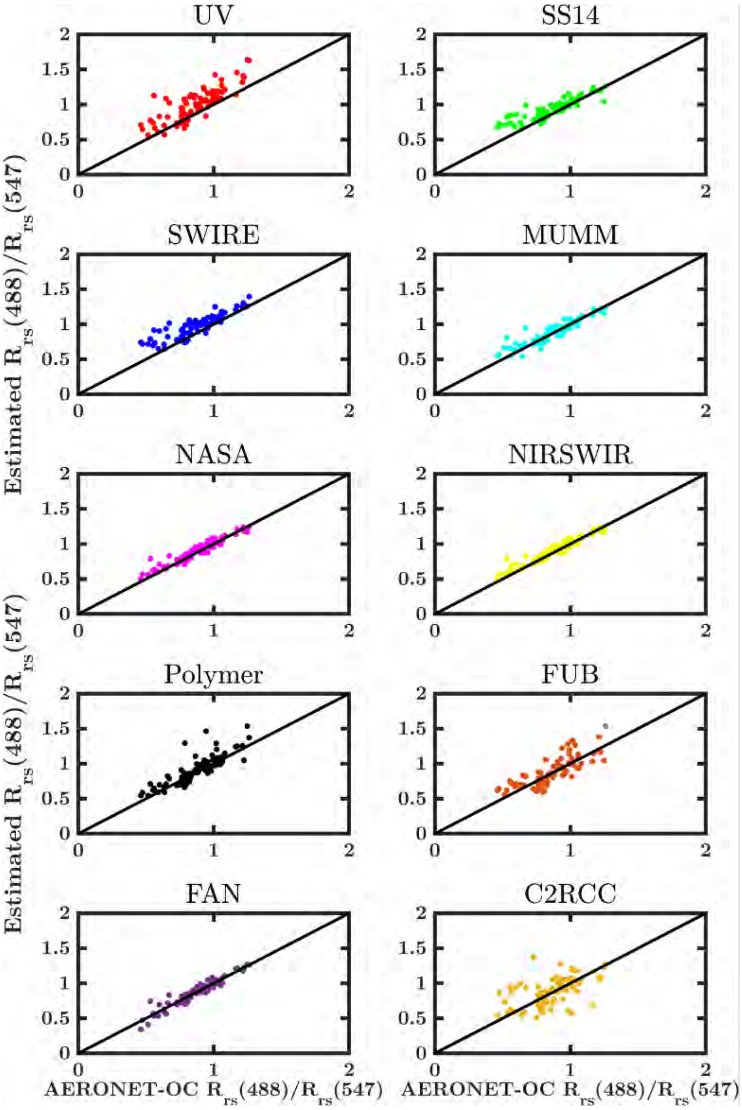
UV
SS14
SWIRE
MUMM
NASA
NIRSWIR
Polymer
FUB
FAN
C2RCC
0
0.5
1
1.5
2
0
1
2
Estimated R_rs(488)/R_rs(547)
AERONET-OC R_rs(488)/R_rs(547)

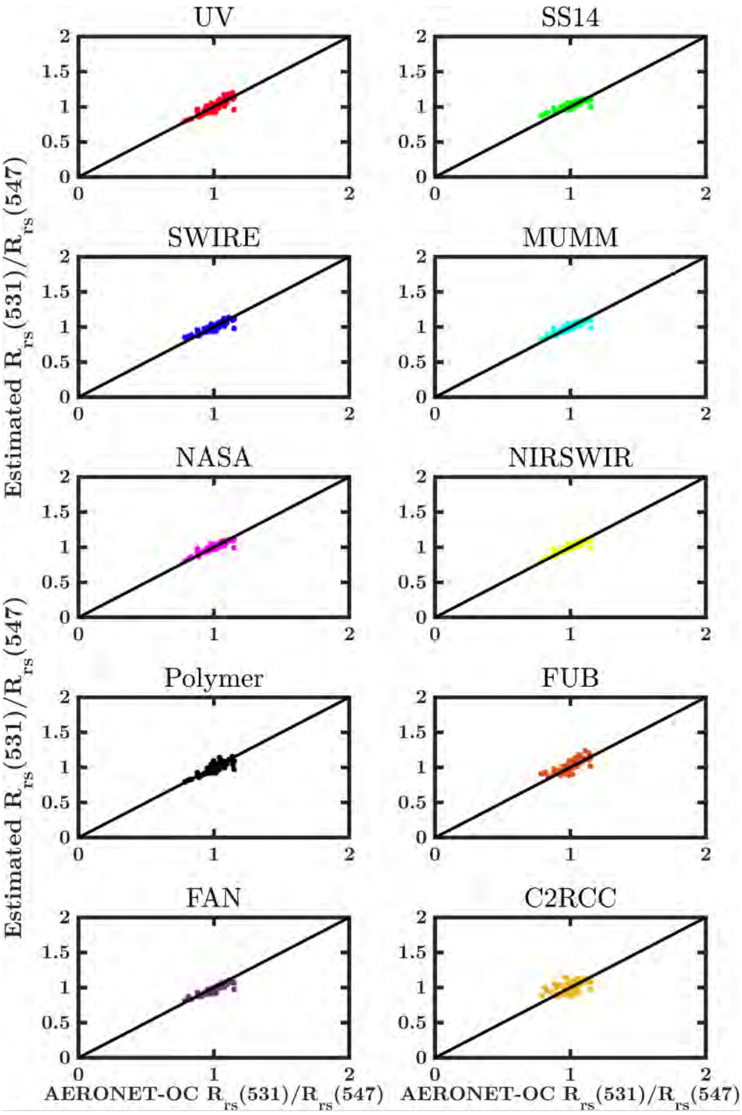
UV
SS14
SWIRE
MUMM
NASA
NIRSWIR
Polymer
FUB
FAN
C2RCC
Estimated $R_{rs}(531)/R_{rs}(547)$
Estimated $R_{rs}(531)/R_{rs}(547)$
AERONET-OC $R_{rs}(531)/R_{rs}(547)$
AERONET-OC $R_{rs}(531)/R_{rs}(547)$
0
0.5
1
1.5
2
0
1
2

Appendix E

Individual scatterplots for the simulated dataset

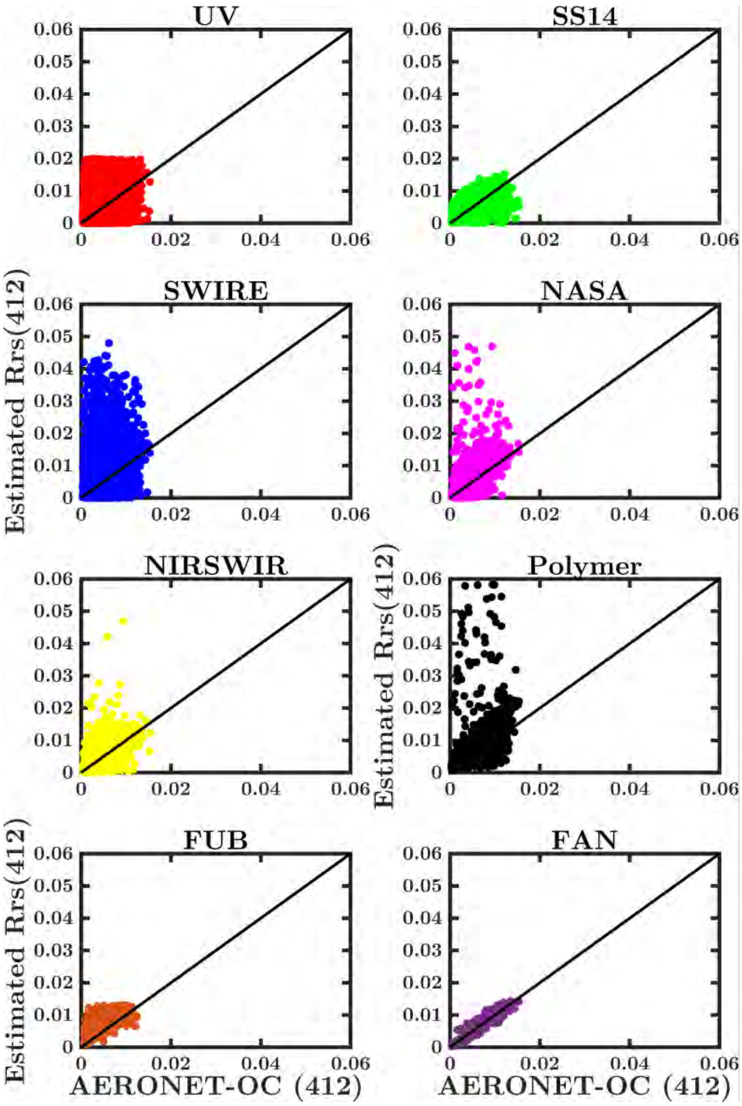

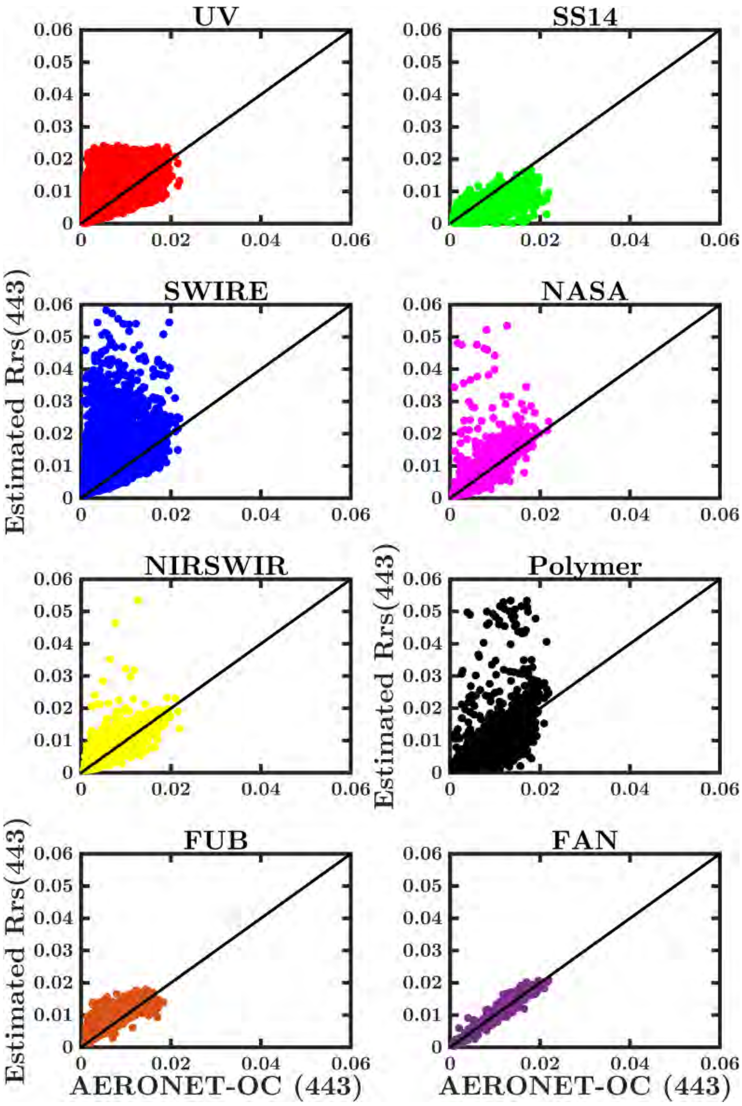
UV
SS14
SWIRE
NASA
NIRSWIR
Polymer
FUB
FAN
Estimated Rrs(443)
AERONET-OC (443)
0
0.01
0.02
0.03
0.04
0.05
0.06

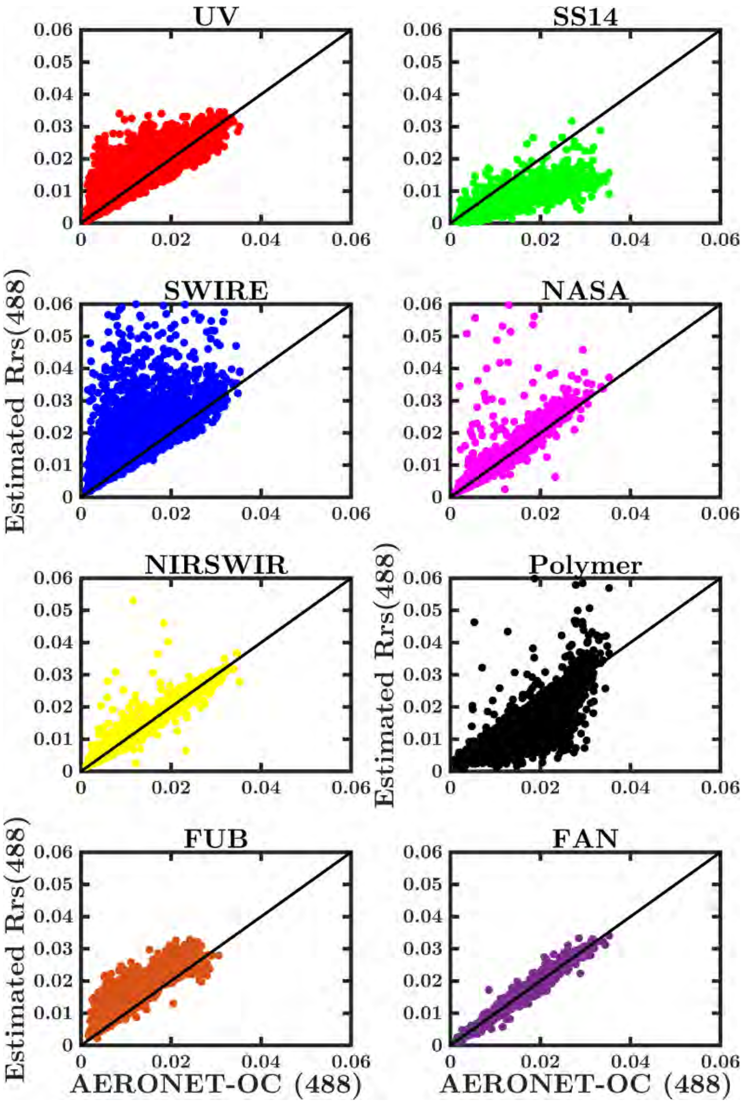
UV
SS14
SWIRE
NASA
NIRSWIR
Polymer
FUB
FAN
Estimated Rrs(488)
AERONET-OC (488)
0
0.01
0.02
0.03
0.04
0.05
0.06

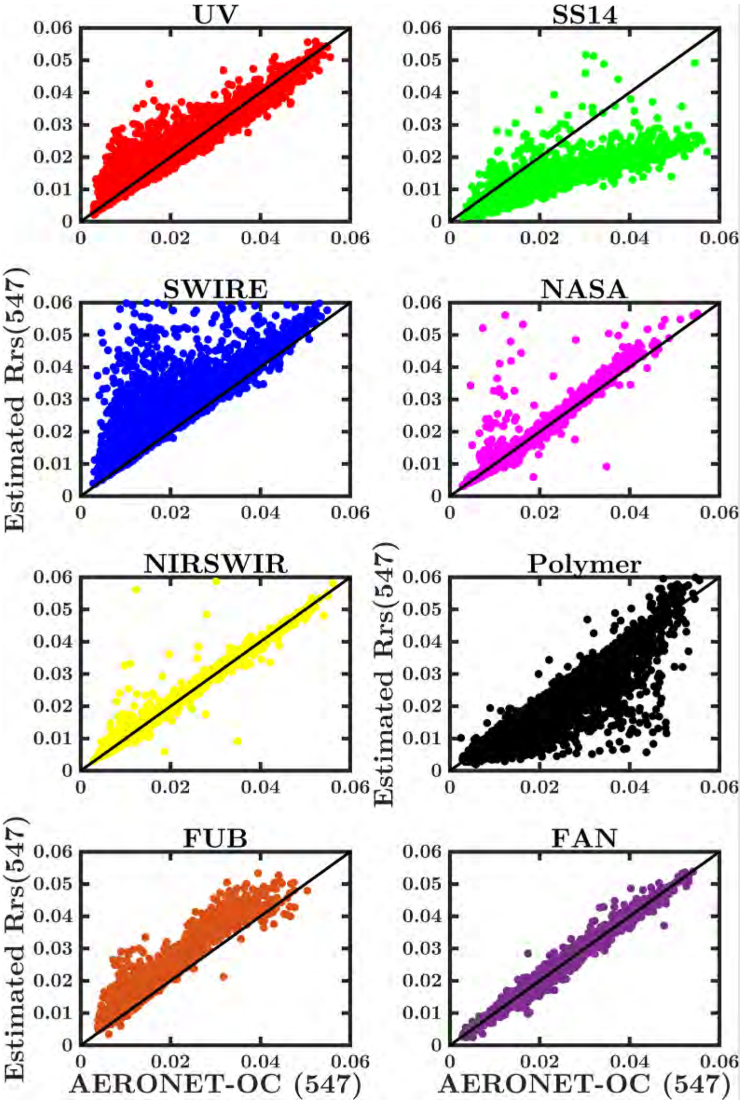
UV
SS14
SWIRE
NASA
NIRSWIR
Polymer
FUB
FAN
Estimated Rrs(547)
AERONET-OC (547)
0
0.01
0.02
0.03
0.04
0.05
0.06

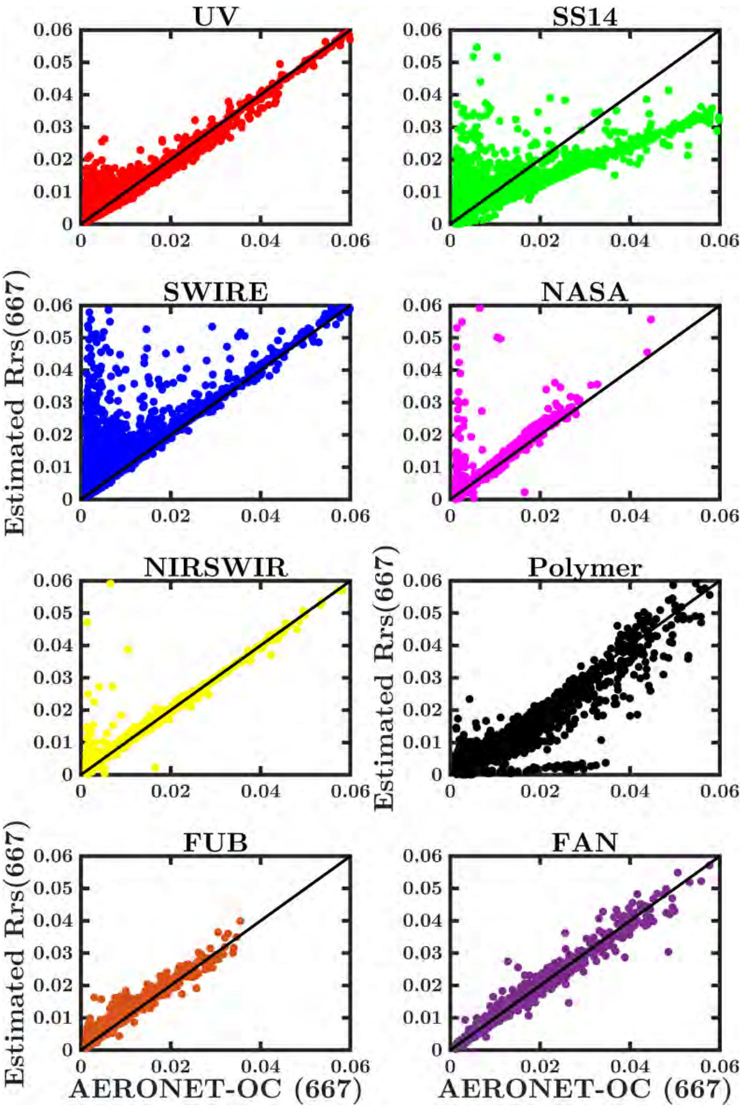
UV
SS14
SWIRE
NASA
NIRSWIR
Polymer
FUB
FAN
Estimated Rrs(667)
AERONET-OC (667)
0
0.01
0.02
0.03
0.04
0.05
0.06

Appendix F

Individual density scatterplots for the simulated dataset

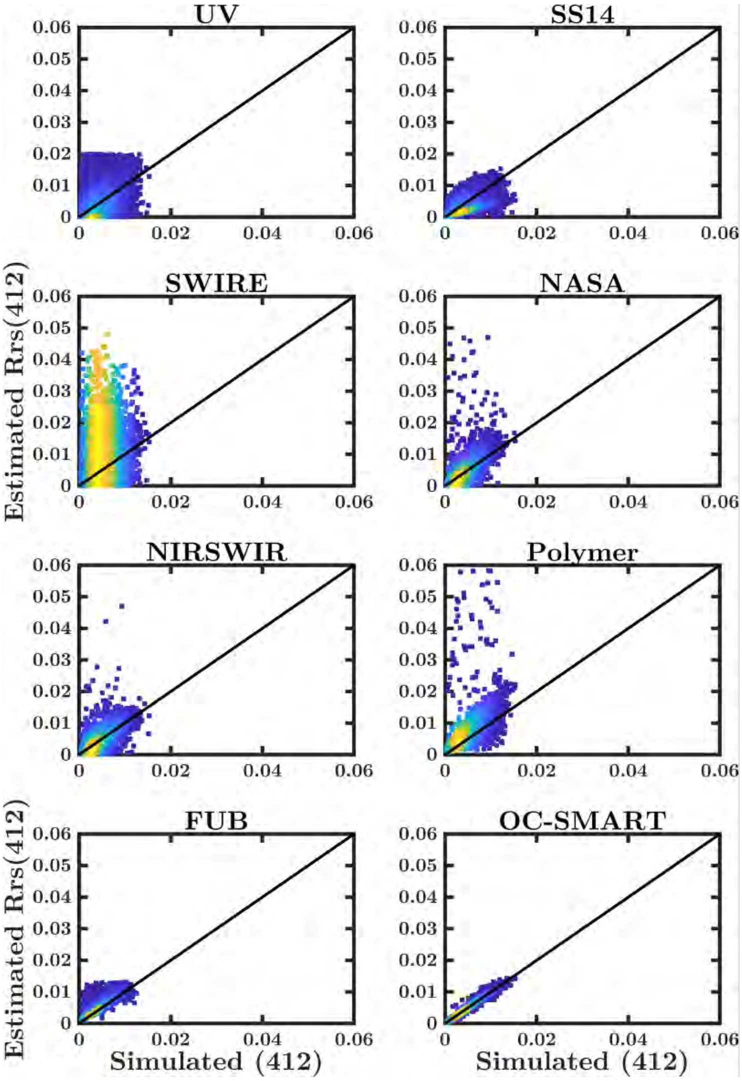

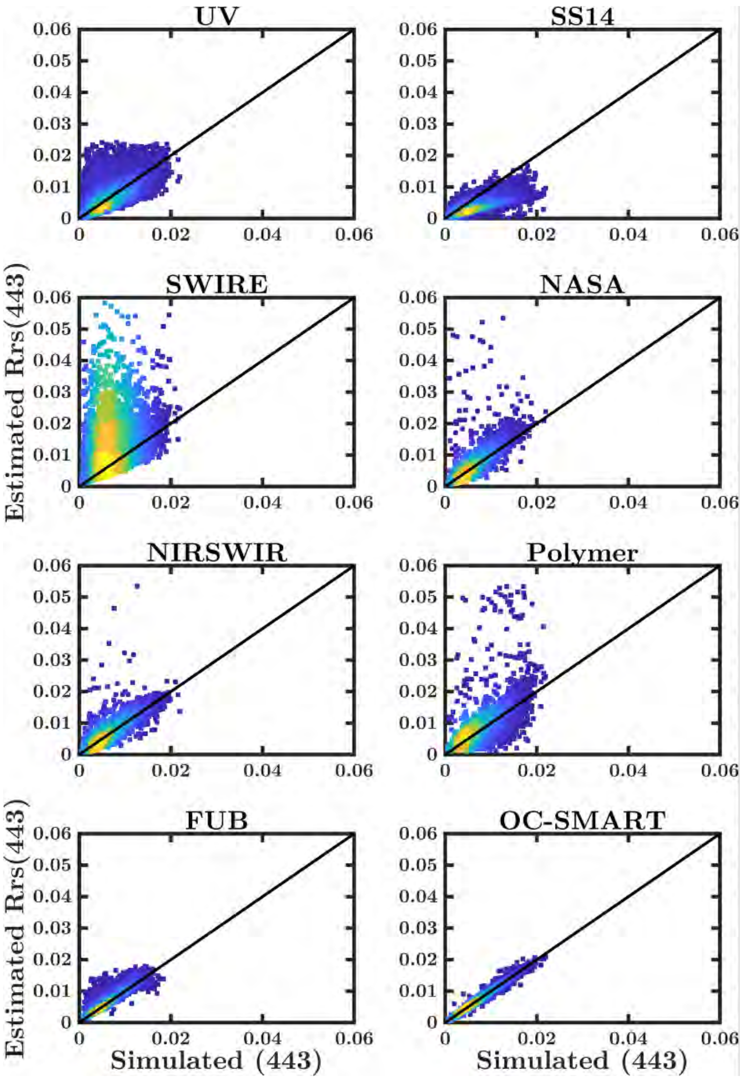
UV
SS14
SWIRE
NASA
NIRSWIR
Polymer
FUB
OC-SMART
Estimated Rrs(443)
Estimated Rrs(443)
Simulated (443)
Simulated (443)
0
0.01
0.02
0.03
0.04
0.05
0.06
0
0.02
0.04
0.06

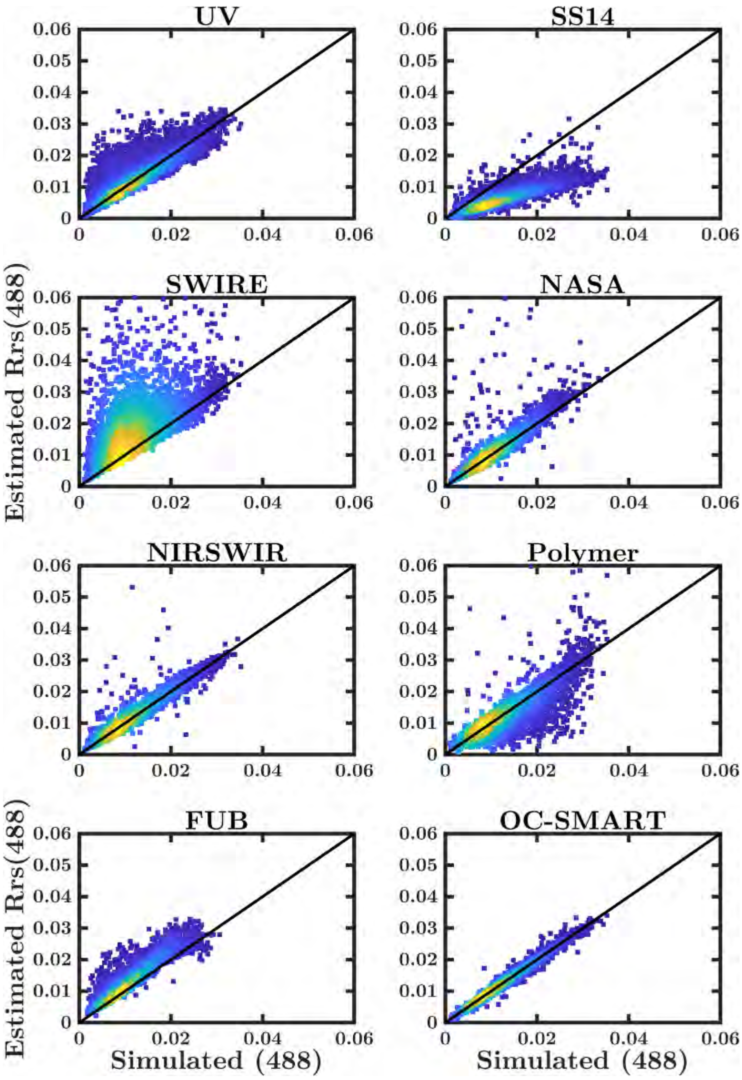
UV
SS14
SWIRE
NASA
NIRSWIR
Polymer
FUB
OC-SMART
Estimated Rrs(488)
Estimated Rrs(488)
Simulated (488)
Simulated (488)
0
0.01
0.02
0.03
0.04
0.05
0.06

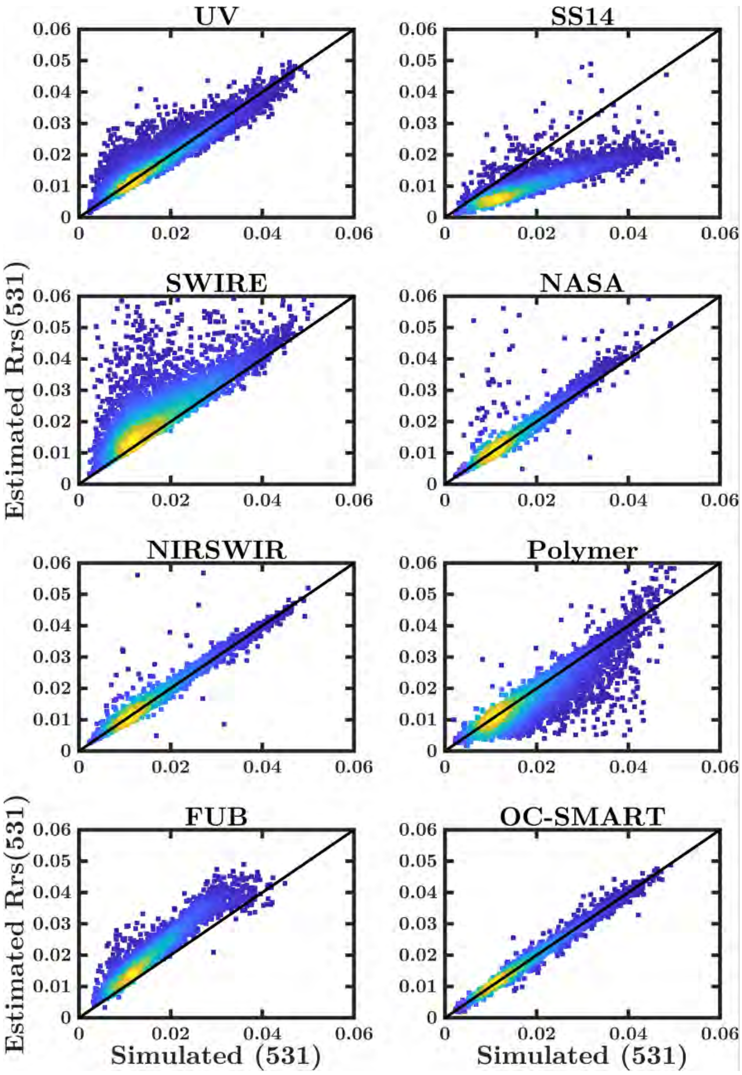
UV
SS14
SWIRE
NASA
NIRSWIR
Polymer
FUB
OC-SMART
Estimated Rrs(531)
Simulated (531)
0
0.01
0.02
0.03
0.04
0.05
0.06

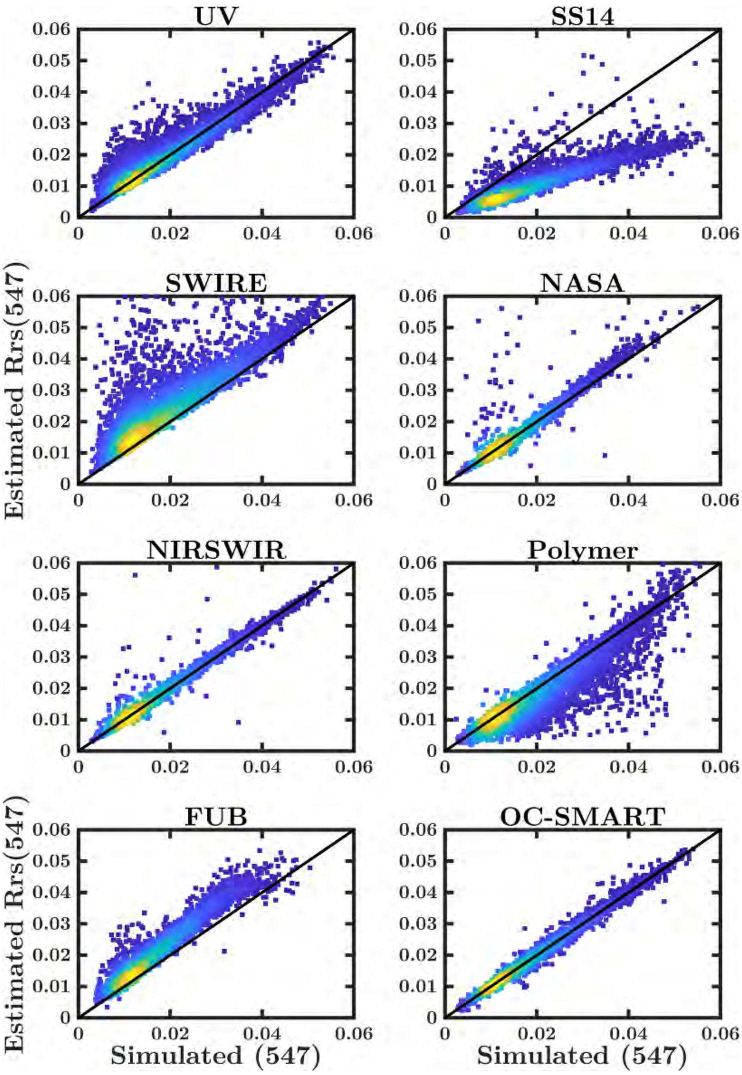
UV
SS14
SWIRE
NASA
NIRSWIR
Polymer
FUB
OC-SMART
Estimated Rrs(547)
Estimated Rrs(547)
Simulated (547)
Simulated (547)
0
0.01
0.02
0.03
0.04
0.05
0.06

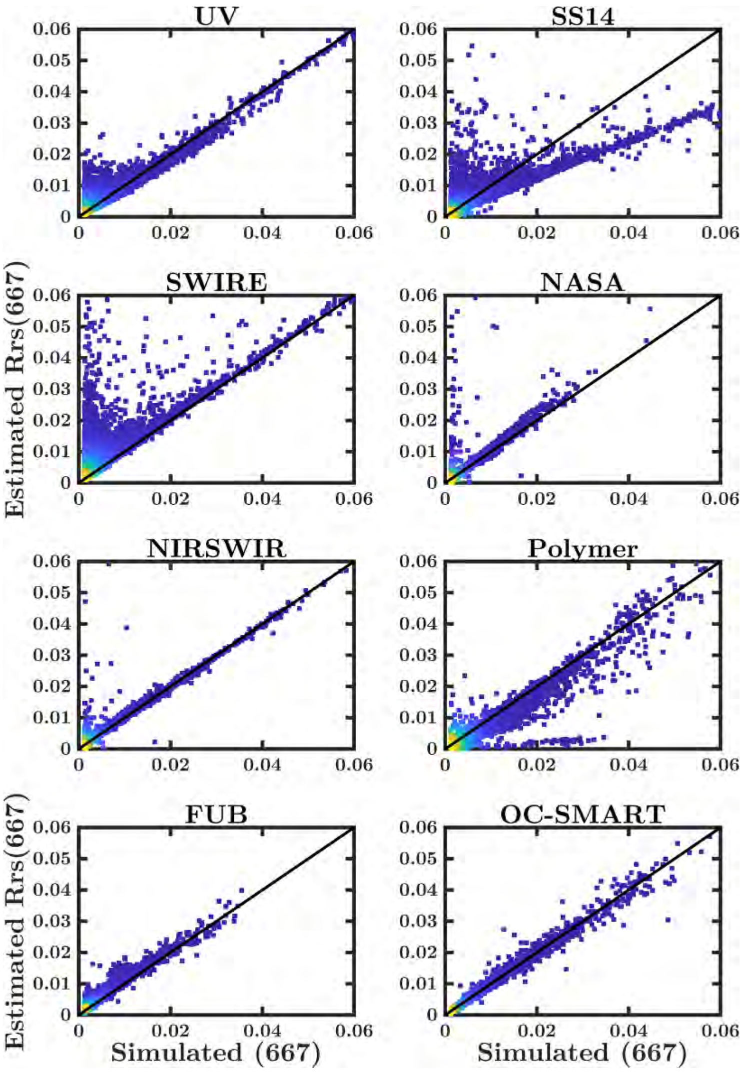
UV
SS14
SWIRE
NASA
NIRSWIR
Polymer
FUB
OC-SMART
Estimated Rrs(667)
Simulated (667)
0
0.01
0.02
0.03
0.04
0.05
0.06

Appendix G

Scatterplot of $R_{rs}(\lambda)$ ratios for the simulated dataset

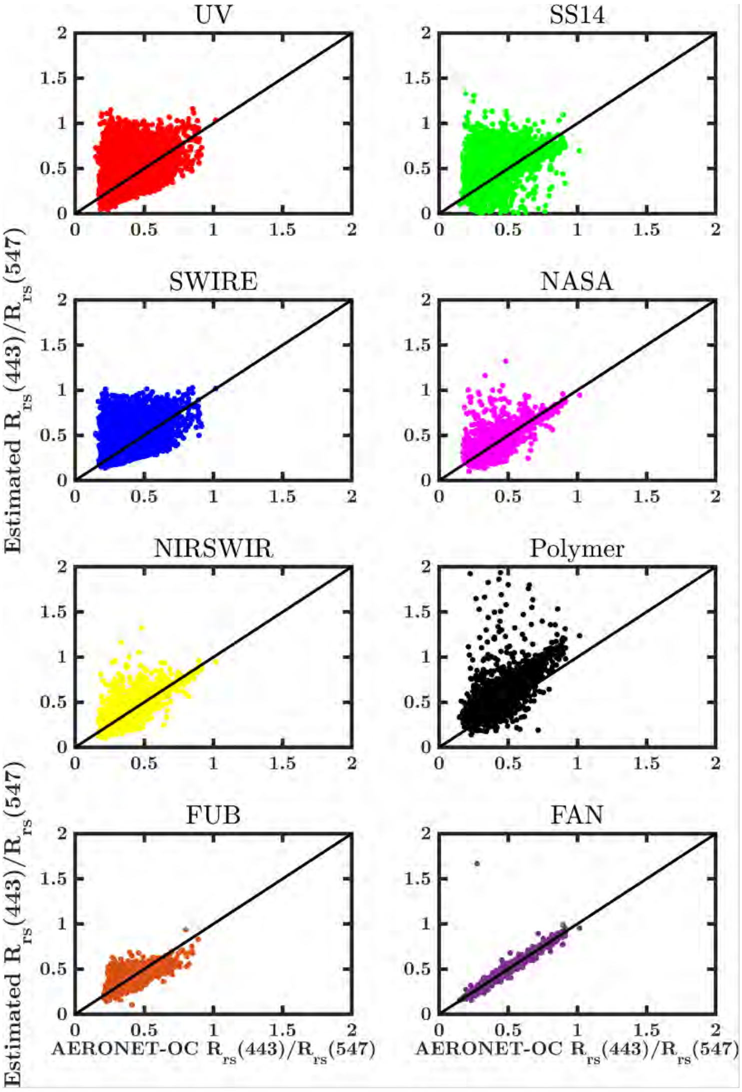

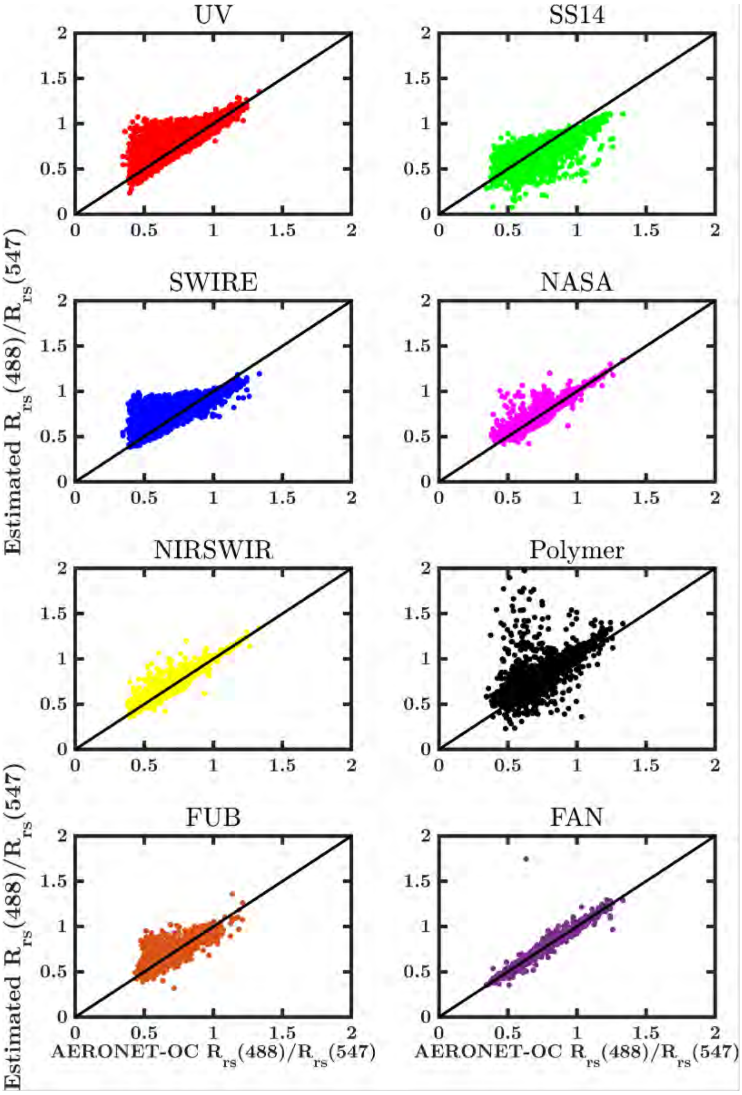
UV
SS14
SWIRE
NASA
NIRSWIR
Polymer
FUB
FAN
0
0.5
1
1.5
2
Estimated R$_{rs}$(488)/R$_{rs}$(547)
AERONET-OC R$_{rs}$(488)/R$_{rs}$(547)

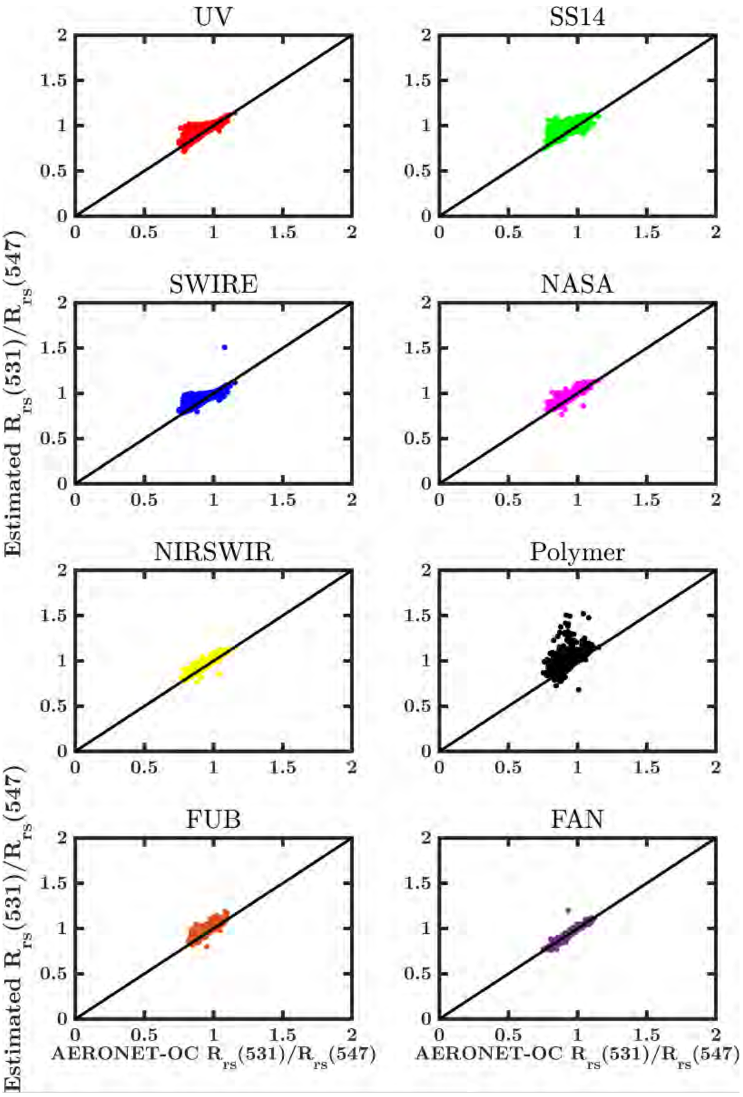
UV
SS14
SWIRE
NASA
NIRSWIR
Polymer
FUB
FAN
0
0.5
1
1.5
2
Estimated $R_{rs}(531)/R_{rs}(547)$
AERONET-OC $R_{rs}(531)/R_{rs}(547)$

Acronyms and Abbreviations

AC	Atmospheric Correction
AccuRT	A Radiative Transfer model for the coupled atmosphere-water system
AERONET-OC	AErosol RObotic NETwork Ocean Colour
ANN	Artificial Neural Networks
AOPs	Apparent Optical Properties
AOD	Aerosol Optical Depth
AOT	Aerosol Optical Thickness
BRDF	Bidirectional Reflectance Distribution Function
C2RCC	Case 2 Regional CoastColour
CCRR	CoastColour Round Robin
CDOM	Coloured Dissolved Organic Matter
CHL	Chlorophyll-a
COASTLOOC	Coastal Surveillance Through Observation of Ocean Color
CV	Coefficient of Variability
CZCS	Coastal Zone Color Scanner
DOC	Dissolved Organic Carbon
DOM	Dissolved Organic Matter
EO	Earth Observation
ESA	European Space Agency
EUMETSAT	European Organisation for the Exploitation of Meteorological Satellites
FUB	Freie Universität Berlin AC algorithm of Schroeder & coworkers 2005, 2007
GLI	Global Land Imager
GSM	Garver-Siegel-Maritorena model
GW94	AC Approach of Gordon & Wang, 1994
HICO	Hyperspectral Imager for the Coastal Ocean
IOPs	Inherent Optical Properties
IR	Infrared
JAXA	Japan Aerospace Exploration Agency
L1	Level-1 data
L2	Level-2 data
L3	Level-3 data
MERIS	Medium Resolution Imaging Spectrometer
MIN	Mineral Particles
MODIS	Moderate resolution Imaging Spectroradiometer
MOMO	Matrix-Operator-MOdel
MSE	Mean Squared Error
MSI	Multispectral Imager
MUMM	Management Unit of the North Sea Mathematical Models

NAP	Non-Algal Particles
NASA	National Aeronautics and Space Administration
NASA-AC	NASA Standard AC Algorithm of Bailey & coworkers 2010
NIR	Near Infra-Red
NIRSWIR	Near+Shortwave Infra-Red AC algorithm of Wang & Shi, 2007
NOAA	National Oceanic and Atmospheric Administration (USA)
OC-SMART	Ocean Color - Simultaneous Marine and Aerosol Retrieval Tool
OAC	Optically Active Constituent
OBPG	Ocean Biology Processing Group (NASA)
OCR	Ocean Colour Radiometry
OCI	Ocean Colour Imager
OLCI	Ocean and Land Colour Imager
OPAC	Optical Properties of Aerosols and Clouds
OWT	Optical Water Type
PACE	Plankton, Aerosol, Cloud, ocean Ecosystem
PCOART	vector Coupled Ocean–Atmosphere Radiative Transfer model
Polymer	AC algorithm of Steinmetz & coworkers 2011
PSD	Particle Size Distribution
QAS	Quality Assurance Score
QWIP	Quality Water Index Polynomial
R10	Simulations from IOCCG Report 10 (2010)
RAA	Relative Azimuth Angle
RD	Relative Difference
RH	Relative Humidity
RMSD	Root Mean Square Difference
RTM	Radiative Transfer Model
SAA	Solar Azimuth Angle
SAR	Synthetic Aperture Radar
SeaDAS	SeaWiFS Data Analysis System
SeaWiFS	Sea-viewing Wide Field-of-view Sensor
SLSTR	Sea and Land Surface Temperature Radiometer
SNAP	Sentinel Application Platform
S-NPP	Suomi National Polar-orbiting Partnership
SNR	Signal-to-Noise Ratio
SOM	Self-Organizing Map
SPM	Suspended Particulate Matter
SS14	Gaussian-spectral relationship AC algorithm of Singh & Shanmugam, 2014
SSP	Spectral Shape Parameter
SVC	System Vicarious Calibration
SWIR	Shortwave Infra-Red
SWIRE	Shortwave Infra-Red AC Algorithm of He & Chen, 2014
SZA	Solar Zenith Angle
TOA	Top of Atmosphere
TSM	Total Suspended Matter

TSS	Total Suspended Solids
UAV	Unmanned Aerial Vehicle
UV	Ultraviolet
UV-AV	Ultraviolet AC Algorithm of He & coworkers 2012
VAA	Viewing Azimuth Angle
VIIRS	Visible Infrared Imaging Radiometer Suite
VIS	Visible
VZA	Viewing Zenith Angle
WG	Working Group

Mathematical Notation

Symbol	Description	Typical Units
θ_0	solar zenith angle	rad
ϕ_0	solar azimuth angle	rad
θ_v	viewing zenith angle	rad
ϕ_v	viewing azimuth angle	rad
$\Delta\phi$	relative azimuth angle	rad
τ	optical depth	dimensionless
τ_{TOA}	top-of-atmosphere optical depth	dimensionless
τ_a	total optical depth of atmosphere	dimensionless
τ_a^+	total optical depth just above air-water interface	dimensionless
τ_a^-	total optical depth just below air-water interface	dimensionless
α_{MIN}	absorption coefficient for mineral particles	[m^{-1}]
α_{pig}	absorption coefficient for pigmented particles	[m^{-1}]
α_{CDOM}	absorption coefficient for CDOM	[m^{-1}]
β_{MIN}	scattering coefficient for mineral particles	[m^{-1}]
β_{pig}	scattering coefficient for pigmented particles	[m^{-1}]
γ_{MIN}	attenuation coefficient for mineral particles	[m^{-1}]
γ_{pig}	attenuation coefficient for pigmented particles	[m^{-1}]
ρ	reflectance	
ρ_{rc}	Rayleigh-corrected reflectance	
ρ_w	water leaving reflectance	
ρ_{TOA}	top-of-atmosphere reflectance	
κ	band ratio correction factor	
$p_{Ray}(\cos\Theta)$	Rayleigh scattering phase function	
$p_{PET}(\cos\Theta)$	Petzold scattering phase function	
$p_{FF}(\cos\Theta)$	Fournier-Forand (FF) scattering phase function	
F_0	extraterrestrial solar irradiance	[W m^{-2} nm^{-1}]
$\bar{F}_0$	extraterrestrial solar irradiance at the mean distance from the Sun	[W m^{-2} nm^{-1}]
L_a	radiance due to scattering/absorption by aerosols in the absence of air molecules	[W m^{-2} nm^{-1} sr^{-1}]
L_{ra}	the radiance due to the interaction between aerosols and air molecules (aerosols-Rayleigh scattering)	[W m^{-2} nm^{-1} sr^{-1}]
L_g	the radiance due to specular reflection of Sunlight by the sea surface (Sun glint)	[W m^{-2} nm^{-1} sr^{-1}]
L_R	radiance due to scattering by air molecules (Rayleigh scattering) in the absence of aerosols	[W m^{-2} nm^{-1} sr^{-1}]
L_{TOA}	radiance measured at the top of the atmosphere	[W m^{-2} nm^{-1} sr^{-1}]
L_{sea}	radiance computed for a non-black sea	[W m^{-2} nm^{-1} sr^{-1}]

$L_{black\ sea}$	radiance computed for a black sea	[W m^{-2} nm^{-1} sr^{-1}]
L_w	water-leaving radiance	[W m^{-2} nm^{-1} sr^{-1}]
nL_w	normalized water-leaving radiance	[W m^{-2} nm^{-1} sr^{-1}]
$L_{w,TOA}$	contribution of radiance emerging from the sea to TOA radiance	[W m^{-2} nm^{-1} sr^{-1}]
L_{wc}	the radiance due to white caps	[W m^{-2} nm^{-1} sr^{-1}]
L_{wN}^{ex}	exact normalized water-leaving radiance	[W m^{-2} nm^{-1} sr^{-1}]
$\bar{d}$	mean Earth-Sun distance	
d	actual Earth-Sun distance	
$\mathcal{F}$	anisotropy correction factor	
t^+	upward diffuse transmittance	dimensionless
t^-	downward diffuse transmittance	dimensionless
$E_d(\tau_a^+)$	downward irradiance just above the surface	[W m^{-2}]
$E_d(\tau = 0)$	downward TOA irradiance	[W m^{-2}]
$t = t^- \times t^+$	diffuse transmittance	dimensionless
R_{rs}	remote sensing reflectance	[sr^{-1}]
R^2	coefficient of determination	dimensionless
S_{total}	total score	dimensionless
T	direct transmittance from the surface to the sensor	dimensionless

Bibliography

Ahmad, Z., B. A., Franz, C.R., McClain, E.J., Kwiatkowska, J., Werdell, E.P., Shettle and B. N., Holben (2010). New aerosol models for the retrieval of aerosol optical thickness and normalized water-leaving radiances from the SeaWiFS and MODIS sensors over coastal regions and open oceans, Applied Optics, 49, 5545-5560.

Ahn, J.-H., and Y.-J., Park (2020). Estimating Water Reflectance at Near-Infrared Wavelengths for Turbid Water Atmospheric Correction: A Preliminary Study for GOCI-II, Remote Sensing, 12, https://doi.org/10.3390/rs12223791.

Al Shehhi, M.R., I., Gherboudj, J., Zhao and H., Ghedira (2017). Improved atmospheric correction and chlorophyll-a remote sensing models for turbid waters in a dusty environment, Remote Sensing of Environment, 133, 46-60.

Aryal, K., P.-W., Zhai, M., Gao, B.A., Franz, K., Knobelspiesse and Y., Hu (2024). Machine learning based aerosol and ocean color joint retrieval algorithm for multiangle polarimeters over coastal waters. Optics Express, 32, doi: 10.1364/OE.522794.

Babin, M., (2000), Coastal surveillance through observation of ocean colour (COASTLOOC). Final Report, Project ENV4-CT96-0310, 233 pp., Laboratoire de Physique et Chimie Marines, Villefranche-sur-mer, France.

Babin, M., A. D. Stramski, G. M. Ferrari, H. Claustre, A. Bricaud, G. Obelesky, and N. Hoepffner (2003a) Variations in the light absorption coefficients of phytoplankton, nonalgal particles and dissolved organic matter in coastal waters around Europe, J. Geophys. Res. 108, 3211, doi:10.1029/2001JC000882

Babin, M., A. Morel, V. Fournier-Sicre, F. Fell, and D. Stramski (2003b) Light scattering properties of marine particles in coastal and open ocean waters as related to the particle mass concentration, Limnol. Oceanogr. 28, 843-859.

Bai, R., X., He, Y., Bai, T., Li, Q., Zhu and F., Gong (2020), Characteristics of water leaving reflectance at ultraviolet wavelengths: radiative transfer simulations. Optics Express, 28, 29714-29729.

Bai R., He X., Bai Y., Gong F., Zhu Q., Wang D., and Li T. (2023), Atmospheric correction algorithm based on the interpolation of ultraviolet and shortwave infrared bands. Optics Express, 31, 6805-6826.

Bailey, S.W., and P.J., Werdell (2006). A multi-sensor approach for the on-orbit validation of ocean color satellite data products. Remote Sensing of Environment, 102, 12–23.

Bailey, S.W., B.A., Franz and P.J., Werdell (2010). Estimating of near-infrared water-leaving reflectance for satellite ocean color data processing, Optics Express, 18, 7521-7527.

Banzon, V.F., H.R., Gordon, C.P., Kuchinke, D., Antoine, K.J., Voss and R.H., Evans (2009). Validation of a SeaWiFS dust-correction methodology in the Mediterranean Sea: Identification of an algorithm-switching criterion, Remote Sensing of Environment, 113, 2689-2700.

Brajard, J., C., Jamet, C., Moulin and S., Thiria (2006). Use of a neurovariational inversion for retrieving oceanic and atmospheric constituents from ocean color imagery: Application to absorbing aerosols, Neural Networks, 19, 178-185.

Bricaud, A., A. Morel, M. Babin, K. Allali, and H. Claustre (1998). Variations in light absorption by suspended particles with chlorophyll concentration in oceanic (case 1) waters: Analysis and implications for bio-optical models, J. Geophys. Res. 103, 31,033-31,044.

Bulgarelli, B. and G., Zibordi, G. (2018a). Seasonal Impact of Adjacency Effects on Ocean Color Radiometry at the AAOT Validation Site. IEEE Geoscience and Remote Sensing Letters, 15, 488.

Bulgarelli, B., and G., Zibordi (2018b). On the detectability of adjacency effects in ocean color remote sensing of mid-latitude coastal environments by SeaWiFS, MODIS-A, MERIS, OLCI, OLI and MSI. Remote Sensing of Environment, 209, 423–438.

Bulgarelli, B., G., Zibordi, and F., Mélin (2018). On the minimization of adjacency effects in SeaWiFS primary data products from coastal areas. Optics Express, 26, A709–A728.

Burazerovic, D., R., Heylen, B., Geens, S., Sterckx, P., Scheunders (2013). Detecting the Adjacency Effect in Hyperspectral Imagery With Spectral Unmixing Techniques. IEEE J. Sel. Top. Appl. Earth Obs. Remote. Sens. 6(3), 1070-1078.

Castagna, A., and Q., Vanhellemont (2022). Sensor-agnostic adjacency correction in the frequency domain: application to retrieve water-leaving radiance from small lakes. ESA Living Planet Symposium 2022, abstract.

Carswell, T., M., Costa, R., Young, N., Komick, J., Gower and R., Sweeting (2017). Evaluation of MODIS-Aqua atmospheric correction and chlorophyll products of Western North American coastal waters based on 13 years of data, Remote Sensing, 9, 1063, doi: 10.3390/rs9101063.

Chomko, R.M., and H.R., Gordon (1998). Atmospheric correction of ocean color imagery: use of the Junge power-law aerosol size distribution with variable refractive index to handle aerosol absorption, Applied Optics, 37, 5560-5572.

Chomko, R.M., and H.R., Gordon (2001). Atmospheric correction of ocean color imagery: test of the spectral optimization algorithm with the Sea-viewing Wide Field-of-view Sensor, Applied Optics, 40, 2973-2984.

Chomko, R.M., H.R., Gordon, S., Maritorena and D.A., Siegel (2003). Simultaneous retrieval of oceanic and atmospheric parameters for ocean color imagery by spectral optimization: a validation, Remote Sensing of Environment, 84, 208-220.

Cohen, D., S. Stamnes, T. Tanikawa, E. R. Sommersten, J. J. Stamnes, J. K. Lotsberg, and K. Stamnes (2013). Comparison of discrete ordinate and Monte Carlo simulations of polarized radiative transfer in two coupled slabs with different refractive indices, Opt. Expr., 21, 9592-9614, 2013. DOI:10.1364/OE.21.009592.

Concha, J.A., M., Bracaglia and V.E., Brando (2021). Assessing the influence of different validation protocols on Ocean Colour match-up analyses, Remote Sensing of Environment, 259, https://doi.org/10.1016/j.rse.2021.112415.

Correa, K., E., Machu, J., Brajard, D., Diouf, S.M., Sall, and H., Demarcq (2023). Adaptation of a Neuro-Variational Algorithm from SeaWiFS to MODIS-Aqua Sensor for the Determination of Atmospheric and Oceanic Variables. Remote Sensing, 15, https://doi.org/10.3390/rs15143613

Diehl, P. and H. Haardt (1980). Measurement of the spectral attenuation to support biological re- search in a "plankton tube" experiment, Oceanol. Acta 3, 89-96.

Dierssen, H.M., R.A., Vandermeulen, B.B., Branes, A., Castagna, E., Knaeps and Q., Vanhellemont (2022). QWIP: A Quantitative Metric for Quality Control of Aquatic Reflectance Spectral Shape Using the Apparent Visible Wavelength, Frontiers in Remote Sensing, 3, doi: 10.3389/frsen.2022.869611

Diouf, D., A. Niang, J. Brajard, M. Crépon, and S. Thiria, (2013). Retrieving aerosol characteristics and sea-surface chlorophyll from satellite ocean color multi-spectral sensors using a neural-variational method. Remote Sensing of Environment, 130, 74–86.

Doerffer, R., and H., Schiller (2007) The MERIS case 2 water algorithm, International Journal of Remote Sensing, 28, 517-535.

Doerrfer, R. (2015). Algorithm Theoretical Bases Document (ATBD) for L2 processing of MERIS data of case 2 waters, reprocessing. MERIS Case 2 water ATBD 4th reproc, 55 pages.

El Hourany, R., M., Abboud-Abi Saab, G., Faour, O., Aumont, M., Crépon and S., Thiria (2019a). Estimation of secondary phytoplankton pigments from satellite observations using self-organizing maps (SOMs). Journal of Geophysical Research, 124, 1357–1378, https://doi.org/10.1029/2018JC014450

El Hourany, R., M., Abboud-Abi Saab, G., Faour, C., Mejia, M., Crépon, M., and S., Thiria (2019b). Phytoplankton diversity in the Mediterranean Sea from satellite data using self-organizing maps. Journal of Geophysical Research, 124, 5827–5843. https://doi.org/10.1029/2019JC015131

Fan, Y., W., Li, K.J., Voss, C.K., Gatebe, and K., Stamnes (2016). Neural network method to correct bidirectional effects in water-leaving radiance. Applied Optics, 55, 10-21, https://doi.org/10.1364/AO.55.000010.

Fan, Y., W. Li, C. K. Gatebe, C. Jamet, G. Zibordi, T. Schroeder, and K. Stamnes (2017). Atmospheric correction and aerosol retrieval over coastal waters using multilayer neural networks, Remote Sensing of the Environment, 199, 218-240, 2017.

Fan, Y., S., Li, X., Han and L., Stamnes (2020). Machine learning algorithms for retrievals of aerosol and ocean color products from FY-3D MERSI-II instrument, Journal of Quantitative Spectroscopy & Radiative Transfer, 250, https://doi.org/10.1016/j.jqsrt.2020.10704.

Fan, Y., W., Li, N., Chen, J.-H., Ahn, Y.-J., Park, S., Kratzer, T., Schroeder, J., Ishizaka, R., Chang and K., Stamnes (2021). OC-SMART: A machine learning based data analysis platform for satellite ocean color sensors, Remote Sensing of Environment, 253, https://doi.org/10.1016/j.rse.2020.112236.

Feng, H., D., Vandemark, J.W., Campbell, and B.N., Holben (2008). Evaluation of MODIS ocean color products at a northeast United States coast site near the Martha's Vineyard Coastal Observatory. International of Remote Sensing, 29, 4479–4497.

Feng, L., and C. Hu (2017), Land adjacency effects on MODIS Aqua top-of-atmosphere radiance in the shortwave infrared: Statistical assessment and correction. J. Geophys. Res. Oceans, 122, 4802–4818, doi:10.1002/2017JC012874

Fournier, G. and J. L. Forand (1994). Analytic phase function for ocean water. In Ocean Optics XII SPIE Vol. 2258, J. S. Jaffe (ed.), 194-201.

Frouin, R., B., Franz, A., Ibrahim, K., Knobelpiesse, Z., Ahmad, B., Cairns, J., Chowdhary, H.M., Dierssen, J., Tan, O., Dubovik, X., Huang, A.B., Davis, O., Kalashnikova, D.R., Thompson, L.A., Remer, E., Boss, O., Coddington, P.-Y., Deschamps, B.-C., Gao, L., Gross, O., Hasekamp, A., Omar, B., Pelletier, D., Ramon, F., Steinmetz and P.-W., Zhai (2019). Atmospheric correction of satellite ocean-color imagery during the PACE era, Frontiers in Earth Sciences, 7, doi: 10.3380/feart.2019.00145.

Gilerson, A., E., Herrera-Estrella, R., Foster, J., Agagliate, C., Hu, A., Ibrahim and B.A., Franz B (2022). Determining the Primary Sources of Uncertainty in Retrieval of Marine Remote Sensing Reflectance From Satellite Ocean Color Sensors, Frontiers in Remote Sensing, 3, doi: 10.3389/frsen.2022.857530.

Gordon, H.R. (1997). Atmospheric correction of ocean color imagery in the Earth Observing System era, Journal of Geophysical Research, 102, 17081-17106.

Gordon, H.R., and M., Wang (1994). Retrieval of water-leaving radiance and aerosol optical thickness over the ocean with SeaWiFS: a preliminary algorithm, Applied Optics, 443-452.

Gossn, J.I.; K.G., Ruddick, and A.I., Dogliotti (2019) Atmospheric Correction of OLCI Imagery over Extremely Turbid Waters Based on the Red, NIR and 1016 nm Bands and a New Baseline Residual Technique. Remote Sensing, 11, https://doi.org/10.3390/rs11030220.

Gossn, J.I., R., Frouin, A.I., Dogliotti (2021). Atmospheric Correction of Satellite Optical Imagery over the Río de la Plata Highly Turbid Waters Using a SWIR-Based Principal Component Decomposition Technique. Remote Sensing, 13, https://doi.org/10.3390/rs13061050.

Goyens, C., C., Jamet and T., Schroeder (2013). Evaluation of four atmospheric correction algorithms for MODIS-Aqua images over contrasted coastal waters, Remote Sensing of Environment, 131, 63-75.

Goyens, C., C., Jamet, and K., Ruddick (2013b). Spectral relationships for atmospheric correction. I. Validation of red and near infra-red marine reflectance relationships, Optics Express, 21, 21,162-21,175.

Goyens, C., C., Jamet, and K., Ruddick (2013c). Spectral relationships for atmospheric correction. II. Improving NASA's standard and MUMM near infra-red modeling schemes, Optics Express, 21, 21,176-21,187.

Hamre, B., S. Stamnes, K. Stamnes, and J.J. Stamnes (2014). A versatile tool for radiative trans- fer simulations in the coupled atmosphere-ocean system: Introducing AccuRT, Ocean Optics XXII, Portland, ME.

Han, B., H., Loisel, V., Vantrepotte, X., Mériaux, P., Bryère, S., Ouillon, D., Dessailly, Q., Xing and J., Zhu (2016). Development of a semi-analytical algorithm for the retrieval of suspended particulate matter from remote sensing over clear to very turbid waters, Remote Sensing, 8, doi: 10.3390/rs8030211.

H*ä*nel, G. (1976). The properties of atmospheric aerosol particles as functions of the relative humidity at thermodynamic equilibrium with the surrounding moist air, in Advances in Geophysics, H. E. Landsberg and J. V. Miehem, eds. (Academic), Vol. 19.

He, Q., and C., Chen (2014). A new approach for atmospheric correction of MODIS imagery in turbid coastal waters: a case study for the Pearl River Estuary. Remote Sens. Lett., 5, 249-257, DOI: 10.1080/2150704X.2014.898192

He, X., D. Pan, and Z. Mao (2004). Atmospheric correction of SeaWiFS imagery for turbid coastal and inland waters. Acta Oceanologica Sinica,23(4), 609-615.

He, X., D. Pan, Y. Bai, Q. Zhu, F. Gong (2007). Vector radiative transfer numerical model of coupled ocean-atmosphere system using matrix-operator method. Science in China Series D: Earth Sciences, 50(3), 442-452

He, X., Y. Bai, Q. Zhu, F. Gong (2010). A vector radiative transfer model of coupled ocean–atmosphere system using matrix-operator method for rough sea-surface. Journal of Quantitative Spectroscopy and Radiative Transfer, 111(10), 1426-1448

He, X., Y. Bai, D. Pan, J. Tang, and D. Wang (2012). Atmospheric correction of satellite ocean color imagery using the ultraviolet wavelength for highly turbid waters, Opt. Express, 20, 20754–20770.

He, X., Y. Bai, D. Pan, N. Huang, X. Dong, J. Chen, C.-T. A. Chen, Q. Cui (2013). Using geostationary satellite ocean color data to map the diurnal dynamics of suspended particulate matter in coastal waters. Remote Sensing of Environment, 133, 225-239.

He, X., T., Pan, Y., Bai, P., Shanmugam, D., Wang, T., Li, and F., Gong (2024). Intelligent atmospheric correction algorithm for polarization ocean color satellite measurements over the open ocean. IEEE Transactions on Geoscience and Remote Sensing, DOI: 10.1109/TGRS.2023.3348159

Heege, T., V., Kiselev, M., Wettle and N., Hung (2014). Operational multi-sensor monitoring of turbidity for the entire Mekong Delta. International Journal of Remote Sensing, 35, 2910. https://doi.org/10.1080/01431161.2014.890300

Hieronymi, M., S., Bi, D., Müller, E.M., Schütt, D., Behr, C., Brockmann, C., Lebreton, F., Steinmetz, K., Stelze and Q., Vanhellemont (2023). Ocean color atmospheric correction methods in view of usability for different optical water types, Frontiers in Marine Science, doi: 10.3389/fmars.2023.1129876

Holben, B., T.F., Eck, I., Slutsker, D., Tanré, J.P., Buis, A., Setzer, E., Vermote, J.A., Reagan, Y.J., Kaufman, T., Nakajima, F., Lavenu, I., Jankowiak and A., Smirnov (1998). AERONET - A federated instrument networks and data archive for aerosol characterization, Remote Sensing of Environment, 66, 1-16.

Holben, B. N., D. Tanre, A. Smirnov, T. F. Eck, I. Slutsker, N. Abuhassan, W. W. Newcomb, J. Schafer, B. Chatenet, F. Lavenue, Y. J. Kaufman, J. Vande Castle, A. Setzer, B. Markham, D. Clark, R. Frouin, R. Halthore, A. Karnieli, N. T. O'Neill, C. Pietras, R. T. Pinker, K. Voss, and G. Zibordi (2001). An emerging ground-based aerosol climatology: aerosol optical depth from AERONET, J. Geophys. Res. 106, 12067-12097.

Hu, C., K.L., Carder and F.E., Muller-Karger (2000). Atmospheric correction of SeaWiFS imagery over turbid coastal waters: a practical method, Remote Sensing of Environment, 74, 195-206.

Hu, Y.-X., B. Wielicki, B. Lin, G. Gibson, S.-C. Tsay, K. Stamnes, and T. Wong (2000). Delta-fit: A fast and accurate treatment of particle scattering phase functions with weighted singular-value decomposition least squares fitting, J. Quant. Spectrosc. Radiat. Transfer, 65, 681-690.

Ibrahim, A., B.A., Franz, Z., Ahmad and S.W., Bailey (2019). Multiband atmospheric correction algorithm for ocean color retrievals, Frontiers in Earth Science, 7, doi: 10.3389/feart.2019.00116.

Ibrahim, A., B.A., Franz, A.M., Sayer, K., Knobelspiesse, M., Zhang, S.W., Bailey, L.I.W., McKinna, M., Gao and P.J., Werdell (2022). Optimal estimation framework for ocean color atmospheric correction and pixel-level uncertainty quantification, Applied Optics, 61, 6453-6475.

IOCCG (2006). Remote Sensing of Inherent Optical Properties: Fundamentals, Tests of Algorithms, and Applications. Lee, Z.-P. (ed.), Reports of the International Ocean-Colour Coordinating Group, No. 5, IOCCG, Dartmouth, Canada.

IOCCG (2010). Atmospheric Correction for Remotely-Sensed Ocean-Colour Products. Wang, M. (ed.), Reports of the International Ocean-Colour Coordinating Group, No. 10, IOCCG, Dartmouth, Canada.

IOCCG (2019). Uncertainties in Ocean Colour Remote Sensing. (ed. Mélin F.) Dartmouth, NS, Canada, International Ocean-Colour Coordinating Group (IOCCG), 164pp. Reports of the International Ocean-Colour Coordinating Group, No. 18. http://dx.doi.org/10.25607/OBP-696

Jaelani, L.M., B., Matsushita, W., Yang and T., Fukushima (2015). An improved atmospheric correction for applying MERIS data to very turbid inland waters. International Journal of Applied Earth Observation and Geoinformation, 39, 128-141.

Jamet., C., S., Thiria, C., Moulin and M., Crepon (2004). Use of a neurovariational inversion for retrieving oceanic and atmospheric constituents from ocean color imagery: a feasibility study, Journal of Atmospheric and Oceanic Technology, 22, 460-475.

Jamet., C., H., Loisel, C.P., Kuchinke, K., Ruddick, G., Zibordi and H., Feng (2011). Comparison of three SeaWiFS atmospheric correction algorithms for turbid waters using AERONET-OC measurements, Remote Sensing of Environment, 115, 1955-1965.

Jamet, C., A., Ibrahim A, Z., Ahmad, F., Angelini, M., Babin, M.J., Behrenfeld, E., Boss, B., Cairns, J., Churnside, J., Chowdhary, A.B., Davis, D., Dionisi, L., Duforêt-Gaurier, B., Franz, R., Frouin, M., Gao, D., Gray, O., Hasekamp, X., He, C., Hostetler, O.V., Kalashnikova, K., Knobelspiesse, L., Lacour, H., Loisel, V., Martins, E., Rehm, L., Remer, I., Sanhaj, K., Stamnes, S., Stamnes, S., Victori, P.J., Werdell and P.-W. Zhai (2019). Going Beyond Standard Ocean Color Observations: Lidar and Polarimetry. Frontiers in Marine Science, 6:251. doi: 10.3389/fmars.2019.00251

Jiang, L., and M., Wang (2014). Improved near-infrared ocean reflectance correction algorithm for satellite ocean color data processing, Optics Express, 22, doi:10.1364/OE.22.021657

Jiang, D., J., Scholze, X., Liu, S., Simis, K. , Stelzer, D., Müller, P., Hunter, A., Tyler, and E., Spyrakos (2023). A data-driven approach to flag land-affected signals in satellite derived water quality from small lakes. Int. J. Appl. Earth Obs. Geoinformation, 117, 103188.

Jin, Z. and K. Stamnes (1994). Radiative transfer in nonuniformly refracting layered media: atmosphere- ocean system, Appl. Opt. 33, 431–442.

Keshava, N. (2004). Distance metrics and band selection in hyperspectral processing with applications to material identification and spectral libraries, IEEE Transactions on Geoscience and Remote Sensing, 42, 1552-1565.

Kiselev, V., B., Bulgarelli, and T., Heege (2015). Sensor independent adjacency correction algorithm for coastal and inland water systems. Remote Sensing of Environment, 157, 85-95.

Knaeps, E., A.I., Dogliotti, D., Raymaekers, K., Ruddick and S., Sterckx (2012). *In situ* evidence of non-zero reflectance in the OLCI 1020 nm band for a turbid estuary, Remote Sensing of Environment, 120, 133-144.

Koepke, P., J., Gasteiger, and M., Hess (2015). Technical note: optical properties of desert aerosol with non-spherical mineral particles: data incorporated to OPAC. Atmospheric Chemistry and Physics, 15, 5947–5956. http://dx.doi.org/10.5194/acp-15-5947-2015.

Kohonen, T. (2013). Essentials of the self-organizing map, Neural Networks, 37, 52-65.

Kou, L., D. Labrie, and P. Chylek (1993). Refractive indices of water and ice in the 0.65 µm to 2.5 µm spectral range, Appl. Opt. 32, 3531-3540.

Kruse, F., A., Lefkoff, J., Boardman, J., Heidebrecht, A., Shapiro, P., Barloon and A., Goetz (1993). The spectral image processing system -interactive visualization and analysis of imaging spectrometer data, Remote Sensing of Environment, 44, 145-163.

Kuchinke, C.P., H.R., Gordon, L.W., Harding, and K.J., Voss (2009). Spectral optimization for constituent retrieval in case 2 waters: II Implementation and performance, Remote Sensing of Environment, 13, 571-587.

Lavender, S.J., M.H., Penkerton, G.F., Moore, J., Aiken and D., Blondeau-Patissier (2005). Modification to the atmospheric correction of SeaWiFS ocean color images over turbid waters, Continental Shelf Research, 25, 539-555.

Li, W., K. Stamnes, R. Spurr, and J. J. Stamnes (2008). Simultaneous Retrieval of Aerosols and Ocean Properties: A Classic Inverse Modeling Approach. II. SeaWiFS Case Study for the Santa Barbara Channel, Int. J. Rem. Sens., DOI: 10.1080/01431160802007632 29, 5689-5698.

Liu, H., X., He, Q., Li, S., Kratzer, J., Wang, T., Shi, Z., Hu, C., Yang, S., Hu, Q., Zhou and G., Wu (2021). Estimating ultraviolet reflectance from visible bands in ocean colour remote sensing, Remote Sensing of Environment, 258, https://doi.org/10.1016/j.rse.2021.112404.

Loisel, H. and A. Morel (1998). Light scattering and chlorophyll concentration in case 1 waters: a re-examination, Limnol. Oceanogr. 43, 847-857.

Loisel, H., L., Duforet, D., Dessailly, M., Chami, and P., Dubuisson (2008). Investigation of the variations in the water leaving polarized reflectance from the POLDER satellite data over two biogeochemical contrasted oceanic areas, Optics Express, 16, 12,905-12,918

Lolli, S. (2023). Machine Learning Techniques for Vertical Lidar-Based Detection, Characterization, and Classification of Aerosols and Clouds: A Comprehensive Survey. Remote Sens. 2023, 15, 4318. https:// doi.org/10.3390/rs15174318

Mao, Z., B., Tao, P., Chen, J., Chen, Z., Hao, Q., Zhu and H., Huang (2020). Atmospheric correction of satellite ocean color remote sensing in the presence of high aerosol loads, 12, https://doi.org/10.3390/rs12010031.

Maritorena, S., D.A., Siegel and A.R., Peterson (2002). Optimization of a semianalytical ocean color model for global-scale applications. Applied Optics, 41, 2705-2714.

McCave, I. N. (1983). Particulate size spectra, behavior, and origin of nephloid layers over the Nova Scotia continental rise, J. Geophys. Res. 88, 7647 - 7660.

Melin, F. (2022). Validation of ocean color remote sensing reflectance data: Analysis of results at European coastal sites, Remote Sensing of Environment, 280, 113153.

Melin, F., P., Colandrea, P., de Vis and S.E., Hunt (2022). Sensitivity of ocean color atmospheric correction to uncertainties in ancillary data: a global analysis with SeaWiFS data, IEEE Transactions on Geosciences and Remote Sensing, 60, 1-18, doi: 10.1109/TGRS.2022.315040.

Mobley, C.D. (1989). A numerical model for the computation of radiance distributions in natural waters with wind-roughened surfaces, Limnol. Oceanogr., 34(8), 1989, 1473-1483

Mobley, C. D. (1994). Light and Water: Radiative Transfer in Natural Waters, Academic Press, San Diego, CA.

Mobley, C. D., B. Gentili, H. R. Gordon, Z. Jin, G. W. Kattawar, A. Morel, P. Reinersman, K. Stamnes, and R. H. Stavn, (1993). Comparison of numerical models for computing underwater light fields. Appl. Opt., 32, 7484-7504

Mobley, C. D., L. K. Sundman, and E. Boss (2002). Phase function effects on oceanic light fields, Appl. Opt. 41, 1035–1050.

Mobley, C.D., J., Werdell, B., Franz, Z., Ahmad and S., Bailey (2016). Atmospheric correction for satellite ocean color radiometry - A tutorial and documentation of the algorithms used by the NASA Ocean Biology Processing Group, NASA report, 80 pages.

Moore, G.F., J., Aiken, and S.J., Lavender (1999). The atmospheric correction of water color and the quantitative retrieval of suspend particulate matter in case II waters: Application to MERIS, International Journal of Remote Sensing, 20, 1713-1733.

Moore, T.S., J.W., Campbell, M.D., Dowell (2009). A class-based approach to characterizing and mapping the uncertainty of the MODIS ocean chlorophyll product, Remote Sensing of Environment, 113, 2424-2430, https://doi.org/10.1016/j.rse.2009.07.016.

Morel, A. (1974). Optical properties of pure water and pure seawater, in Optical Aspects of Oceanography, N. G. Jerlov and E. S. Nielsen (eds.), pp. 1–24, Academic, San Diego, Calif.

Morel, A., D., Antoine, and B., Gentili (2002). Bidirectional reflectance of oceanic waters: accounting for Raman emission and varying particle scattering phase function. Applied

Optics, 41, 6289–6306. http://dx.doi.org/10.1364/AO.41.006289.

Moulin, C., H.R., Gordon, V.F., Banzon and R.H., Evans (2001a). Assessment of Saharan dust absorption in the visible from SeaWiFS imagery, Journal of Geophysical Research, 106, 18239-18249.

Moulin, C., H.R., Moulin, R.M., Chomko, V.F., Banzon and R.H., Evans (2001b). Atmospheric correction of ocean color imagery through thick layers of Saharan dust, Geophysical Research Letters, 28, 5-8.

Müller, D., J., Krasemann, R.J., Brewin, C., Brockmann, P.-Y., Deschamps, R., Doerffer, N., Fomferra, B.A., Franz, M.G., Grant, S.B., Groom, F. Mélin, T., Platt, P., Regner, S., Sathyendranath, F., Steinmetz and J., Swinton (2015). The Ocean Colour Climate Initiative: I. A methodology for assessing atmospheric correction processors based on in-situ measurements, Remote Sensing of Environment, 162, 242-256.

Niang, A., F., Badran, C., Moulin, M., Crépon, and S., Thiria (2006). Retrieval of aerosol type and optical thickness over the Mediterranean from SeaWiFS images using an automatic neural classification method. Remote Sensing of Environment, 100, 82–94. https://doi.org/10.1016/J.RSE.2005.10.005

Nobileau, D., and D., Antoine (2005). Detection a blue-absorbing aerosols using near infrared and visible (ocean color) remote sensing observations, Remote Sensing of Environment, 95, 368-387.

Oo, M., M., Vargas, A., Gilerson, B., Gross, F., Moshary and S., Ahmed (2008). Improving atmospheric correction for highly productive coastal waters using the shortwave infrared retrieval algorithm with water-leaving reflectance constraints at 412 nm, Applied Optics, 2008, 47, 3846-3859.

O'Reilly, J.E., S., Maritonera, B.G., Mitchell, D.A., Siegel, K.L., Carder, S.A., Garver, M., Kahru and C., McClain (1998). Ocean color chlorophyll algorithms for SeaWiFS, Journal of Geophysical Research, 103, 24,937-24,953.

O'Reilly, J.E., and P.J., Werdell (2019). Chlorophyll algorithms for ocean color sensors -OC4, OC5 & OC6, Remote Sensing of Environment, 229, 32-47.

Pahlevan, N., A., Mangin, S.V., Balasubramian, B., Smith, K., Alikas, K., Arai, C., Barbosa, S., Bélanger et al. (2021). ACIX-Aqua: A global assessment of atmospheric correction methods for Landsat-8 and Sentinel-2 over lakes, rivers, and coastal waters. Remote Sensing of Environment, 258, https://doi.org/10.1016/j.rse.2021.112366

Pan, Y., and S., Bélanger (2024). Genetic Algorithm for Atmospheric Correction (GAAC) of water bodies impacted by adjacency effects, Remote Sensing of Environment, 317, https://doi.org/10.1016/j.rse.2024.114508

Pan, Y., S., Bélanger and Y., Huot (2022). Evaluation of Atmospheric Correction Algorithms over Lakes for High-Resolution Multispectral Imagery: Implications of Adjacency Effect. Remote Sensing, 14, 2979, https://doi.org/10.3390/rs14132979

Pan, Y., F., Shen and W., Verhoef (2017). An improved spectral optimization algorithm for atmospheric correction over turbid coastal waters: A case study from the Changjiang (Yangtze) estuary and the adjacent coast. Remote Sensing of Environment, 191, 197-214.

Park, Y.-J. and K., Ruddick (2005). Model of remote-sensing reflectance including bidirectional effects for case 1 and case 2 waters. Applied Optics, 44 , 1236-1249

Petzold, T. L. (1972). Volume scattering functions for selected ocean waters, Visibility Lab. Report, Scripps Inst. Oceanogr., 72–78.

Pitarch J., Vittorio Ernesto Brando, Marco Talone, Constant Mazeran, Davide D'Alimonte, Tamito Kajiyama, Ewa Kwiatkowska, David Dessailly, Juan Ignacio Gossn (2025). Analytical modeling and correction of the ocean colour bidirectional reflectance across water types, Remote Sensing of Environment, https://doi.org/10.1016/j.rse.2025.114920.

Pope, R. M. and E. S. Fry (1997). Absorption spectrum (380-700 nm) of pure water, II, Integrating cavity measurements, Appl. Opt. 36, 8710 - 8723.

Qiao, F., J., Chen, Z., Mao, B., Han, Q., Song, Y., Xu, and Q.A., Zhu (2021). Novel Framework of Integrating UV and NIR Atmospheric Correction Algorithms for Coastal Ocean Color Remote Sensing. Remote Sensing, 13, https://doi.org/10.3390/rs13214206

Robinson, W.D., B.A., Franz, F.S., Patt, S.W., Bailey, and P.J., Werdell (2003). Masks and flags updates. In S. B. Hooker, & E. R. Firestone (Eds.), SeaWiFS Postlaunch Technical Report Series, Chap.6, NASA/TM-2003-206892. Greenbelt, Maryland, NASA Goddard Space Flight Center volume 22, 34–40.

Ruddick, K., F., Ovidio, and M., Rijkeboer (2000). Atmospheric correction of SeaWiFS imagery for turbid coastal and inland waters. Applied Optics, 39, 897–912.

Ruddick, K.G., V., De Cauwer, Y.-J., Park, and G., Moore (2006). Seaborne measurements of near infrared water-leaving reflectance: The similarity spectrum for turbid waters. Limnology and Oceanography, 51, 1167. https://doi.org/10.4319/lo.2006.51.2.1167

Ruddick, K.G. and the COASTCOLOUR team (2010). DUE CoastColour Round Robin Protocol v1.2, 27 pages.

Santer, R., and C., Schmechtig (2000). Adjacency effects of water surfaces: primary scattering approximation and sensitivity study. Applied Optics, 39(3), 361-375.

Santer, R., and F., Zagolski (2009). Improved Contrast between Ocean and Land (ICOL) algorithm theoretical basis document. Tech. Rep. Université du Littoral Côte d'Opale, Wimereux, France, 15 p.

Schamberger, L., A., Minghelli, M., Chami, and F., Steinmetz (2022). Improvement of atmospheric correction of satellite Sentinel-3/OLCI data for oceanic waters in presence of sargassum, Remote Sensing, 14, 386. https://doi.org/10.3390/rs14020386

Schiller, H. and R., Doerffer (1997). Neural network for emulation of an inverse model – operational derivation of Case II water properties from MERIS data. International Journal of Remote Sensing, 20, 1735-1746.

Schroeder, T., Fischer, J., Schaale, M., & Fell, F. (2003). Artificial-neural-network-based atmospheric correction algorithm: application to MERIS data. Proc.SPIE 4892, Ocean Remote Sensing and Applications. https://doi.org/10.1117/12.467293

Schroeder, T. (2005). Fernerkundung von Wasserinhaltsstoffen in Küstengewässern mit MERIS unter Anwendung expliziter und impliziter Atmosphärenkorrekturverfahren (Remote sensing of coastal waters with MERIS on basis of explicit and implicit atmospheric correction algorithms), Doctoral Dissertation, Freie Universität Berlin]. https://doi.org/10.17169/refubium-11210

Schroeder, T., I. Behnert, M. Schaale, J. Fischer, and R. Doerffer (2007). Atmospheric correction algorithm for MERIS above case-2 water, International Journal of Remote Sensing, 28, 1469-1486.

Schroeder, T., M., Schaale, J., Lovell and D., Blondeau-Patissier (2022). An ensemble neural network atmospheric correction for Sentinel-3 OLCI over coastal waters providing inherent model uncertainty estimation and sensor noise propagation, Remote Sensing of Environment, 270, https://doi.org/10.1016/j.rse.2021.112848.

Segelstein, D. J. (1981). The complex refractive index of water, M. S. Thesis – Department of Physics. University of Missouri-Kansas City.

Shettle, E. P. and R. W. Fenn (1979). Models for the Aerosols of the Lower Atmosphere and the Effects of Humidity Variations on their Optical Properties (Air Force Geophysics Laboratory, Hanscomb AFB, Mass.).

Shi, W., and M., Wang (2007). Detection of turbid waters and absorbing aerosols for the MODIS ocean color data processing, Remote Sensing of Environment, 110, 149-161.

Siegel, D.A., M., Wang, S., Maritorena and W., Robinson (2000). Atmospheric correction of satellite ocean color imagery: the black pixel assumption, Applied Optics, 39, 3582-3591.

Singh, R.K., Shanmugam, P., (2014). A novel method for estimation of aerosol radiance and its extrapolation in the atmospheric correction of satellite data over optically complex oceanic waters. Remote Sens. Environ. 142, 188–206. https://doi.org/10.1016/j.rse.2013.12.001.

Singh; R.K., P., Shanmugam, X., He and T., Schroeder (2019). UV-NIR approach with non-zero water-leaving radiance approximation for atmospheric correction of satellite imagery in inland and coastal zones, Optics Express, 27, A1118-A1145, https://doi.org/10.1364/OE.27.0A1118.

Smith, R. C. and K. S. Baker (1981). Optical properties of the clearest natural waters (200-800nm), Appl. Opt. 20, 177–184.

Sogandares, F. M. and E. S. Fry (1997). Absorption spectrum (340-640 nm) of pure water. I. Photothermal measurements, Appl. Opt. 36, 8699–8709.

Song, Z., He, X., Bai, Y., Wang, D., Hao, Z., Gong, F., Zhu, Q. (2020). Changes and predictions of vertical distributions of global light-absorbing aerosols based on CALIPSO observation. Remote Sens. 12 (18), 3014.

Song, Z., He, X., Bai, Y., Wang, D., Gong, F., Zhu, Q., Li, T., Li, H. (2022). Effect of the vertical distribution of absorbing aerosols on the atmospheric correction for satellite ocean color remote sensing. IEEE Transactions on Geosciences and Remote Sensing. 60, 1–12.

Song, Z., X. He, Y. Bai, X. Dong, D. Wang, T. Li, Q. Zhu, and F. Gong (2023). Atmospheric correction of absorbing aerosols for satellite ocean color remote sensing over coastal waters. Remote Sensing of Environment, 290, 113552.

Ssenyonga, T., Ø, Frette, B., Hamre, K., Stamnes, D., Muyimbwa, N., Ssebiyonga, and J.J, Stamnes (2021). A New Algorithm for Simultaneous Retrieval of Aerosols and Marine

Parameters. Algorithms, 15, https://doi.org/10.3390/a15010004

Stamnes, K., W., Li, B., Yan, H., Eide, A., Barnard, W.S., Pegau and J.J., Stamnes (2003). Accurate and self-consistent ocean color algorithm: simultaneous retrieval of aerosol optical properties and chlorophyll concentrations, Applied Optics, 42, 939-951.

Stamnes, K., G.E., Thomas, and J.J., Stamnes (2017). Radiative Transfer in the Atmosphere and Ocean, Cambridge University Press, second edition.

Stamnes, K., B., Hamre, S., Stamnes, N., Chen, Y., Fan, W., Li, Z., Lin, and J. J., Stamnes (2018). Progress in forward-inverse modeling based on radiative transfer tools for coupled atmosphere-snow/ice-ocean systems: A review and description of the AccuRT model, Applied Sciences, 8, 2682.

Steinmetz, F.; Deschamps, P.-Y. & Ramon, D. Atmospheric correction in presence of sun glint: application to MERIS (2011). Optics Express, Optical Society of America, 19, 9783-9800.

Stephens, G.L, , D.G., Vane, R.J., Boain, G.G., Mace, K., Sassen, Z., Wang, A.J., Illingworth, E.J., O'connor, W.B.,Rossow, S.L., Durden and S.D., Miller (2002). The CloudSat mission and the A-Train: A new dimension of space-based observations of clouds and precipitation. Bulletin of the American Meteorological Society, 83, :1771-90.

Sterckx, S., R., Knaeps, K., Ruddick (2011). Detection and correction of adjacency effects in hyperspectral airborne data of coastal and inland waters: the use of the near infrared similarity spectrum. International Journal of Remote Sensing, 32(21), 6479-6505.

Sterckx, S., E., Knaeps, S., Kratzer, and K., Ruddick (2015). SIMilarity Environment Correction (SIMEC) applied to MERIS data over inland and coastal waters. Remote Sensing of Environment, 157, 96-110.

Stumpf, R. P., Arnone, R. A., Gould, R. W., and Ransibrahmanakul, V. (2003). A partially coupled ocean-atmosphere model for retrieval of water-leaving radiance from SeaWiFS in coastal waters. In Hooker, S. B. and Firestone, E. R., editors, NASA/TM-2003-206892, volume 22, pages 51{59, Greenbelt, Maryland, NASA Goddard Space Flight Center.

Subirade, C., C., Jamet, M., Duy Tran, V., Vantrepotte, and B., Han (2024). Evaluation of twelve algorithms to estimate suspended particulate matter from OLCI over contrasted coastal waters. Optics Express, 32, 45,719-45,744.

Thomas, G. E. and K. Stamnes (1999). Radiative Transfer in the Atmosphere and Ocean, Cambridge University Press, 1999; second edition.

Van der Zande, D., Q., Vanhellemont, and K., Ruddick (2016). Validation of Landsat-8/OLI for ocean colour applications with AERONET-OC sites in Belgian coastal waters, Proceedings of the 2016 Ocean Optics Conference, Victoria, BC, Canada, 23-28 October 2016.

Vanhellemont, Q., K., Ruddick (2021). Atmospheric correction of Sentinel-3/OLCI data for mapping of suspended particulate matter and chlorophyll-a concentration in Belgian turbid coastal waters, Remote Sensing of Environment, 256, 112284.

Vantrepotte, V., H. Loisel, D. Dessailly, X. Mériaux (2012), Optical classification of contrasted coastal waters, Remote Sensing of Environment, 123, 306-323, https://doi.org/10.1016/j.rse.2012.03.004.

Wang, M., and W., Shi (2005). Estimation of the ocean contribution at the MODIS near-infrared wavelengths along the east coast of the U.S.: Two case studies, Geophysical Research Letters, 32, doi: 13160.11029/12005GL022917.

Wang, M., and W., Shi (2007). The NIR-SWIR combined atmospheric correction approach for MODIS ocean color data processing, Optics Express, 15, 15722-15733.

Wang, M., and W., Shi 2012). Sensor noise effects of the SWIR bands on MODIS-derived ocean color products, IEEE Transactions on Geoscience and Remote Sensing, 50, 3280-3292.

Wei, J., Z.P., Lee and S., Shang (2016). A system to measure the data quality of spectral remote-sensing reflectance of aquatic environments, Journal of Geophysical Research, 121, 8189-8207, doi: 10.1002/2016JC012126.

Weitkamp, C. (2005). LIDAR : range-resolved optical remote sensing of the atmosphere editor, Springer series in optical sciences, ISSN 0342-4111 ; 102

Werdell P.J and S.W. Bailey (2005). An improved in-situ bio-optical data set for ocean color algorithm development and satellite data product validation, Remote Sensing of Environment, 98, doi:10.1016/j.rse.2005.07.001

Werdell, P.J., B.A., Franz and S.W. Bailey (2010). Evaluation of shortwave infrared atmospheric correction for ocean color remote sensing of Chesapeake Bay, Remote Sensing of Environment, 114, 2238-2247.

Xue, C., S., Chen, Z.-P., Lee, L., Hu, X., Shi, M., Lin, J., Liu, C., Ma, Q., Song and T., Zhang (2021). Iterative near-infrared atmospheric correction scheme for global coastal waters, ISPRS Journal of Photogrammetry and Remote Sensing, 179, 92-107, https://doi.org/10.1016/j.isprsjprs.2021.07.005.

Yan, B., K. Stamnes, W. Li, B. Chen, J. J. Stamnes, and S. C. Tsay (2002). Pitfalls in atmospheric correction of ocean color imagery: How should aerosol optical properties be computed? Appl. Opt. 41, 412-423.

Zhang, M., C., Hu, J., Cannizzaro, D., English, B.B., Barnes, P., Carlson and L., Yarbro (2018). Comparison of two atmospheric correction approaches applied to MODIS measurements over North American waters, Remote Sensing of Environment, 216, 442-455.

Zhang, M., C., Hu and B.B., Barnes (2019). Performance of POLYMER Atmospheric Correction of Ocean Color Imagery in the Presence of Absorbing Aerosols, IEEE Transactions on Geoscience and Remote Sensing, 57, 6666-6674, doi: 10.1109/TGRS.2019.2907884.

Zibordi, G., B., Holben, F., Mélin, J.-F., Berthon, I., Slutsker, D., Giles, D., Vandemark, G., Feng, K., Rutledge, G., Schuster, A., Al Mandoos (2006). A network for standardized ocean color validation measurements, EOS Transaction AGU, 87, 293-304.

Zibordi, G., Berthon, J. -F., Mélin, F., D'Alimonte, D., & Kaitala, S. (2009a). Validation of satellite ocean color primary products at optically complex coastal sites: Northern Adriatic Sea, Northern Baltic Proper and Gulf of Finland. Remote Sensing of Environment, 113, 2574–2591.

Zibordi, G., B., Holben, I., Slutsker, D., Giles, D., D'Alimonte, F., Mélin, J.-F., Berthon, D., Vandemark, H., Feng, G., Schuster, B.E., Fabbri, S., Kaitala and J., Sepala (2009b).

Aeronet-OC: A network for the validation of ocean color primary products. Journal of the Atmospheric and Oceanic Technology, 26, 1634–1651.

Zibordi, G., F., Mélin, J.-F., Berthon and M., Talone (2015). In situ autonomous optical radiometry measurements for satellite ocean color validation in the Western Black Sea, Ocean Science, 11, 275-286.

Zibordi, G., B. N., Holben, M., Talone, D., D'Alimonte, I., Slutsker, D.M., Giles, and M.G., Sorokin (2021). Advances in the Ocean Color Component of the Aerosol Robotic Network (AERONET-OC), Journal of Atmospheric and Oceanic Technology, 38(4), 725-746.